Modelling of excess pore pressure accumulation in sand around cyclically loaded foundations

Von der Fakultät für Bauingenieurwesen und Geodäsie
der Gottfried Wilhelm Leibniz Universität Hannover
zur Erlangung des Grades

Doktor-Ingenieur
Dr.-Ing.

genehmigte Dissertation von

Jann-Eike Sören Saathoff

2023

Die vorliegende Arbeit wurde als Dissertation im Rahmen des Promotionsverfahrens an der Fakultät für Bauingenieurwesen und Geodäsie der Leibniz Universität Hannover eingereicht und angenommen.

Referent: Prof. Dr.-Ing. Martin Achmus
Korreferent: Prof. Subhamoy Bhattacharya, PhD (University of Surrey, UK)
Kommissionsmitglied: Prof. Dr.-Ing. Arndt Hildebrandt
Vorsitz: Prof. Dr. sc. nat. ETH Insa Neuweiler

Tag der Promotion: 15.12.2022

To my beloved wife.

Gratiam ago vobis, qui mihi auxiliati estis meque adiuvistis.

Vorwort des Herausgebers

Die für den Ausbau der Erneuerbaren Energien wichtige Installation von Windenergieanlagen auf dem Meer bzw. Offshore hat neue Herausforderungen für die Geotechnik gebracht. Aufgrund der speziellen Belastungsbedingungen von Offshore-Windenergieanlagen (große Wind- und Wellenlasten auf Strukturen mit relativ geringem Eigengewicht) treten neue Fragestellungen hinsichtlich der Bemessung der Gründungselemente in den Fokus, mit denen wir uns am Institut mittlerweile seit vielen Jahren beschäftigen. Von besonderer Relevanz ist dabei, dass Offshore-Gründungsstrukturen intensiv zyklisch beansprucht werden. Daraus resultierende Effekte sind die Akkumulation von Porenwasserüberdrücken, wodurch die Tragfähigkeit der Struktur temporär reduziert wird, sowie die Akkumulation bleibender Verformungen mit zunehmender Lastzyklenzahl.

In den Bemessungsverfahren für Offshore-Gründungsstrukturen werden diese Effekte in stark vereinfachter Form überschlägig (und meist konservativ) berücksichtigt. In bestimmten Fällen ist jedoch eine genauere Prognose wünschenswert bzw. gefordert. Dafür werden explizite Berechnungsverfahren eingesetzt, in welchen die Ergebnisse zyklischer Elementversuche als Eingabewerte einer numerischen Simulation verwendet werden. Diesbezüglich gibt es bislang jedoch kein anerkanntes und allgemein einsetzbares Berechnungsverfahren. Die in Praxisprojekten eingesetzten und in der Literatur zum Teil dokumentierten Verfahren sind überdies meist nicht vollständig transparent.

Hier setzt die Arbeit von Herrn Saathoff an. Er hat eine Methodik entwickelt, welche auf Grundlage der Ergebnisse zyklischer Laborversuche (im Wesentlichen zyklischer Einfachscherversuche) eine Prognose von akkumulierten Porenwasserüberdrücken im Sandboden um eine zyklisch belastete Gründung ermöglicht. Ein wichtiges Ziel war, dass die Methode möglichst einfach und damit in der Praxis einsetzbar sein sollte. Sie ist deshalb modular aufgebaut, d. h. in jedem Teilschritt der Berechnung können Teilmodule gegen solche mit unterschiedlichen Annahmen oder Idealisierungsgraden ausgetauscht und damit gegebenenfalls verfeinert werden. Am Beispiel eines Monopilesystems werden die Auswirkungen unterschiedlicher Annahmen in den Teilmodulen untersucht und bewertet. Damit hat Herr Saathoff einen wichtigen Beitrag zur Prognose von Porenwasserüberdrücken infolge zyklischer Belastungen geliefert.

Eine abschließende Validierung der entwickelten Methodik steht zwar noch aus, weil entsprechende Versuchsdaten fehlen. Sie stellt aber eine sehr gute Basis für die Entwicklung eines grundsätzlich auf beliebige Gründungsstrukturen anwendbaren, transparenten und vergleichsweise einfach handhabbaren Verfahrens zur Prognose infolge zyklischer Belastung akkumulierter Porenwasserüberdrücke dar.

Martin Achmus

Author's preface

The cyclic assessment is an essential part within the design of offshore foundations, although it is still a challenging subject for offshore engineers. Even if research on this topic is performed for over 50 years, no general applicable method is available due to the inherent complexity of the soil-structure interaction. Independent of structure type and soil, an efficient cyclic assessment is mandatory for an economical design. The use of numerical methods is a good way to achieve this goal and, above all, offers many different modelling possibilities. There are usually several simplifications related to the choice of the different (cyclical) approaches. The influences of these decisions are generally little known or unknown.

This uncertainty was the basis for the presented elaboration. The method developed is based on a systematic evaluation of various existing approaches and is a step towards a more simplified procedure that is robust and widely applicable considering this complex subject. The focus lies on performance and evaluation of cyclic laboratory tests and on the correct implementation in finite element analysis. An approach for practical applications is presented, which is thoroughly studied for the first time by the example of sandy material. The method is both modular and directly applicable to other soil types and layered soils.

My special thanks go to Prof. Dr.-Ing. Martin Achmus, who not only gave me the opportunity to do research on this topic, but from whom I was also able to learn many skills. The possibility to get the necessary support from him at any time is very much appreciated and made my work much easier. Moreover, I want to thank Prof. Bhattacharya as co-examiner for his valuable assessment. I also want to thank Prof. Dr.-Ing. Arndt Hildebrandt as member of the committee and Prof. Dr. sc. nat. ETH Insa Neuweiler acting as head of the committee.

I would like to thank my colleagues for their support and the pleasant atmosphere at the institute. A special thanks goes to Dr.-Ing. Klaus Thieken, who provided valuable advice and who was always available for long and in-depth discussions. Lively exchanges about numerical problems with Dr.-Ing. Patrick Gütz also contributed to the success of this work, which I would like to acknowledge here.

Above all, I want to thank my wife for her tireless support; without her this work would not have been possible. The gratitude for this is certainly beyond words.

Jann-Eike Saathoff

Abstract

In particular during storm events an accumulation of excess pore pressures may occur in the soil around cyclically loaded offshore foundations. The excess pore pressure build-up reduces the effective stresses in the soil and, hence, may negatively affect the structural integrity by influencing the soil-structure interaction. Besides a loss in bearing capacity, large plastic deformations may occur to the structure. Especially for offshore wind turbines an accurate estimation of such deformations is of great importance. Even though the consideration of this degradation effect on the bearing capacity is commonly demanded by the involved certification or approval bodies, no general applicable and accepted method for the calculative verification currently exists. Over the past decades several researchers investigated the excess pore pressure build-up around offshore foundations due to environmental cyclic loads. They tried to capture the loss of bearing capacity, the accumulation of plastic rotation and the essential influence on the serviceability limit state and fatigue design. However, even if there are some sophisticated concepts, none of them is seen as the simple general applicable choice.

Within this thesis a new numerical method – termed Excess Pore Pressure Estimation method (EPPE) – is presented in great detail. This method allows for the transfer of the soil behaviour obtained in cyclic simple shear tests to the bearing behaviour of the entire foundation. Herein, the numerical model accounts for the cyclic excess pore pressure accumulation by respecting the element-based mean stress and stress amplitude as well as an equivalent number of load cycles. The simulation of the excess pore pressure build-up due to certain cyclic loading is based on undrained conditions, i.e. the excess pore pressure build-up due to cyclic loading is derived by disregarding the simultaneous consolidation process. The respected transfer method, in the form of contour plots, enables the consideration of site-specific cyclic direct simple shear and triaxial test results from laboratory devices to elements within the finite element model. Each integration point is evaluated individually. Based on the derived excess pore pressure field, a consolidation analysis takes place in the second step. The actual accumulated excess pore pressure in each element at the end of the storm (or cyclic loading event) is then found by analytically superposing the excess pore pressure decay curves from the consolidation analysis.

For a deeper understanding of cyclic soil behaviour, the cyclic response in different laboratory devices with different densities and under varying stress states was investigated by the author. A contour approach based on cyclic load- and displacement-controlled test results is derived to study the element response from the numerical point of view and use these for the calibration of an implicit model. Moreover, different explicit approaches are presented and compared in terms of their estimation behaviour of cyclic excess pore pressure generation, their predicted foundation capacity and their model assumptions. The intention is hence to examine existing approaches and their applicability by means of an elaborate comprehensive study. A simple modular explicit model is presented which can be easily assessed with engineering judgment. If needed, the different individual calculation steps can be exchanged with more sophisticated ones.

For a reference sandy soil, results of cyclic laboratory tests are presented and used on a reference monopile foundation for a predefined storm event. The EPPE approach helps to quantify the risk of capacity degradation as well as to evaluate an appropriate safety margin. It is possible with the current methodology to evaluate the degradation potential for different sites quite easily and fast.

Key words: *contour plot, cyclic element tests, finite element simulation, foundation design, direct simple shear, excess pore pressure accumulation, monopile, offshore, partially drained conditions*

Résumé

En particulier, pendant les tempêtes, une accumulation de pressions interstitielles excessives peut se produire dans le sol autour des fondations offshore soumises à des charges cycliques. L'accumulation de pressions interstitielles excessives réduit les contraintes effectives dans le sol et, par conséquent, peut avoir une influence négative sur l'intégrité structurelle par l'interaction sol-structure. Outre une perte de capacité portante, la structure peut subir d'importantes déformations plastiques. En particulier pour les éoliennes offshore, il est essentiel d'évaluer avec précision de telles déformations. Bien que les organismes de certification ou d'approbation concernés exigent de prendre en compte cet effet de dégradation, il n'existe actuellement aucune méthode générale applicable et acceptée pour la vérification par calcul. Au cours des dernières décennies, plusieurs chercheurs se sont penchés sur l'accumulation des pressions interstitielles excessives autour des fondations offshore en raison des charges cycliques environnementales. Ils ont essayé de saisir la perte de capacité portante, l'accumulation de la rotation plastique et l'influence essentielle sur l'état limite d'aptitude au service et la conception de la fatigue. Cependant, même s'il existe des concepts élaborés, aucun d'entre eux n'est considéré comme l'option générale applicable simple.

Dans le cadre de cette thèse, une nouvelle méthode numérique – appelée méthode d'estimation des pressions interstitielles excessives (EPPE) – est présentée de manière très détaillée. Cette méthode permet de transférer le comportement du sol obtenu dans les essais cycliques de cisaillement simple au comportement de l'ensemble de la fondation. Le modèle numérique prend en compte l'accumulation cyclique des pressions interstitielles excessives en respectant la contrainte moyenne et l'amplitude de la contrainte basées sur les éléments ainsi qu'un nombre équivalent de cycles de charge. La simulation de l'accumulation des pressions interstitielles excessives due à certaines charges cycliques est basée sur des conditions non drainées, c'est-à-dire que l'accumulation des pressions interstitielles excessives, due aux charges cycliques, est dérivée en ignorant le processus de consolidation simultané. La méthode de transfert respectée, sous forme de tracés de contours, permet de prendre en compte les résultats des essais cycliques de cisaillement simple direct et triaxial, spécifiques au site, réalisés à partir de dispositifs de laboratoire, dans les éléments du modèle d'éléments finis. Chaque point d'intégration est évalué individuellement. Une analyse de consolidation est effectuée dans la deuxième étape sur la base du champ dérivé des pressions interstitielles excessives. L'accumulation réelle des pressions interstitielles excessives dans chaque élément à la fin de la tempête (ou du chargement cyclique) est alors trouvée en superposant analytiquement les courbes de décroissance des pressions interstitielles excessives de l'analyse de consolidation.

Pour mieux comprendre le comportement cyclique du sol, l'auteur a étudié la réponse cyclique dans différents dispositifs de laboratoire avec différentes densités et sous différents états de contrainte. Une approche de contour basée sur les résultats d'essais cycliques contrôlés par la charge et le déplacement est dérivée pour étudier la réponse de l'élément du point de vue numérique et l'utiliser pour l'étalonnage d'un modèle implicite. De plus, différentes approches explicites sont présentées et comparées en termes de comportement d'évaluation de la génération de pressions interstitielles excessives, de capacité de fondation prévue et d'hypothèses de modèle. L'objectif est donc d'examiner les approches existantes et leur applicabilité au moyen d'une étude approfondie. Un modèle explicite modulaire simple, pouvant être facilement évalué par un jugement technique, est présenté. Si nécessaire, les différentes étapes de calcul peuvent être remplacées par des étapes plus poussées.

Pour un sol sableux de référence, les résultats d'essais cycliques en laboratoire sont présentés et utilisés sur une fondation monopieu de référence pour un événement de tempête prédéfini. L'approche EPPE permet de quantifier le risque de dégradation de la capacité et d'évaluer une marge de sécurité suffisante. Avec la méthodologie actuelle, il est possible d'évaluer le potentiel de dégradation de différents sites assez facilement et rapidement.

Mots clés : *tracé de contour, essais par éléments cycliques, simulation par éléments finis, conception de fondation, cisaillement simple direct, accumulation de pressions interstitielles excessives, monopieu, offshore, conditions partiellement drainées*

Kurzfassung

Insbesondere bei Sturmereignissen kann es im Boden an zyklisch belasteten Offshore-Fundamenten zu einer Akkumulation von Porenwasserüberdrücken kommen. Der Porenwasserüberdruck reduziert die effektiven Spannungen im Boden und kann daher die strukturelle Integrität negativ beeinflussen, indem dieser die Boden-Bauwerk-Interaktion zusätzlich beeinträchtigt. Insbesondere für Offshore-Windenergieanlagen ist eine genaue Abschätzung von Verformungen von großer Bedeutung. Obwohl die Berücksichtigung dieses Degradationseffekts auf die Tragfähigkeit von den beteiligten Zertifizierungs- oder Genehmigungsstellen gefordert wird, existiert derzeit keine allgemein anwendbare und akzeptierte Methode für den rechnerischen Nachweis. In den vergangenen Jahrzehnten untersuchten mehrere Forschende die zyklische Porenwasserüberdruckakkumulation, die sich um Offshore-Windenergieanlagen aufgrund von zyklischen Belastungen aufbaut. Sie versuchten, den Verlust der Tragfähigkeit und die Akkumulation der plastischen Rotation zu quantifizieren. Auch wenn einige Konzepte existieren, so wird keines als allgemeingültige Methodik angesehen.

In dieser Arbeit wird eine neue numerische Methode – die sogenannte Excess Pore Pressure Estimation Methode (EPPE) – vorgestellt, die es erlaubt, das in zyklischen Einfachscherversuchen ermittelte Bodenverhalten auf das Tragverhalten des gesamten Fundaments zu übertragen. Dabei berücksichtigt das numerische Modell die zyklische Porenwasserüberdruckakkumulation unter Verwendung der element-spezifischen mittleren Spannung und Spannungsamplitude sowie der äquivalenten Zyklenzahl. Die Simulation des Porenwasserüberdruckaufbaus infolge bestimmter zyklischer Beanspruchungen basiert auf undrainierten Bedingungen, d.h. der Porenwasserüberdruckaufbau infolge bestimmter zyklischer Beanspruchungen wird unter Vernachlässigung des gleichzeitigen Konsolidierungsprozesses abgeleitet. Die Übertragung von Laborergebnissen auf Elemente innerhalb des Finite-Elemente-Modells in Form von Konturdiagrammen ermöglicht die Berücksichtigung von standortspezifischen zyklischen Einfachscher- und Triaxialversuchsergebnissen. Jeder Integrationspunkt wird individuell auf der Grundlage von last- oder weggesteuerten zyklischen Laborversuchsergebnissen ausgewertet. Die gesamte Porenwasserüberdruckakkumulation während eines Sturmereignisses, wird dann für einen bestimmten Bemessungssturm ermittelt. Auf Grundlage des abgeleiteten Porenwasserüberdruckfeldes wird im zweiten Schritt eine Konsolidierungsanalyse durchgeführt. Als Ergebnis der Analyse werden elementbasierte Porenwasserdruckabbaukurven abgeleitet. Der Verlauf des akkumulierten Porenwasserüberdrucks bis hin zum Ende des Sturms (oder des zyklischen Belastungsereignisses) wird durch analytische Superposition ermittelt.

Für ein tiefgehendes Verständnis des zyklischen Bodenverhaltens wird das zyklische Antwortverhalten in verschiedenen Laborgeräten bei unterschiedlichen Lagerungsdichten und unter verschiedenen Spannungszuständen untersucht. Ein Konturansatz, der auf last- und verschiebungsgesteuerten Versuchsergebnissen basiert, wird abgeleitet. Um die Elementantwort aus numerischer Sicht zu untersuchen, wurde auch ein implizites Modell kalibriert. Die Ergebnisse werden im Detail erläutert. Anschließend werden verschiedene explizite Ansätze vorgestellt und hinsichtlich ihres Abschätzungsverhaltens der zyklischen Porenwasserüberdruckerzeugung, ihrer prognostizierten Gründungskapazität und ihrer Modellannahmen verglichen. Damit ist beabsichtigt, bestehende Ansätze und deren Anwendbarkeit in einer umfassenden Gesamtstudie zu untersuchen. Es wird ein generisches und modulares, explizites Modell vorgestellt, das leicht mit fachspezifischem Sachverstand bewertet werden kann. Die verschiedenen Berechnungsschritte können nach Bedarf durch weitere Schritte ergänzt werden.

Im Rahmen dieser Arbeit werden Ergebnisse aus zyklischen Laborversuchen für einen beispielhaften Nordseesand vorgestellt und auf eine Referenz-Monopile-Gründung innerhalb eines vordefinierten Sturmereignisses angewendet. Der EPPE-Ansatz hilft bei der Quantifizierung des Verflüssigungsrisikos und der Ermittlung eines angemessenen Sicherheitsniveaus. Mit der aktuellen Methodik ist es möglich, das Degradationspotenzial für verschiedene Standorte einfach und schnell zu bewerten.

Schlagworte: *Einfachscherversuche, Finite-Elemente-Simulation, Konturplot, Offshore, Monopile, Partiell dränierte Bedingungen, Porenwasserüberdruckakkumulation, Zyklische Elementversuche*

Contents

List of Figures

List of Tables

List of Symbols

Latin letters

A_0	Dilatancy parameter in SANISAND	1
A	Regression parameter	1
a	Regression parameter	1
b	Regression parameter	1
c'	Effective cohesion	F/L^2
C_C	Coefficient of curvature	1
c_h	Plastic modulus parameter in SANISAND	1
C_i	Regression parameter	1
c_i	Regression parameter	1
C_U	Coefficient of uniformity	1
c_v	Consolidation coefficient	L^2/T
c_z	Fabric-dilatancy tensor parameter in SANISAND	1
c	Critical state parameter in SANISAND	1
d_{10}	Grain diameter at 10% passing	L
d_{30}	Grain diameter at 30% passing	L
d_{60}	Grain diameter at 60% passing	L
D_r	Relative density	1
d_{drain}	Representative drainage length	L
D	Damping ratio	1

D	Pile diameter	L
d	Grain diameter	L
e	Void ratio	1
e_0	Critical state parameter in SANISAND	1
e_{max}	Maximum void ratio	1
e_{min}	Minimum void ratio	1
E_{r}	Stiffness modulus of un- and reloading	F/L^2
E_{s}	Oedometric stiffness	F/L^2
E	Young's modulus	F/L^2
e	Load eccentricity	L
f_{Π}	HCA function	1
f_{ampl}	HCA function	1
F_{cyc}	Load amplitude	F
f_{e}	HCA function	1
F_{max}	Maximum load	F
F_{mean}	Mean load	F
F_{min}	Minimum global load	F
F_{min}	Minimum load	F
f_{N}	HCA function	1
f_{p}	HCA function	1
f_{R}	Resonant frequency	$1/T$
F_{ult}	Global bearing load	F
f_{Y}	HCA function	1
F	Lateral load	F
f	Load frequency	$1/T$

G_0	Initial shear modulus	F/L^2
G	Shear modulus	F/L^2
g	Gravitational acceleration	L/T^2
h_0	Parameter in SANISAND	1
h_w	Water depth	L
h	Height of sample	L
I_P	Plasticity index	1
J_i	Deviatoric stress invariant	F/L^2
k_0	Earth pressure coefficient at rest	1
k_f	Hydraulic conductivity of the soil	L/T
K	Bulk modulus	F/L^2
k	Earth pressure coefficient	1
L	Embedded pile length	L
M_c	Critical state parameter SANISAND	1
M_f	Inclination of failure line	1
m_v	Coefficient of compressibility	L^2/F
M	Moment load	FL
m	Parameter in SANISAND	1
n_b	Plastic modulus parameter in SANISAND	1
n_d	Dilatancy parameter in SANISAND	1
$N_\mathrm{eq,dissi}$	Number of equivalent cycles after dissipation	1
N_eq	Number of equivalent cycles	1
N_liq	Number of cycles to liquefaction	1
N	Number of cycles	1
n	Regression exponent	1

p_{ref}	Reference pressure (100 kPa)	F/L^2
p	Bedding resistance	F/L^2
p'	Octahedral effective pressure	F/L^2
PI	Plasticity index	1
q_{cyc}	Deviatoric stress amplitude	F/L^2
q_{mean}	Mean deviatoric stress	F/L^2
q	Deviatoric stress	F/L^2
$R_{\mathrm{u,dissi}}$	Excess pore pressure ratio after dissipation	1
R_{u}	Normalized excess pore pressure	1
R	Maximum radius	L
r	Radius	L
s_{u}	Undrained shear strength	F/L^2
$T_{\mathrm{ch,dr}}$	Characteristic drainage parameter	T
T	Cyclic load period	T
t	Time	T
u_0	Initial excess pore pressure	F/L^2
u_{hydro}	Hydrostatic pore pressure	F/L^2
u_{max}	Maximum excess pore pressure	F/L^2
u_x	Lateral displacement at mudline	L
v_{s}	Shear wave velocity	L/T
w_{l}	Liquid limit	1
X	Regression parameter	1
x	Distance	L
y	Lateral displacement in p-y curve	L
z_{max}	Parameter in SANISAND	1

Greek letters

β	Regression parameter	1
γ	Shear strain	1
γ'	Buoyant unit weight of the soil	F/L^3
γ_{cyc}	Shear strain amplitude	1
$\gamma_{\mathrm{eq,cyc}}$	Equivalent shear strain amplitude	1
γ_{mean}	Mean shear strain	1
γ_{td}	Degradation shear strain threshold value	1
γ_{tf}	Failure shear strain threshold value	1
γ_{tl}	Linear shear strain threshold value	1
γ_{tv}	Volumetric shear strain threshold value	1
γ_{w}	Weight of pore fluid	F/L^3
$\Delta\sigma'_{\mathrm{eq,cyc}}$	Increment of cyclic equivalent effective stress	F/L^2
$\Delta\tau_{\mathrm{xy}}$	Increment of shear stress	F/L^2
$\Delta\varepsilon_{\mathrm{vd}}$	Load amplitude	1
Δn	Increment in porosity	1
Δu	Excess pore pressure	F/L^2
Δ	Change of particular value	1
δ	Logarithmic decrement	1
ε	Strain	1
ε_{v}	Volumetric strain	1
ζ_{b}	Cyclic load type value	1
ζ_{c}	Cyclic load type value	1
η	Stress ratio	1
Θ	Lode angle	$^{\circ}$

λ	Critical state parameter in SANISAND	1
ν	Poisson's ratio	1
ξ	Critical state parameter SANISAND	1
ρ	Density	M/L^3
σ	Total stress	F/L^2
σ'	Effective stress	F/L^2
σ'_{oct}	Octahedral effective stress	F/L^2
σ'_{v}	Vertical effective stress	F/L^2
$\sigma'_{eq,cyc}$	Equivalent effective stress	F/L^2
σ_1	Principal stress 1	F/L^2
σ_2	Principal stress 2	F/L^2
σ_3	Principal stress 3	F/L^2
τ	Shear stress	F/L^2
τ_{cyc}	Cyclic shear stress amplitude	F/L^2
τ_{mean}	Mean shear stress	F/L^2
τ_{max}	Maximum shear stress	F/L^2
φ'	Effective angle of internal friction	$^\circ$
φ'_{red}	Reduced effective friction angle	$^\circ$
φ_{c}	Critical state angle of friction	$^\circ$
ψ	Diltancy angle	$^\circ$

Subscripts

1	Principal direction
2	Principal direction
3	Principal direction
acc	Accumulated
contour	Value from contour plot
cyc	Cyclic
c	Consoldiation
DA	Double shear strain ampliutude
diss	Dissipated
DSS	Direct simple shear
d	Design value
eff	Effective
eq	Equivalent
$\mathrm{F}_{\mathrm{max}}$	Maximum global load
$\mathrm{F}_{\mathrm{mean}}$	Mean global load
$\mathrm{F}_{\mathrm{min}}$	Minimum global load
FE	Value from finite element model
i	Arbitrary index
j	Arbitrary index
liq	Liquefaction
max	Maximum value
min	Minimum value
mean	Mean value
par	Partially drained

$_{\mathrm{perm}}$	Permanent
$_{\mathrm{q}}$	Deviatoric
$_{\mathrm{ref}}$	Reference case
$_{\mathrm{Ru}}$	Value for specific R_u isoline
$_{\mathrm{SA}}$	Single shear strain amplitdue
$_{\mathrm{N=10}}$	For number of cycles N = 10
$_{\mathrm{Tri}}$	Triaxial
$_{\mathrm{u}}$	Undrained
$_{\mathrm{v}}$	Vertical
$_{\mathrm{v}}$	Volumetric
$_{\mathrm{x}}$	Direction
$_{\mathrm{y}}$	Direction
$_{\mathrm{z}}$	Direction

Legend

Length	L
Mass	M
Time	T
Force	$\mathrm{F = ML/T^2}$

Abbreviations

ALS	accidental limit state
API	American Petroleum Institute
CNL	constant normal load
CPT	cone penetration testing
CSL	critical state line
CSR	cyclic stress ratio
CV	constant-volume
DLC	design load case
DNV	Det Norske Veritas
DSS	direct simple shear device
EPPE	Excess Pore Pressure Estimation method
FLS	fatigue limit state
HCA	High Cycle Accumulation
LTR	load type ratio
LVDT	linear variable displacement transducer
MSR	mean stress ratio
OCR	overconsolidation ratio
OWT	offshore wind turbine
PDCAM	partially drained cyclic pore pressure accumulation model
PTL	phase transformation line
SLS	serviceability limit state
SDM	stiffness degradation method

UDCAM	undrained cyclic strain accumulation model
UDCAM-S	simplified undrained cyclic strain accumulation model
ULS	ultimate limit state

1 Introduction

1.1 Offshore renewable energy

In recent years, wind energy has taken a key role in the expansion of renewable energies. A sustainable development based on renewable energy sources is politically and socially required. At the same time as environmental awareness has increased, so has the demand. The current energy demand is already high, but will increase dramatically in the coming years. The required energy can be generated from onshore as well as offshore wind energy turbines. Compared to onshore wind, offshore wind power offers higher and more continuous energy generation since the offshore wind is generally more consistent, has less turbulence, and shows a higher average wind speed.

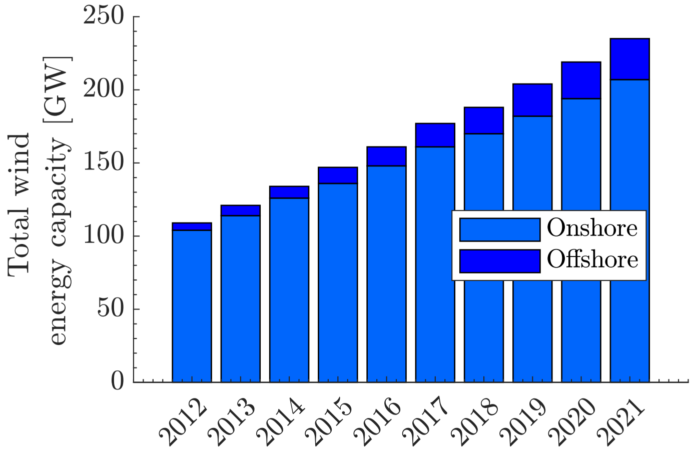

Figure 1.1: Increase in total wind energy power capacity over the last ten years in Europe (Wind Europe, 2021).

Global cumulative wind power amounts to 743 GW, of which an additional 82 GW were installed worldwide in 2020 alone (Global Wind Energy Council, 2021). However, the political goals are still ambitious, as an additional cumulative power of 180 GW is needed every year to achieve the climate targets (Global Wind Energy Council, 2021). Currently, 236 GW of wind power capacity is installed in Europe (Figure 1.1). In Europe alone, a total of 116 GW will be installed in the next 5 years (Figure 1.2). The offshore sector is expected to account for a quarter of the total capacity. In a best case scenario, even more offshore farms will be built to keep the global climate agreements (Global Wind Energy Council, 2021) (see Figure 1.2).

The energy output is larger for an increased converter size due to the greater wind speeds and the non-linear relation between energy output and wind input. A scaling in size of

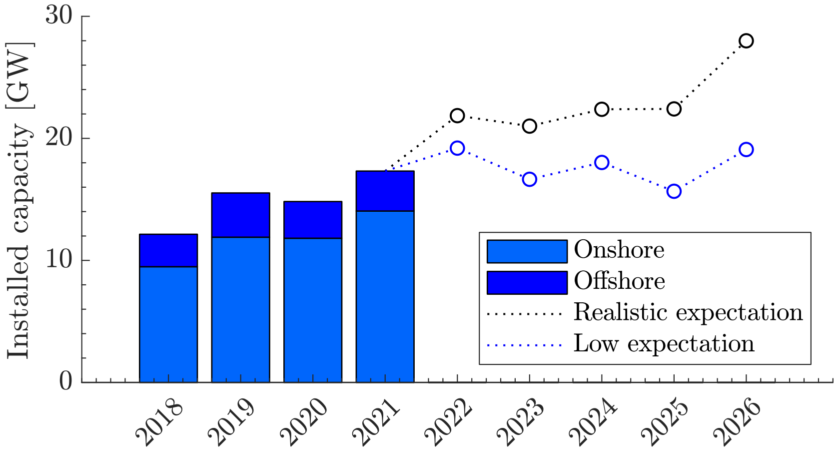

Figure 1.2: New installations per year in Europe with realistic and low expectation forecast to 2026 (Wind Europe, 2021).

offshore wind energy structures is easier compared to their onshore counterparts. Regarding the offshore sector, the expansion is currently not only happening in Europe, but Asia is also expanding its offshore programs (Global Wind Energy Council, 2021). Therefore, this sector will continue to grow and many design assessments and feasibility studies will be required for all sorts of different site conditions.

1.2 Motivation

Offshore wind turbines (OWTs) will be increasingly used for renewable energy generation in the future. Both proven foundation solutions, such as monopiles, and innovative foundation solutions, such as bucket foundations, will be used to support the offshore structures. Offshore wind turbines and accordingly their foundation structures are particularly exposed to cyclic loads, especially wind and wave loads. The purpose of an OWT is to harvest energy from the wind for which they need to be anchored to, or embedded in the subsoil. In order to achieve higher energy outputs, larger structures are required in greater water depths. These conditions in particular present additional challenges that must be overcome to ensure a reliable expansion process. The capacity of offshore turbines is typically at 8 - 10 MW and beginning to expand to 12 - 15 MW megastructures (Dührkop et al., 2019). These conditions will transfer higher loads to the structure which in turn are not allowed to create excessive tilting (DNV-ST-0126; Savidis et al., 2018).

Regardless of the foundation type, significant cyclic loads from the offshore environment must be transferred from the structure to the subsoil. An altered bedding reaction caused by cyclic loads may change the stress distribution in the near-field along the pile and subsequently influence the eigenfrequency (Zachert and Wichtmann, 2020). The consideration of these influences is only addressed in a few sections in the current design codes such as American Petroleum Institute (API), DIN EN ISO 19901-4:2017-01, DIN EN ISO 19902:2021-03 or Det Norske Veritas (DNV). Large numbers of load cycles are applied within the design process and related deformations can develop due to the prevailing

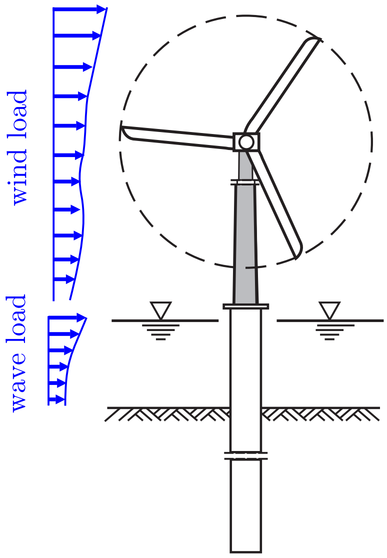

Figure 1.3: Cyclically loaded offshore wind energy turbine.

harsh cyclic loading during the lifetime of the structure (Figure 1.3). Under undrained or partially drained conditions, the corresponding shear stresses in the soil can lead to a build-up of accumulated excess pore pressures, which in turn can cause a reduction in shear strength. As a result, cyclic loading can lead to deterioration in bearing capacity, which must be considered in the design of cyclically loaded offshore foundations. Even though the consideration of a cyclic degradation effect on the bearing capacity due to excess pore pressure is commonly demanded by the involved certification or approval bodies (e.g. DNV-RP-C212; BSH No. 7005), no general applicable and accepted method for the calculative verification currently exists. The build-up of excess pore pressure and, hence, partial or full liquefaction can affect the integrity of offshore structures. Both capacity and serviceability are compromised when liquefaction occurs. Liquefaction can be caused by cyclic loading with partial or no dissipation between adjacent load events. Since there is no standardised procedure for the verification required for the design, it is necessary to compare the existing methods and find an optimal consideration in the design process. Optimized design can save steel material and subsequently increase the economic efficiency. A simple procedure that can be easily verified with engineering judgment is needed.

1.3 Objective and concept

To investigate the behaviour of soil elements under cyclic loading, various laboratory tests are carried out in practice (e.g. drained or undrained cyclic simple shear tests or cyclic triaxial tests). The soil behaviour determined in the element tests needs to be transferred to the global soil-structure interaction. Despite that there are already different numerical (explicit and implicit) approaches in the literature, no approach has become widely accepted nor thoroughly validated. Implicit methods calculate each cycle individually and must be calibrated beforehand. This can be very time consuming, and the subsequent numerical calculation is also computationally intensive. In addition, there are only a limited number of cycles before the numerical error becomes predominant. Therefore, explicit models should be used where the cyclic system response is primarily and directly based on the results of high-quality cyclic laboratory tests and no individual cycles are calculated.

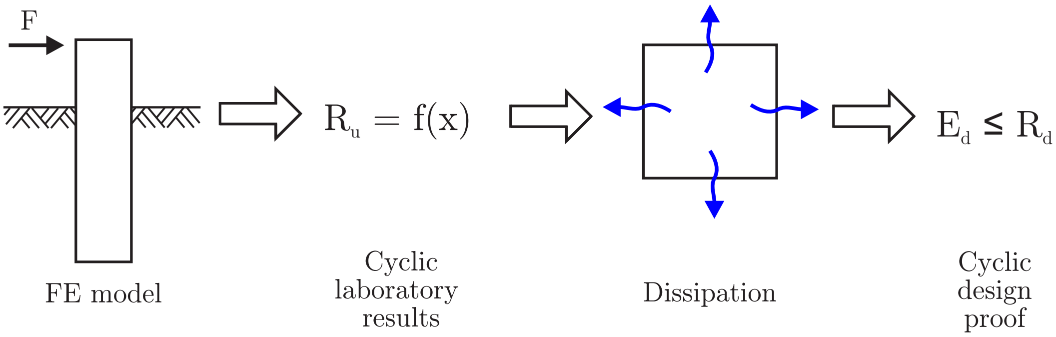

Figure 1.4: Components of the concept to be presented.

There is a lack of fundamental knowledge about which cyclic tests are the most representative and simultaneously the most efficient ones in terms of time and costs for excess pore pressure estimation. Another aspect is how the results of these tests should be taken into account in the design to consider cyclic accumulation effects. This is where the present thesis focuses on. The aim of this work is to provide the necessary basic knowledge and a reliable method for taking partially drained cyclic loading into account in order to realistically describe the bearing behaviour of offshore structures. The approach is intended to be integrable into any finite element software and to benefit from laboratory tests performed as part of a general purpose project, so that only a small number of additional specific tests will be required.

The concept consists of a numerical reference calculation which is then combined with undrained cyclic laboratory tests (Figure 1.4). A flow net calculation takes the partially drained dissipation behaviour into account. Finally, the post-cyclic response can be evaluated and a design proof is performed. The numerical component is partly based on earlier work by Taiebat (1999), Rahman et al. (1977) and Andersen (2015). The overall goal is to develop a generic methodology for predicting the load-bearing behaviour of intensively cyclically loaded foundations using cyclic laboratory test results.

The presented concept is designed to account for the excess pore pressure accumulation and, thus, the capacity degradation due to cyclic lateral loading during a storm event in saturated, predominantly non-cohesive soils. Due to its modular design, it can be modified for more complex aspects and higher accuracies.

1.4 Scope

The present knowledge regarding the cyclic excess pore pressure accumulation behaviour was fundamentally gained from many (cyclic) laboratory tests and an in-depth literature analysis. The thesis will present insights into how soil behaves for undrained conditions under cyclic loading and on how to transfer the knowledge to global foundation response. Additionally, it focuses on different modelling techniques in the numerical framework and how these affect the post-cyclic bearing capacity. Some questions were asked in advance and act as waypoints through this thesis.

- How can the partially drained cyclic loading of a design storm and the related excess pore pressure accumulation be considered within the overall design?
- What is the difference in global response between the most accurate and the most practical way to consider these partially drained accumulation effects?
- How can partially drained conditions be considered in the best possible way in terms of superposition in a numerical framework?
- What are the differences in global structural responses between implicit and explicit methods for the very same soil?
- What laboratory tests are most appropriate under which conditions (load- or displacement-controlled; direct simple shear or triaxial tests)? What is the influence on the element result as well as on the structural response?
- What is the best way to derive contour plots? What is the easiest way to implement these into a finite element model?
- Which modelling techniques affect the outcome to what extent? What effects must strictly be considered?

To answer these questions, the cyclic response in undrained cyclic displacement- as well as load-controlled tests is assessed and used within the numerical procedure in order to estimate the difference in global response. The main objective of the research presented is to provide a simple, easy handable concept for estimating excess pore pressure accumulation around cyclically loaded offshore foundations that gives sufficiently accurate results and is applicable in practical design. To achieve this goal, mainly the bearing behaviour of monopile foundations is investigated, but the developed generic concept applies to all types of structures.

This thesis is divided into two parts. The first part deals with the development and understanding of the soil response under cyclic loading with a special focus on excess pore pressure accumulation (Chapter 2 and Chapter 3). In this part, general definitions are explained as a basis for the following chapters. Subsequently, the existing explicit and implicit numerical approaches are presented with their advantages and disadvantages (Chapter 4). Chapter 5 shows the results of a detailed classification of one sandy soil as well as its cyclic characteristics under mainly undrained conditions. These cyclic soil responses are to be used within the numerical procedure and a comparison of the global structural response is made. A concept for the degradation of bearing capacity due to excess pore pressure accumulation under partially drained conditions was developed in order to facilitate the inherent complex cyclic loading into a simple estimation procedure.

The developed procedure incorporates the most essential aspects. A more detailed explanation of the development and application of the proposed explicit design approach is given in Chapter 6.

The second part deals with the practical application of the theoretical work in the design of an offshore foundation, and the general capabilities of the approach are explored. The method is used with a simple constitutive model in conjunction with ABAQUS (Dassault Systèmes, 2016), a general purpose finite element program (Chapter 7). This work not only addresses general cyclic soil behaviour by deriving contour plots, but also compares implicit and explicit modelling for one particular sandy material. The implicit model gives insights into the element response around an offshore foundation, which can be used to gather a deeper understanding for the optimization of the explicit approach. Different explicit modelling approaches for excess pore pressure accumulation are compared against each other so that a sound recommendation for the practical application can be made. A discussion is followed in which the significance of this work regarding excess pore pressure estimation and potential future applications are presented. The thesis closes with recommendations for a practical design considering all presented sub-methods and a summary. Additional applications, such as the derivation of an equivalent number of cycles as well as multistage cyclic laboratory tests to validate these concepts and also results of displacement-controlled tests, can be found in Appendix B, C and D. Additional information on specific chapters are presented in Appendix A.

2 Cyclically loaded offshore foundations

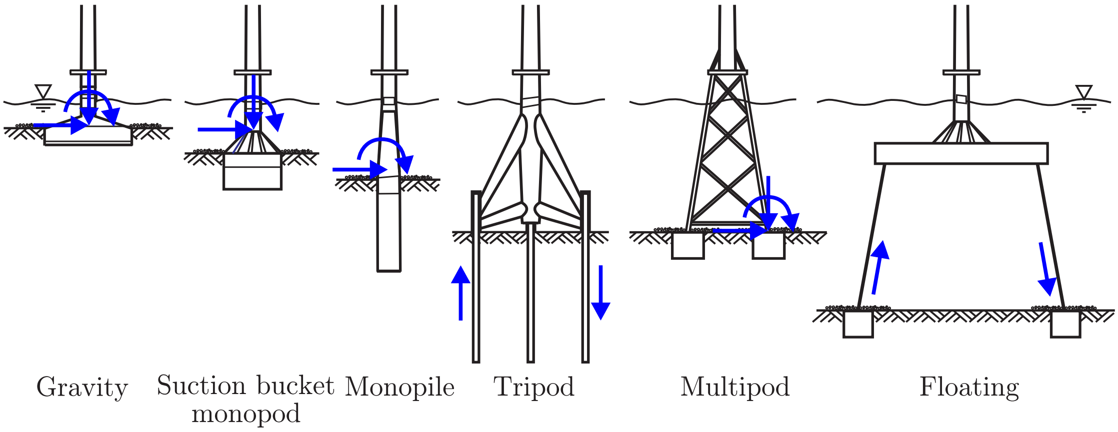

Figure 2.1: Different foundation concepts with main load characteristics following Thieken (2015).

The offshore wind turbine (OWT) generates electrical energy from the kinetic energy of the wind, which reduces the wind velocity and creates a substantial force on the structure and the foundation. In general, there are four main ground-based foundation designs: monopiles, jackets, suction buckets and gravity foundations (Figure 2.1). The concepts are briefly described below.

- A gravity-based foundation supports itself with its own dead weight under moment load, so design considerations such as sliding, tilting and gapping must be taken into account. The foundation is hollow and can be rafted in place. No installation by pile driving or suction is required. However, the seabed may need to be prepared. They can be designed with a skirt, which is used to prevent erosion from water seeping under the foundation.

- Suction buckets are installed primarily with suction and are therefore more environmentally friendly. They can be used in a monopod or multipod arrangement. They also have the advantage of easy decomposition.

- Monopile foundations are open-ended steel piles which are subjected to mainly lateral loads. The vertical loads play only a minor role, because of the large diameter and, hence, high axial capacities. Monopiles currently have a diameter of 8 m with rotor diameters of 167 m with approximately 12 MW (Zachert and Wichtmann, 2020), with larger foundations already in planning. Research projects investigate the feasibility and implementation of 20 MW plants (Schuster et al., 2021). Monopiles are driven into the subsoil in water depths of up to 40 m. Their diameter has increased in recent years due to higher water levels. They are connected to the tower by a transition piece, which is usually grouted, bolted or flanged. The general concept is well known and easy to handle, both in terms of transportation and installation. Almost no seabed preparation is required unless heavy scour is expected. The main problems are decomposition and noise immissions during installation. The overall system has lower stiffness than a multipod arrangement. The length-to-diameter ratio has steadily decreased over the years. Larger drainage paths are created, which pose an additional risk in partially drained soils and may create substantial amounts of excess pore pressure. Low permeability and rapid loading can lead to excess pore pressure accumulation. Moreover, monopiles account for 81% of all foundations in Europe and are the most widely used ones (Wind Europe, 2021).

- Jackets are a lattice-type structure with a square or triangular footprint. The moment load is converted into vertical loads in the corner piles.
- Floating OWT are deployed in deep waters and towed to their location where they are anchored, moored, or partially submerged (e.g., Tension Leg-Platform). Floating or moored systems have advantages e.g. when other structures would become too large and expensive to transport.

The foundation concepts can be divided into monopod and multipod foundation. For multipods, the exact soil-structure interaction and overall response depends on the footprint (i.e. location of the footings), number of legs and loading direction. Overall, the choice of foundation depends on an interaction between structure (turbine), soil profile, water depth and resulting loading condition. The foundations also differ in their bearing mechanism. Monopods are single supporting structures and bear with higher moment loads (H-M). Multipod structures are loaded in tension and compression since the global lateral effect generates axial, moment and lateral load (H-V-M) at each pile or bucket (Figure 2.1).

2.1 Geotechnical design of OWT

Although various foundation concepts can be used, this thesis will focus on monopiles since it is the most common foundation type.

2.1.1 Analytical design of monopile foundations

Analytical methods are important for a fast estimation of the foundation response, which is essential for any subsequent cyclic design. For monopiles the Winkler model is a well-known tool in the design process (Winkler, 1867). It uses p-y springs (for lateral behaviour) and t-z springs (for axial behaviour). The springs are independent of each other

(Cox et al., 1974; O'Neill and Murchison, 1983; Reese et al., 1974). The method of calculating the lateral response was introduced by Reese and Matlock (1956) and McClelland and Focht Jr. (1958). The p-y curves define the relationship between the soil resistance p and the lateral displacement of the spring y. However, even if this approach is used in daily practice, cyclic degradation can only partially be approximated (Dash and Bhattacharya, 2015; Byrne et al., 2017; Zhang et al., 2019). Liquefaction due to seismic events is not part of this thesis. However, the same problems apply here. Similarly, degraded p-y curves can be used for a simplified analysis of monopiles under seismic loading or a finite element model is needed (Bhattacharya et al., 2021).

Arany et al. (2017) present a simplified analytical design of a monopile in 10 steps. Cyclic design is done with empirical correlations, which however, can only be used for a very approximate result. The number of cycles is derived by using an assumed peak storm duration divided by an assumed wave period. Nevertheless, such a simplified calculation may give a first good estimation in preliminary analysis. For an accurate cyclic design proof, numerical calculations are unavoidable due to the spatially distributed and soil-specific accumulation of deformations and excess pore pressures. For this reason, the main design under cyclic loading is nowadays performed with finite element models at almost all locations within a wind farm. In these models, the whole stress-strain relationship of the different elements around the foundations is modelled. Finite element calculations can be applied to complex soil and system geometries by using sophisticated soil models and accounting for spatial variations in soil properties. Their use is permissible according to DIN 1054:2021-04 and DNV-RP-C212.

2.1.2 Design load cases

Offshore structures are designed to withstand harsh environmental conditions. Several design standards state requirements to ensure sufficient safety such as ANSI/API RP 2GEO, DNV-RP-C212, DNV-ST-0126, DIN EN ISO 19901-4:2017-01, DIN EN ISO 19902:2021-03, DIN EN 1997-1:2014-03, DIN 1054:2021-04 and DIN 18088-4:2019-01. The design is aimed at different aspects. DNV-ST-0126 distinguishes four different design limit states, these are the ultimate limit state (ULS), serviceability limit state (SLS), fatigue limit state (FLS) and accidental limit state (ALS). These are intended to include all possible (geotechnical) failure mechanisms.

In this context, the ULS aims at analysing the bearing capacity using a 50-year design storm and is intended to ensure sufficient lateral capacity. Here, the soil condition at failure is of interest. The SLS estimates settlement and tilting. The permanent accumulated head rotation needs to be smaller than a project-specific limit value; often the total structure's inclination at seabed level should not exceed 0.5°. The FLS targets cyclic loading in terms of foundation stiffness affecting natural frequency. The initial stiffness of the structure is used to investigate the overall natural eigenfrequencies. Herein, the initial stiffness and damping are important (Thieken et al., 2018; Saathoff et al., 2019). The ALS targets accidental impacts. The ULS and ALS calculations are performed with safety factors applied to characteristic values of loads and resistances in order to establish a predefined level of safety.

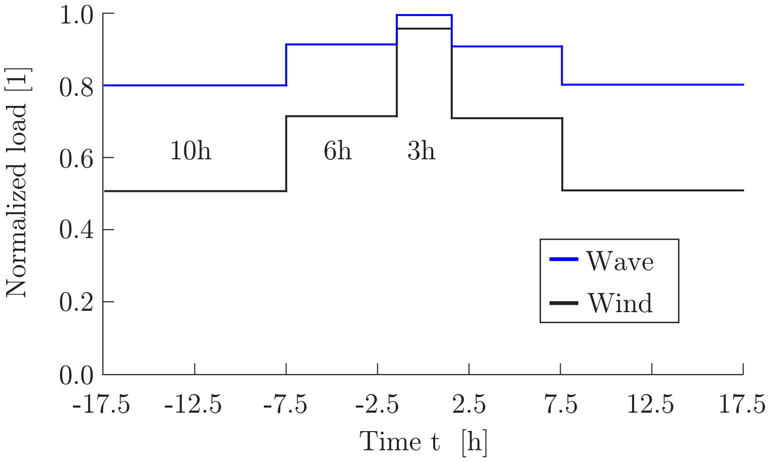

Figure 2.2: 35-hour design storm (BSH No. 7005).

2.1.3 Loading conditions

Design proofs for all four design limit states are carried out. Herein, not all loads that act on an offshore foundation originate from the same source. DNV-ST-0126 defines the main load components as:

- permanent loads such as weight, ballast or equipment. These loads do not vary in direction, magnitude or time period
- variable loads varying in direction and amplitude
- accidental loads from technical failure, fire, collision, breaking wave or impact
- deformation loads from temperature or settlement
- environmental loads from ice, marine growth, earthquake, tidal current, snow, wind and hydrodynamic (cyclic nature)

All load cases need to be considered in different combinations (DNV-ST-0126; DIN 18088-4:2019-01). The loads are categorized as quasi-static, cyclic or transient. For the cyclic SLS design, a distinction must be made between a short-term (partially drained) storm load event and long-term (drained) soil behaviour during the lifetime of the OWT when dealing with sandy material. The storm load, under which partially drained conditions are present, consists of a spectrum of different wave heights, periods and directions. Wave conditions during the storm are required for the design. Therefore, wave heights and wave periods including their probability of occurrence are needed. To simplify this, a 35 h-design storm is used (Figure 2.2).

The pre-defined design storm consists of two storm build-up phases, in which the loads are increasing in their magnitude and a peak phase, which considers the largest acting loads. The duration of this peak phase is assumed with 3 h according to BSH No. 7005. Afterwards, the storm calms down again. Here, especially for cyclic loading, not only the maximum force, but also the load history plays an important role in evaluating the structural response (see Section 3.2.2 and Section 3.2.2). The assumed storm and the storm phases may influence an excess pore pressure accumulation since it specifies the storm durations of individual phases. During storm build-up, the storm frequency may also increase up to the point of maximum storm loading. Monopiles within the North Sea can be designed based on a 50-year probability of occurrence design storm (following the design load case (DLC) 6.1 in DIN EN IEC 61400-3-1:2020-11).

2.2 Cyclic loading

The acting storm loading is multidirectional, but usually only one main loading direction is investigated in the geotechnical design (DIN EN IEC 61400-3-1:2020-11). An example of wind and wave loads, in terms of significant wave height, coming from different directions and evaluated for one location is shown in Figure 2.3. Thereby, the cyclic loads lead to an accumulation of soil deformations and, thus, also to changes in the stress conditions in the soil – which in turn induces a change in the load-bearing behaviour of the foundation – and, in the case of partially drained conditions, to an accumulation of excess pore pressures with a corresponding reduction in strength.

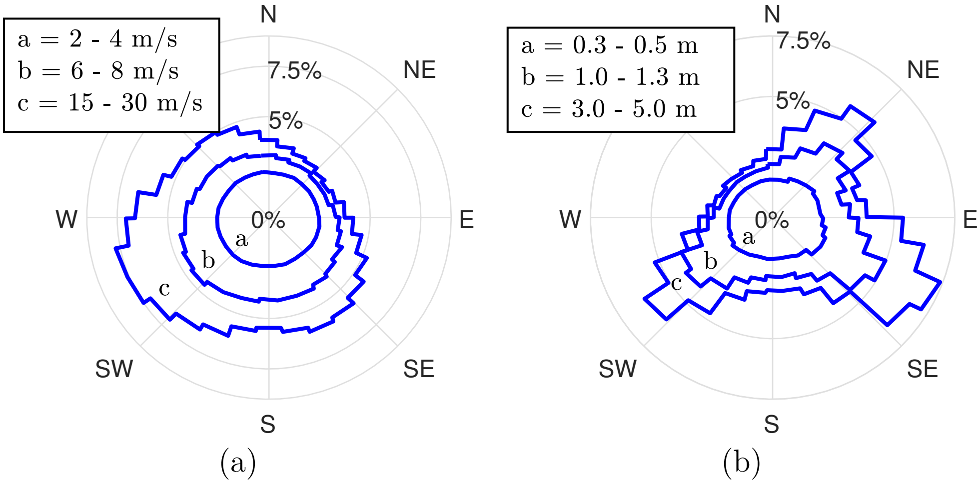

(a) (b)

Figure 2.3: Exemplary wind (a) and significant wave height (b) roses with different directions and percentage of occurrence (based on Hodgson et al. (2016)).

Figure 2.4 (a) shows schematically an irregular storm load over time. Since it is very computationally expensive to calculate the total irregular cyclic load and because numerical errors may accumulate, the storm is sorted into different load bins (Matsuishi and Endo, 1968). All loads within a sorted storm bin have the same load amplitude and mean load. Each load bin has a certain number of equivalent cycles (Figure 2.4 (b)). The maximum load in each storm bin is the sum of the mean load and the cyclic load amplitude (Equation 2.1).

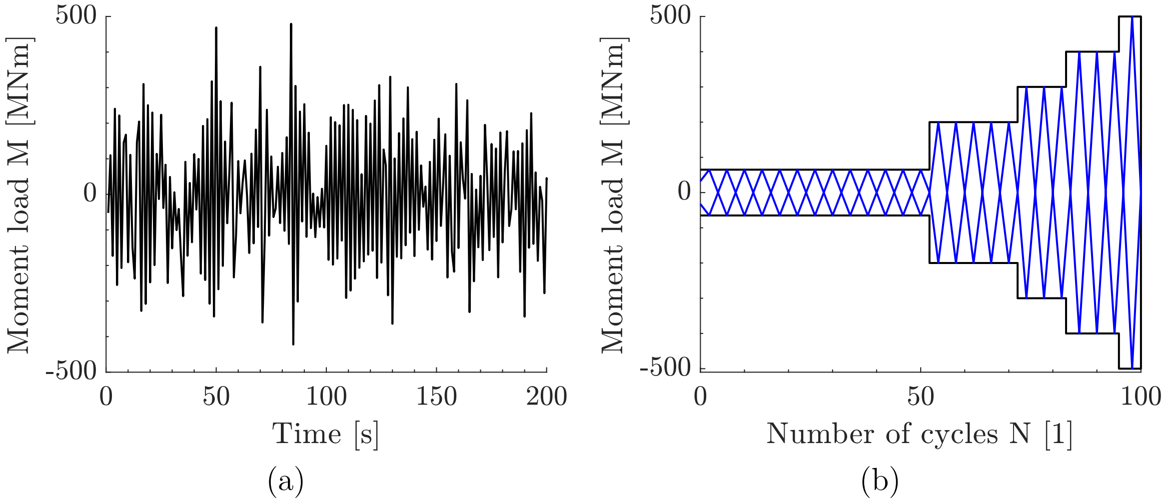

Figure 2.4: Irregular loading (a) translated to regular load bins (b) (schematic).

$$F_{max} = F_{mean} + F_{cyc} \tag{2.1}$$

Figure 2.5 shows an example storm with entries in moment load at mudline. Hereby, small loads have a large number of cycles and large loads only have a small number of equivalent cycles. Each load bin is related to a predefined load frequency. Since repetitive offshore loads mainly have a frequency less than 1 Hz, they can be considered as cyclical where there is mainly a plastic response with no inertia effects (Gotschol, 2002). Zienkiewicz and Bettess (1982) report that for these conditions dynamic effects can be neglected.

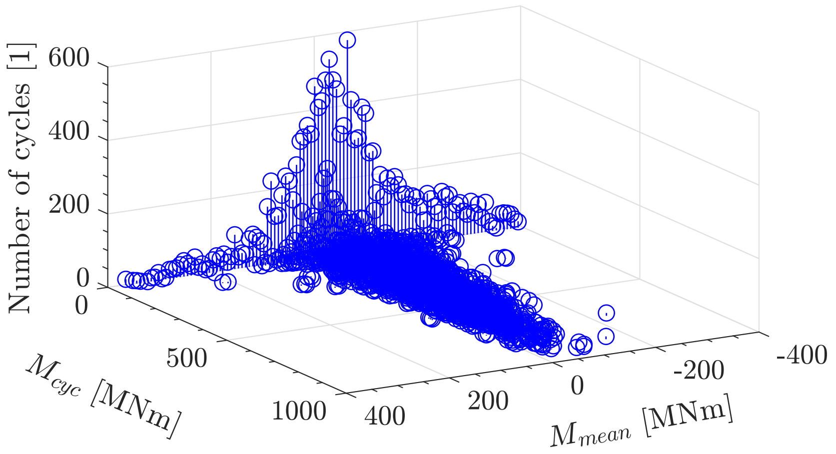

Figure 2.5: Schematic storm load with mean moment load over amplitude and number of cycles in the form of a scatter diagram.

The mean and cyclic load amplitude can occur in different combinations creating one-way or two-way loads as well as symmetric or asymmetric load scenarios. The mean load is equal to the load amplitude in case of symmetric one-way load conditions and zero for a symmetric two-way load. Equation 2.2 depicts the normalized parameters ζ_c and ζ_b (Leblanc et al., 2010) with which the load characteristic can be described (Figure 2.6).

$$\zeta_c = \frac{F_{min}}{F_{max}} \qquad \zeta_b = \frac{F_{max}}{F_{static}} \tag{2.2}$$

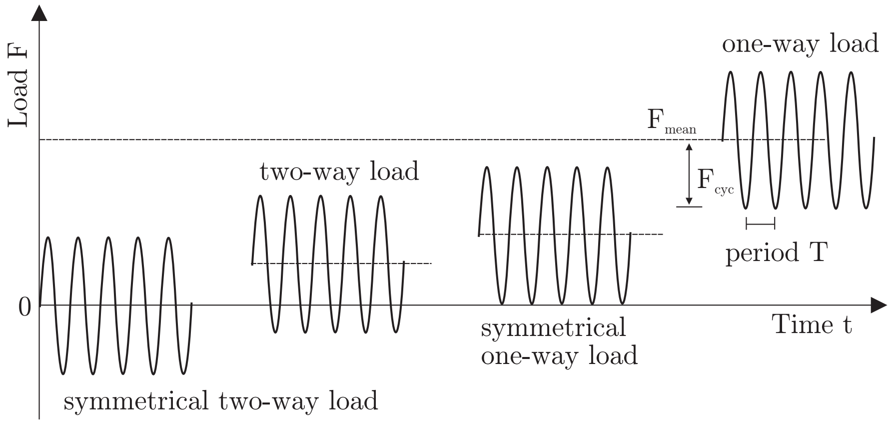

Figure 2.6: Definition of cyclic load parameters.

A one-way load without stress-reversal falls within the range of $0 \leq \zeta_c \leq 1$. When $-1 \leq \zeta_c \leq 0$, the OWT exhibits two-way loading with stress-reversal. Jalbi et al. (2019) investigated the different load types for existing wind farms based on measurements. The load scenarios that occurred are shown in Figure 2.7. For small water depths, there is mainly one-way loading, but for deeper water depths also two-way loading occurs. Symmetric one-way loading does not occur as often as symmetric two-way loading for extreme loads. Moreover, ζ_c strongly correlates with the water depth.

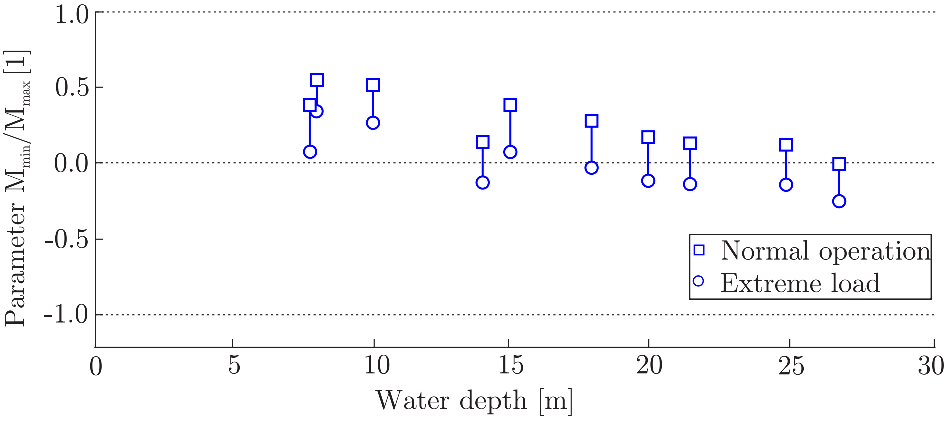

Figure 2.7: Measured load types from offshore sites (Jalbi et al., 2019).

Figure 2.5 and Figure 2.6 show the influence of the different load type combinations (cyclic and mean). Hence, always both values (ζ_c and ζ_b) are needed to describe the load type correctly. For two-way loading there will be a large stiffness degradation, but for one-way loading there may be an additional ratcheting effect, leading to larger plastic mean deformations due to the one directional incremental deformation accumulation. The aforementioned components can be represented in a so-called interaction diagram, where the cyclic component (cyclic stress ratio – CSR) is plotted against the mean (mean stress ratio – MSR) component (Figure 2.8). Different variations of cyclic and mean component lead to the definition of the load type ratio (LTR) (Equation 2.3). The values of cyclic stress ratio (CSR) and mean stress ratio (MSR) relate to the mean load and cyclic load amplitude (cf. Chapter 3).

$$LTR = \frac{F_{mean}}{F_{cyc}} = \frac{MSR}{CSR} = \frac{1+\zeta_c}{1-\zeta_c} \tag{2.3}$$

For a value of LTR = 1, a symmetric one-way loading and for LTR = 0 a symmetric two-way loading is assumed. Therefore, within the global interaction diagram, differentiation can be made either on the basis of different mean components or on the basis of the type of loading. Figure 2.8 shows in dotted-black a differentiation between MSR and in dashed-blue different inclination relating to different LTR values.

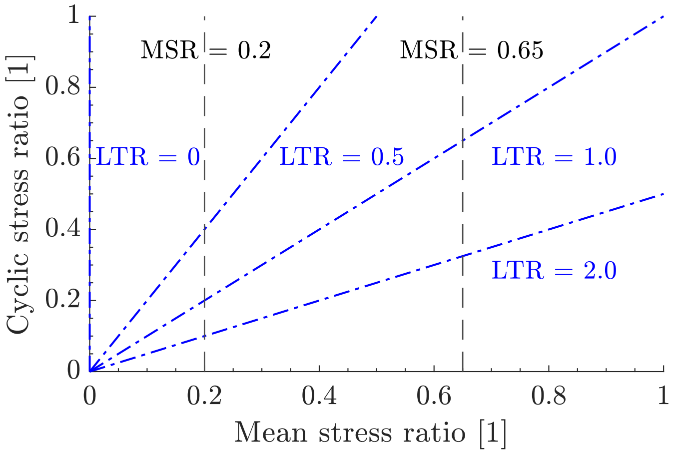

Figure 2.8: Cyclic stress ratio over mean stress ratio with different load type ratios.

2.3 General liquefaction phenomenon

With cyclic loading, there is an accumulation of deformation. The extent of deformation depends on the level of cyclic loading. When long drainage paths are present or in the case of low permeabilities, partially drained condition arise causing excess pore pressure accumulation potentially leading to liquefaction. For this condition, large volumetric strains may not accumulate, but additional deformations may arise in the course of partially drained cyclic loading. Liquefaction is a state of continuous deformation without resistance (Seed and Booker, 1976). In general, large deformations occur when the excess pore pressure reaches the confining stress. Excess pore pressure is best explained by the concept of effective stresses (Terzaghi, 1936) (Equation 2.4).

$$\sigma = \sigma' + u_{hydro} + \Delta u \tag{2.4}$$

In the equation above, σ is the total stress of the element, σ' is the effective (confining) stress, u_{hydro} the hydrostatic water pressure and Δu the excess pore pressure.

Under drained conditions, the excess pore pressure can dissipate when the element is loaded and the volume decreases leading to a denser packing. If the fully saturated soil exhibits contractive behaviour due to shearing under constant-volume condition, the effective stress decreases and the excess pore pressure increases. The excess pore pressure cannot dissipate and the grains cannot be compacted to a denser packing since they are hindered by the almost incompressible water within the voids. The volume does not change, but there is excess pore pressure, which at the same time reduces the effective stress. This reduces the shear resistance which in turn leads to larger shear strains.

This phenomenon does not only occur in clayey material. For larger monopile diameters in cohesionless soils, partially drained and undrained conditions become more pronounced (Li et al., 2019). It is important to keep in mind that the risk of liquefaction is an interaction of generation and simultaneous dissipation of excess pore pressure under partially drained conditions. It is caused by a potential contractive tendency of the soil in combination with limited hydraulic conductivity and the nearly incompressibility of water. The stiffness and the strength of the soil is altered when excess pore pressure builds up. The excess pore pressure travels upwards to the surface which potentially results in hydraulic failures. However, liquefaction failure for dense sand is not as pronounced as for loose soils. Dense soils show a dilative behaviour under large shear strain levels thus the excess pore pressure is reduced. For small shear strains the dilative response does not govern the soil response, but for larger shear strains this behaviour dominates and reduces the excess pore pressures. However, not all of the soil around the structure is potentially affected. Only some regions will fail partially or completely (Taiebat, 1999). In this case, the SLS and ULS are at risk. Even if the excess pore pressure is fully dissipated after the storm, large plastic deformations may have developed.

The focus of this work is on excess pore pressure accumulation and partial liquefaction. However, if sufficient excess pore pressure is accumulated, liquefaction may occur. Hence, the topic overlaps with full liquefaction analysis which may be found in the field of seismic loading and earthquake engineering. Herein, liquefaction depends on many different aspects. One of them is the soil type as well as the prevailing stress situation (more in Chapter 3). These factors can be influenced by different installation methods – especially for pile foundations. For smaller piles, plugging can lead to a more compacted soil around the pile. Compared to drilled piles, vibrated piles show less cyclic sensitivity with respect to deformation accumulation (Long and Vanneste, 1994). The stress conditions from the pile installation are usually not considered for the cyclic accumulation estimation and hence do not affect the cyclic design proofs. However, there are numerical investigations which try to take installation effects in terms of different cyclic accumulations into account (Staubach et al., 2022). Due to potentially larger stresses around the pile foundations, the accumulation effect is positively affected leading to smaller accumulation rates.

There are several criteria for estimating the liquefaction tendency of a soil. For a first estimation, mainly the grain size distribution is used and compared with for instance recommendations like the KTA 2201.2 (2012-11). In zone 1 of Figure 2.9 there are fine sands without large fines contents. For increasing fines content and fine gravel liquefaction may still occur. With clay and gravel, however, the risk is low (Figure 2.9 (a)). In terms of relative density, loose soils are more prone to compaction and are therefore more susceptible to liquefaction (Figure 2.9 (b)). Due to the predominantly dense soil states in the North Sea, there is only limited liquefaction potential. Comparing the grain size distribution of liquefiable soils with the grain size distribution of a representative North Sea sand, there is a theoretical liquefaction risk (Figure 2.9 (a)).

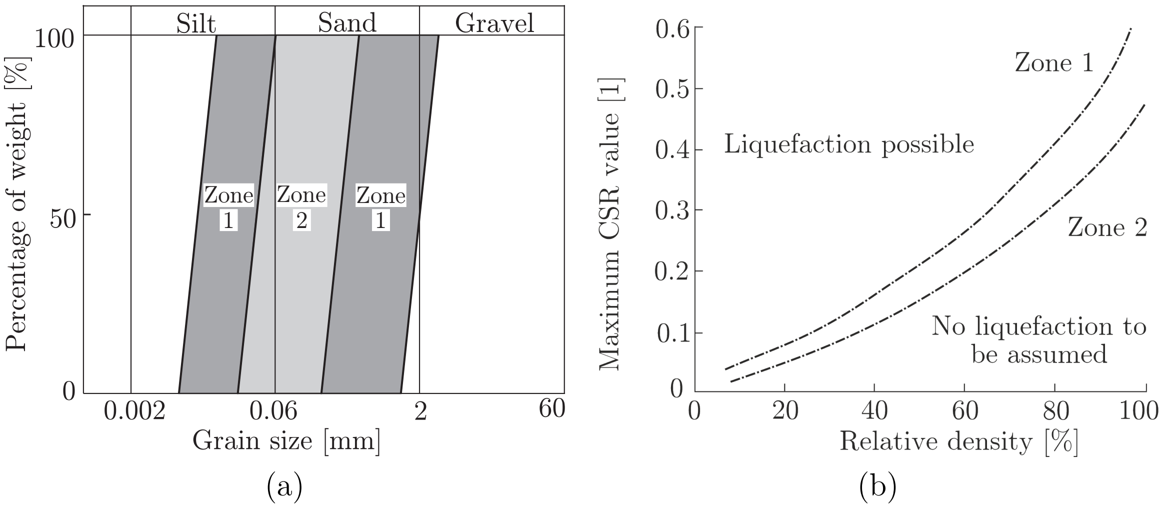

Figure 2.9: Liquefiable soils with regard to grain sizes (a) and relative density (b) according to KTA 2201.2 (2012-11).

Excess pore pressure can also build up due to a change in water level during wave propagation (Martin et al., 1980; Siddharthan, 1987; Tsotsos et al., 1989; Pastor et al., 2006). However, this topic is beyond the scope of this thesis.

2.4 Guideline recommendations on excess pore pressure estimation within the design

The consideration of the aforementioned aspects is specified in various international guidelines. They are mainly based on the experience of the oil and gas industry in the 1970s. However, enormous progress has been made in the offshore sector in recent decades due to the rise of the offshore wind sector. The calculative verification against cyclic degradation effects on the bearing capacity due to excess pore pressure is demanded (by e.g. DNV-RP-C212, BSH No. 7005), but neither detailed methods nor exact implementations are further explained in the guidelines and standards. In the following, the requirements of the different international guidelines and standards shall briefly be presented.

2.4.1 BSH

The BSH No. 7005 states that due to cyclic loading the bearing capacity may be reduced and plastic deformation may accumulate. Under certain circumstances unfavourable excess pore pressure accumulates and depending on the site conditions, liquefaction is possible. Within the design, it must be ensured that no potential changes in the mechanical properties of the soil occur. A standardized concept for the estimation of cyclic accumulation is not available. In order to assess the potential changes in the load-bearing behaviour of foundation elements the involvement of experts is necessary.

2.4.2 DIN/ISO standards

The DIN 18088-4:2019-01 states that it must be verified that any excess pore pressure that may occur does not endanger the foundations stability. All variables influencing the development of excess pore pressure must be taken into account. The admissibility of neglecting excess pore pressure accumulations in the calculations under cyclic loading must be justified. For this purpose, the volumetric cyclic shear strain threshold according to, for instance, Vucetic (1994) may be used as a criterion (cf. Chapter 3). The 35-hour-storm load case is to be applied for the investigation or geotechnical verification of the potential reduction in bearing capacity and deformation accumulation of a cyclically loaded foundation system during a storm event with a return period of 50-years and a turbine stand still. With regard to a design approach for the accumulation of excess pore pressures, there is currently no generally accepted procedure.

The DIN EN 1998-1:2010-12 deals with earthquake analysis and emphasises the importance of the influence that accumulated excess pore pressure can have. It states that when modelling the mechanical behaviour of soils, it is important to consider the decrease in stiffness with increasing magnitude of deformations, as well as possible effects of the increase in excess pore water pressure under cyclic loading.

The DIN EN ISO 19902:2021-03 specifies many sources for cyclically loaded offshore structures in clay, but concepts are not explained in greater detail. No method is recommended.

2.4.3 API

The American Petroleum Institute (ANSI/API RP 2GEO) notes that cyclic loading can create excessive excess pore pressures and subsequently decrease the coefficient of friction for pile-soil interaction. It states that for axially loaded piles, explicit modelling of cyclic loading can provide information about soil reactions and a possible decrease in pile capacity and stiffness. Directly addressed are solely anchors. For these, repeated loading can lead to the generation of excessive pore pressure and a reduction in effective stresses around the anchor – this is also the case for monopile foundations. The standard emphasizes the importance of considering cyclic loading, which can lead to a reduction in load-bearing capacity and accumulation of deformations. However, not much further information is provided. The same applies to Danish Energy Agency (2001).

2.4.4 DNV

Cyclic shear stresses can lead to an accumulation of excess pore pressure and an increase in cyclic and permanent shear strains. The shear strength of the soil may be reduced. Permanent foundation rotations must also be evaluated (DNV-OS-J101; DNV-ST-0126). For gravity foundations, an effective stress stability analysis must be performed that evaluates not only the initial pore pressure and the build-up of pore pressures due to the cyclic load history, but also the transient pore pressures during each load cycle and the effects of dissipation.

Section 10 of the DNV-RP-C212 contains the most information compared to all other guidelines. It vaguely explains a soil fatigue model based on cyclic laboratory tests. Drainage is to be included and settlement and structure inclination are to be estimated. Strain and pore pressure contour diagrams shall be used for a relative density derived from cone penetration testing (CPT). These diagrams indicate the relationship between excess pore pressure (or strain), cyclic loading, and number of cycles. DNV-RP-C212 states that for a storm period of 10 s, there is no need to consider inertia of the structure and soil, since the problem can be treated as quasi-static. In the laboratory tests, a period $T = 10\,\mathrm{s}$ should be chosen to match the wave frequency. Special care must be taken with sandy soils, since the response is more complex due to dilatancy and dissipation. The strain accumulation procedure should be used, with the load packages arranged in ascending order (DNV-RP-C212). If no anisotropy is to be considered or no triaxial tests have been performed, direct simple shear device (DSS) test results shall be used. For the numerical approach, the contour plots with a representative stress path are used. The initial mobilized mean shear stresses must be considered within the path. The slope of the path is the ratio of cyclic and mean shear stresses. It can be evaluated for total and cyclic displacement analysis. The procedure is similar to the simplified undrained cyclic strain accumulation model (UDCAM-S) explained in Chapter 4. No more information on the consideration of excess pore pressure dissipation and dilatant soil behaviour is given. Mainly, the information given is based on the response of clayey material.

2.5 Conclusion

The proof against cyclic loading is an essential part within the design and can only hardly be performed with simplified semi-empirical or analytical methods. Regardless of the applied load type, whether irregular storm loading or a simplified equivalent number of cycles, the cyclic effect on the structure must be taken into account according to the standards. In addition to the accumulated deformation that occurs in drained and undrained conditions, undrained conditions can also cause a decrease in load bearing capacity. A proof according to international standards based on cyclic laboratory test results is needed. However, the standards do not specify a uniform procedure. Only the DNV-RP-C212 specifies an explicit procedure in combination with high-quality cyclic laboratory results. Such a procedure is followed in this work.

3 Behaviour of cohesionless soil under cyclic loading

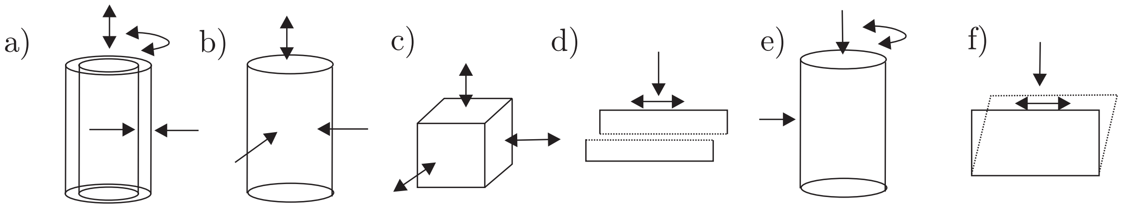

Figure 3.1: Cyclic laboratory tests following Le (2015).

The behaviour of soil under cyclic loading is characterized by the accumulation of plastic deformation. The main cause is compaction and re-orientation of soil particles. In addition to the increase in deformation that also occurs under drained conditions, (cohesionless) soils may also experience an accumulation of excess pore pressure under partially drained conditions.

The estimation of cyclic soil behaviour has been studied since the 1970s, and several methods have been developed. The main cyclic mechanisms have been identified, however, the cyclic soil response cannot be derived in one single (commonly available) laboratory test. A differentiation between at least compression, extension and shear loading is necessary. Furthermore, not only the device itself, but also the treatment and preparation of the specimen have a huge influence on the soil response. The general soil response and influencing parameter are briefly presented for a better understanding of the cyclic behaviour in order to apply their key features to the explicit numerical method (Chapter 6).

3.1 Laboratory tests

In geotechnical engineering, various (cyclic) laboratory tests are used to describe the soils' strength and stiffness properties (Figure 3.1). In these tests, the specimen is cyclically rotated (a, e), compressed (b, c, e) or sheared (d, f). Depending on the loading direction and specimen shape, different test results are obtained. The most important tests required for this work are briefly described below.

3.1.1 Triaxial test

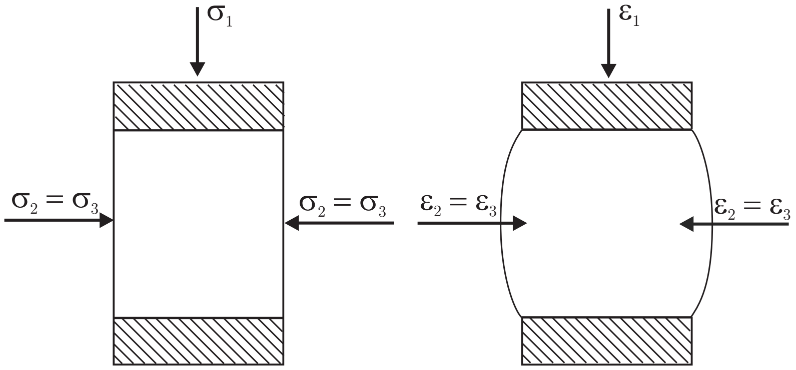

Figure 3.2: Deformation pattern in triaxial test.

One of the most well-known geotechnical tests is the triaxial test (Figure 3.2). Within the triaxial test a specimen is axially loaded while it is not restrained radially. The axial principal stress is in most cases the largest and termed σ_1; and the radial stresses are termed σ_2 and σ_3 (Figure 3.2). Depending on the applied stresses it is possible to perform compression (sample experiences vertical compaction) and extension tests (sample experiences vertical extension).

During the test, the axial and volumetric deformations are measured while the axial and radial stresses are controlled. The acting octahedral and deviatoric stress can be derived according to Equation 3.1. The representative shear component τ is half of the deviator q and is the shear stress acting in 45° plane (Vucetic and Dobry, 1986). The related strains can be calculated with Equation 3.2. The triaxial test can be performed in a load-controlled cyclic manner to evaluate the liquefaction potential of a soil sample (ASTM D5311-13).

$$p' = \sigma'_{oct} = \frac{\sigma'_1 + 2\sigma'_3}{3} \qquad q = \sigma'_1 - \sigma'_3 = \frac{3}{\sqrt{2}}\sigma'_{oct} \tag{3.1}$$

$$\varepsilon_v = \varepsilon_1 + 2\varepsilon_3 \qquad \varepsilon_q = \frac{2(\varepsilon_1 - \varepsilon_3)}{3} \qquad \gamma = \varepsilon_1 - \varepsilon_3 \tag{3.2}$$

3.1.2 Direct simple shear test

A more sophisticated version of the shear box test is the direct simple shear test (DSS) (Figure 3.3). It provides the soil response under pure shear loading, similar to a shear box test but without a predefined failure plane. The stress and deformation state is representative for e.g. soil elements in and near the failure surfaces, elements near axially loaded piles or soil elements during earthquake loading.

The device consists of an axial press, a specimen in confining teflon-coated rings and external displacement transducers. The specimen is inserted into a soft membrane within

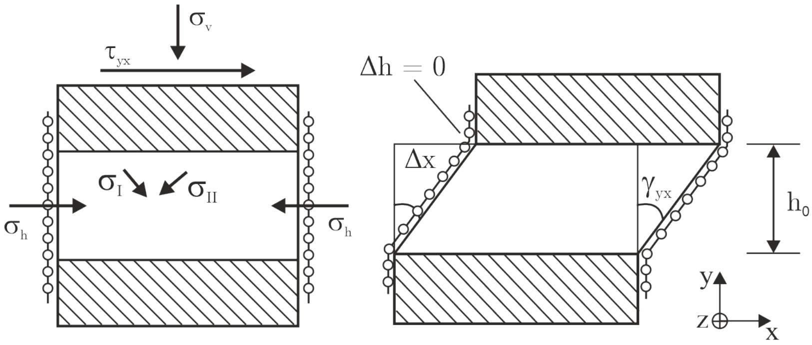

Figure 3.3: Deformation pattern in constant-volume direct simple shear test.

a stack of rigid rings. A small height-to-diameter ratio results in the most homogeneous stress distribution and pure shear (Seed, 1979). Stresses can freely rearrange in the specimen and form shear bands – similar to a triaxial test. However, the direct simple shear apparatus also has confining rings that resemble an oedometric test ($\varepsilon_{xx} = \varepsilon_{zz} = 0$) and result in rotation of the principal axis during shearing. The stress during consolidation results to $\sigma_1 = \sigma'_v$ and $\sigma_3 = k_0\,\sigma'_v$ and $\tau_{xy} = 0$ (Silver and Seed, 1971b). A deviatoric stress arises for an anisotropic consolidation state in case of a coefficient of earth pressure at rest smaller than unity. Additional shear stresses are generated during the shear phase (Figure 3.3). The strains are calculated as:

$$\varepsilon_{yy} = \Delta h/h_0 \qquad \gamma_{yx} = \Delta x/h_0 \qquad \varepsilon_v = \varepsilon_{yy} \tag{3.3}$$

The undrained cyclic soil behaviour is mainly derived from cyclic undrained tests. This test is common in offshore geotechnical laboratories and closely resembles the field boundary conditions. However, because of the immense time savings, constant-volume tests with dry and non-saturated soil samples are often used instead of true undrained tests. The decrease in vertical stress determined on a dry sample can be interpreted approximately as the increase in excess pore water pressure of a fully saturated sample in a true undrained test (Airey and Wood, 1986; Finn and Vaid, 1977; Feda, 1971) (for clay also Dyvik et al. (1987)). ASTM D8296-19 assumes that the soil reaction under constant-volume conditions is equal to truly undrained conditions. In addition, the literature assumes that constant-volume experiments on sand tend to be conservative (Pickering, 1973; Finn and Vaid, 1977).

3.1.3 Resonant column test

The resonant column test is not primarily used to investigate cyclic accumulation of excess pore pressure for sandy material, because its main area of application are small shear strains. The shear modulus decreases for increasing shear strains. The resonant column device (RC) can be used to partly derive the shear modulus degradation curve. It is a standard test for deriving dynamic parameters such as the initial shear modulus G_0 and the damping ratio D. The shear modulus G describes the correlation between shear strain and shear stress and depends mainly on void ratio e and octahedral stress σ'_{oct}.

The shear modulus is derived from the measured first eigenfrequency of the soil specimen within the RC device. The influencing parameters of sands are fines content as well as particle shape and grain size distribution (Wichtmann and Triantafyllidis, 2013).

The resonant column test is evaluated by 1D wave theory in an elastic medium. A specimen is subjected to torsional loads about the central axis (in the case of shear modulus derivation). Shear waves are generated, which are used to derive G_0. The shear modulus is derived from the shear wave velocity v_s (Equation 3.4) within an elastic cylinder based on the measured resonant frequency f_R and the sample density ρ. A free decay test is performed in order to estimate the damping (logarithmic decrement δ). Almost no cyclic damage is induced due to the low shear strains.

$$v_s = \sqrt{\frac{G}{\rho}} \tag{3.4}$$

3.2 Soil behaviour in cyclic laboratory tests

Offshore turbines are subjected to cyclic loading and partially drained condition may occur. Even if partially drained conditions can be considered in laboratory tests, these tests are very time consuming. On the other hand completely undrained conditions and the general liquefaction potential have been studied by many researchers (Polito, 1999; Vucetic and Dobry, 1986; Dobry et al., 1982; Seed et al., 1975b; Seed and Lee, 1966; Silver et al., 1976). In undrained conditions, excess pore pressure is generated by shearing of the soil element, since the volumetric strain is zero. In undrained cases, the soil skeleton carries the shear forces and the normal stress is carried by the pore water. The water cannot maintain a shear stress, and the particles lose their contact to some extent so that the reaction becomes softer overall due to the volumetrically constant boundary condition resulting from the incompressibility of water. The overall cyclic soil behaviour depends on several factors, such as stress history (preconditioning), confining pressure, load type, soil type, fines content, grain size distribution, and even the different cyclic soil tests have differences due to their test boundary conditions (e.g. axis rotation).

3.2.1 General behaviour and definitions

In cyclic undrained tests, the excess pore pressure Δu is often normalized to the normalized excess pore pressure ratio R_u by the effective vertical consolidation stress for one-dimensional or the octahedral consolidation stress for three-dimensional boundary conditions (ASTM D8296-19; ASTM D5311-13):

$$R_u = \frac{\Delta u}{\sigma'_{v,c}} \quad and \quad R_u = \frac{\Delta u}{\sigma'_{oct}} \tag{3.5}$$

The amount of excess pore pressure depends on the induced shearing. This is usually represented with the cyclic stress ratio (CSR) value. The CSR is defined with the cyclic amplitude of the deviatoric stress q_{cyc} for triaxial conditions and τ_{cyc} for direct simple shear conditions (Equation 3.6). Equation 3.7 also shows analogue the definition of the mean stress ratio (MSR).

$$CSR = \frac{\tau_{cyc}}{\sigma'_{v,c}} \quad and \quad CSR = \frac{q_{cyc}}{2\,\sigma'_{oct}} \tag{3.6}$$

$$MSR = \frac{\tau_{mean}}{\sigma'_{v,c}} \quad and \quad MSR = \frac{q_{mean}}{2\,\sigma'_{oct}} \tag{3.7}$$

In the case of liquefaction, the horizontal stress is usually less than the vertical stress, so liquefaction is achieved more rapidly in that direction due to the reduction in the isotropic part of the stress tensor. This theoretical problem can be solved by using the octahedral stress for the normalized excess pore pressure in all cases, but this is not usually done in direct simple shear tests. Another approach uses the distance u_{max} from the stress point under consideration p'_c to the failure line in p'-q space (Equation 3.8).

$$R_u = \frac{\Delta u}{\Delta u_{max}} \quad \Delta u_{max} = p'_c - \frac{q_0}{M_f} \tag{3.8}$$

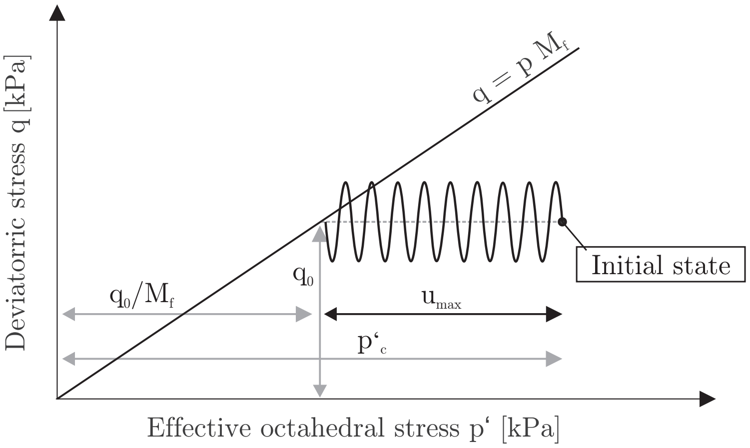

Figure 3.4: Definition of u_{max} in p'-q space for anisotropic consolidation.

This definition in p'-q (3D) or $\tau - \sigma'_v$ (1D) space is used by Taiebat and Carter (2000) and Mao et al. (1999) (Figure 3.4). In the p'-q diagram, the soil cannot necessarily sustain liquefaction of the full value of p'_c in the form of excess pore water pressure under anisotropic loading. This is due to the failure line. The distance between the consolidation stress and the failure line is referred to as u_{max} (Equation 3.8 and Equation 3.9).

$$M_f = \frac{3(a-1)}{3+(1+b)(a-1)} \quad a = \frac{1+sin(\varphi')}{1-sin(\varphi')} \quad b = \frac{\sigma'_2 - \sigma'_3}{\sigma'_1 - \sigma'_3} \tag{3.9}$$

M_f is the slope of the failure line in p'-q space. The number of cycles for which failure in terms of liquefaction is assumed, is termed N_{liq}. For example, this would be the case if the excess pore pressure Δu is equal to u_{max}. This simply represents another definition, and although this second definition is well founded, normalization with the vertical or octahedral stress from the cyclic laboratory tests brings a more intuitive approach and will be used below (as also done in ASTM D8296-19).

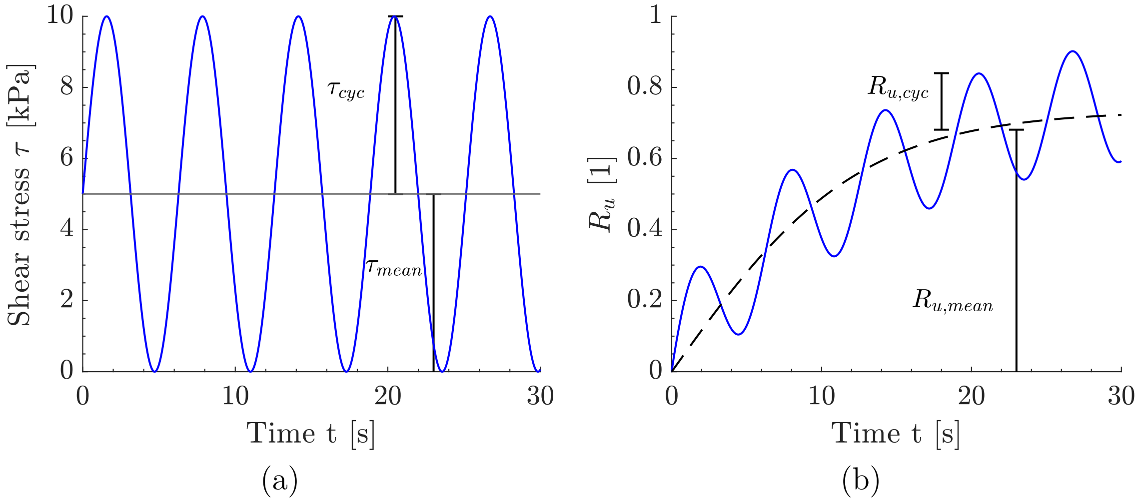

Figure 3.5: Definition of mean and cyclic components in a load-controlled undrained cyclic element tests.

The soil is tested in load-controlled monotonic and cyclic element tests. Figure 3.5 shows the increase of excess pore pressure for a harmonic cyclic shear stress load. A complete cycle is given when the initial value is reached for the second time. The cyclic response can be divided into mean and cyclic components. Besides the cyclic and mean component, the permanent values are of most interest for the design. Due to the hysteretic behaviour of soils, especially for higher shear stresses, the mean and permanent values do not have to coincide. The permanent excess pore pressure (and shear strain) is defined as the excess pore pressure at the end of a complete cycle. The mean value is half of the peak-to-peak value. Minimum deviations to the permanent pore pressure are obtained for the mean excess pore pressure between maximum and minimum of the excess pore pressure bandwidth (cf. ASTM D8296-19).

Failure criteria

In case of load-controlled tests there are two triggering criteria for the derivation of the number of cycles to liquefaction N_{liq}. The first criterion is defined as the loss of confining pressure for the first time (Seed and Lee, 1966; Seed et al., 1975b; ASTM D5311-13). A normalized excess pore pressure value of 1.0 may be sometimes difficult to achieve in laboratory tests and, hence, a value of 0.95 seems more practical (Wu et al., 2004; Ishihara, 1993). Furthermore, the generation of excess pore pressure can be accompanied by large shear deformations and reduced strength and stiffness parameters. These deformations are the result of reduced contact force between particles due to an increase in excess pore pressure until the octahedral stress reaches the failure line. The second criterion is hence a deformation criterion. Many investigations were done by for instance De Alba et al. (1976), Ladd (1977) and Silver et al. (1976). They found that in most cases a chosen (axial) strain value for failure of 3%, 5% or 10 % has only a marginal effect on the resulting number of cycles to failure (El Mohtar, 2009). A double axial strain amplitude of 5% was introduced by Ishihara (1985) (Ishihara, 1993; Carraro et al., 2003; Wu et al., 2004), who performed cyclic triaxial tests. Seed et al. (1975b) also agrees with a double axial strain amplitude of 5%, because of the high level of deformation.

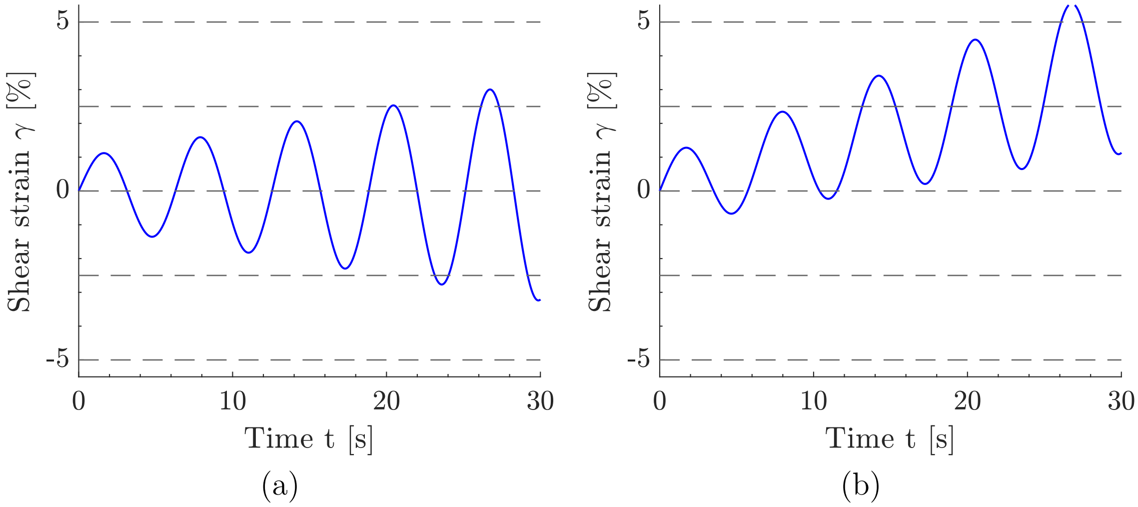

Figure 3.6: Double (a) and single shear strain amplitude (b) failure criterion for 5% following Wu et al. (2004).

Figure 3.6 shows how the single and double strain criterion is used by using the shear strain instead of axial strain. The 5% criterion was originally derived for the axial strain from triaxial testing, which would result in a shear strain value for undrained conditions of 7.5% (ASTM D8296-19). However, often a shear strain value of 5% is used to define failure (Zografou et al., 2016; ASTM D8296-19). Figure 3.7 shows a comparison between different relative densities and a shear strain failure at a double amplitude of 5%. The normalized excess pore pressure for a small number of cycles did only reach 0.85 whereas for a larger number of cycles almost 100% was reached. Hence, a small influence of the shear strain criterion on the actual excess pore pressure accumulation can be seen.

Liquefaction phenomena

When dealing with liquefaction the terminology flow liquefaction needs to be differentiated from cyclic mobility and initial liquefaction (Figure 3.8). Flow liquefaction is a rapid increase in excess pore pressure and a loss of strength and stiffness of the soil. The stress state is reduced to an octahedral stress of zero. For flow liquefaction the shear strength is reduced to a point where it is smaller than the needed strength to maintain stability (Seed, 1979). In contrast, general liquefaction can be described as the reduction of grain-to-grain contact forces which may influence the strength and the stiffness of the soil.

In case of cyclic mobility, there is no sudden loss of strength, but a cyclic accumulation of deformation in dilative soils. Cyclic mobility is characterised by incremental accumulation of excess pore pressure and deformation with a shear strength of the liquefied soil larger than the static shear stress (Castro and Poulos, 1977). After the loss of strength at

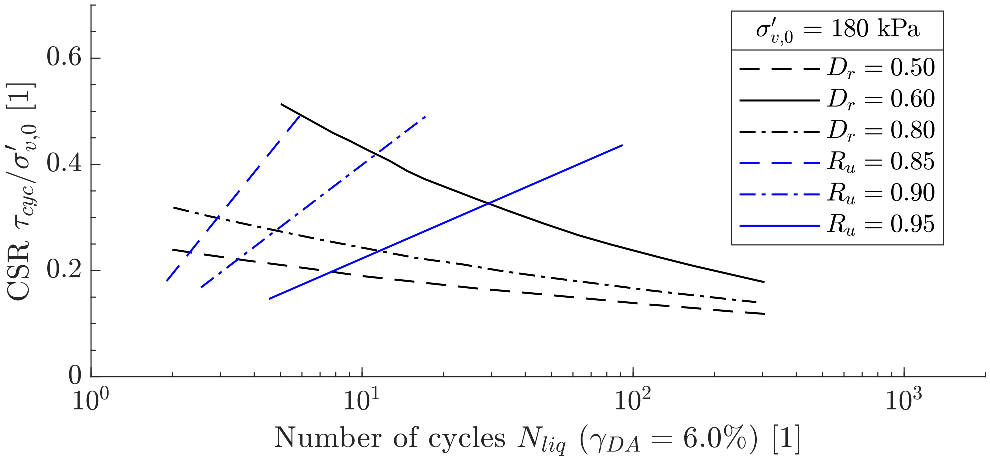

Figure 3.7: Comparison of normalized excess pore pressure values for a failure of 6% double shear strain amplitude for different relative densities from DSS tests according to Wu et al. (2004).

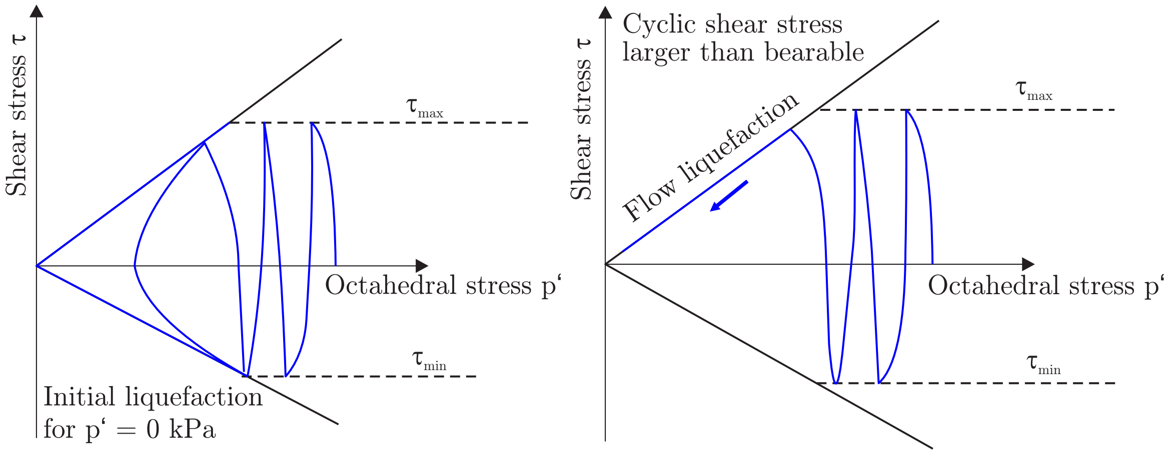

Figure 3.8: Definition of flow liquefaction, cyclic mobility and initial liquefaction.

zero octahedral stress (which is termed initial liquefaction), a strength remobilisation may occur during cyclic shearing due to dilative soil behaviour. The soil will dilate and generate negative pore pressure, which in turn increases the effective stresses until they are again reduced. This pattern is repeated. Deformation increases incrementally over the number of cycles. The stiffness and strength is decreased due to a decrease in effective stress up to a critical state (progressive stiffness degradation) (Lenart, 2008; Seed, 1979). Excess pore pressure and deformation are accumulated within each cycle. If the specimens are further sheared, they show the same shear strength but have larger deformations accumulated.

A more detailed differentiation between the failure types and an estimation of the specific liquefaction failure based on a characteristic drainage time were done by Robertson (1994), Robertson (2010), de Groot et al. (2006a) and de Groot et al. (2006b), respectively.

3.2.2 Parameters influencing the cyclic soil response

Several researchers have been working on liquefaction for many years and identified various influencing parameters related to the cyclic soil response and especially related to the cyclic strength ($\approx N_{liq}$). The first detailed investigations have been published among others by Castro (1975), Finn et al. (1970), Ishibashi and Sherif (1974), Lee and Seed (1967), Peacock and Seed (1968), Seed and Idriss (1967), Shibata et al. (1972). In the following section, the general cyclic soil behaviour will briefly be described.

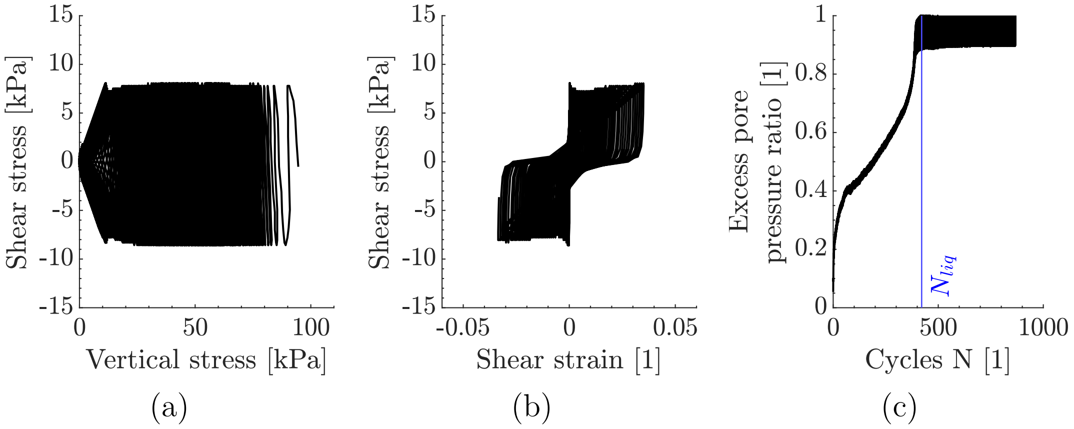

Figure 3.9: Shear stress over vertical stress (a), shear stress over shear strain (b) and excess pore pressure over number of applied cycles with number of cycles to liquefaction in blue (c) for a load-controlled constant-volume cyclic direct simple shear test with a vertical consolidation stress of 100 kPa performed by the author.

Figure 3.9 (a) shows the shear stress over the vertical stress in the case of a cyclic direct simple shear test under constant-volume conditions. The vertical stress decreases and the deviatoric stress is constant over the course of the test, indicating a load-controlled test. Figure 3.9 (b) shows the same test with the shear stress over the evolving shear strain. The shear strain increases with the number of cycles. The resulting cyclic shear strain amplitude depends on the loading type. For some load types, mean shear strain predominates and for some, cyclic shear strain predominates. The decreasing shear modulus can be seen from the hysteresis as well as indirectly from the increasing shear strain at constant shear stress. The excess pore pressure accumulates with decreasing stress. Figure 3.9 (c) shows the excess pore pressure ratio increase over the number of cycles. Larger shear strains occur as the sample reaches liquefaction, since larger strains are required to develop any shear resistance and to maintain stress equilibrium.

The trend of shear strain and excess pore pressure was obtained for this specific shear stress from the DSS device. However, not only the maximum shear stress but also the load type plays an important role in the soil response. The same maximum load e.g. 15 kPa with a different minimum load (changed LTR) will not lead to the same cyclic behaviour. In the case of a minimum shear stress of -15 kPa, a symmetric two-way load arises, whereas for a minimum load of 10 kPa, a non-symmetric one-way load is present.

This applies furthermore to the same deviatoric boundary conditions but a test performed within a different laboratory device, because of a rotation of principal axes.

The most common influencing parameters are discussed below. In the following, the cyclic stress ratio is plotted against the number of cycles to liquefaction (cf. Figure 3.9 (c)). Certainly, the trend of the pore pressure accumulation over the number of cycles may be influenced, but for simplicity this is not assessed. Moreover, a differentiation between load- and displacement-controlled test conditions is made.

Static components

The anisotropic consolidation can influence the cyclic resistance compared to the isotropic consolidation (Lee and Seed, 1967; Vaid and Chern, 1983; Hosono and Yoshimine, 2004; Pan and Yang, 2018; Yang and Sze, 2011). The influence of different anisotropic consolidations is shown in Figure 3.10 (a). Seed and Peacock (1971) show that a smaller earth pressure coefficient at rest k_0 leads to smaller cyclic strength. Figure 3.10 (b) shows shear strain contours for the number of cycles to liquefaction over the CSR for different MSR values. For a specific CSR and increasing MSR, the number of cycles to failure for a defined shear strain value decreases. Hence, a faster failure is expected. Similar results have been presented by Hyodo et al. (1994). The effect of MSR and CSR will be discussed later in Section 5.2 in greater detail.

In displacement-controlled tests, there is no influence of the mean shear strain. Only the amplitude of the cyclic shear strain influences the excess pore pressure accumulation process.

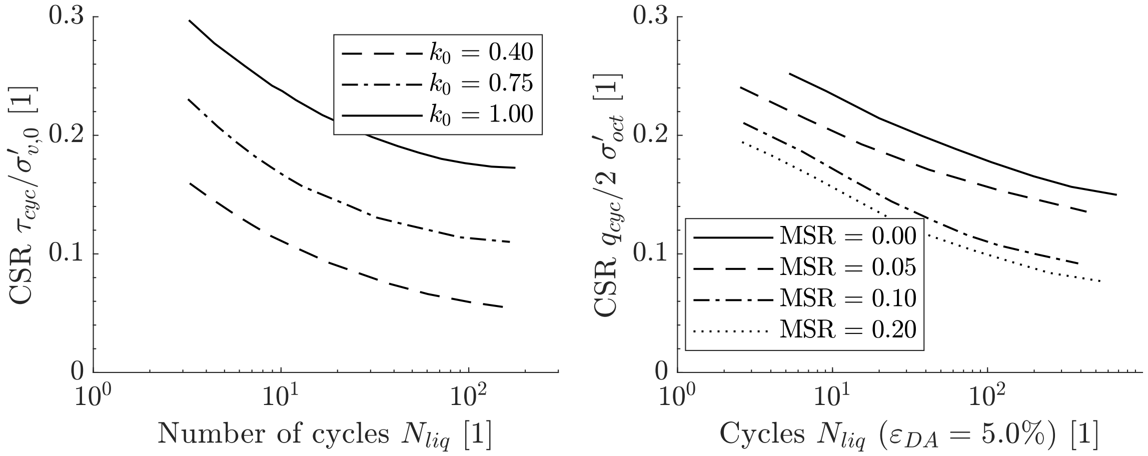

(a) (b)

Figure 3.10: Influence of anisotropic consolidation after Seed and Peacock (1971) (a) as well as CSR over number of cycles to liquefaction for different mean shear stress ratios according to Pan and Yang (2018) from cyclic triaxial tests for a failure double amplitude strain of 5% and a relative density of $D_r = 0.6$ (b).

Confining stress

For load-controlled tests, the influence of confining stress can be bypassed by using the normalized CSR value. In this case, only a small influence of the stress remains (Marr Jr. and Christian, 1981; Wichtmann et al., 2009). Andersen (2015) increases the accuracy by using an empirical derived exponent within a power function (n = 0.9) to consider the confining stress state.

For displacement-controlled tests, the influence of stress was found to not be very pronounced by Dobry et al. (1982) in undrained triaxial tests. The compaction behaviour in drained tests can at least quantitatively be correlated with a potential excess pore pressure build-up under undrained conditions. In this case similar results were found by Silver and Seed (1971a) in drained triaxial tests. The general response depends on the initial void ratio (Silver and Seed, 1971b; Youd, 1972; Pyke, 1973) and a certain volumetric threshold γ_{tv} (see Section 3.2.2). The cyclic shear strain amplitude needs to be larger than this value in order to accumulate excess pore pressure or permanent compaction. However, other researchers found a stress dependency for displacement-controlled drained and undrained tests (Schaefer et al., 2019; Saathoff and Achmus, 2021).

Frequency

The load frequency for cyclic laboratory tests is usually chosen representative for the investigated boundary conditions in the field. For offshore structures and a storm period of approximately 10 s this would result in a load frequency of 0.1 Hz. However, the influence of the frequency is not very pronounced for cyclic loading of dry sand up to 1 Hz (Gotschol, 2002; Youd, 1972).

Relative density

The relative density D_r has a great influence when it comes to load-controlled tests (Boulanger and Idriss, 2006; Suzuki and Yamamoto, 2004). The effect was already partly shown in the last chapter. Loose soil exhibits a different failure mechanism and tends to have a more pronounced contractive behaviour compared to dense sand. One of the first studies was conducted by De Alba et al. (1975) on direct simple shear tests for different relative densities and up to 100 cycles. In general, greater cyclic resistance occurs with denser soil.

The influence of relative density is present in displacement-controlled tests, but much less so in undrained tests (Dobry et al., 1982; Saathoff and Achmus, 2021).

Amplitude

The cyclic load amplitude has a great influence on the cyclic accumulation. For an increased amplitude, an increased excess pore pressure accumulation (or volumetric strain in drained tests) can be observed. This also applies to the shear strain amplitude in displacement-controlled tests; if certain threshold values are exceeded, the accumulation is even larger.

Particle shape and grain size distribution

Accumulation correlates with the contractive response of the soil. This in turn correlates with the general soil particle shape (Figure 3.11) (Powers (1953)). Soils with round particles have lower shear resistances, so do poorly-graded soils. The particle shape can affect the number of cycles to liquefaction by up to 200% (Kudo et al., 1993). Uniformly graded sand with round particles has the greatest liquefaction potential (Castro, 1969); soils with angular particles are not as strongly affected.

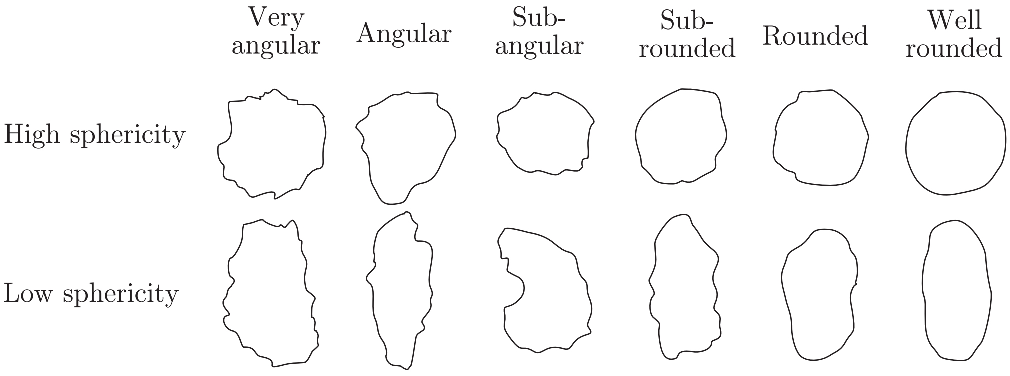

Figure 3.11: Particle shape categorisation according to Powers (1953).

Overconsolidation ratio

The overconsolidation ratio (OCR) has an additional influence on the soil response. A larger OCR results in a higher cyclic liquefaction resistance (Ishihara and Takatsu, 1979) (Figure 3.12).

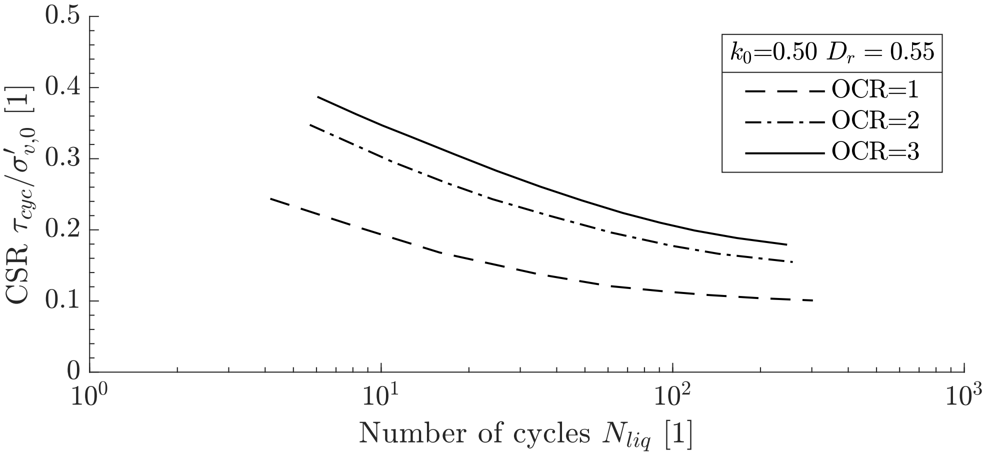

Figure 3.12: Soil response for different overconsolidation ratios from cyclic torsional shear test on Fuji river bed sand after Ishihara and Takatsu (1979).

Application of mean shear stress

When cyclic direct simple shear tests under constant-volume conditions are performed, not only the absolute value of the mean shear stress has an influence on the cyclic soil response, but it also matters how the load is applied. In the cyclic laboratory tests, a consolidation phase is first carried out in which the specimen is loaded with a stress according to the desired representative depth. The volumetric strain is analysed, and at a specific time, the consolidation is stopped. Subsequently, the mean shear load of the cyclic load package is applied in a drained manner. The mean shear load can be applied in a drained or undrained manner where this mainly depends on site-specific parameters such as permeability, foundation dimensions, and most importantly, the frequency of the storm load. When the specimen is loaded with a drained mean load, a slow build-up of the storm is assumed. The specimen (and so the theoretical element in the field) is free to drain during this phase. For clay, for example, both the mean and load amplitude must be applied under undrained conditions, because of the low permeability.

Shear strain thresholds for displacement-controlled tests

When a specimen is sheared, the soil response gets softer with increasing deformation. This behaviour can be plotted in the shear modulus degradation curve, which is normalized to the (initial) maximum shear modulus. There are different general soil responses for different shear strain bandwidths within the shear modulus degradation curve. For very small shear strains the stress-dependent initial shear modulus G_0 is expected (Figure 3.13). The first threshold γ_{tl} marks the end of the absolute linear elastic response and the beginning of the elastoplastic response up to the second threshold. The second value is the volumetric threshold below which no significant volumetric strain or excess pore pressure accumulation can be expected (Vucetic, 1994). The value of the absolute shear strain can be interpreted as the shear strain amplitude in the case of cyclic loading. At the degradation threshold γ_{td}, the shear modulus starts to decrease more rapidly and for cyclic loading, it decreases even further with an increasing number of cycles (Chen et al., 2019). For the degradation threshold and the flow threshold γ_{tf}, there is mainly a plastic soil response.

Effect of specimen preparation

The cyclic response can be affected by the sample preparation procedure. Proper preparation should result in a homogeneous soil sample that is as close to field conditions as possible. Sample preparation and thus the influence of the material have been studied by many researchers (Tatsuoka et al., 1986; Ladd, 1974; Yamashita and Toki, 1993). The different preparation methods lead to different orientation, spatial arrangement of particles and form different voids (Brewer, 1964; Oda and Iwashita, 1999). Primarily, dry or wet, tamped or floated preparations can be used. Other methods include vibrations with different frequencies. Mulilis et al. (1977) performed many load-controlled cyclic triaxial tests on Monterey No. 0 sand with $D_r = 0.5$ using various methods (Figure 3.14). They found that specimen prepared under air or water pluviation are more susceptible to cyclic loading than prepared with moist tamping. Specimen which are prepared wet under vibration are expected to produce higher cyclic strength than dry tamped specimen.

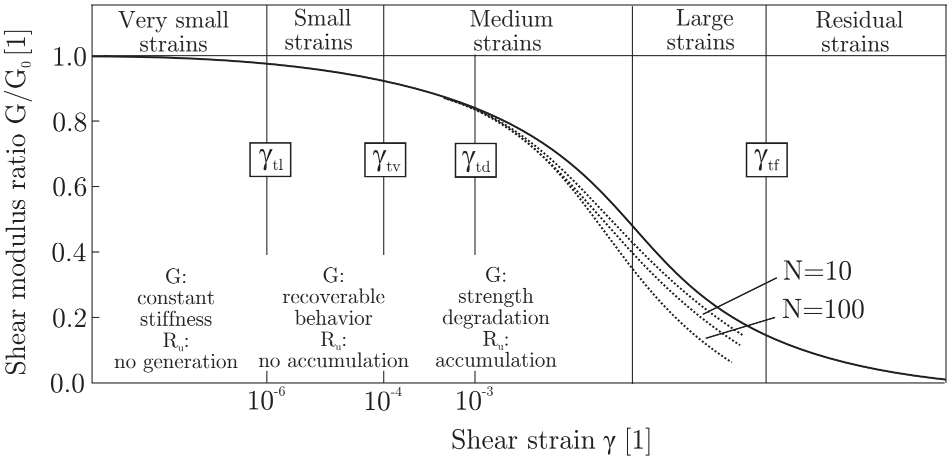

Figure 3.13: Shear modulus degradation curve with marked shear strain thresholds after Díaz-Rodríguez and López-Molina (2008).

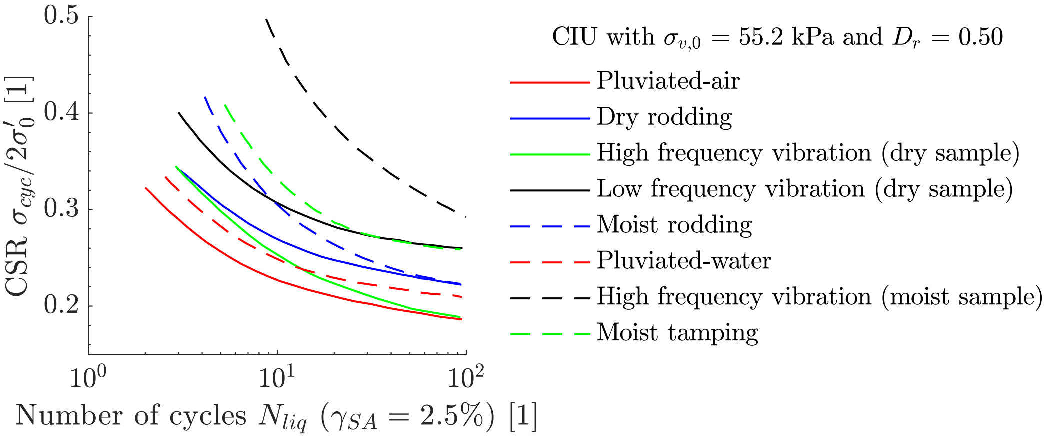

Figure 3.14: Different sample preparation techniques and their impact on the number of cycles to liquefaction according to Mulilis et al. (1977).

Vibration produces a stiffer specimen that develops smaller shear strains (Ladd (1977) with $D_r = 0.83$). Mulilis et al. (1977) showed that horizontal or vertical vibration does not appear to affect cyclic strength. In moist tamping, the particle orientation is more honeycombed, while in dry deposition it is strongly anisotropic and the particles are horizontally oriented (Sze and Yang, 2014). Elongated grains align differently in the different preparation processes. The honeycomb structure is more sensitive to compaction than the horizontally aligned particle layers. The preparation method influences not only the cyclic behaviour but also the monotonic response, e.g. the critical state line (DeGregorio, 1990; Mulilis et al., 1977).

Effect of pre-conditioning

Preconditioning in the form of pre-shearing is often performed prior to cyclic testing to improve soil strength, to obtain a response closer to field conditions, to reduce the effects of sample preparation and to homogenise the samples to some extent. The boundary conditions before shearing are not standardised. Pre-shearing can have a positive or negative effect on soil strength (especially with sand). It can result in better interlocking of the sand grains by changing the grain arrangement and not primarily change the relative density (Lee and Focht Jr., 1975). The grains will optimize their packing to a more stable soil skeleton (Song, 1990). Finn et al. (1970) report on cyclic pre-sharing increased resistance. Andersen et al. (2013) used 400 cycles with a CSR = 0.04 to pre-shear in order to consider a storm build-up and enhance the resistance to match the resistance in the field. Oda et al. (2001) report that for larger loads the cyclic strength decreases due to higher shear strains which lead to shear bands in which large void ratios are present. Within these areas large pore pressures are developed leading to a smaller number of cycles to liquefaction N_{liq}. Additionally, large preshearing under CNL conditions can, especially for loose soil, lead to plastic axial deformation.

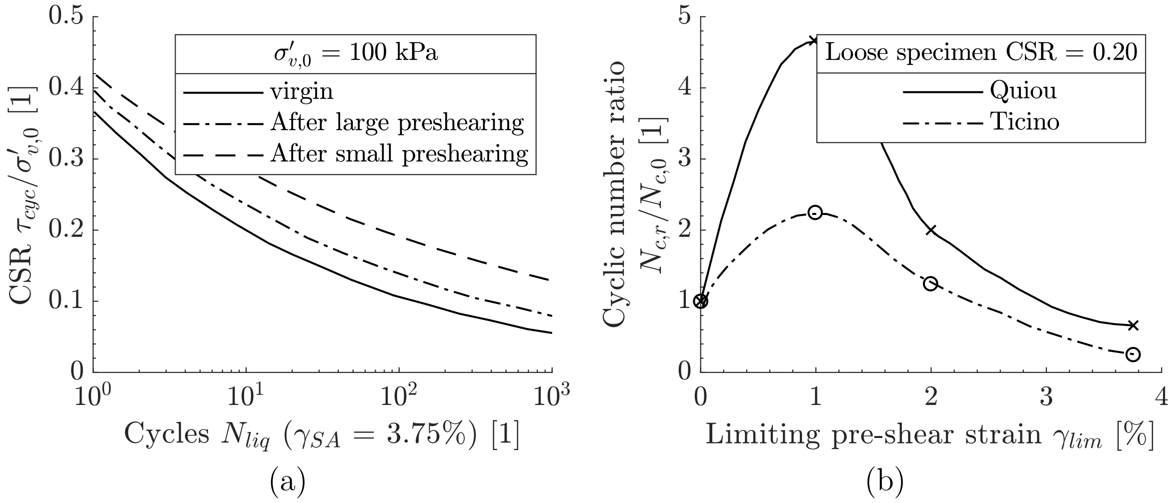

Figure 3.15: Influence of pre-shearing on number of cycles to liquefaction for small and large pre-shearing values on a loose soil sample (a) and influence of pre-shearing shear strain value for one CSR value related to the number of cycles to liquefaction for two different sands (b) from DSS tests (Porcino et al., 2009).

Even with a small amount of pre-shearing the resistance is usually increased. A positive effect of pre-shearing was found by Tokimatsu and Hosaka (1986); Wichtmann et al. (2005); Seed et al. (1975a) (Figure 3.15 (a)). Nelson and Okamura (2019) and Okamura et al. (2018) performed a large study and found that the resistance of Toyoura Sand at 45% relative density in cyclic triaxial tests depended on the resulting volumetric strain due to pre-shearing. A small volumetric strain of 1% doubled the resistance. The volumetric strain after the pre-shearing phase was used as an indicator for the change in resistance. Smits et al. (1978) performed cyclic triaxial tests with intermittent drainage stages and related the pre-shearing effect to the volumetric strain (change in porosity). The incremental change in volumetric strain was related to incremental reorientation of the particles and hence a change in fabric. A model to consider the change in porosity was later proposed by Meijers and Luger (2012). According to Ishihara and Okada (1978) (Ishihara and Okada, 1982; Suzuki and Toki, 1984), there is a change in response depending on whether the stress crosses the phase transformation line (PTL), distinguishing dilative and contractive behaviour. The phase transformation line can be drawn in $\varepsilon_v - \gamma$ or $\varepsilon_v - \varepsilon_1$ plots at the maximum volumetric strain. The acting shear stress and normal stress can be read and correspondingly plotted in the p'-q space (cf. Chapter 5). The phase transformation line (PTL) is the limit for small and large pre-shearing (Suzuki and Toki, 1984). If the shear stress in pre-shearing is smaller than the phase transformation line, a beneficial effect is expected and the undrained phase is going to show a stiffer and, hence, small excess pore pressure accumulation response (Porcino et al., 2009).

For displacement-controlled tests, Finn et al. (1970) found a shear strain amplitude larger than 1% yields the largest increase in resistance (Nelson and Okamura, 2019) (Figure 3.15 (b)). However, the exact influence is difficult to estimate and not only depends on the load type (load- or displacement controlled pre-shear phase), but also if the phase is done under drained or undrained conditions. Moreover, different results arise if a reconsolidation after the preconditioning is done, in the case that this phase is done under undrained conditions and excess pore pressure builds up.

Effect of repeated liquefaction

Soil elements around cyclically loaded offshore foundations are not just loaded until liquefaction, but also repeated liquefaction (reliquefaction) can occur. Teparaksa and Koseki (2017) show the increase in relative density as well as the shift of the number of cycles to liquefaction in the $CSR - N_{liq}$ curve to higher number of cycles to liquefaction N_{liq}. However, the effect may be less pronounced for a different initial relative density. Seed et al. (1977) performed shaking table tests under simple shear conditions simulating earthquakes and found an increase in cyclic strength. Several authors have presented that in repeated (full) liquefaction a smaller excess pore pressure accumulation occurs after liquefaction (dissipation) (Yasuhara and Andersen, 1991; Glasenapp, 2016). This phenomenon cannot only be explained with the changed or increased relative density, because Jostad et al. (2020) describe only a small volumetric change, so an altered soil fabric is an additional factor. This behaviour can also be identified for normally consolidated clay samples. Figure 3.16 shows results of re-liquefaction tests according to Yasuhara and Andersen (1991), which very clearly show the reduced accumulation response over the number of re-liquefactions.

Effect of multi-directional loading

For model tests with changing loading direction (Dührkop, 2009; Rudolph et al., 2014) and for element tests (Yamada and Ishihara, 1982; Wichtmann, 2005) the soil tends to forget the stress history after a larger number of cycles, especially for increasing load intensity. For multi-directional load additional influencing parameters are involved and make its consideration very complex. More information about the cyclic soil response relating to multi-directional loading can be found, for instance, in Glasenapp (2016), Werkmeister (2004), Gotschol (2002) and Hinz (2009).

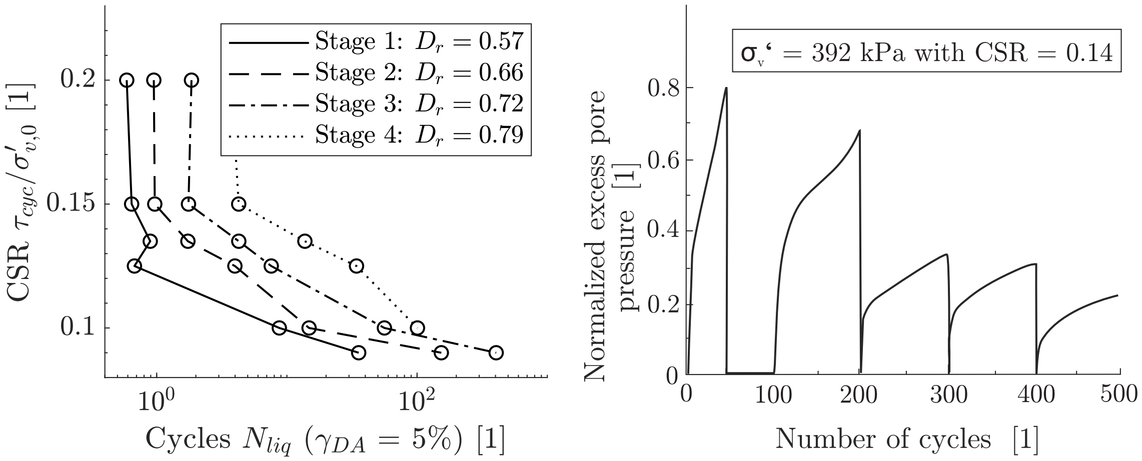

(a) (b)

Figure 3.16: Cyclic triaxial tests with four different reliquefaction stages (Teparaksa and Koseki, 2017) (a) and reliquefaction over number of cycles for normally consolidated clay from DSS test (Yasuhara and Andersen, 1991) (b).

3.2.3 Representative control type of cyclic laboratory tests

Prior to any cyclic tests the control type has to be chosen. The cyclic tests can be performed load- or displacement-controlled. It is important to perform tests which are representative for the investigated foundation case. This implies that the load scenario of the offshore structure needs to be known a priori. In most cases, the soil elements around offshore structures are assumed to be loaded in a load-controlled manner. However, displacement-controlled tests yield several advantages which are worth mentioning. The load conditions in the field, and hence the representative conditions in the laboratory, are assumed by many authors, but no in-depth analysis about the exact loading boundary conditions to the knowledge of the author exists. Evidently, the most realistic representation would be a combination of both boundary conditions, however, there may be one load state which is more dominant. The boundary conditions are often assumed to be well represented with load-controlled test conditions.

Generally, excess pore pressure is generated by a redistribution of particles which is directly correlated to shear strains. Within displacement-controlled tests, specific shear strain values can directly be used, as there are several shear strain threshold values defined (see 3.2.2). Silver and Seed (1971a), Youd (1972) and Martin et al. (1974) found that the shear strain amplitude is proportional to the intergranular strain. As there are already effects due to different devices and technicians, displacement-controlled tests are less sensitive to sample preparation and other influencing parameters (Ladd et al., 1989; Dobry et al., 1982) (Figure 3.17 (b) with different sample preparation and laboratories).

Under displacement-controlled conditions, the shear strain shows no rapid failure for loose soils as in case for load-controlled tests. For displacement-controlled tests, the sample undergoes N cycles with γ_{cyc}, whereas in load-controlled tests the sample shows the same γ_{cyc} only after a specific number of cycles and when γ has built-up. The resulting shear stress is in both cases different. Chen et al. (2019) compared the trend and soil response for displacement- and load-controlled tests (Figure 3.17 (a)) and showed that in load-controlled samples there is less damage induced.

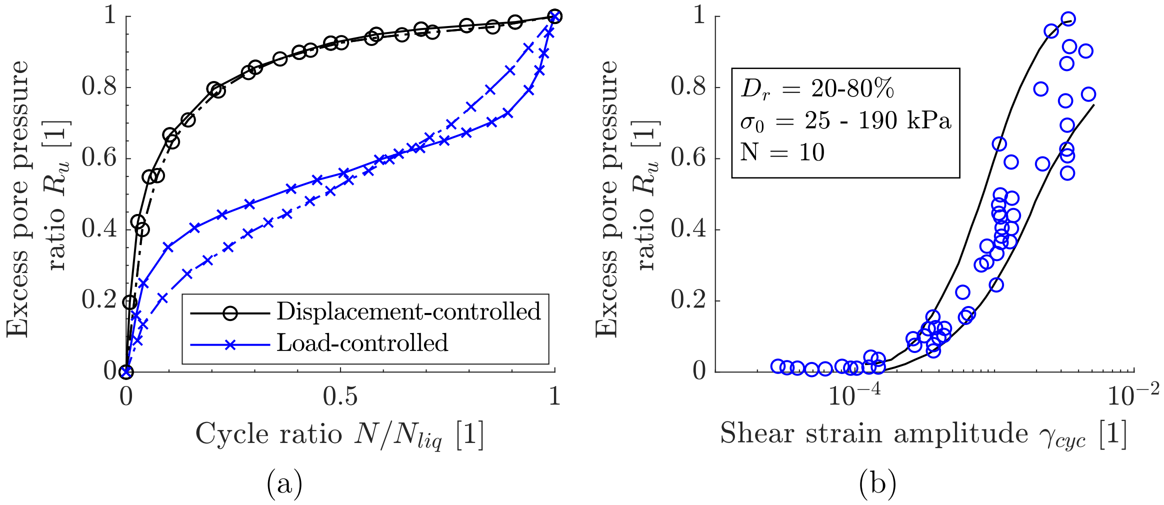

Figure 3.17: Comparison of normalized excess pore pressure over number of cycles to liquefaction for two load- and two displacement-controlled cyclic undrained tests with different loading boundary conditions for medium dense sand (Chen et al., 2019) (a) and normalized excess pore pressure over cyclic shear strain amplitude for displacement-controlled tests for four different preparation techniques and eight different sands from cyclic triaxial tests (Dobry et al., 1985a) (b).

3.3 Influence of different stress states

For different stress paths, different soil responses occur. These can be approximated with different laboratory tests. In the triaxial test with three degrees of freedom there is no rotation of the principal stresses, whereas in the DSS test there is a rotation. A more sophisticated analysis can be performed with the hollow cylinder apparatus.

The exact stress state around cyclically loaded foundations is difficult to determine, and not all stress paths can be investigated in laboratory tests. A simple schematic example helps to understand the overall behaviour and is best explained by analysing the stress states under a gravity foundation (Andersen et al., 1994). As shown in Figure 3.18, underneath the foundation, there is a symmetrical direct simple shear state, followed on the failure line by a triaxial compression and an asymmetric direct simple shear state; finally there is a triaxial extension state. The vertical stress is larger than the horizontal stress and, hence, a compression state arises (vertical cyclic compression). For the passive zone, due to the weight of the structure, a larger horizontal stress than vertical is present and leads to an extension state. For a horizontal shearing the direct simple shear test is most representative. A mean shear stress results from the mean storm load, but additionally, an initial deviatoric stress state from k_0 conditions (for $k_0 < 1$) occurs as $(1-k_0)\sigma'_v = q_{init}$. The differentiation is more complex for monopiles with wedge and flow around failure but the general idea can be transferred to other structures as well.

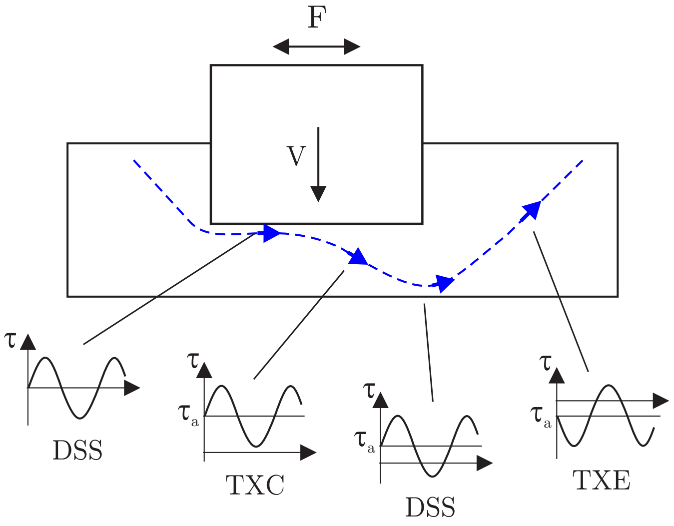

Figure 3.18: Stress states under gravity foundation (Andersen et al., 1994).

3.4 Representation of cyclic laboratory results in contour plot form

Andersen (1976) derived contour plots for two-way loading for designing gravity based offshore platforms in clay and for back-calculating field tests (Andersen et al., 1994). They used these plots to explicitly consider the effects of cyclic loading and the influence on soil elements at offshore foundations. Their general approach was primarily developed for gravity foundations in clayey material and accounted for decreasing soil stiffness without simulating all load cycles individually. Over the years, these contour plots have evolved to include several cyclic soil parameters such as cyclic shear strength, cyclic shear modulus, permanent shear strain, excess pore pressure, and damping for various loading conditions. There are more contours in the literature for shear strain than for excess pore pressure, which is the reason why shear strain representations will be used in the following. The general method however can be used for all different kinds of cyclic properties. Naturally, contour plots are usually based on a mathematical framework and the isocurves are not just linearly interpolated between performed cyclic laboratory test results (cf. Section 5.3). However, with this kind of representation, it is much easier to assess the cyclic response of a specific soil by looking at the trend of the isocurve, the distances between the isocurves, the maximum CSR value as well as the asymptotic CSR value.

Contour plots combine different influencing parameters as well as different cyclic soil responses. They can be used for the design of laterally loaded piles, gravity foundation or design of axially loaded piles (Jardine and Standing, 2012; Andersen et al., 2013). The contour plots are derived from a number of different cyclic tests with different load levels.

Not only the number of cycles to liquefaction, but also the general soil behaviour can be derived from laboratory tests. With regression analyses the true soil response can be interpolated between the different test boundary conditions in order to derive contour

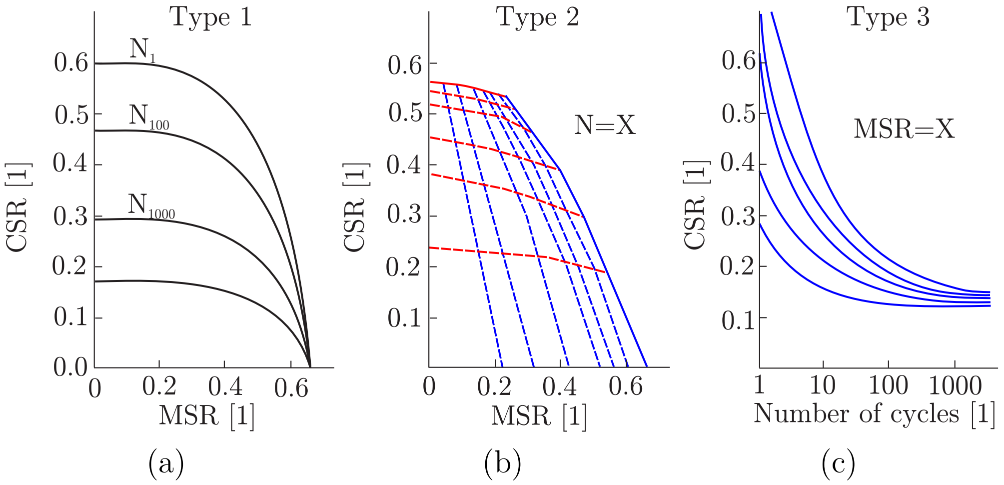

(a) (b) (c)

Figure 3.19: Type 1 (a), type 2 (b) and type 3 (c) contour plots for clarification purposes with fictitious isolines for cyclic properties based on Puech and Garnier (2017).

plots (Andersen et al., 1988). For a complete and accurate generation of new contour plots many tests are needed. It is recommended to use site-specific calibration of existing data with a small number of cyclic laboratory tests (as explained in Andersen (2015)).

There are three different types of contour plots (Figure 3.19). The axes are represented by the CSR and MSR or by CSR and N. The cyclic properties can be the cyclic shear strain (γ_{cyc}), the mean shear strain (γ_{mean}) and the normalized permanent excess pore pressure (R_u). Type 1 plots show the CSR over MSR to number of cycles to failure (Figure 3.19 (a)). The type 2 plot shows CSR over MSR for a specific number of cycles N with the cyclic property (Figure 3.19 (b)) and type 3 plots show the CSR for a specific MSR over the number of cycles N (Figure 3.19 (c)). The type 3 contour plots can be generated for different loading scenarios such as one-way loading, two-way loading (dependent on load type ratio - LTR) or sorted by mean stress level (MSR). Type 1 plots are not discussed further in this thesis. The best representation of the complete soil response is hence a full contour plot (multiple type 3 representations for different MSR values).

Figure 3.20 (a) shows the derivation of contour plots by means of shear strain. The cyclic component is depicted over the mean shear component for a specific number of cycles read from the element test results. For each test within this representation the cyclic property of interest is plotted. In Figure 3.20 (a) each point represents one test and shows the mean and cyclic shear strain for a specific number of cycles. The static curve is located at zero cyclic shear stress.

The data points from Figure 3.20 are then interpolated in order to generate isolines and results in a typical type 2 contour plot (Figure 3.20 (b)). The shear strain increases due to the decrease in the shear modulus for larger strains and because of a reduction in effective stresses by means of an excess pore pressure build-up. Isolines are derived for each predefined shear strain value. The solid red lines in Figure 3.20 (b) represent a failure mode due to cyclic shear strain; the solid blue lines a large mean shear strain equal to the failure shear strain of 5%. The failure shear strain value is not uniformly

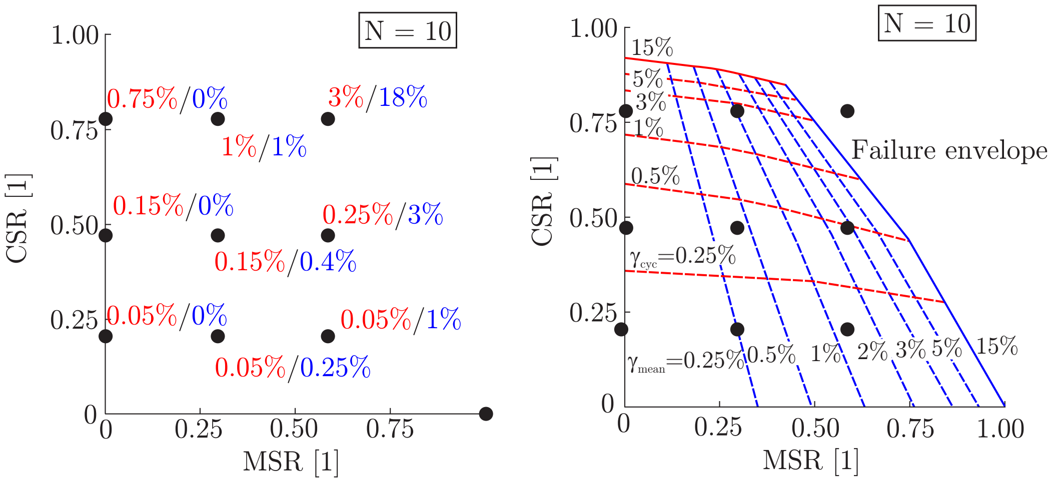

(a) (b)

Figure 3.20: Fictitious results from cyclic tests at N = 10 for different CSR and MSR values with cyclic shear strain in red as well as mean shear strain in blue (a) and derived contour lines based on the laboratory results (b) (following Andersen (2015)).

defined and varies between 3% and 15% (Zografou et al., 2016). Because they only show the stress-strain response for one specific number of cycle (here N = 10), the same has to be done for other numbers of cycles and for the normalised excess pore pressure R_u.

The response over the number of cycles N can be seen in a type 3 plot for a specific MSR in Figure 3.21. This type of plot is easier to fit since it already considers the element response over the number of cycles. In Figure 3.21 three tests are depicted for which the cyclic soil property, in this case the shear strain, increases over the number of cycles. For predefined values isocurves are derived. After the contour plot was calibrated to all possible boundary conditions, a three-dimensional representation can be made. For an increasing ratio of cyclic load, the cyclic shear strain amplitude increases and for increasing mean shear stress the mean shear strain increases up to failure. The failure mechanism changes at a specific load combination. Thereby, the bearing capacity for $N_{eq} = 10$ is larger than for the case of e.g. $N_{eq} = 100$, but smaller than for $N_{eq} = 1$, because the shear strain contour plots shrink over the number of cycles, whereas the excess pore pressure impact increases (cf. Figure 3.19 (c)). Example contours can also be found in Blaker and Andersen (2019) and Andersen (2015). They performed cyclic tests on dense to very dense silica sand.

3.5 Semi-empirical approaches to predict cyclic excess pore pressure build-up

There are different approaches to estimate the excess pore pressure response (Cetin and Bilge, 2012). The different methodologies are represented by four major groups: stress-based models, strain-based models, energy-based models, plasticity-theory-based and others, from which the first two will be presented.

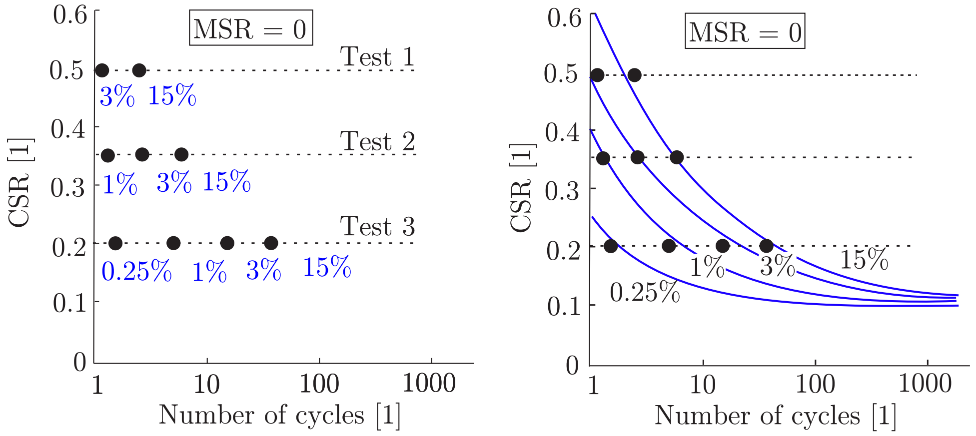

(a) (b)

Figure 3.21: Fictitious results from three cyclic tests for a MSR = 0 and CSR = 0.20, 0.35 and 0.50 and the value of cyclic shear strain (a); derived contour lines based on the laboratory results with related contour line 0.25%, 1%, 3%, 15% (b).

3.5.1 Stress-based empirical approaches

One of the earliest investigations regarding cyclic soil behaviour has been carried out by Lee and Seed (1967) with load-controlled cyclic triaxial tests. Seed et al. (1975b) later normalized the excess pore pressure curve based on results of De Alba et al. (1975) over the number of cycles by the number of cycles to liquefaction and found that it has roughly the same shape for different shear stress amplitudes (Figure 3.22 (a)). It is a two-parameters stress-based model:

$$R_u = \frac{1}{2} + \frac{1}{\pi} asin \left(2 \left(\frac{N}{N_{liq}} \right)^{\frac{1}{\beta}} - 1 \right) \tag{3.10}$$

The β value is the calibration factor for the shape of the normalized curve. Booker et al. (1976) suggests a value $\beta = 0.7$ for clean sand. Lee and Albaisa (1974) show that there is a range of β and proposed upper and lower bounds. Within their equation, the excess pore pressure build-up depends on the ratio of applied load cycles N to the number of load cycles that yield full liquefaction N_{liq}. The dependency of the number of cycles to liquefaction N_{liq} on the cyclic stress ratio for a certain soil has to be determined by a series of cyclic tests (Equation 3.11 with two regression parameters a and b).

$$N_{liq} = \left(\frac{CSR}{D_r \; a} \right)^{-(1/b)} \tag{3.11}$$

The establishment of a $CSR - N_{liq}$ curve is very straightforward (Figure 3.22 (b)). The CSR is correlated to the number of cycles to liquefaction. For a higher cyclic load the element can withstand a smaller number of cycles until it liquefies. The relationship between CSR and N_{liq} can be described with a power function. The number of cycles to

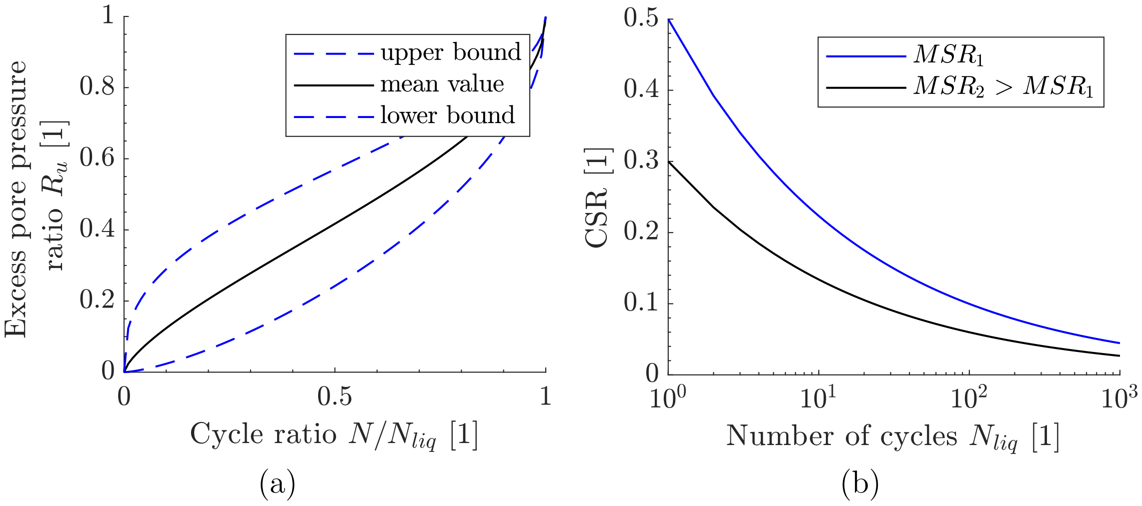

Figure 3.22: Excess pore pressure ratio over normalized number of cycles (Equation 3.10) (a) and schematic cyclic stress ratio over numbers of cycles to liquefaction for different MSR (Equation 3.11) (b).

liquefaction for sandy soils depends on the relative density and two regression parameters. The curves can furthermore be fitted to different MSR values.

Regarding the shape of the curve depicted in Figure 3.22 (a), it is mathematically not very flexible. There are other stress-based approaches for the estimation of excess pore pressure for instance according to Mao et al. (1999) (Equation 3.12).

$$\frac{\Delta u}{\Delta u_{max}} = \left[1 - \left(1 - \frac{N}{N_{liq}}\right)^{m}\right]^{\left[\frac{1}{\Theta}\right]} \qquad \Theta = \Theta_0 + p\left(\frac{\tau_{mean}}{\tau_{cyc}}\right) \tag{3.12}$$

Based on Seed's equation, Polito et al. (2008) propose an empirical equation derived from 145 cyclic triaxial tests with a factor β, in which the fines content is given in percent as well as the relative density (Equation 3.13).

$$\beta = c_1 FC + c_2 D_r + c_3 CSR + c_4 \tag{3.13}$$

The effect of pre-shear can be incorporated according to Smits et al. (1978) (also Meijers and Luger (2012)). The value of X is found to be between 500 and 1000. The term 10^A gives the response without pre-shearing (n = 0) and Δn can be used to consider the change in porosity (Equation 3.14).

$$\beta = 10^{A+X\Delta n} \quad N_{liq} = N_{liq,0} 10^{-X\Delta n} \tag{3.14}$$

3.5.2 Strain-based empirical approaches

Dobry et al. (1985a) published a strain-based approach based on isotropic consolidated cyclic triaxial tests. They correlated the excess pore pressure directly to the shear strain and took the starting point of excess pore pressure build-up (volumetric threshold) into account (Equation 3.15).

$$R_u = \frac{pfNF(\gamma - \gamma_{tv})^b}{1 + NF(\gamma - \gamma_{tv})^b} \tag{3.15}$$

Herein, γ_{tv} is the volumetric threshold (see Section 3.2.2) of roughly 0.0001, γ is the shear strain, N is the number of cycles. The value f is used for the differentiation between one- or two-way shaking. The values p, b and F are regression parameters. Dobry et al. (1982) state that the build-up of excess pore pressure is independent of the vertical stress and sample preparation. The overall trend and the results of the tests are reproducible, because the results are only slightly dependent on factors such as mean shear strain and void ratio. Their model was included into effective-stress-based non-linear ground response models (Matasovic, 1993).

Martin et al. (1974) developed an equation which relates the volumetric strain measured in drained tests for dry sand to the theoretical related generation of excess pore pressure in undrained test conditions. They assumed the volumetric strain to be independent of the vertical stress, which is later adopted by many other researchers (Finn et al., 1977). A slightly modified approach was published by Byrne (1991). It was used by Kluge (2007) for liquefaction analysis with a standard Mohr-Coulomb plasticity model for offshore foundation. Numerical methods that estimate the excess pore pressure based on accumulated shear strain are also presented by Dobry et al. (1982), Dobry et al. (1985b), Ivsić (2006) and Finn and Bhatia (1981).

The advantage of strain-based approaches is the close relationship between pore pressure and shear strain, but shear strains are more difficult to predict (Kramer, 1996). Therefore, stress-based approaches are more commonly used.

3.5.3 Other empirical approaches

There are many other empirical correlations and approaches. Plasticity-based approaches are presented by Prevost (1985) and Elgamal et al. (2003). There are also approaches based on energy or damage parameters (Berril and Davis, 1985; Ahn and Park, 2013; Azeiteiro et al., 2017). They can consider both shear stress and shear strain and hence reproduce results for irregular loading. However, there are numerous mathematical models most of which are not applicable for the intended use within this thesis. They are not compatible for integration into the developed explicit method, where simple contour plots are more advantageous.

4 State of the art modelling methods

The excess pore pressure accumulation and the general cyclic soil response are not only dependent on the factors presented in Chapter 3, but also on the interaction of generation and dissipation rates as well as spatial influences. This is for instance the layering or the interaction of structure and soil. These site-specific boundary conditions can only be included by using some kind of approximation of the field condition, which mostly involve numerical models. There are different approaches how the numerical model performs the calculation. For example, all cycles can be calculated individually, or the element response is estimated based on a combination of numerical calculation and cyclic laboratory test results. Additional effects result from the constitutive law or from calibration and regression effects.

4.1 Implicit numerical methods

Many engineering problems can be solved by investigating the monotonic foundation response with numerical simulations. This is often done with simple constitutive models such as the Mohr-Coulomb or the Drucker-Prager material law in two as well as in three dimensions. However, in some cases more advanced numerical tools are needed in order to investigate the stress-strain response for the accurate prediction of the soil response. The generation and dissipation of excess pore pressure, the redistribution of stresses as well as the development of plastic strains is of significant importance. Some problems require simple differentiation between monotonic and un- and reloading moduli which lead, for instance, to the use of the popular Hardening soil (small) model (Benz, 2007; Bentley Systems, 2022).

Sandy soils are an assembly of different particles with intrinsic parameters such as the shape, the particle bulk modulus, the grain size distribution and the particle density as well as state parameters such as void ratio. The general stress-strain relationship can already be described very well with advanced models for monotonic loading, but this goal has not yet been fully achieved for cyclic loading. Cyclic soil behaviour is extremely complex and can often only be partially approximated. First implicit models with cyclic characteristics have been created for example by Mrŏz et al. (1978), Dafalias and Popov (1976), Ohno and Wang (1993). Similar approaches were already done by for instance Prevost (1977), Prevost et al. (1980) and Andersen et al. (1978) with a set of yield surfaces. Prevost et al. (1980) were able to very well back-calculate load- as well as displacement-controlled triaxial and direct simple shear tests over a representative number of cycles. However, these methods reach their limits not only with respect to the computational effort but also with respect to the possible accuracy when relatively large numbers of load cycles (N > approx. 20) are to be considered (Safinus et al., 2011; Niemunis et al., 2005). With numerical simulation models, which use highly developed material laws – such as hypoplasticity with intergranular strain (Niemunis and Herle, 1998) or SANISAND (Dafalias and Manzari, 2004) – the system behaviour can be calculated in the best possible way. In sophisticated models, the overall soil response depends on pressure, load history and void ratio from which a correct contractive and dilative behaviour is simulated for different cyclic boundary problems. In general, there are many different soil models, of which the most common advanced approaches will be briefly presented.

Hypoplasticity and Hardening soil small model

For a long time the hypoplasticity model with intergranular strain (Kolymbas, 1988; Von Wolffersdorff, 1996; Gudehus, 1996; Niemunis and Herle, 1998) was the first choice when it came to sophisticated soil models for both monotonic and cyclic problems. In particular, because the extension of Niemunis and Herle (1998) takes the realistic effects of soil behaviour under unloading and reloading into account. The model does not distinguish between elastic and plastic parts as there is no plastic yield surface. It requires 13 parameters and is often compared with the Hardening Soil small model (HSsmall) (Marcher et al., 2000; Sheil and McCabe, 2016; Benz, 2007). The basic hypoplastic material model requires eight parameters and the extension for the intergranular strain concept five additional parameters. The HSsmall model is an elasto-plastic, stress-dependent, non-linear model with small strain consideration and isotropic hardening using 11 parameters. However, the main advantage of hypoplasticity over the HSsmall is that it is state-dependent and soil densification is taken into account. In general, the stress level, the soil density, dilatancy, contractance and peak friction angle are considered with one single equation without a potential function for plastic or elastic deformation. Within the HSsmall model every accumulated displacement relates to stiffness degradation and not to an altered void ratio. This is the reason why the hypoplasticity was extensively used to investigate the soil response under cyclic loading (Taşan, 2011; Grabe et al., 2004). The shortcoming of the hypoplasticity model is that dilatancy only depends on stresses and therefore volumetric strain and excess pore pressure can only be generated by stress changes and not by shearing (Niemunis and Herle, 1998).

The hypoplasticity model was frequently used in order to back-calculate small- or large-scale model tests. Taşan et al. (2010) and Grabe et al. (2005) used a two-phase model with a hypoplasticity model with intergranular strain for fully saturated soils to investigate the excess pore pressure within multiple cycles and were able to identify several influencing parameters. Taşan (2011) (Taşan, 2017; Taşan et al., 2010) identified influences of the number of cycles, the loading type, the relative density, the loading frequency, the soil permeability, and the pile diameter. Anyway, no method for practical estimation of excess pore pressure for site-specific conditions is given. Due to the soil-specific accumulation behaviour and the soil-structure interaction, the results can only be transferred to boundary conditions of practical projects to a limited extent. Similar investigations were performed by Cuéllar (2011); Cuéllar et al. (2012, 2014).

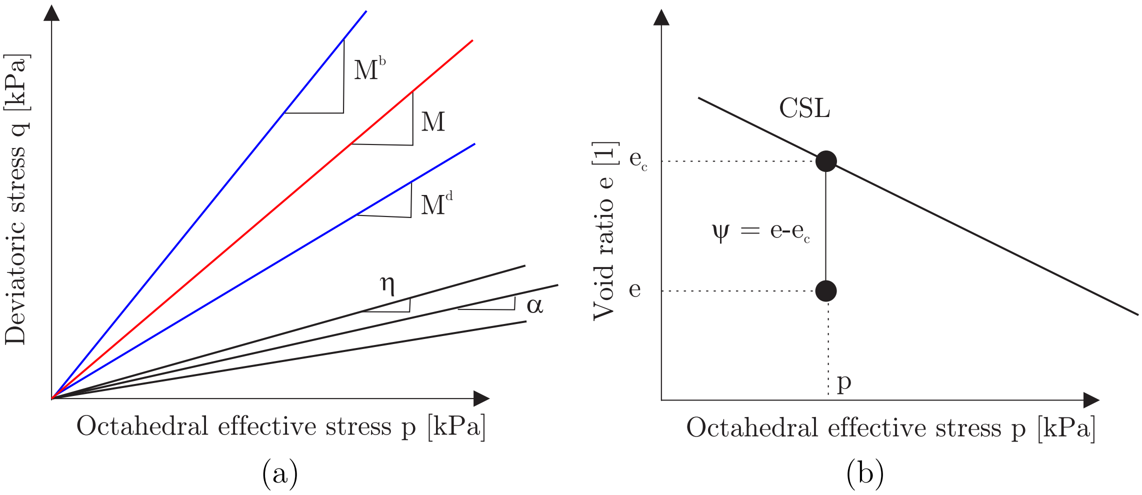

Figure 4.1: Bounding, dilatancy and yield surface in p'-q space (a) and CSL in e-p' space with distance between current void ratio and critical void ratio (b).

Simple anisotropic sand plasticity model

Most sophisticated implicit models are based on a critical state approach with an advanced dilatancy model and bounding surface plasticity. Especially, with faster computers and better algorithms, the use of more sophisticated models will become more important. The simple anisotropic sand plasticity model (SANISAND) was derived based on the critical state two-surface model with an open wedge yield surface in the stress space for sands by Manzari and Dafalias (1997) and the bounding surface plasticity (Dafalias and Popov, 1975; Dafalias, 1986). The bounding surface envelopes the possible stress states and the dilatancy surface separates contractive from dilative behaviour. There is an additional yield surface for the current stress state (Figure 4.1). Dilatancy and volumetric strain caused by changes in stress and void ratio are considered by means of the critical state line (CSL). The correct dilatancy behaviour is important as it relates the volumetric strain to shear strain. The plastic stiffness is considered with the distance from the centre of the yield surface to the bounding surface.

There are different versions of the SANISAND model, but all go back to Dafalias et al. (2004). The model was successfully used for the prediction of the compaction of dry sand and the build-up of excess pore pressure for fully saturated soils in for instance earthquakes on embankment dams (Yang et al., 2020) or dynamic loading of for instance monopiles (Esfeh and Kaynia, 2020). This model is continuously developed (Taiebat and Dafalias, 2008). Liu et al. (2018b) implemented a memory surface based on the work of Corti (2016), which was also the basis for the most developed versions according to Yang et al. (2022) and Liu et al. (2021).

An overview of typical values for the SANISAND model is given in Table 4.1. The model is explained in detail in Appendix A.1.

Table 4.1: Input parameters for SANISAND04 model (Yang et al., 2020; Jostad et al., 2020; Dahl et al., 2018; Wichtmann et al., 2019; Pak et al., 2016) (cyclic values in brackets).

Symbol	Ottawa F65	Toyoura	Nevada	NGI	Montere	Karlsruhe
G_0	125	125	150	250	130	150
ν	0.05	0.05	0.05	0.05	0.05	0.05
M	1.26	1.25	1.14	1.49	1.27	1.34
c	0.735	0.712	0.78	0.6	0.712	0.7
λ	0.0287	0.019	0.027	0.013	0.02	0.112
e_0	0.78	0.934	0.83	0.71	0.858	1.103
ξ	0.7	0.7	0.45	0.67	0.69	0.205
m	0.02	0.02	0.02	0.02	0.02	0.05
h_0	5.0	7.05	9.7	5.0(7.0)	8.5	10.5
c_h	0.968	0.968	1.02	1.1	0.968	0.75
n_b	0.6	1.25	2.56	6.0(1.3)	1.05	1.2
A_0	0.5	0.704	0.81	0.6	0.6	0.9
n_d	0.5	2.1	1.05	5.0(8.0)	2.5	2.0
z_{max}	11.0	2.0	5.0	8.0	4.0	20
c_z	500	600	800	100	50.0	10000

Other implicit models

There are also many other cyclic models in addition to the SANISAND constitutive laws, whereby all models have different advantages and disadvantages, as no model can currently be considered universally applicable. One of these models is the intergranular strain anisotropy (ISA) model (Fuentes and Triantafyllidis, 2015; Wichtmann et al., 2019), which is a rate-type model and combines bounding surfaces and Karlsruhe hypoplasticity (Boulanger and Ziotopoulou, 2013; Fuentes and Triantafyllidis, 2015). The main goal of the latest ISA model is to incorporate the influence on soil response not only dependent on the void ratio and effective stress but also on the deposition method. It accounts for the inherent fabric effect by using an initial isotropic fabric structure with predominant round-shaped particles (Fuentes and Triantafyllidis, 2015). The model adopts the intergranular strain concept with which small strain effects can be captured due to the recent strain history. It uses the same dilatancy surface as the SANISAND model and requires a total of 15 parameters.

The PM4Sand model by Boulanger and Ziotopoulou (2015) simulates the response of cohesionless material under dynamic loading. It originates from Dafalias and Manzari (2004) and is an effective stress model with 21 input parameters. Most of them can be derived from practical on-site measurements such as cone penetration test (CPT) or standard penetration test results and it is mainly used in earthquake engineering.

For the consideration of liquefaction in saturated soils the University of British Columbia implemented an extension of the UBCSAND in Plaxis called UBCSAND-PLM (Puebla et al., 1997; Tsegaye, 2010; Petalas and Galavi, 2012). This constitutive model is an effective-stress model based on classical plasticity with a hyperbolic hardening rule (dilatancy theory (Rowe, 1962)). The model requires 15 parameters to simulate the mechanical behaviour of liquefied soils, including six stiffness parameters, three advanced (curve fitting from undrained triaxial and DSS tests) and two strength parameters. It was extensively used for liquefaction analysis of embankment dams under seismic loading (Yang et al., 2020).

4.2 Explicit numerical methods

Besides the use of complex material models with up to some 20 material parameters and the implicit calculation of cyclic loading, explicit methods can be used to estimate excess pore pressure accumulation with a very limited number of calibrated soil parameters. In comparison with implicit models, explicit models do not calculate each cycle individually. Simple numerical models are combined with results from high-quality laboratory tests. First explicit approaches with simple pore pressure generation and dissipation can be found in Rahman et al. (1977); Kagawa (1986); Taiebat (1999); Taiebat and Carter (2000). A more recent approach is used by Andresen et al. (2011), who combine information from site-specific cyclic direct simple shear and triaxial tests as input for the numerical simulations. The stress states in a soil element that are passed through in the course of a cycle are calculated using a simple constitutive law. This simple (elasto-plastic) constitutive law alone would not be able to predict excess pore pressure or cyclic accumulation in the absence of hardening. For this feature, additional cyclic input in the form of contour plots is needed. There are also other explicit models with similar modelling techniques such as the stiffness degradation method (SDM) for a drained cyclic analysis of deformation accumulation (Achmus et al., 2009).

4.2.1 High Cycle Accumulation model

Wichtmann (2016) gives a comprehensive overview of the state of knowledge regarding the behaviour of soils under cyclic loading. This work also describes the High Cycle Accumulation (HCA) model. It predicts settlements and excess pore pressures for a very large number of cycles. It is based on extensive laboratory work on drained cyclic triaxial and multiaxial DSS tests (Wichtmann, 2005).

Within the HCA, the first cycles are calculated implicitly and used further for the explicit part of the model in combination with an empirical regression of laboratory results (Niemunis et al., 2005; Wichtmann, 2005; Wichtmann et al., 2008, 2010). An implicit control calculation is performed after a certain number of load cycles. Several element tests with up to 10^6 cycles are to be used for the empirical regression. The HCA is an explicit method which requires seven different sub-functions to consider the different influences found in cyclic soil tests. It considers the load history, the polarization, the strain amplitude, the void ratio, the confining pressure and the stress ratio (Equation 4.1).

$$\varepsilon_{acc} = f_N \; f_{\Pi} \; f_{ampl} f_e \; f_p \; f_Y \tag{4.1}$$

The model was used extensively for validation and calibration with a large amount of laboratory tests. Many calculations have been performed, mostly setting the polarisation equal to 1 and thus neglecting it. Good agreement was found in back-calculations of cyclic laboratory tests in Wichtmann et al. (2011). Regarding the sub-function of most interest f_N, Niemunis et al. (2005) developed the following approach based on Sawicki and Swidzinski (1989):

$$f_N = C_1 \; ln(1 + C_2 \; N + C_3) \tag{4.2}$$

Herein, C_N are constants of the fitting function. All parameters can be established with a limited number of cyclic triaxial tests. The method is theoretically very well founded, but is more suitable for basic scientific investigations and less for practical applications. The validation and various applications are presented in Zachert and Wichtmann (2020) and Jostad et al. (2020).

4.2.2 Cyclic accumulation model

A method for predicting the load-bearing behaviour of foundation structures under cyclic loading that is conceptually applicable to a variety of general cyclic problems was presented by Jostad and Andresen (2009) and is based on ideas according to Andersen (1976) and Andersen et al. (1978). They combine the information from site-specific cyclic direct simple shear and cyclic undrained triaxial tests in the form of contour plots as input for the numerical simulations (cf. Chapter 3). The general approach is based on the stress path philosophy (Lambe, 1967; Lambe and Marr, 1979; Bjerrum, 1973). Herein, representative tests are chosen for representative stress states of elements. It implies that different laboratory test results can be seen as representative and be used to describe the soil response (Wood, 1990). In general, this requires true triaxial tests; however, since these are not feasible for practical application, triaxial tests and direct simple shear tests are used. The problem is mainly that the stress path does not only depend on the soil element itself, but that stresses are redistributing. The model assumption hence is that the element follows exactly this stress path. By using the contour plots for different representative load types over the number of cycles, no separate constitutive framework is needed due to the additional inter- and extrapolation of laboratory results. The general method can be used for both undrained (UCDAM) and partially drained (PDCAM) analyses (Jostad et al., 1997, 2014). An approximate implementation is given in Appendix F.2.

Undrained conditions

The undrained cyclic strain accumulation model (UDCAM) analyses the undrained behaviour under mean and cyclic load as a non-linear stress-strain response with anisotropic features (Andersen, 2009). It is solely based on cyclic laboratory results and uses total stresses. This means that the non-linear stress - strain curve is theoretically extracted without any derivation of e.g. a stiffness modulus or undrained cohesion of the soil from laboratory tests required for a constitutive model. However, in order to have a mathematical representation some values are still derived in reality. For clarification, this undrained method is explained prior to the partially drained model. The UDCAM method can only be used for completely undrained conditions, which occur mainly with cohesive materials. A first implementation was presented in Jostad and Andresen (2009) and an extension to three-dimensional application in Jostad et al. (2014). The model uses the strain accumulation procedure (Andersen, 1976) (explanation in Appendix C) and accounts for cyclic soil degradation in the form of reduced stiffness due to accumulated strains in the integration points of the numerical model for a calculated equivalent number of cycles. The laboratory results are not fitted to advanced constitutive models but are rather directly used (Andresen et al., 2011) – either as a look-up table or as a mathematical framework. It uses results of cyclic triaxial compression and extension tests for the estimation of the cyclic response dependent on the individual stress state; and for all other stress states cyclic direct simple shear test results.

UDCAM-S

A simplified version of the UDCAM model is implemented in the finite element code PLAXIS (Bentley Systems, 2022) and termed UDCAM-S (Jostad et al., 2014). The simplified model is easier to handle, but has some limitations. It is still mainly intended for the application of undrained soil behaviour of clay or silt with low permeabilities. This model is being explained prior to the full UDCAM model since it is more comprehensible.

The UDCAM-S model in PLAXIS is strictly speaking a pre-processor for the input values of the elasto-plastic anisotropic shear strength (NGI-ADP) constitutive model with anisotropic shear strength and anisotropic hardening function (Grimstad et al., 2012). The NGI-ADP was developed for monotonic anisotropic soil response. Cyclic loading is considered by means of contour plots. Hence, the main input are the contour plots for different boundary conditions. The NGI-ADP is an improved model which is based on plane strain conditions (model of Davis and Christian (1971)). The model requires the shear strain at failure for these three different stress types (direct simple shear, triaxial compression and triaxial extension), as well as the shear strength values for the different states normalized to the static shear strength s_u as input parameters. It uses an elliptical interpolation between the three stress states. The design cases FLS, SLS and ULS can be investigated by extracting the associated values from the contour plots (see Section 3.4). For isotropic soil conditions, only the soil response from DSS tests is assessed. The result of the analysis are load-deformation curves for cyclic (FLS), average (SLS) or total loads (ULS). The default contour plots are for Drammen clay with a specific w_l, PI and I_P. But also contour plots for sandy materials exist. In order to perform an analysis on other soil, this plot can be scaled vertically according to site specific data for stronger or weaker soil responses. The dominant influence is the CSR, which is the vertical axis. Scaling is done to match a reference contour plot to cyclic test data for the soil being calibrated.

The calibration procedure is mainly done by the “cyclic accumulation tool”. The procedure shall briefly be described. First an equivalent number of cycles N_{eq} is derived with the strain accumulation procedure under symmetric two-way loading (cf. Appendix C). The result is a type 2 contour plot for this N_{eq} (Figure 4.2 (a)). A stress path is needed which defines the relationship between normalized cyclic and mean shear stress (Figure 4.2 (b)). The stress path is one of a few relevant parameters and the value must be chosen carefully.

If the ratio is small, the behaviour will be dominated by the mean response, if the ratio is high, the behaviour will be dominated by the cyclic response. For a practical value, the stress path should be derived from the cyclic and the mean loading of the structure. The path starts at zero normalized cyclic and mean shear strain. For structures under dead-weight, the starting point should be the mean dead-weight (MSR), since this shear stress is already mobilized. Since this is done before the numerical calculations, no exact stress conditions are considered. Furthermore, no stress redistributions are considered. After N_{eq} and a stress path inclination have been chosen, the next step is to evaluate the type 2 contour plots. The sum of mean and cyclic shear strain and shear stress (termed cyclic shear strength) is used for ULS case. In case of dynamic analysis, only the cyclic shear strain component is evaluated. The NGI-ADP model is fitted to the stress-strain path by means of a simple particle swarm optimisation.

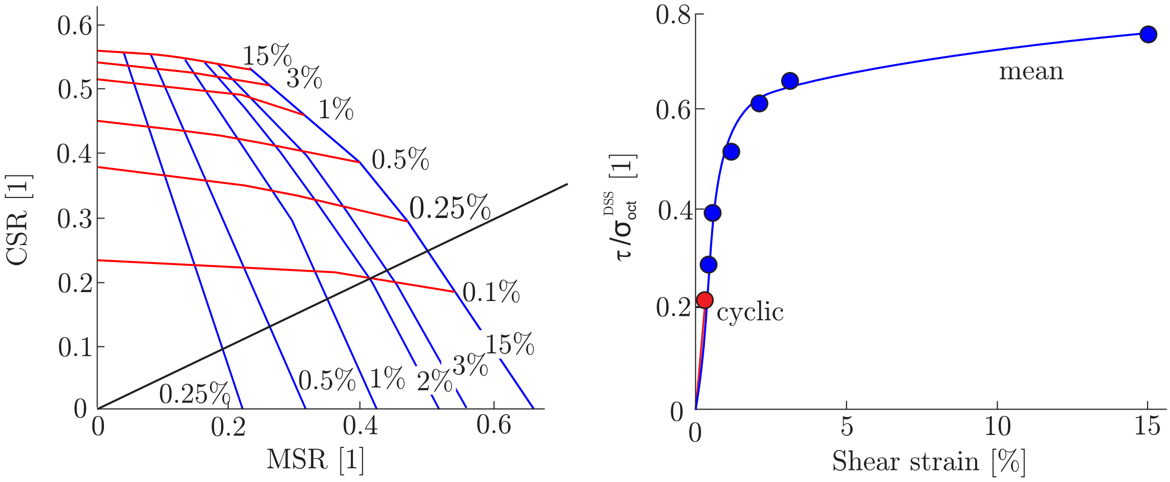

(a) (b)

Figure 4.2: Schematic contour plot (a) and resulting total shear-stress - shear-strain relation for LTR = 2 (b) (modified after Andersen (2015)).

UDCAM

The UDCAM overcomes some of the limitations of the simplified UDCAM-S. The UDCAM evaluates the stress states in each integration point. This is especially relevant for large shear strains and hence elements at failure. However, if the stress path is chosen correctly, the UDCAM-S simplification may save a lot of computational effort and hence calculation time. Nevertheless, the chosen stress-path would be an approximation and be not correct for all integration-points in the model. One additional advantage of the UDCAM is that it directly incorporates the strain-accumulation procedure and hence equivalent number of cycles N_{eq} are calculated for each integration point after each storm bin.

The general procedure of the UDCAM is as follows. The soil is undrained during one cycle and the cyclic degradation is estimated based on the soil response in the integration points. In a finite element model the global mean load F_{mean} is applied. In a different model the global cyclic load amplitude F_{cyc} is applied. Within the contour plots the memory variable e.g. pore pressure or shear strain can be followed through different boundary conditions such as N, τ_{cyc} or τ_{mean}. For a given storm load consisting of different bins, the procedure can be used in order to find a N_{eq}. The material for mean and cyclic soil is updated between each phase which is related to a specific N of the storm for each integration point up to this point within the storm. Iterations are performed to update the mean shear stress based on the results for the cyclic model. The output values are γ_{cyc} and γ_{mean}. For plane strain conditions $\gamma_{cyc,tri} = \varepsilon_x - \varepsilon_z$ and $\gamma_{cyc,DSS} = \gamma_{xz}$ are used (Jostad and Andresen, 2009). For the model with F_{mean} the output is a function of γ_{cyc} and for the F_{cyc} model the output is function of γ_{mean}. Afterwards a new N is calculated from the ΔN of the storm bin and the $N_{eq,old}$ (see Appendix C). Finally, the materials are updated. The stress-strain responses from laboratory results are elliptically interpolated between different stress states and are used within the finite element framework (for a derived N_{eq} which is representative for a specific storm load bins and integration point). The first calculation starts the iteration with $\gamma_{cyc} = 0$ within the mean model. The mean model outputs γ_{mean} for each integration point as an input for the cyclic model.

More information can be found in Jostad and Andresen (2009), Andersen et al. (1978), Khoa and Jostad (2017) and Jostad et al. (2014).

Summarising, the UDCAM model is not implemented trivially and an implementation is not publicly available. The UDCAM-S model can be used with PLAXIS (Bentley Systems, 2022). The shortcomings are that the strain compatibility procedure is used, but was intended for cohesive material and gravity foundations in which the elements within the failure surface need to have the same shear strain. Such a dominant failure surface does not exist for instance at monopile foundations. Here, a procedure based on excess pore pressure should be used. Within the UDCAM-S procedure the mean shear stress is neglected. Furthermore, the assumed stress path, which is equal for all elements, bases on a global load ratio assumption and is not derived from a numerical model. No excess pore pressure is separately considered since the total soil response in the form of shear strain plots does already indirectly consider this. Furthermore, no dissipation is considered which can lead to very conservative and even uneconomical designs for cohesionless soils. However, for application to cohesive soil this is not necessary. Furthermore, only one degradation set is evaluated; for gravity based foundations this seems reasonable due to the limited influenced depth, but for monopiles there is a non-homogenous degradation field which cannot be captured with one simple stress - strain curve. Hence, the UDCAM-S approach seems to lack applicability for monopile foundations. Klinkvort et al. (2020) use the approach in combination with an axisymmetric model (with Fourier transformation) called super-fast monopile design (SUMO); even though the strain compatibility procedure is not recommended for monopiles and the soil degradation shows a large spatial variation (Skau et al., 2017; Andersen et al., 2013). For the investigated case of cohesionless soils the UDCAM (UDCAM-S and SUMO) model appears not well suited due to the aforementioned reasons.

PDCAM

The UDCAM was mainly developed for the soil response of material with negligible drainage. The soil response of sandy material is more complex due to dilatancy and drainage effects. Therefore, the partially drained cyclic pore pressure accumulation model (PDCAM) was developed (Andersen et al., 1994; Jostad et al., 1997). PDCAM uses a pore pressure accumulation procedure in which the pore pressure can dissipate between the cycle packages (cf. Appendix C). The model is not intended to calculate the effective stresses for different cycles, but rather to represent the response of excess pore pressure and volumetric strain during the cyclic load history (Jostad et al., 2015a). The model works only with inter- and extrapolation of the stress - strain relation from the contour plots without an elasto-plastic framework. Based on the dissipated excess pore pressure, PDCAM also predicts the volumetric strain after the number of cycles. It can hence estimate the structures' deformation after the storm – similar to the stiffness degradation method (SDM) by Achmus et al. (2009). The PDCAM model works in a similar way as the UDCAM model, but dissipation is allowed under mean loads (Jostad et al., 2015a; Andersen et al., 1992, 1994). It uses an effective stress model for the mean load component. The input parameters for the PDCAM model are the contour plots from undrained cyclic laboratory tests, drained triaxial tests as well as oedometer and permeability test results. The main disadvantage is that it is not publicly available and that the implementation is not well documented. Hence, no critical evaluation can take place.

A first implementation of the elasto-plastic framework presented in Jostad et al. (1997) was based on a constitutive model from Kavli et al. (1989), which was a two surface soil model with end closing cap, stress-dependent stiffness and mobilized friction angle related to plastic shear strain. The calculation procedure is explained in Jostad et al. (1997) for axisymmetric conditions (a slightly different implementation is presented in Jostad et al. (2015b)). The description of the procedure over the years is not entirely stringent and at some points lacks details. The global mean load and the global cyclic load are coupled as done in the UDCAM model. In the case of storm load, individual load bins start with a restart command from the individual models for which the coupling is done via a database. For stress-redistributions an iterative calculation is performed. The calculation of volumetric strains during consolidation is done similar to the concept explained in Section 4.3.2.

4.2.3 Other explicit approaches

Seed and Rahman (1978) and Rahman et al. (1977) present a procedure which combines the generation and dissipation of excess pore pressure due to wave-induced loading of the ocean floor in a very simple way (also Dingle et al. (2017)). The procedure estimates the shear loads and, with the equation according to Seed et al. (1975b), the excess pore pressure, which is subsequently dissipated in a flow net calculation. With this approach a complete design storm with different packages can be evaluated (see also O'Riordan and Seaman (1993)). A similar approach, based on the method of Rahman et al. (1977), was used for the analysis of axial pile response by Lee and Poulos (1988).

The soil cluster degradation method was first presented by Wiesener et al. (2016) followed by Zorzi et al. (2019) and Zorzi et al. (2020). It is an explicit method specifically aimed at the calculation of pore water pressure accumulation for offshore monopiles, for which the results of cyclic constant volume simple shear tests are used as input values. PLAXIS is not capable of manipulating every integration point without writing a user defined material model. Hence, the soil is divided into clusters with homogeneous soil properties. The discretization is done by taking into account the local soil behaviour. Within this finite element model, the stresses and strains are calculated with quasi-static loads. The strain increase (plastic and elastic) is modelled by reducing the shear modulus in each step. The general procedure resembles the SDM method for the serviceability limit state design proof. An additional drainage step is not performed (Zorzi et al., 2019).

All approaches found in the literature are based on quite similar theoretical principles. They differ by different estimation steps or empirical regressions. Zorzi et al. (2019) used empirical regression of the cyclic laboratory results in the form of contour plots, whereas Rahman et al. (1977) (Meijers and Luger, 2012; Meijers et al., 2014) used regressions based on the approach according to Seed and Booker (1976). Dingle et al. (2017) used the excess pore pressure power law regression equation according to Mao et al. (1999) (see Equation 3.12). Others (Martin et al., 1974; Byrne, 1991) use concepts based on cyclic displacement-controlled tests.

When comparing all presented methods, some concepts are not directly applicable in practical projects due to the presented reasons. Hence, a practical method termed Excess Pore Pressure Estimation method (EPPE) was introduced by Achmus et al. (2018) and is continuously developed (Saathoff and Achmus, 2020). The procedure is already successfully used in practice (detailed explanation given in Chapter 6).

4.3 Modelling partially drained conditions

In order to consider partial drainage within the numerical explicit method from a general point of view, further understanding of these conditions is required. Undrained soil behaviour differs from (partially) drained behaviour in two main aspects. Firstly, the accumulated excess pore pressure is able to dissipate and secondly, volumetric strains ε_v occur. During dissipation, there is an initial increase within the specimen due to compression of the soil skeleton and therefore an increase in excess pore pressure due to loading and compaction. The effective stress decreases and so does the stiffness. The excess pore pressure builds up to a peak value and a slow change in soil response occurs for the investigated case according to Sakai et al. (2003) (Figure 4.3). First the generation and then the dissipation predominates (cf. Hyodo et al. (1988)). A starting dissipation leads to a reduction in void ratio and a change in fabric. A greater liquefaction resistance develops. The excess pore pressure decreases to a state of equilibrium between generation and dissipation. This behaviour can be seen in many partially drained test set-ups (Sakai et al., 2003). Compared to the undrained test, the accumulation tendency is softer and, depending on the drainage conditions, no peak value may develop (Mitchell and Dubin, 1986). The trend can also be seen in the 1g small-scale test results published by Kluge (2007) (see Section 6.2). It should be pointed out that the development of a peak value and subsequent decrease of excess pore pressure seems to be not the case in every test, but also depends on the load conditions and relative density. Nevertheless, a softer accumulation trend is expected. Partially drained parameter studies on cohesionless soils are quite rare in the literature. Jostad et al. (2021) published data of partially drained triaxial tests. They controlled the degree of drainage with a long thin tube between the filter and the volume measure device (Suzuki et al., 2020). The authors conclude that there is still a need for research.

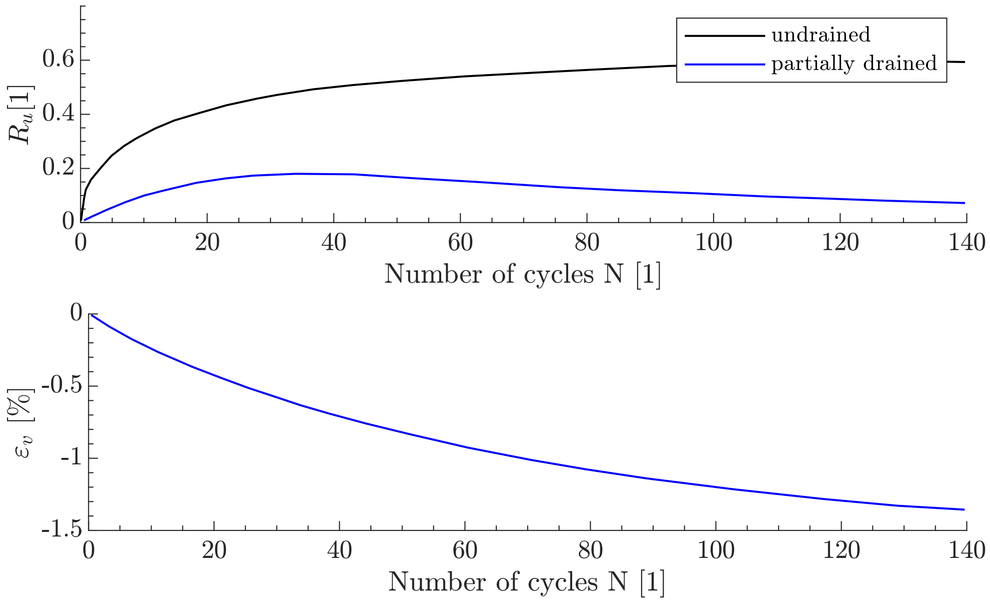

Figure 4.3: Comparison of undrained and partially drained triaxial test results with excess pore pressure ratio (upper) and volumetric strain (lower) over number of cycles (Sakai et al., 2003).

Whether partially drained or undrained conditions prevail can be checked with a criterion according to de Groot et al. (2006b). This is done by estimating characteristic drainage time, which is a ratio between structural dimensions and permeability (Equation 4.3).

$$T_{char,dr} = \frac{A\, d_{drain}^2}{c_v} \qquad u = u_0 \;\; exp(t\, T_{ch,dr}) \tag{4.3}$$

Herein, A is a factor mostly chosen to one and d_{dr} is a representative drainage length. The characteristic drainage time can be used to generate a very rough decay curve. If the value is small, fast dissipation occurs whereas for a large value the accumulation would prevail. Estimating the representative drainage length is very difficult and hardly manageable for monopiles. The relation between excess pore pressure generation and dissipation does also affect the resulting failure mode (cf. de Groot et al. (2006b)). At a relative density of e.g. 0.5 and $T_{char,dr}$ less than 20, no liquefaction is relevant. Jostad et al. (2021) have also investigated the characteristic drainage length without giving a specific criterion. Therefore, in most cases a numerical flow net calculation in the form of finite elements or finite volumes is necessary in order to estimate the drainage length and thus the soil response. This procedure is also required by the approval bodies for offshore designs.

4.3.1 Different dissipation formulation

Instead of using a characteristic drainage length, a simplified partially drained dissipation analysis can be used. Regarding the mathematical description, there are sophisticated ways which are based on 1D consolidation and finite difference (FD) calculation (Paul et al. (2014) based on Davis and Raymond (1965) or Ni et al. (2012)). Ni (2012) created a modified cam clay model and was able to predict the partially drained response of cyclic laboratory element tests. Using this modified cam clay model, a good agreement between calculated and measured responses is shown by Wride et al. (2019) for cohesive material (Ni et al., 2012). This implicit modelling with a hydro-mechanically coupled model may not be used for a simplified explicit dissipation analysis. However, the soil model can accurately predict the soil response by considering several soil mechanical aspects.

An analytical procedure is introduced by Hyodo et al. (1992) (Hyodo et al., 1988, 1994). They assume that the increase Δu_p under partially drained conditions before drainage is equal to the increase under undrained conditions Δu_u. This is a model assumption since Δu_u is dependent on load history and dissipation behaviour. In order to be able to apply a simplified analytical superposition procedure for the creation of a partially drained state, the characteristic dissipation behaviour is required (such as according to Hyodo et al. (1992)). Andersen et al. (1994) describe a simplified dissipation analysis based on solution of the differential equation of radial dissipation done by Madshus and Harvik (1988). The radial dissipation can roughly be estimated with the characteristic drainage time and the consolidation coefficient under a gravity foundation for which the maximum excess pore pressure is assumed to be uniformly distributed under the foundation base. At the side of the foundation, free drainage is assumed. This approach bases on nomograms, which are the solution of the partial differential equation. However, for a monopile foundation the model assumptions are not valid and the governing equation considering radial consolidation needs to be solved.

The fastest way to have a simplified dissipation analysis is to solve the differential equation for radial or horizontal flow with 1D finite differences with an implicit backward Euler method and Neuman boundary conditions at the first nodes and Dirichlet boundary conditions of 0 for the drainage length. The differential equation which needs to be solved for radial symmetric flow is:

$$\frac{\delta u}{\delta t} = c_v \left(\frac{\delta^2 u}{\delta r^2} + \frac{1}{r} \frac{\delta u}{\delta r} \right) \tag{4.4}$$

Herein, c_v is the coefficient of consolidation (Equation 4.5).

$$c_v = \frac{k_f}{m_v \gamma_w} \tag{4.5}$$

For one-dimensional horizontal flow the partial differential equation is as follows:

$$\frac{\delta u}{\delta t} = c_v \frac{\delta^2 u}{\delta z^2} \tag{4.6}$$

These approaches can be used in order to estimate the dissipation behaviour for a specific permeability over time.

4.3.2 Consideration of volumetric strain

During consolidation, volumetric strains develop in case of partially drained conditions. Martin et al. (1974) state that the equivalent incremental volumetric strain ε_v from drained conditions can be calculated by using the current accumulated excess pore pressure Δu under undrained conditions and the additional excess pore pressure of the current cycle Δu_p times the coefficient of compressibility m_v for the case of complete dissipation (Equation 4.7). Herein, the term $\varepsilon_{v,acc}$ represents the already accumulated volumetric strain. Finn and Bhatia (1981) were able to back-calculate undrained tests based on constant normal load tests very well with this idea.

$$\varepsilon_v = m_v \left(\Delta u + \Delta u_p\right) + \varepsilon_{v,acc} \tag{4.7}$$

$m_v = 1/E_r$ is the drained tangent modulus of a one dimensional unloading curve (Finn et al., 1976, 1977). The concept is explained in Figure 4.4 based on a conventional oedometer test. It shows the similarities between a drained conventional compression test and the path of an undrained oedometric test with drainage between adjacent load steps (Yasuhara and Andersen, 1991; Jostad et al., 1997; Andersen and Høeg, 1992; Andersen et al., 1978). The test is performed under drained conditions and during unloading both the void ratio and the stress changes. During the undrained test, the void ratio must remain constant due to waters' incompressibility conditions. The soil reacts differently to initial loading, unloading and reloading. Figure 4.4 (b) shows the initial state A and the build-up of excess pore pressure to point B (undrained). During dissipation, volumetric strains build up and the void ratio changes. The accumulated excess pore pressure is the distance from A to B and the dissipated excess pore pressure from B to C. The difference to a drained test is the unchanged void ratio during unloading in the undrained condition (Figure 4.4 (a)). The calculation of volumetric strain from the dissipated excess pore pressure is done by using the coefficient of compressibility (inclination of the un- and reloading branch in oedometer test) (Equation 4.7). By using a constant coefficient of compressibility, a stress-dependency is neglected. This can be done after each cycle (several drainage cycles with decreasing void ratio) or after the storm (drainage once).

To increase accuracy a stress-dependent regression can be applied to the entire oedometer test result (Andersen, 2015; Andersen and Schjetne, 2013). Hence, the loading, unloading and reloading path is approximated.

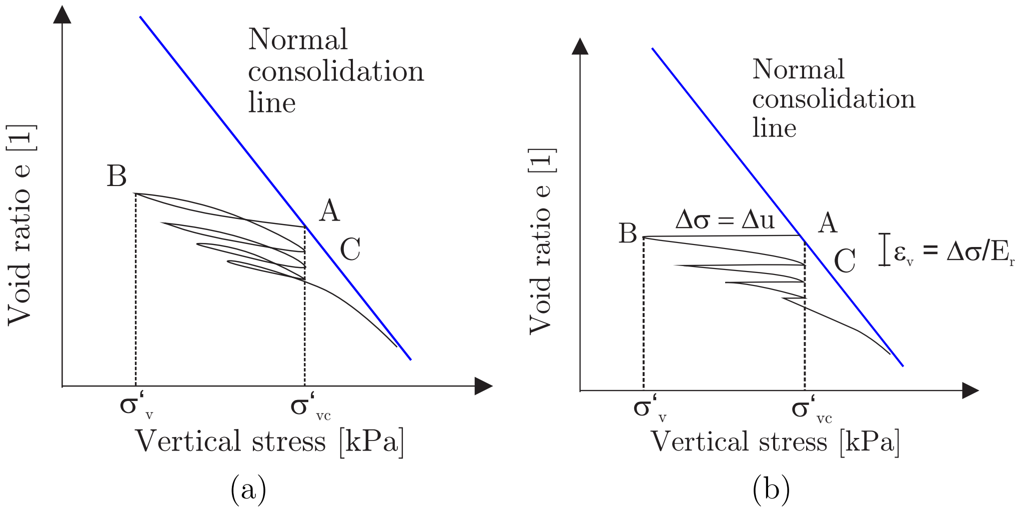

Figure 4.4: Schematic comparison of drained (a) and undrained (b) results in e - σ'_v space.

4.4 Conclusion

The critical evaluation of the current state of the art shows that although concepts for describing the load-bearing behaviour of cyclically loaded foundations exist, they are either very limited in their suitability for use in design practice or have not been satisfactorily validated, at least for generic application. Currently, the critical state approaches, and in particular the SANISAND model, are of great interest to constitutive modelling. With faster computers and better algorithms, the use of more sophisticated models will become more important. Implicit computation with an appropriate soil model can improve understanding of soil-structure interaction under complex loading conditions such as cyclic loading. However, calibration is currently very complex and non-trivial, and not all ground properties can be calibrated in one calibration set. Nevertheless, there is still much progress to be made in the area of constitutive modelling. Yet, the accumulation of errors as well as the very tedious calibration process make their use in practical projects almost impossible. The HCA model is one of the most advanced models that includes many different effects. The different effects are associated with different functions. Nevertheless, it is more suited for scientific purposes and not for practical projects.

Direct use of the results of cyclic tests is considered a promising method in terms of practical applicability. It remains to be clarified which cyclic tests with which boundary conditions should be usefully employed and how these test results can be incorporated into the prediction of system behaviour. Approaches have been made by UDCAM-S (developed to super fast monopile design (SUMO) according to Klinkvort et al. (2020)), however there are several model assumptions. Some steps within models such as PDCAM are not trivial to understand and their influence on the total accuracy is not documented. Therefore, the main objective of this work is to develop a generic methodology as simple and transparent as possible for predicting the bearing behaviour of a cyclically loaded foundation based on cyclic element tests, to validate it with experiments, and to make it possible for engineers to implement the procedure.

5 Laboratory tests on reference sand

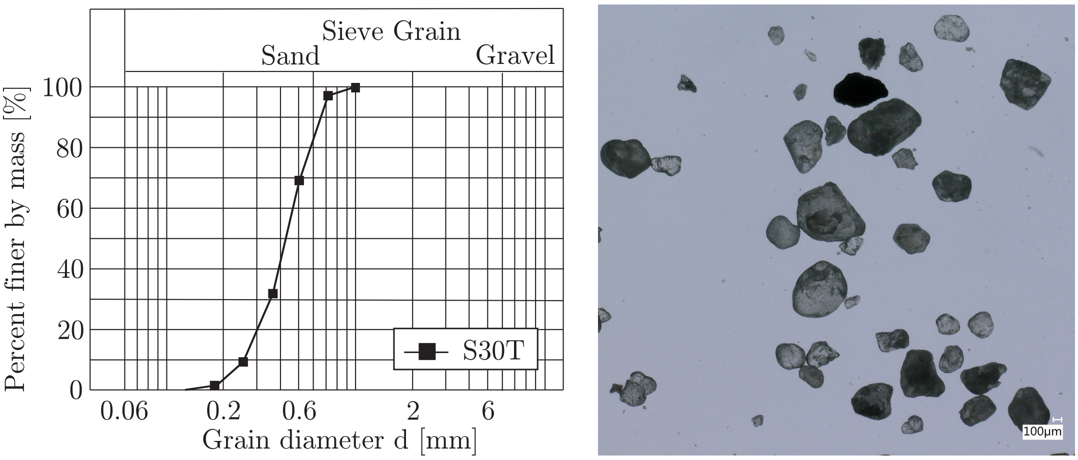

(a)

(b)

Figure 5.1: Grain size distribution (a) and microscopic image (b) of reference soil.

Various laboratory tests were carried out for this thesis on a non-cohesive soil termed S30T in order to use the data for the numerical model. The grain size distribution of the reference soil is shown in Figure 5.1 (a). Most of the tests were performed at a relative density D_r of 0.85, which was chosen as representative for North Sea conditions. The soil is a quartz sand with a subangular shape of the particles (Figure 5.1 (b)).

5.1 Monotonic behaviour

Several soil classification tests as well as monotonic tests were performed for different relative densities to be able to describe the general soil response. Thereby, the results for the reference relative density shall be presented. The tests include shear box tests, simple shear tests, oedometric tests, isotropic triaxial tests, triaxial compression tests under drained and undrained conditions, resonant column tests, ring shear tests, and repose angle tests. Exemplary results are presented below and can be found in Appendix A.

5.1.1 Classification

The grain size distribution was derived and the coefficient of uniformity was estimated to 1.8 and the coefficient of curvature to 1.02. The soil is categorized to medium grained poorly graded sand. The soil properties are summarized in Table 5.1. Due to the low uniformity, the soil can be used for all different kinds of preparation investigation without the tendency of segregation e.g. at pluviation. The angle of repose was estimated to $\varphi_c = 30.9°$. The particle density was derived to $\rho_s = 2.65\,\mathrm{g/cm^3}$. The minimum and maximum void ratio have been determined to 0.493 and 0.789, respectively.

Table 5.1: Soil properties of reference soil.

Name [-]	e_{max} [1]	e_{min} [1]	d_{10} [mm]	d_{30} [mm]	d_{60} [mm]	ρ_s [g/cm^3]
S30T	0.789	0.493	0.256	0.347	0.461	2.65

5.1.2 Triaxial test

Several drained and undrained monotonic triaxial tests for different relative densities have been performed in accordance with DIN EN ISO 17892-9:2018-07 (ASTM D5311-13 and ASTM D4767-11). The relative density was varied between a medium dense to dense state with confining pressures between 50 kPa and 500 kPa. The specimens were dry tamped before wetting and freezing the samples. The frozen samples were then installed into the triaxial cell with a support pressure of 30 kPa. The specimens were consolidated under isotropic conditions. For monotonic undrained tests, the results of the deviatoric stress over the axial strain are shown in Figure 5.2. The failure slope can be determined to 1.22, which results in an angle of internal friction of $\varphi = 30.5\,°$. The excess pore pressure increases for an increased axial strain up a peak value and then decreases due to dilative soil behaviour.

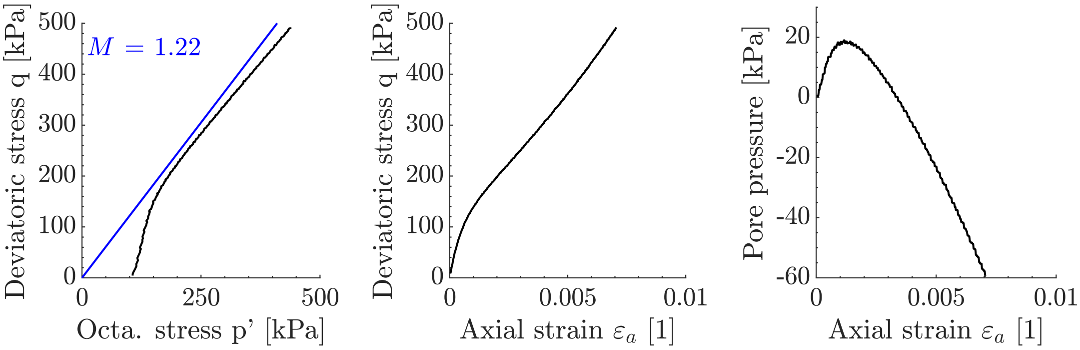

(a) (b) (c)

Figure 5.2: Results for undrained triaxial test (CIU) with deviatoric stress over octahedral stress (a), deviatoric stress over axial strain (b) and pore pressure over axial strain (c) for $D_r = 0.85$.

5.1.3 Permeability test

For partially drained conditions, permeability is an important aspect. The value can be estimated from the grain size distribution according to Beyer (1966):

$$k_f = c(C_U)\ d_{10}^2 \quad c(C_U) = 0.011 \quad for \quad C_U = 1.8 \tag{5.1}$$

A permeability of $k_f = 7.2 \times 10^{-4}$ m/s can be obtained for $d_{10} = 0.256$ mm. However, additional tests were carried out both in a permeability test stand as well as in a triaxial cell. Since permeability depends on the temperature-dependent pore fluid viscosity, the results have been adjusted to the given temperature. The permeability is shown in Figure 5.3 over different void ratios in the representation according to Taylor (1948) (often used in Kozeny-Carman). A larger permeability arises for larger void ratios. For the reference relative density a permeability, which is about half of the analytical obtained one, is derived to 3.7×10^{-4} m/s. Nevertheless, the generalized analytical result can be found for more loose soil.

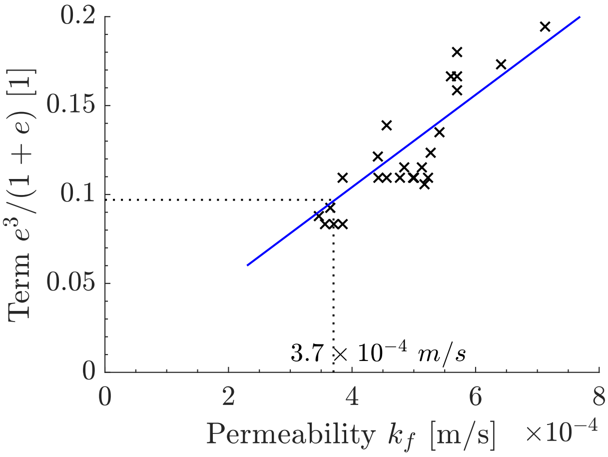

Figure 5.3: Normalized void ratio over permeability.

5.1.4 Direct simple shear test

The specimens in the cyclic direct simple shear device have a diameter of 71.4 mm and a height of 20 mm. The specimens were prepared dry tamped. The cyclic direct simple shear device (machine version EMDCSS) is manufactured by GDS instruments and equipped with a special high-resolution local linear variable displacement transducer (LVDT). Quasi-undrained tests can be accomplished by using constant-volume conditions. Radial deformation is prevented by lateral confinement and the change in height during shear by active height control (ASTM D8296-19). The constant volume conditions are equal to undrained conditions according to ASTM D8296-19 (see also Finn and Vaid (1977)). Special care must be taken into account regarding interface slippage between soil and metal cap of the DSS device. Here, a sintered filter stone with a similar maximum grain diameter compared to the reference soil was used. The test procedure consists of preparation and consolidation of the soil sample and a subsequent monotonic or cyclic test stage. Mainly dry sand was tested under constant normal load (CNL) or constant-volume (CV) conditions. The cyclic tests were performed displacement-controlled or load-controlled. Figure 5.4 shows results for shear stress over vertical stress (a) and shear

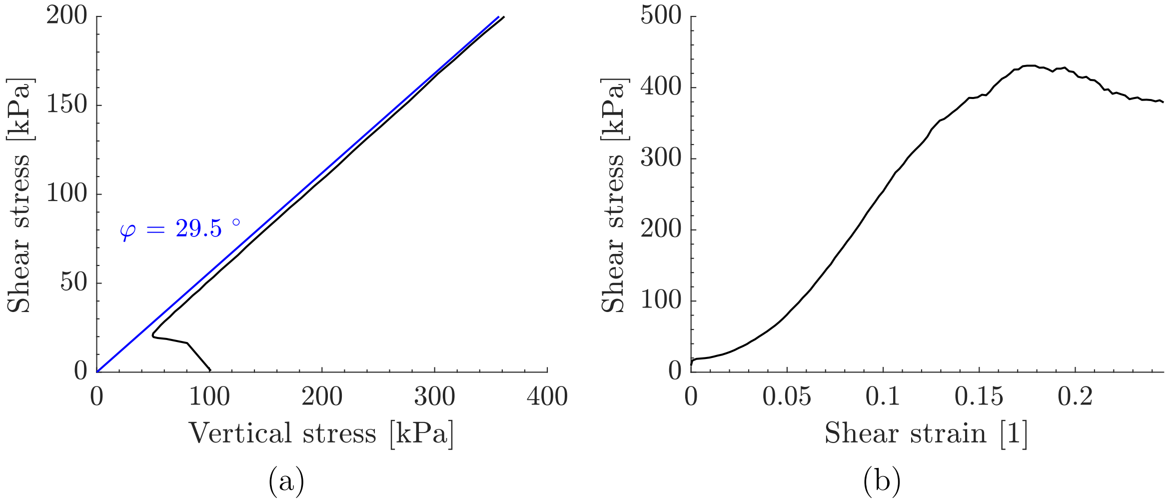

Figure 5.4: Monotonic constant-volume tests from direct simple shear device for reference relative density.

stress over shear strain (b). The phase transformation line can be found at the maximum excess pore pressure development which is equivalent for constant-volume conditions with the lower vertical stress. It can be estimated to be at a shear stress of 20 kPa with a vertical stress of 50 kPa. At this point the maximum excess pore pressure occurs and subsequently the soil response changes from contractive to dilative.

5.2 Cyclic behaviour

5.2.1 Laboratory programme

Several hundred cyclic load- and displacement-controlled tests have been performed in the direct simple shear device as well as in the triaxial device in order to calibrate the empirical approaches for the estimation of excess pore pressure as well as to derive contour plots and investigate the soil response. In the following, mainly the undrained and constant-volume test results shall be presented. The main objective is to create a database for all possible calibrations and considerations in the later numerical steps. The complete data set can be downloaded from the website of the Institute for Geotechnical Engineering Hannover (www.igth.uni-hannover.de).

Cyclic direct simple shear test

The cyclic direct simple shear tests were carried out under constant-volume conditions. The vertical load was applied in a first step and consolidated for 10 minutes. The cyclic phase consists of at least 1000 cycles. In the constant-volume tests, the mean shear stress was always applied under drained conditions, which means that only axial strain but no decrease in vertical stress occurred. This represents the behaviour of a real storm load on an offshore structure in a sandy material. The storm builds up slowly and hence the mean load creates a drained soil response. All cyclic direct simple shear tests have been performed with a frequency of 0.1 Hz. However, in preliminary studies almost no influence of the frequency up to 2 Hz has been observed (cf. Youd (1972)). When using preconditioning, larger cyclic shear strength are expected. However, no preconditioning in the form of pre-shearing was done in order to have one data set without any influencing parameter.

Figure 5.5 shows the anisotropic consolidation condition in principal stresses as well as change of the Mohr Coulomb circle with the application of the mean shear stress and the undrained shear stress amplitude. The initial stress state in the DSS test for a consolidation stress of for instance 100 kPa, by assuming k_0 to 0.5: $\tau_0 = 0\,\mathrm{kPa}$, $\sigma'_I = \sigma'_v = 100\,\mathrm{kPa}$, $\sigma'_{III} = \sigma'_h = 0.5 \times 100\,\mathrm{kPa}$. After the anisotropic consolidation, an additional shear stress is applied whereby the vertical stress remains constant (CNL). This could for instance be a mean shear stress of 20 kPa resulting to: $\tau_{mean} = 20\,\mathrm{kPa}$, $\sigma'_v = 100\,\mathrm{kPa}$, $\sigma'_h = 0.5 \times 100\,\mathrm{kPa}$. This changes the principal stress to $\sigma'_I = 107\,\mathrm{kPa}$ and $\sigma'_{III} = 43\,\mathrm{kPa}$ in the case of an unchanged coefficient of earth pressure at rest. This theoretical consideration will be of importance again later (Chapter 6).

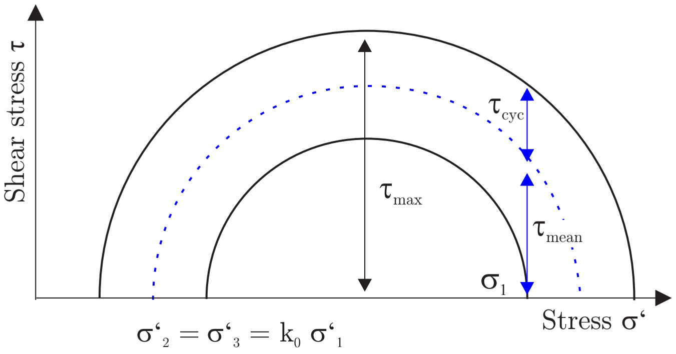

Figure 5.5: Stress states in Mohr Coulomb circle for cyclic direct simple shear test (based on Seed and Peacock (1971)).

Cyclic triaxial test

In order to fully characterise the soil behaviour, undrained (and drained) cyclic compression triaxial tests are performed in addition to the cyclic DSS tests. The performed triaxial test specimen were first tamped and then frozen, and later unfrozen within the cell. Due to the increased time required for preparation, consolidation and saturation, a smaller number of tests was conducted. Influences in comparison to the DSS tests arise from the isotropic consolidation but certainly also from the different sample preparation technique.

Only one isotropic consolidation stress was evaluated for the triaxial case and chosen as 100 kPa according to ASTM D5311-13. The loading frequency was set to 0.1 Hz to facilitate peak and sinusoidal regulation. The other parameters are similar to the monotonic tests. Only symmetric one- and two-way loading was investigated within the triaxial device. The stress path was chosen in a way, that a octahedral stress p’ of 100 kPa was reached after mean deviatoric stress was applied in a drained manner. Figure 5.6 shows the development of the principal stresses for a cyclic CIU test. At first, all stresses

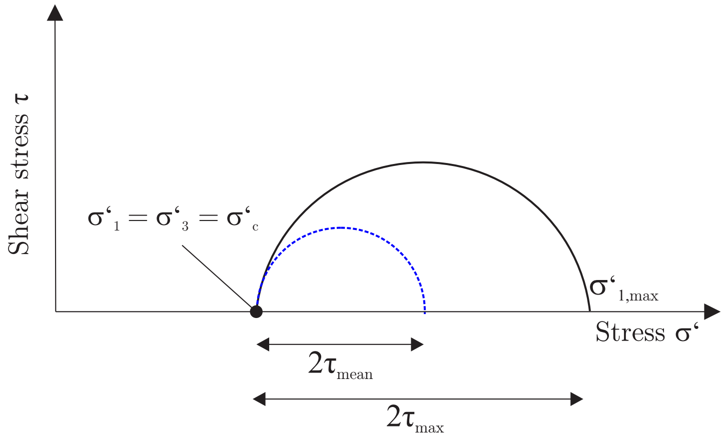

Figure 5.6: Stress states for cyclic triaxial CIU test.

are equal for isotropic consolidation. Subsequently the axial stress is increased and an anisotropic stress state is created.

5.2.2 Load-controlled cyclic constant-volume test results

General response

In the following, the results from load-controlled undrained triaxial and constant-volume DSS tests shall briefly be presented. Most of the characteristic cyclic soil response was already explained in Section 3.2.2.

Figure 5.7 (a) shows the decrease of vertical stress interpreted as an increase in excess pore pressure for different boundary conditions. The constant volume phase starts at a normal stress of 100 kPa and a mean shear stress of 0 kPa. The vertical stress decreases due to an increase in excess pore pressure. The shear stress cycles within the predefined load conditions.The change of soil behaviour at the phase-transformation line is depicted in the $\tau - \sigma'_v$ plane in Figure 5.7 (a). At the crossing point of the phase transformation line (PTL) the response changes. A butterfly loop starts to occur. There is a continuous transition between dilatancy and contractance (for this dense sand state). It is accompanied with the fast generation of large shear strains. The increase of normalized excess pore pressure is depicted in Figure 5.7 (b) with a number of cycles to liquefaction of 421. Such a state of zero effective stress is not possible for all load conditions. For larger MSR values (with a minimum shear stress significantly larger than zero), no initial liquefaction is possible and a different failure mechanism occurs (Studer et al., 2007). In order to investigate the effect of cyclic loading on the final peak friction angle, several cyclic DSS tests with a post-cyclic CNL shearing phase with the initial consolidation vertical stress were performed. The peak resistance was evaluated. The peak resistance was, independent of the prior liquefaction, not altered.

Figure 5.8 (a) shows the increase in shear strain and the stress path in $\gamma - \tau$ plane with a mean shear strain of zero. For non-symmetrical load scenarios with stress reversal this value would increase over the numbers of applied cycles.The dilative response at

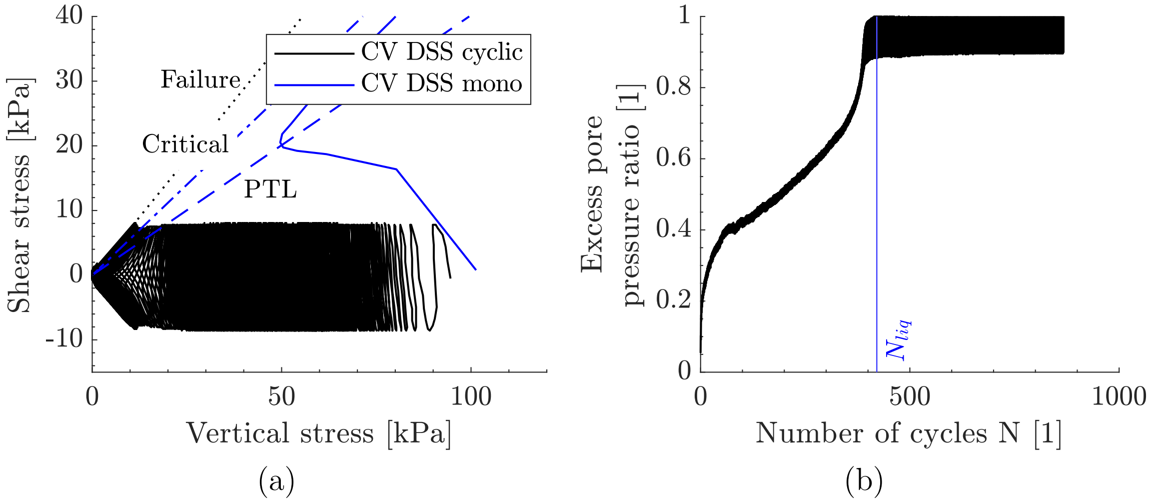

Figure 5.7: Vertical stress against shear stress (a) and excess pore pressure over number of applied cycles for a load-controlled constant-volume cyclic direct simple shear test for a relative density of 85% and a CSR of 0.08 with N_{liq} indicated (b).

large strains can be seen in the shear stress - shear strain plot (Figure 5.8 (a)), with the characteristic S-shape. Figure 5.8 (b) shows the increase in shear strain over the number of cycles. A large increase in shear strain can be seen at the location of small vertical effective stress.

The general soil response is very similar for a sample in a triaxial device. Figure 5.9 (a) shows results for symmetric two-way loading for a consolidation stress of 100 kPa. If sufficient excess pore pressure is accumulated, the vertical stress is reduced up to the failure line. In case of a large MSR value with a small CSR value, full liquefaction cannot be reached. Due to the shear stress boundary conditions, a state of zero stress may not be possible, however, large strains will accumulate after reaching the failure line. For small CSR values, there is only a small excess pore pressure accumulation and hence the failure line is only reached after many cycles. If the CSR is increased, the excess pore pressure accumulates for a smaller number of cycles up to the point of failure. However, for an even larger CSR the failure point is reached even faster, since for a large CSR and a large MSR, a small u_{max} arises. Hence, a medium CSR will accumulate the most excess pore pressure compared to a small and large CSR. The shear strain on the other hand will steadily increase with number of cycles and the CSR. Figure 5.9 (b) shows an increase up to approximately 30 kPa. Most of the damage occurs after only a few cycles and the trend shows only a small additional accumulation with increasing number of cycles.

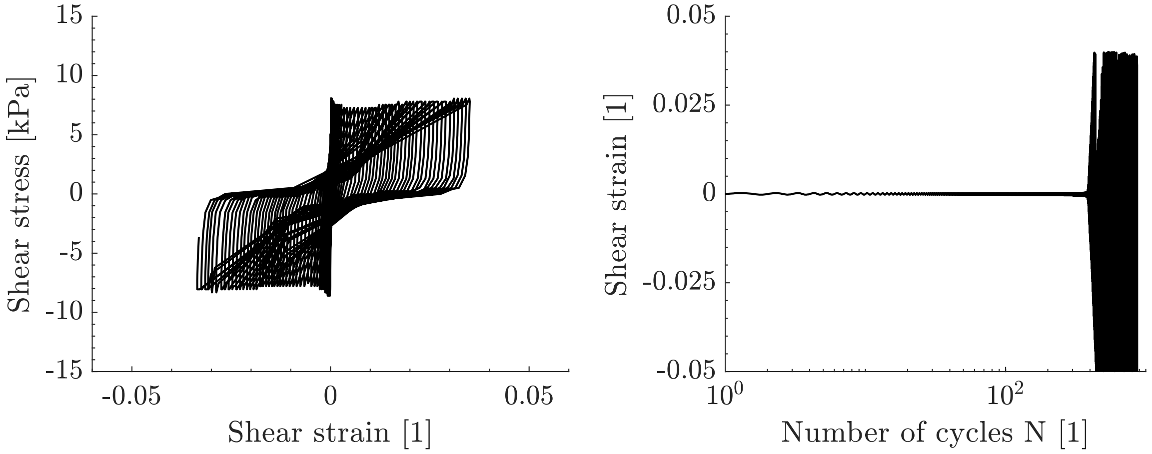

Figure 5.8: Shear stress over shear strain (a) and shear strain over number of cycles (b) for reference density and CSR of 0.08 with same conditions as Figure 5.7.

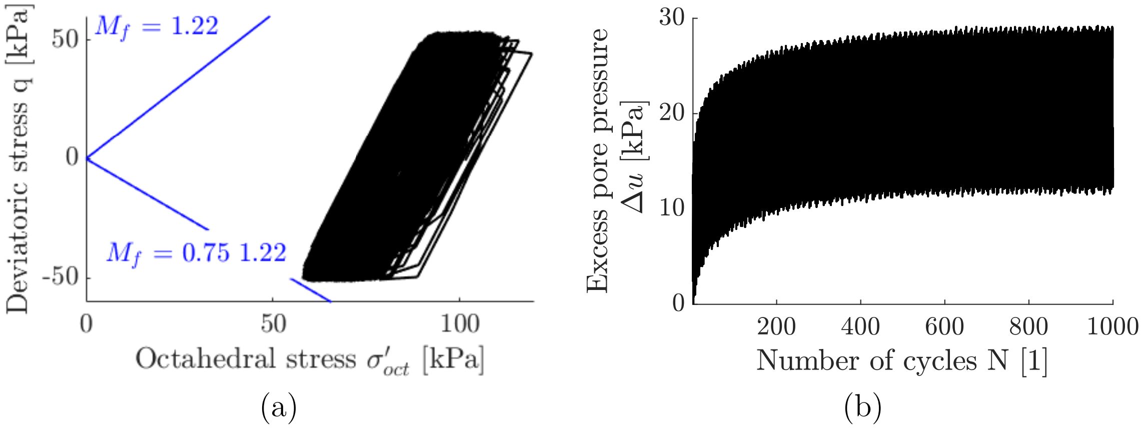

(a) (b)

Figure 5.9: Deviatoric stress over octahedral stress (a) and excess pore pressure over number of cycles (b) for reference density and CSR = 0.25 from a cyclic triaxial test.

Semi-empirical stress-based liquefaction approach

There are several different prediction models (cf. Chapter 3), but the approach by Seed et al. (1975b) is most commonly used because of its simplicity (Equation 3.10 in Section 3.5.1). In order to derive the complete excess pore pressure build-up trend, the liquefaction curve $CSR - N_{liq}$ is required as input. Herein, liquefaction can be defined differently. Figure 5.10 shows the influence of the different definitions with stress and strain criteria on the resulting failure curve. Figure 5.10 (a) compares different shear strain criteria and Figure 5.10 (b) different criteria by means of excess pore pressure. For an increasing double shear strain amplitude, the number of cycles to liquefaction increases. However, the difference between 3% and 5% is not very pronounced – especially considering the experimental standard deviation. For a shear strain of 10% higher number of cycles to liquefaction are obtained. The black dotted line represents the chosen input for the model and is similar in all figures for reasons of comparability. A shear strain value of 5% fits well.

Figure 5.10 (b) shows the difference between the first occurrence of an excess pore pressure ratio of 100% and of a permanent excess pore pressure ratio of 95%. The cyclic tests with a large CSR do not yield permanent excess pore pressures larger than 95%. An excess pore pressure ratio of 1.0 is presented with blue crosses. The general influence of this differentiation is marginal. Furthermore, the results based on an excess pore pressure criterion agree quite well with the most used deformation criterion of 5%.

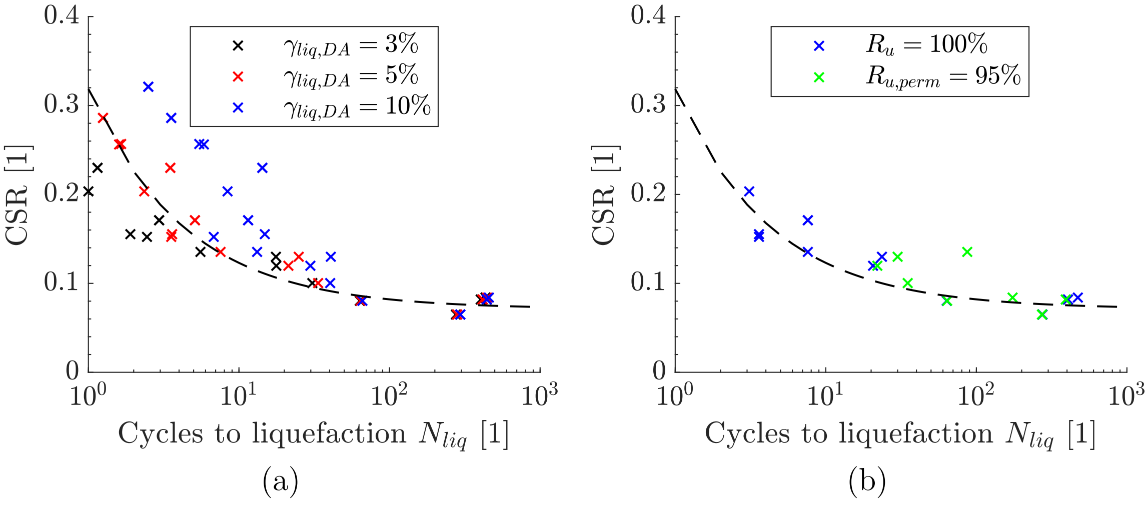

Figure 5.10: CSR over number of cycles to liquefaction with deformation criteria (a) and excess pore pressure ratio criteria (b).

Figure 5.11 (a) shows the results of N_{liq} for different MSR values (regression curves) for the reference sand based on results from the direct simple shear device. The number of bearable cycles is reduced for an increasing mean shear stress. The regression was derived to $CSR = 0.25N_{liq}^{-0.68} + 0.07$ for $D_r = 0.85$ and MSR = 0. This line is depicted in Figure 5.10, Figure 5.11 and Figure 5.12 for a better comparability. Figure 5.11 (b) shows the trend of excess pore pressure over the normalized number of cycles. The grey curves are related to CSR values smaller than the asymptotic value of 0.07 and hence no number of cycles to liquefaction can be associated. The value of β from Equation 3.10 was fitted to 0.7. However, the mathematical performance of the model is improvable and predicts failure for all cyclic tests even if some do not show the tendency to fail.

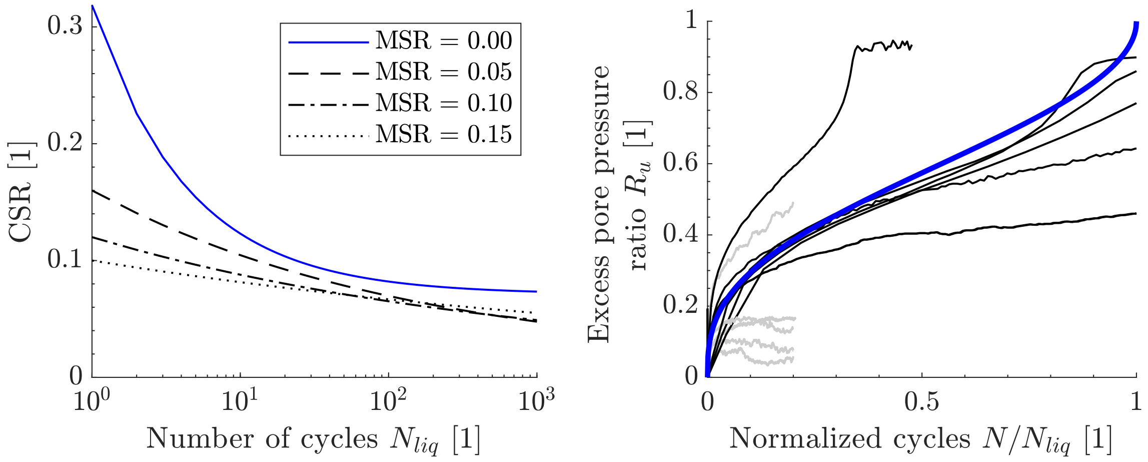

(a)

(b)

Figure 5.11: CSR over number of cycles to liquefaction with regression for different MSR values (a) and comparison of empirical equation with measured results normalized by equation for MSR = 0 (b).

Influencing parameters

The soil behaviour is mainly influenced by the relative density. The impact can be seen in Figure 5.12 (a). The soil fails after a smaller number of cycles in case of a more loose soil.

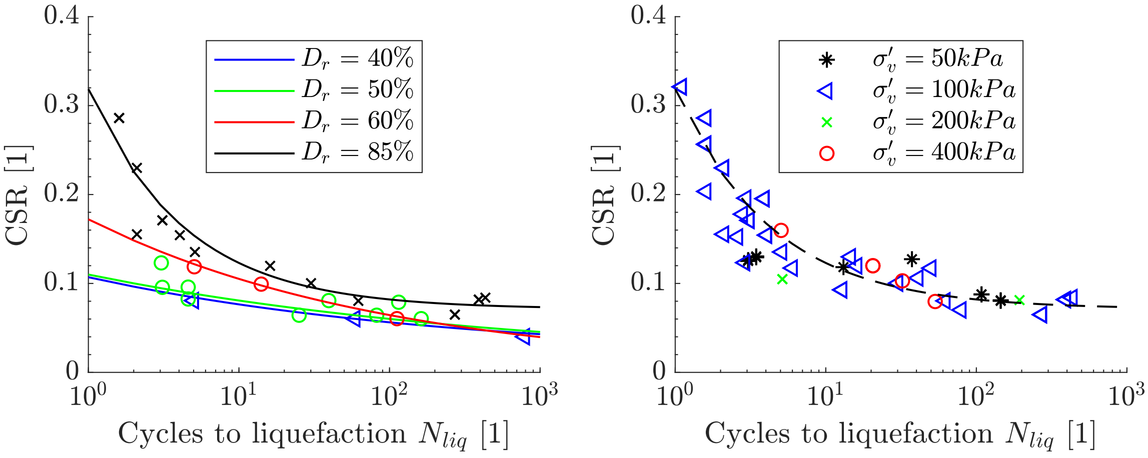

(a)

(b)

Figure 5.12: $CSR - N_{liq}$ curve for a relative density of 40%, 50%, 60% and 85% (a) and for different vertical stresses with a relative density of 85% (b).

Figure 5.12 (b) shows the influence of vertical consolidation stress. The effect is not very pronounced since the cyclic stress is normalized to the vertical stress. Additional effects due to a different dilative soil response for different stress levels lead to the depicted differences. A stress influence is neglected in the course of this work and mainly results for a vertical consolidation stress of 100 kPa are used.

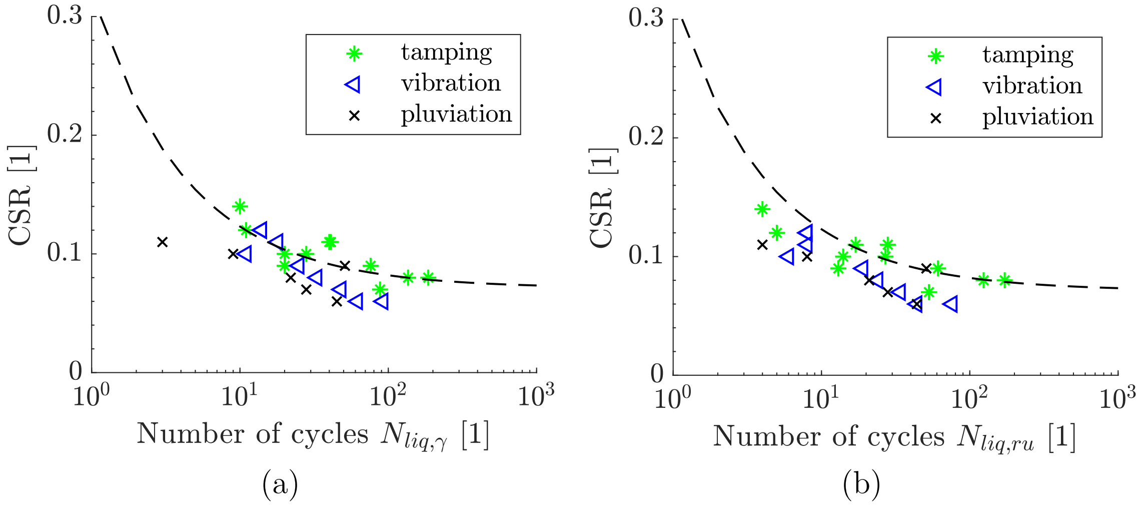

Figure 5.13: Influence of sample preparation with CSR over number of cycles to liquefaction with shear strain criterion (a) and excess pore pressure ratio criterion (b).

The sample preparation can have a significant influence and hence can also influence the results from the numerical model and the design later on. Figure 5.13 shows the influence of different sample preparation techniques on the liquefaction resistance. Figure 5.13 (a) shows a comparison between tamped, vibrated and pluviated specimens under symmetric two-way loading for a relative density of 85%. Vibration leads to a slightly smaller and dry pluviation to slightly larger liquefaction resistance compared to dry tamping. This is consistent with the literature data presented in Chapter 3. Figure 5.13 (b) shows the same image but with an excess pore pressure ratio failure criterion. The same conclusions can be drawn.

The effect of an altered vertical consolidation stress is shown in Figure 5.14. The different vertical stresses lead to a similar relative excess pore pressure build-up as well as a similar shear strain response.

5.2.3 Displacement-controlled cyclic constant-volume test results

A disadvantage of assuming load-controlled conditions and thus using these laboratory tests is the dependency on not only CSR but also MSR (or LTR). Furthermore, the tests are more vulnerable to sample preparation and other environmental influences within the laboratory. For displacement-controlled tests, these parameters have less effect and there is only a dependency of the cyclic shear strain amplitude (see Section 3.5.2). Figure 5.15 shows results for a displacement-controlled test in a cyclic direct simple shear device for a shear strain amplitude of 5×10^{-4} and a vertical stress of 100 kPa. Prior to the cyclic stage, a preconditioning was done with 3 cycles with $\gamma = 0.1$ (2 mm displacement) under

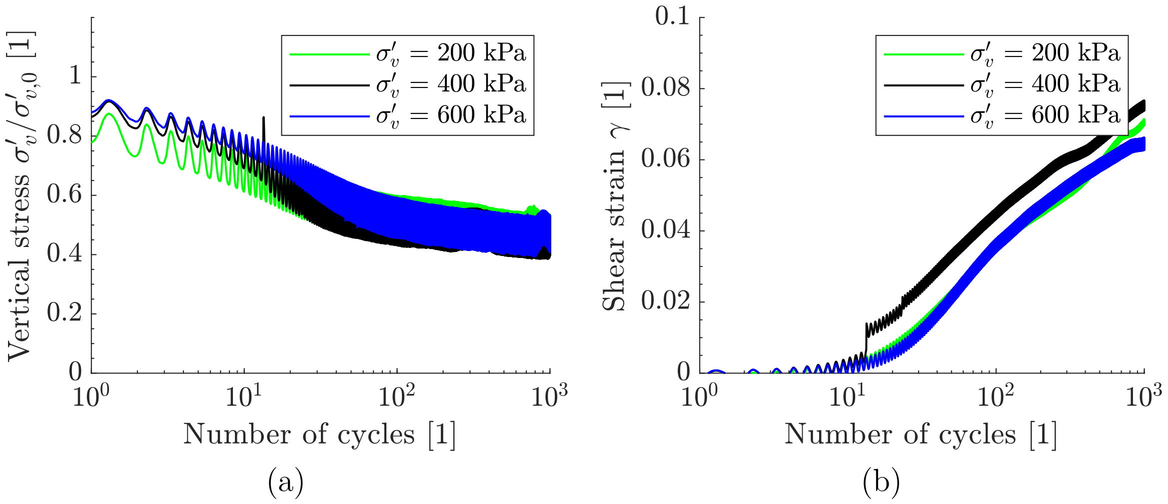

Figure 5.14: Excess pore pressure ratio R_u over number of cycles for CSR = 0.16 (a) and shear strain γ (b) for different vertical stresses for MSR = 0.

constant-volume conditions (depicted in blue in Figure 5.15 (a)). Although this value mobilised almost full shear strength, there is only a small difference to the excess pore pressure trend without pre-shearing. This may occur, because this phase was done under CNL conditions and hence, besides a possible change in fabric, a compaction of the sample occurred. Since there is a small influence of the void ratio, a small measured influence of the preconditioning is suspected with large displacements.

The shear stress decreases as does the vertical stress (Figure 5.15 (b)). The shear strain is kept constant throughout the course of the test. The mean shear strain as well as the cyclic shear strain amplitude is 5×10^{-4}. The trend of the excess pore pressure is depicted in Figure 5.15 (c) and agrees well with the literature data in Figure 3.17 (a).

An extensive presentation of displacement-controlled results can be found in Saathoff and Achmus (2021). In order to capture the highly non-linear behaviour of excess pore pressure accumulation, several tests are necessary. For displacement-controlled tests the shear strain threshold concept can help categorize and estimate the system response.

Summarized, the idea is that shear strain amplitudes smaller than γ_{tv} generate and accumulate no excess pore pressure, shear strains smaller than γ_{td} generate only marginal excess pore pressure; shear strains larger than γ_{td} generate large excess pore pressures. Only some results shall be shown, as the main focus of this thesis lies on load-controlled tests. Displacement-controlled conditions can be found for earthquake loading but also for cyclic loading. Key results regarding the investigations of cyclic displacement-controlled test are:

1. A stable region below a specific shear strain threshold can be seen.

2. There is an influence of the vertical consolidation stress on excess pore pressure generation. This was not found by Dobry et al. (1982) (cf. Figure 5.16 (a)).

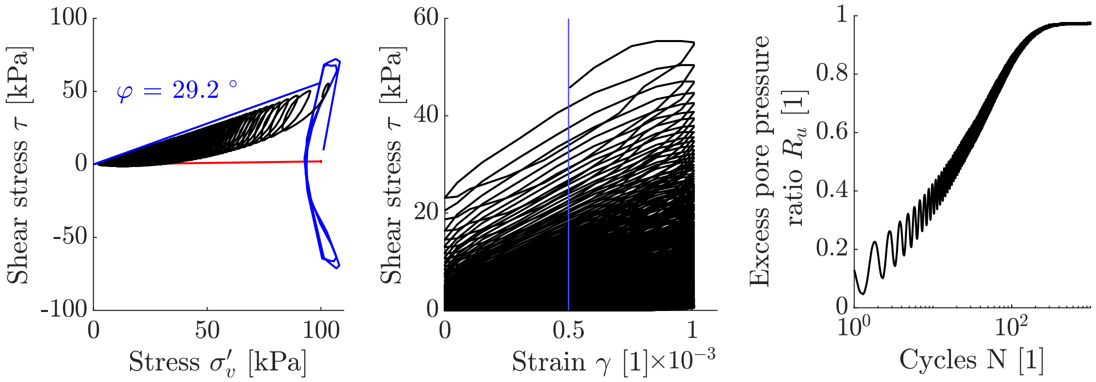

(a) (b) (c)

Figure 5.15: Results for a displacement-controlled test in a cyclic direct simple shear device with shear stress over vertical stress (a), shear stress over strain strain (b) and excess pore pressure ratio over number of cycles (c) for a shear strain amplitude $\gamma_{cyc} = 5 \times 10^{-4}$.

3. The cyclic shear strain amplitude shows the largest influence on the excess pore pressure response. The relative density has only a small influence (Figure 5.16 (b)).
4. A simple procedure for the derivation of optimal laboratory tests was derived and is presented in Saathoff and Achmus (2021).
5. A regression was fitted to the results which is used later on (Figure 5.17).

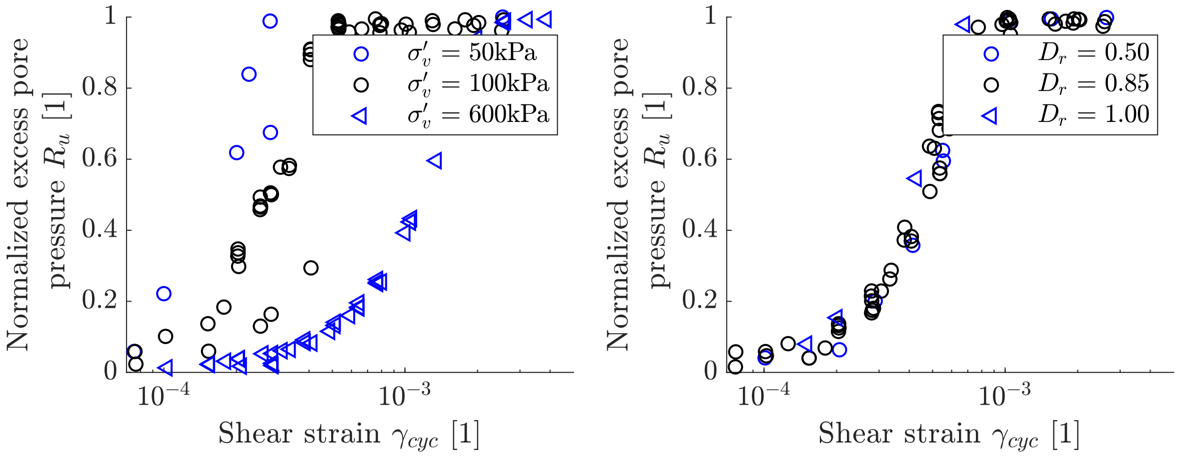

(a) (b)

Figure 5.16: Excess pore pressure ratio over shear strain amplitude for different vertical stresses (a) and for different relative densities (b) for 400 cycles.

An equation framework was derived for the reference sand for stresses between 50 - 600 kPa and a relative density of 0.85. More information can be found in Appendix D. Moreover, the response of a soil element under displacement-controlled boundary conditions

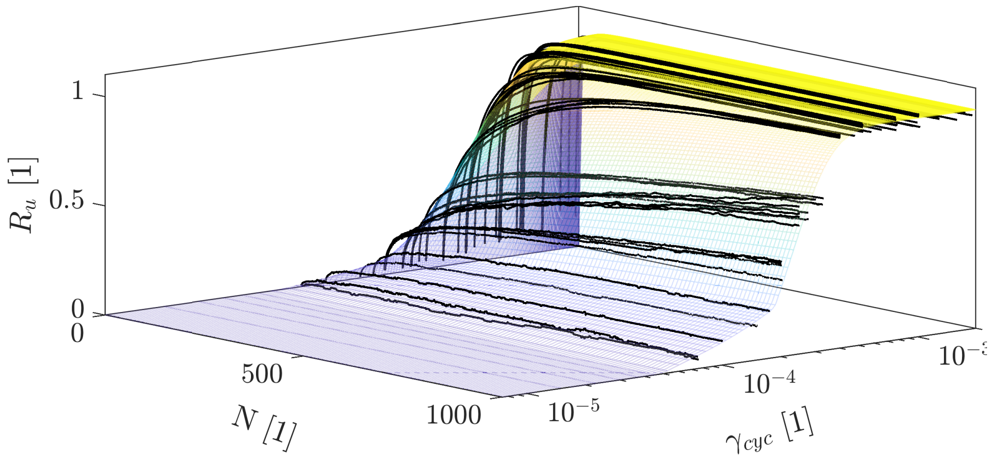

Figure 5.17: 3D plot of excess pore pressure ratio over number of cycles and shear strain amplitude for a vertical stress of 200 kPa.

was back-calculated with load-controlled contour plots and compared with the results of displacement-controlled DSS tests. The procedure is presented in the literature, but to the knowledge of the author was never applied to different soils. In Appendix C is shown that the applicability and accuracy of this method decreases for larger shear strain amplitudes.

5.2.4 Calibration of implicit model

In addition to the use of explicit methods, implicit methods will be used in this thesis for a detailed comparison. With one parameter set the soil model is able to realistically reproduce the soil response under different stress states for drained and undrained conditions. Details on the calibration of the SANISAND model can be found in Appendix A. The chosen parameters will be used in Section 7.5. Some shortcomings were already explained in Section 4.1 and could be overcome with more sophisticated versions (e.g. Liu et al. (2021)), which are not available to the author.

5.2.5 Analysis of repeated liquefaction and estimation of volumetric strain

In order to investigate the influence of repeated liquefaction and the derivation of volumetric strain, constant-volume DSS tests were performed for a vertical consolidation stress of 300 kPa. The test consists of 5 steps each with one constant-volume cycle as well as a subsequent consolidation back to 300 kPa. The relative density was chosen to $D_r = 0.40$ in order to have larger vertical strains. The CSR was also chosen with a large value of 0.13 to generate sufficient amount of excess pore pressure during one cycle ($\tau_{cyc} = 39$ kPa with LTR $= 0$). Figure 5.18 shows the results in terms of the vertical stress over the vertical strain. For a constant-volume test the unloading happens under constant vertical strain. The resulting excess pore pressure decreases with increasing number of steps, similar to the influence of a repeated pre-shearing phase. The maximum excess pore pressure ratio

R_u was reached with 0.40 depicted in Figure 5.18 (b) whereas in the last step this value is under 10%. This happens due to a compaction of the sample, but probably also due to fabric effects. Similar results were shown in Section 3.2.2.

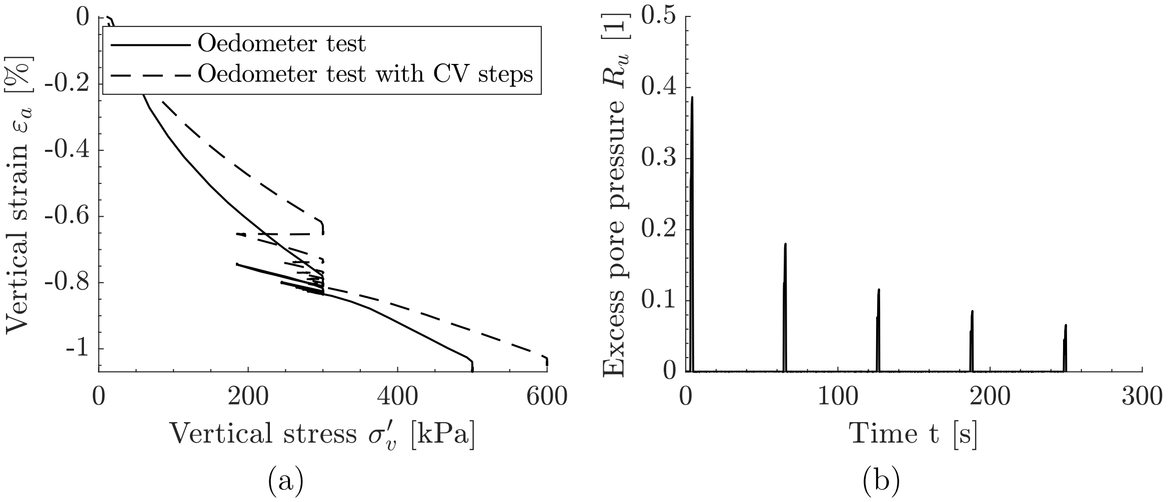

(a) (b)

Figure 5.18: Vertical stress over vertical strain in DSS test under 1D compression with unloading steps in comparison with a drained DSS tests with five intermediate constant-volume steps for CSR = 0.13 (a) and normalized excess pore pressure over time of test (b) for an initial relative density D_r of 40%.

In order to compare the calculation of volumetric strains after dissipation from undrained tests, an oedometer test was performed and compared with an oedometer test with intermediate constant-volume shearing phases. The results are depicted in Figure 5.18 (a).

The recompression modulus from oedometric tests was used to calculate the drained response from the results of constant-volume cyclic direct simple shear tests. The volumetric strain was calculated by the dissipated excess pore pressure multiplied with the inclination of un- and reloading paths from drained analysis. The measured and calculated volumetric strains agree well (Figure 5.19). A reasonable estimation of volumetric strains from the dissipated excess pore pressure for the consideration of consolidation is hence possible.

5.3 Contour plots for reference sand

The results from cyclic element tests can easily be incorporated into the approach according to Seed and Booker (1976). The number of cycles to liquefaction can be estimated for a regression of CSR over number of cycles to liquefaction N_{liq}. However, for small CSR values no N_{liq} can be derived and hence no excess pore pressure accumulation is assumed, which is not correct. The use of a simplified semi-empirical estimation procedure is quite feasible, but for a numerical analysis more fundamental differentiations between deformation and excess pore pressure are required. To increase the applicability and accuracy, contour plots based on more flexible mathematical frameworks can be used. These plots

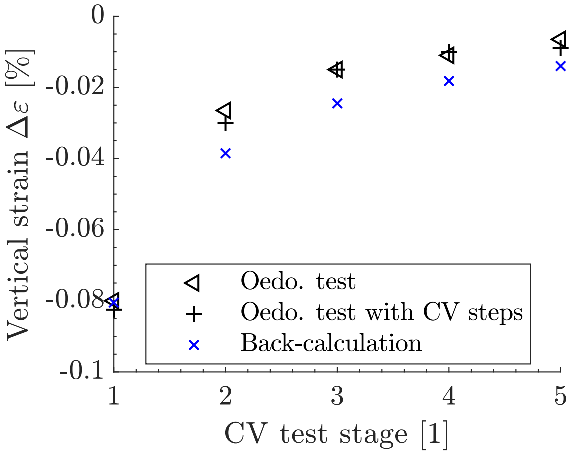

Figure 5.19: Incremental vertical strain for an oedometer test and an oedometer test with constant-volume phases as well as back-calculation with the measured excess pore pressure and the derived m_v.

can be derived from several cyclic laboratory tests and summarize the general soil behaviour. In the design process with explicit methods such plots are needed in order to assess the soil behaviour under arbitrary loading conditions and hence estimate the cyclic foundation response.

5.3.1 Derivation procedure

In order to derive a contour plot, the shear strain and excess pore pressure are plotted over the number of cycles and predefined isolines are interpolated. These can then be connected with an appropriate equation. When deriving the contour plots from laboratory results, it is important to choose the boundary conditions of cyclic laboratory tests carefully (e.g. CSR), because on the one hand the asymptotic value (stable range) should be derived realistically with smaller CSR values, but on the other hand the most influencing excess pore pressures are derived for a small number of cycles and large CSR values. If an insufficient amount of test results is present for this region, a small deviation at the beginning of the liquefaction curve (N $<$ 10) within the regression analysis may have considerable effects later on. For a first estimation the maximum MSR and CSR are needed. For sandy material, the mean load is applied in a drained manner. Hence, for a CSR $=$ 0, the maximum MSR value is $tan(\varphi')$. Regarding the CSR, the failure line and the phase transformation line can help to estimate the maximum CSR. For the reference soil, the undrained dilatant behaviour can be estimated with the PTL position at roughly CSR $=$ 0.2. The testing grid of the reference soil is depicted in Figure 5.20. Most of the points are concentrated for MSR and CSR values smaller than 0.2. If only a small number of tests shall be performed, these should be placed at symmetric two-way and one-way load, since it is possible to use these positions for deriving contour plots and scale existing data.

Exemplary results of these cyclic tests have already been shown. After all data is present, a mathematical regression framework is required. Initially a high degradation rate is needed

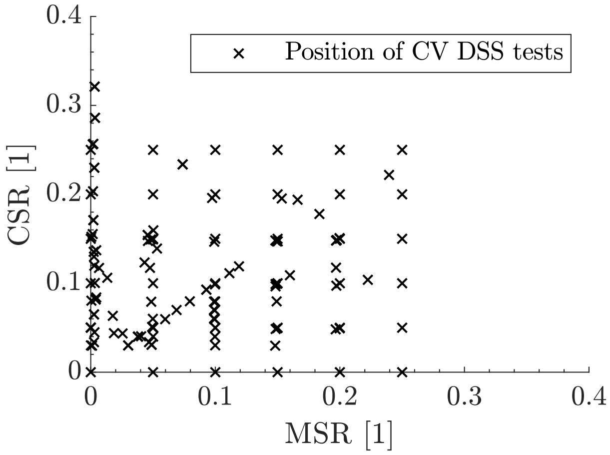

Figure 5.20: Combinations of CSR and MSR within the laboratory program for the reference soil at a relative density of 0.85.

and for larger number of cycles the rate needs to decrease. The power law function given in Equation 5.2 is often used in literature and practice. The equation is used to derive one particular R_u isocurve and hence this has to be done for several different excess pore pressure ratios values.

$$CSR_{R_{u,i}} = a\,N^b + c \tag{5.2}$$

Herein, Zorzi et al. (2019) keep the parameter b constant at -0.35, similar to Boukpeti et al. (2014) for carbonate silt sediments. Both fitted shear strain plots instead of excess pore pressure ratios. Zografou et al. (2019b) used the equation with values for b from 0.00 to -0.35 and c from 0.25 to 0.61. However, they dealt with kaolin clay with failure shear strain assumed at 5%. Since this approach is widely used it shall be investigated in the following.

A different approach is presented by Ronold (1993) (also in a compacted form in DNV-RP-C212). The values a and b in Equation 5.3 are empirical regression parameters and constant for different R_u values.

$$CSR_{R_{u,i}} = \frac{0.0001\,R_u}{(a\,N + b)} \tag{5.3}$$

Equation 5.4 uses a regression for the trend of excess pore pressure over the CSR for N = 1 and adds the degradation over the number of cycles with the second term.

$$CSR_{N=1} = tanh(a\,R_u^b) \qquad CSR_{R_{u,i}} = a\,CSR_{N=1}^b\,(1 + 10N)^{-c} \tag{5.4}$$

Wichtmann and Triantafyllidis (2011) report a logarithmic approach for the description of volumetric strain in cyclic triaxial tests. The approach fits well for poorly graded fine gravel, but the function depends on test material. Hence the following equation was derived in order to fit CSR with the related N and R_u. Equation 5.5 uses the shape of a quadratic form and an apex at the position of N = 1000. The asymptotic CSR value equals the b value within the equation. It can mathematically only be used up to 1000 cycles and needs two regression parameters. This applies to the DSS tests, because mainly 1000 cycles for each test were performed within the test program.

$$CSR_{R_{u,i}} = a * (ln(1000) - ln(N))^2 + b \tag{5.5}$$

After the possible equations have been presented, they shall be applied to the reference soil ($D_r = 0.85$). Figure 5.21 to Figure 5.24 show the fitted contour plots for the reference soil for MSR = 0. Figure 5.21 shows the regression based on Equation 5.2. This equation is also known from practical projects. The regression works well for predefined ranges of the regression parameters ($0 \leq a \leq 1$, $-0.5 \leq b \leq -0.2$, $0 \leq c \leq 0.5$) and the asymptotic CSR value can actively be controlled. In order to have a mathematical framework, the regression parameters are furthermore fitted over the normalized excess pore pressure with a hyperbolic tangent function (Equation 5.6 with parameter definition of a and b) (cf. Figure 5.25).

$$a = tanh(a_1 * R_u^{a_2}) \qquad b = tanh(b_1 * R_u^{b_2}) \tag{5.6}$$

This is done for all the following approaches, based on preliminary analysis. Hence, Equation 5.2 needs in total six fitting values and is the most complex one in terms of fitting.

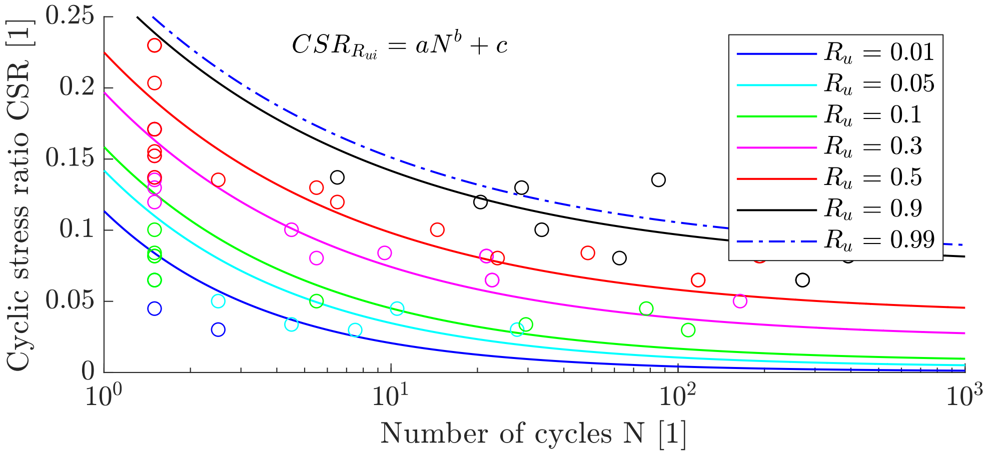

Figure 5.21: Contour plot based on Equation 5.2 for MSR = 0 and the reference relative density from cyclic direct simple shear tests.

Figure 5.22 shows the approach in accordance to the DNV (Equation 5.3). This regression seems to be quite good, but is not easy to control regarding the physical meaning of regression parameters. Figure 5.23 shows the fitting of the values with Equation 5.4.

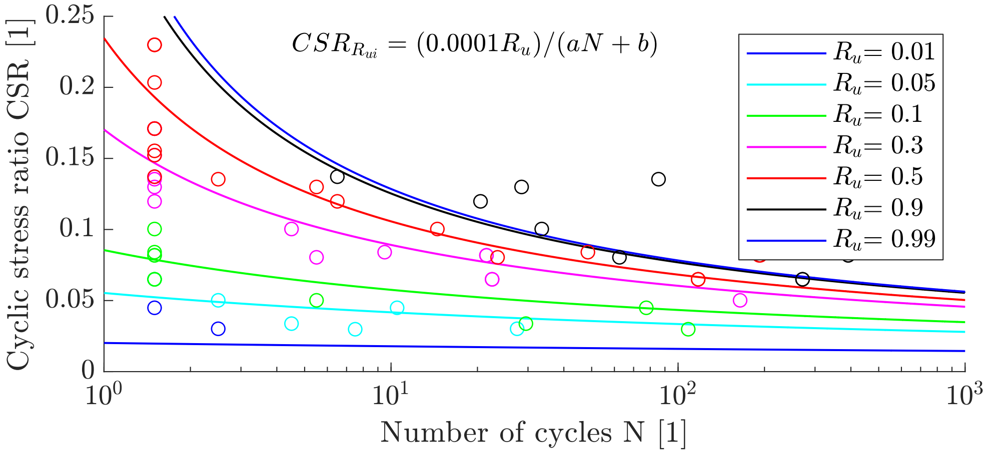

Figure 5.22: Contour plot based on Equation 5.3 for MSR = 0 and the reference relative density from cyclic direct simple shear tests.

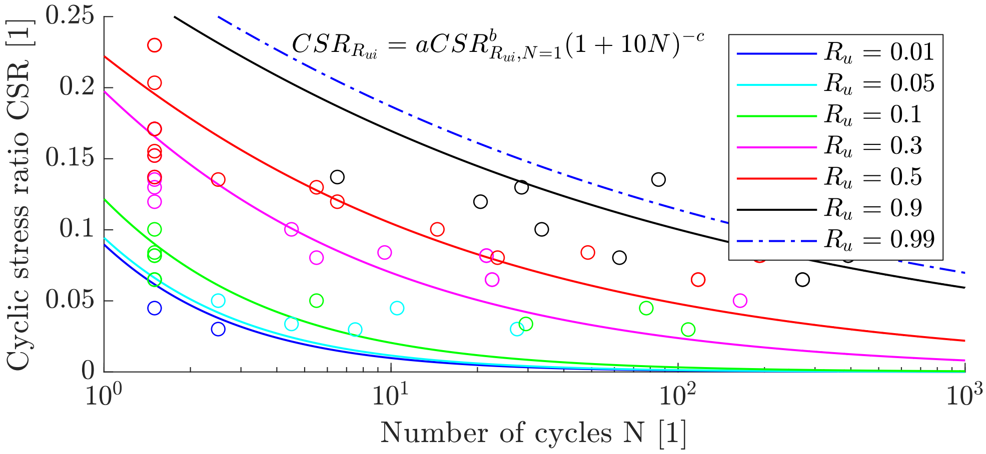

Figure 5.23: Contour plot based on Equation 5.4 for MSR = 0 and the reference relative density from cyclic direct simple shear tests.

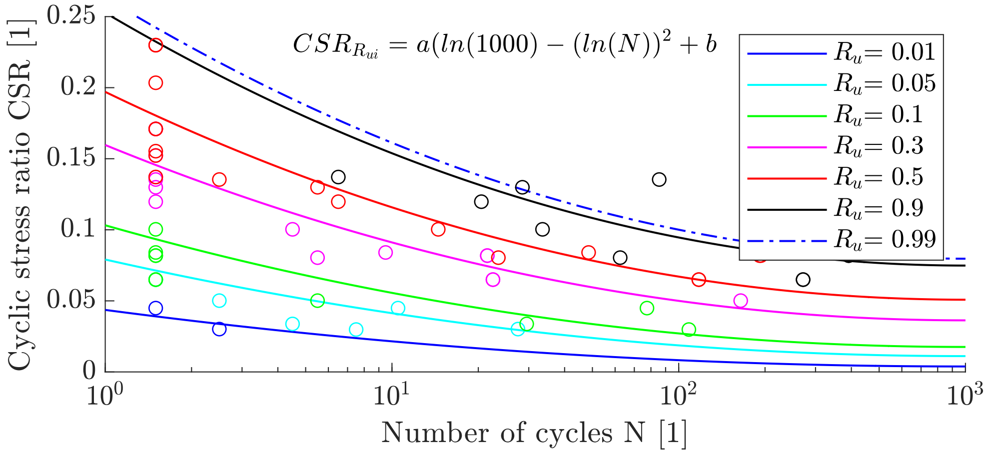

Figure 5.24: Contour plot based on Equation 5.5 for MSR = 0 and the reference relative density from cyclic direct simple shear tests.

Equation 5.4 cannot be fitted to the measured data straightforward since first the curve for N = 1 is needed. It does not give a large decrease over the number of cycles which may become difficult for a larger degradation within the first cycles.

The resulting larger excess pore pressure values are not conservative in comparison with the other approaches. The asymptotic value cannot be fitted separately. Furthermore, the curves are not parallel for 1000 cycles and may intersect for larger numbers of cycles. Figure 5.24 shows the regression based on Equation 5.5. This approach fits the cyclic data very well and the regression parameters can also be fitted easily (Figure 5.25). The regression of the fitting values a and b is done over the excess pore pressure ratios.

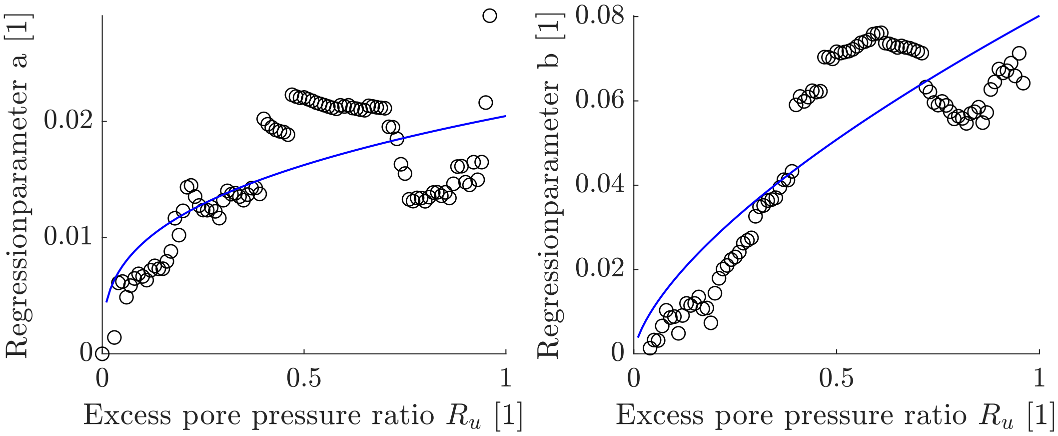

Figure 5.25: Regression of fitting parameter over normalized excess pore pressure ratio for a (a) and b (b) for MSR = 0 for Equation 5.5.

Table 5.2: Final regression parameters for reference soil for excess pore pressure ratio at a relative density of 0.85.

MSR [1]	a_1 [1]	a_2 [1]	b_1 [1]	b_2 [1]
0.00	0.0205	0.3328	0.0804	0.6601
0.05	0.0201	0.7823	0.0580	0.3353
0.10	0.0150	0.8000	0.0476	0.4265
0.15	0.0050	0.9000	0.0378	0.2744
0.35	0.0041	0.9000	0.0237	0.1624

All test results were subsequently fitted with Equation 5.5 to derive plots for different MSR values. The observed laboratory test results, in terms of the excess pore pressure R_u and the cyclic shear accumulation γ over the cyclic load number N, are described by a set of best fit parameters. Table 5.2 gives an overview of the used regression parameters for all presented contour plots. The final excess pore pressure ratio contour plot is depicted in Figure 5.26 with CSR and MSR over a number of cycles for excess pore pressure ratios R_u of 0.01, 0.05, 0.10, 0.20, 0.50, 0.95. The blue lines show the slices of type 3 plots and the red lines the type 2 representations.

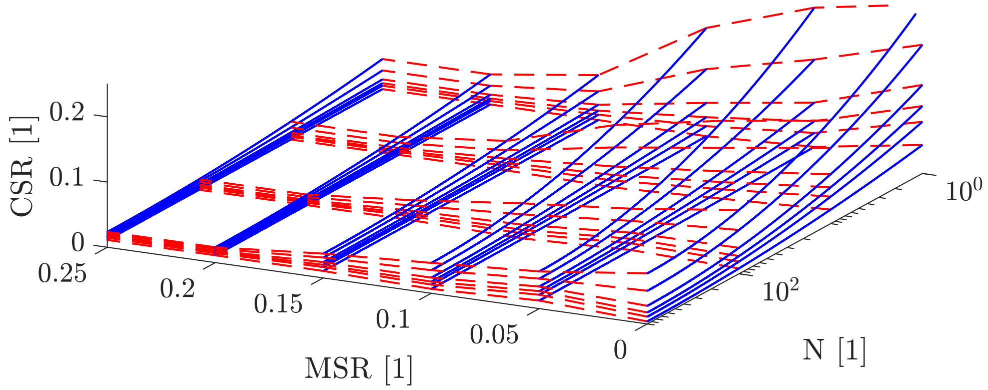

Figure 5.26: Excess pore pressure ratio R_u (from bottom to top: 0.01, 0.05, 0.10, 0.20, 0.50, 0.95) over CSR, MSR and number of cycles N.

5.3.2 Exemplary contour plots

Several contour plots can be derived based on the presented mathematical framework from Table 5.2. Different aspects related to these contour plots shall be presented and explained in the following subsection. The difference between type 3 and type 2 contour plots was already explained in Chapter 3. Type 3 plots can furthermore be derived for constant mean shear stresses (MSR) values or constant load type ratios (LTR). These plots are based on different procedures to evaluate the cyclic results and cannot be easily compared with each other (cf. Figure 2.8). Figure 5.27 depicts the counterintuitive combination of MSR and LTR. A MSR = 0.1, CSR = 0.1 defines symmetric one-way loading, CSR > 0.1 non-symmetric two-way loading and CSR < 0.1 non-symmetric one-way loading. Different LTR values can be located on the equally distributed isocurves for constant MSR values.

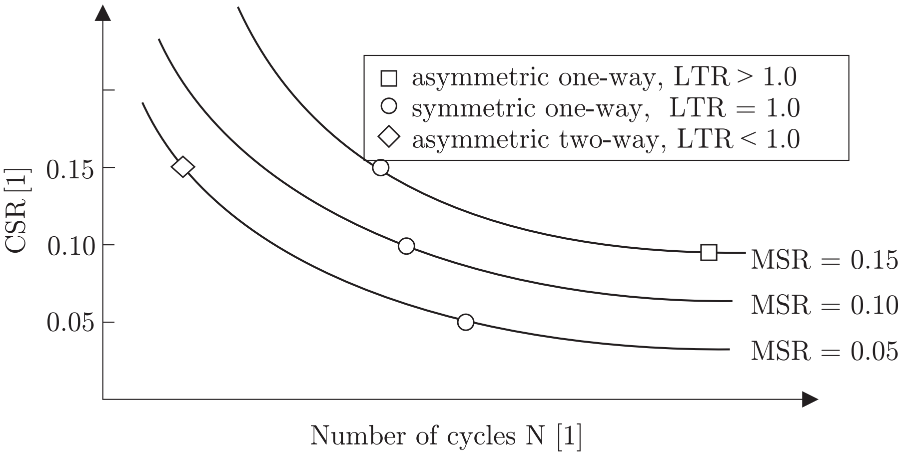

Figure 5.27: Difference between MSR and LTR in contour representation.

Type 3 contour plot (MSR = const.)

In order to derive type 3 contour plots, the aforementioned mathematical framework is used. Figure 5.28 depicts the applied curves considering the mentioned parameters and the laboratory tests for the selected states of R_u = 0.1, 0.25, 0.50, 0.75, 0.90 and for different MSR values. In type 3 plots the stable region can be seen in the lower part. There is a CSR value under which almost no excess pore pressure arises. A larger MSR leads to a smaller bearable CSR value for the same number of cycles. For different MSR values, larger excess pore pressure isocurves are more affected than the isocurves of smaller excess pore pressure values. This agrees with the literature data presented in Chapter 3. The coloured dots in Figure 5.28 were used instead of the exact excess pore pressure ratios from the cyclic tests in order to make the figure more clear and comprehensible. The dots are categorized by colour and each 0.05 larger or smaller (+/- 0.05 R_u) than the corresponding coloured line. A comparison with the exact data and hence the fitting accuracy is done later on (Figure 5.30).

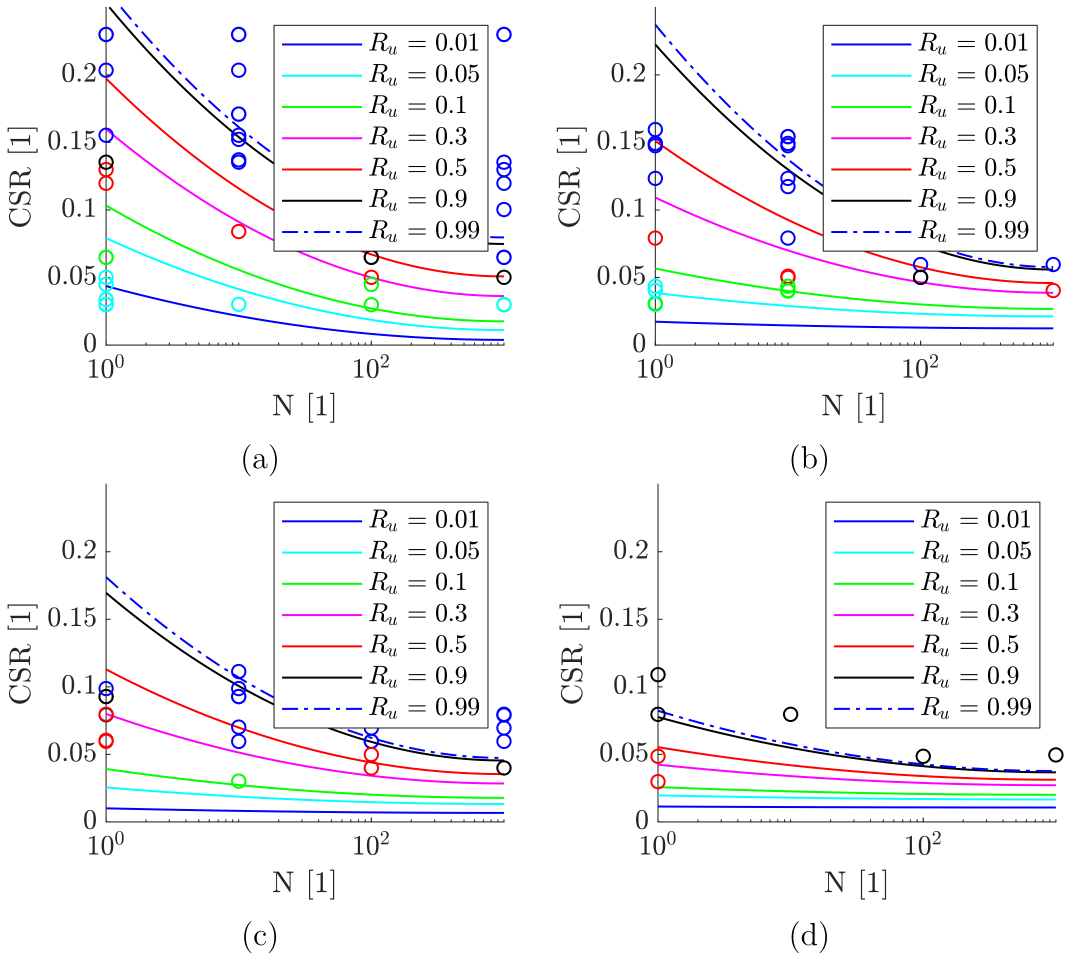

(a) (b) (c) (d)

Figure 5.28: Excess pore pressure ratio type 3 plot for MSR = 0.00 (a), MSR = 0.05 (b), MSR = 0.10 (c) and MSR = 0.15 (d).

Only the mean excess pore pressure ratio is fitted. For an increased CSR an increased accumulation is expected. For a larger relative density, the degradation is smaller. If the MSR is increased, not only is the failure line approached after only a few cycles (as explained above), but also the excess pore pressure span increases (larger cyclic excess pore pressure amplitude), which means that the permanent or mean part of the curve starts to predominate for larger excess pore pressure values.

Type 2 contour plot (N = const.)

The aforementioned plots have been derived for several MSR values and can be plotted in a different way. Figure 5.29 shows the contour plot for N = 1, N = 10, N = 100 and N = 1000 for cyclic direct simple shear constant-volume tests. The results for different MSR are interpolated linearly.

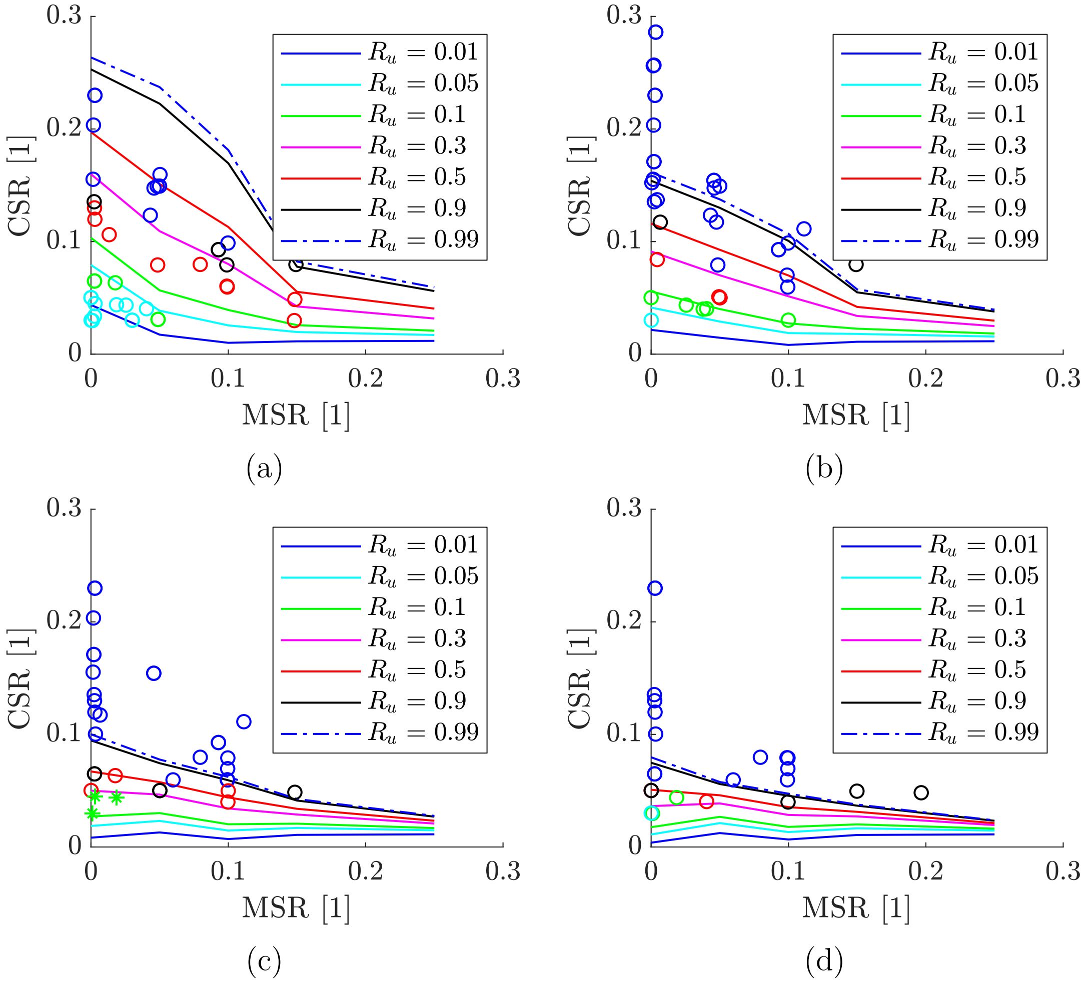

(a) (b)

(c) (d)

Figure 5.29: Excess pore pressure ratio type 2 contour plot for N = 1 (a), N = 10 (b), N = 100 (c) and N = 1000 (d).

Figure 5.29 shows the CSR over MSR for a specific number of cycles N. The MSR is applied in a drained manner, hence it represents test results from CNL test. The values on the x-axis are independent on the number of cycles, since it represents the monotonic (drained) test, which, for larger shear strains, reaches the angle of internal friction. Tests located at MSR = 0 are fully drained without drained mean shear phases. From the x-axis to the y-axis the influence of undrained conditions increases (with decreasing LTR, the influence of undrained condition increase). Hence, for small CSR and large MSR values full liquefaction cannot be expected. If the mean phase would have been applied in an undrained manner, the isocurves of normalized excess pore pressure would have intersected with the x-axis. This would change the appearance of the contour plot. Certainly, due to the project-specific soil layering, drained conditions can be justified, but one has to be aware of the site-specific model assumptions in combination with the stratigraphy and design storm.

The isoline for the normalized excess pore pressures R_u are parallel to the x-axis, even if no liquefaction is expected there. Below the bisecting angle this fit is conservative and purposely simplifies the problem in order to make the application easier. Furthermore, Vucetic (1994) states that for shear strains smaller than the volumetric threshold no excess pore pressure builds up. For small shear stresses the soil reaction in load- and displacement-controlled tests is quite similar and, hence, for a small shear strain value no excess pore pressure accumulation is expected (cf. Figure 5.34).

Fitting accuracy

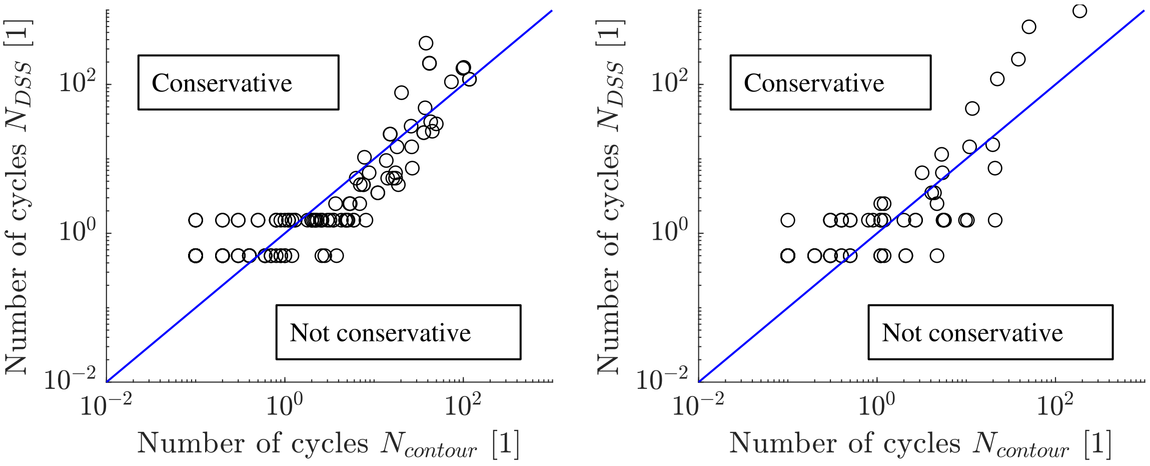

(a)

(b)

Figure 5.30: Fitting accuracy of excess pore pressure ratio for measured and estimated number of cycles for MSR = 0 (a) and MSR = 0.10 (b) with $R^2 = 0.49$ and $R^2 = 0.89$, respectively.

The quality of fit can be compared by using the calculated numbers of cycles and the measured values from laboratory test results for different excess pore pressure ratios (0.05, 0.10, 0.15, 0.20, 0.30, 0.50, 0.95). Figure 5.30 compares the observed laboratory data and the applied approach data for MSR = 0 and MSR = 0.10. Overall, a conservative approach can be seen for both target values. To quantify the fitting, the coefficient of determination R^2 was calculated according to Equation 5.7 to 0.49 and 0.89 for MSR = 0 and MSR = 0.10, respectively. The value for MSR = 0.10 is larger than the value for MSR = 0. However, a fitting with a coefficient of determination of 0.999 is not possible for these kind of tests due to the inherent variability within the physical tests. The fitting accuracy is hence seen as reasonable.

$$R^2 = \frac{[\sum_{i=1}^{n}(y_i - \bar{y})(\hat{y}_i - \bar{y})]^2}{[\sum_{i=1}^{n}(y_i - \bar{y})^2][\sum_{i=1}^{n}(\hat{y}_i - \bar{y})^2]} \tag{5.7}$$

Type 3 contour plot (LTR = const.)

The fitting was done for a constant MSR for the case of DSS tests, however, the load types (LTR) are differentiated by one- or two-way loading. Hence, type 3 contour plots with constant LTR are transferred for a more intuitive comparison ($0 \leq \text{LTR} \leq \infty$). Figure 5.31 shows the resulting contour plots for two different LTR values.

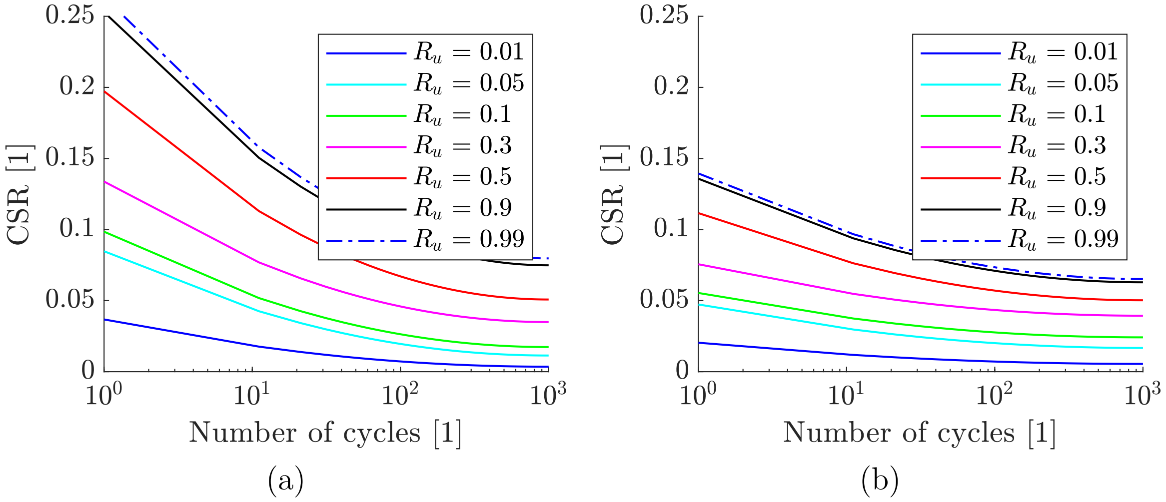

Figure 5.31: Type 3 contour plot for LTR = 0 (a) and LTR = 1 (b).

Figure 5.32 shows the resulting paths over the number of cycles for symmetric two-way and one-way loading. There is less damaged obtained for the soil response derived with a type 3 contour plot for LTR = 1 conditions compared to a contour plot based on MSR conditions.

Type 3 contour plot from triaxial device (LTR)

Some additional undrained cyclic triaxial tests have been performed and are compared with the DSS results for symmetric one-way and two-way loading. For a comparison special care has to be taken to transform the vertical stress to octahedral stresses. Figure 5.33 shows the resulting contour plots for N = 10 and N = 100 for CSR and MSR conditions transferred to vertical stress conditions. This means that the calculated CSR used in the triaxial test is reduced to conditions derived for the vertical stress by using the earth pressure coefficient at rest (cf. Equation 6.5). The difference of the soil response to DSS conditions is larger than initially expected. An excess pore pressure ratio of 0.5 is derived for LTR = 0 at CSR = 0.35. For DSS conditions this value is 0.12. The difference can be attributed to the soil specific behaviour, but also on the different soil preparation procedure. The triaxial samples were frozen and tamped which is an additional factor with

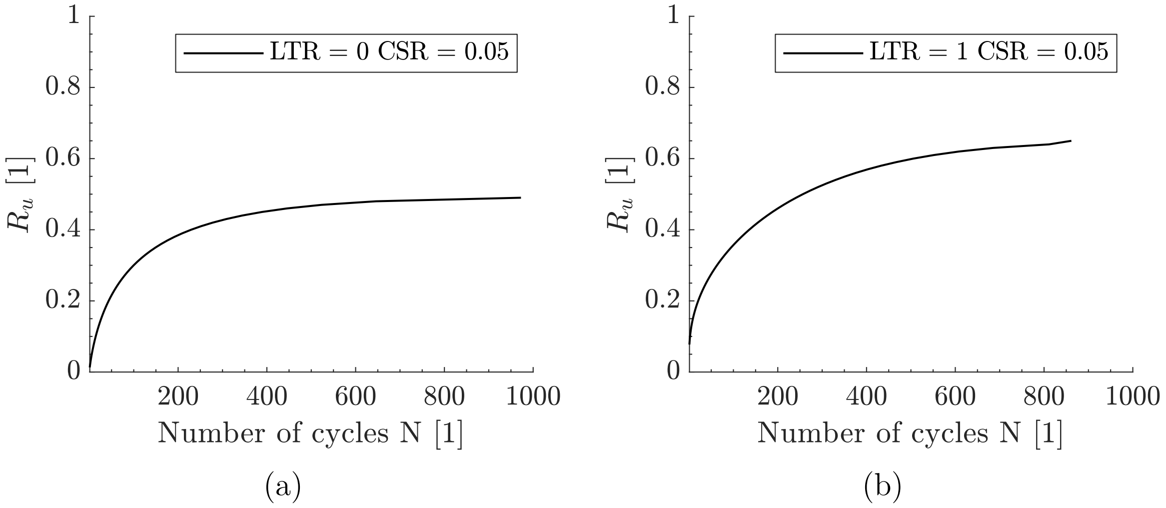

(a) (b)

Figure 5.32: Comparison of excess pore pressure ratio over number of cycles for LTR = 0 (a) and LTR = 1 (b) for CSR = 0.05.

respect to the soil response. Furthermore, the tests are performed as CIU which means they have an even larger cyclic strength when comparing the influence of k_0-conditions from Section 3.2.2.

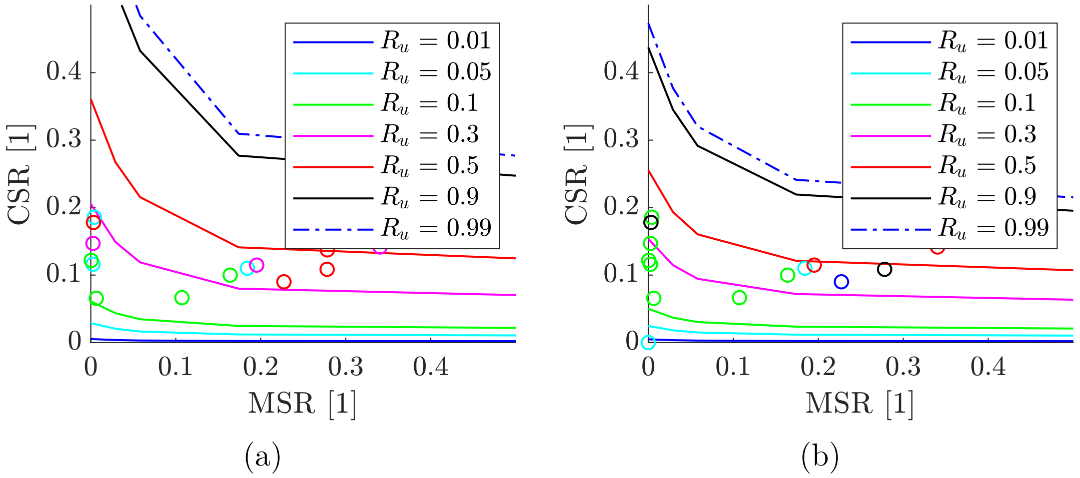

(a) (b)

Figure 5.33: Triaxial data for a relative density of $D_r = 0.85$ for N = 10 (a) and N = 100 (b).

Shear strain contour plots

The mean and cyclic shear strain can be fitted in the same way to the excess pore pressure ratio. Therefore, an appropriate mathematical framework is needed. Ronold (1993) presents an equation for fitting the shear strain, which is also included in DNV-RP-C212. However, it needs five regression parameters. Hence, the same equation as the one used for excess pore pressure is used here (Equation 5.5). The input values for the mathematical framework are depicted in Table 5.3. Results in the form of contour plots are shown in Figure 5.34. The limiting shear strain for sandy soil was chosen to be 5%. The cyclic shear strain is zero for monotonic conditions (CSR = 0) and maximum for MSR = 0.

Below the bisecting angle, the cyclic shear strain decreases, which is not separately considered. To make the fitting easier, the value is assumed to be more or less constant in this region, which is also conservative. Figure 5.35 shows a comparison between measured and derived values. The coefficient of determination is $R^2 = 0.45$ and $R^2 = 0.99$ for MSR = 0 and MSR = 0.10 respectively.

Table 5.3: Final shear strain regression parameters for the reference soil at a relative density of 0.85.

MSR [1]	a_1 [1]	a_2 [1]	b_1 [1]	b_2 [1]	CSR [1]	a_1 [1]	a_2 [1]	b_1 [1]	b_2 [1]
0.00	0.15	0.55	0.17	0.18	0.000	0.0000	0.00	1.614	0.40
0.05	0.14	0.60	0.17	0.18	0.025	0.0040	0.10	0.800	0.43
0.10	0.13	0.65	0.17	0.18	0.050	0.0030	0.06	0.700	0.45
0.15	0.12	0.65	0.17	0.18	0.100	0.0020	0.08	0.700	0.47
0.25	0.11	0.65	0.17	0.18	0.150	0.0010	0.20	0.700	0.50
-	-	-	-	-	0.200	0.0010	0.20	0.700	0.50
-	-	-	-	-	0.400	0.0005	0.20	0.700	0.52

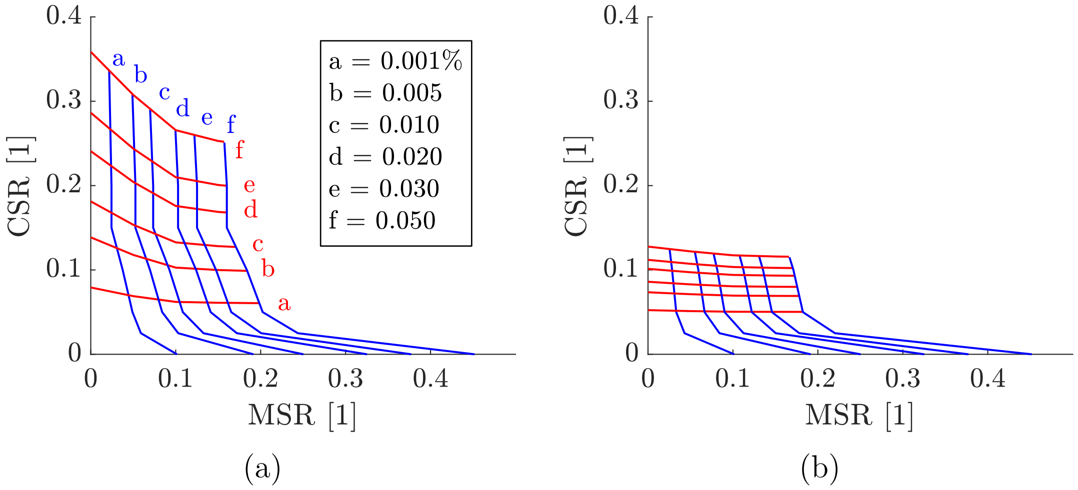

Figure 5.34: Type 2 contour plot for N = 1 (a) and N = 100 (b) for mean shear strain (blue) and shear strain amplitude (red).

Regarding the mean shear strain, the intersecting point for CSR = 0 is derived based on monotonic CNL tests. For MSR = 0 this value is assumed to be zero, even if in some tests a mean shear strain arises due to stress redistributions. The laboratory test positions have been selected for the investigation of excess pore pressure and, hence, only some tests were performed for large CSR and MSR values. Furthermore, for a shear strain of 5% the full mobilisation of the angle of internal friction is not achieved (since $MSR_{max} > 0.50$).

The excess pore pressure criterion was set to 5% shear strain span, which is a cyclic shear strain amplitude of 2.5%. The excess pore pressure isocurve for liquefaction fits well with

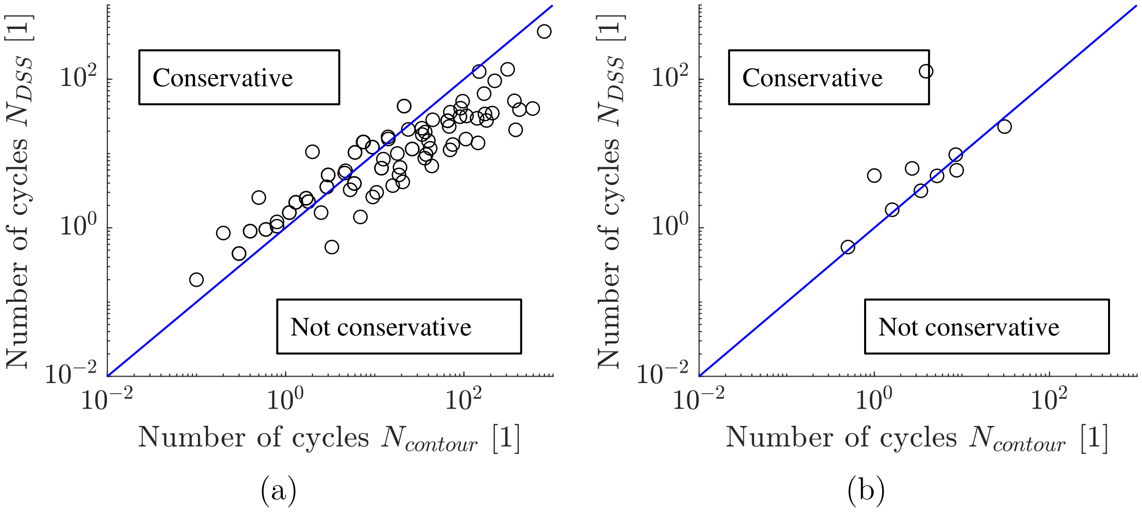

Figure 5.35: Fitting accuracy of shear strain for measured and estimated number of cycles for MSR = 0.00 (a) and MSR = 0.10 (b) with $R^2 = 0.45$ and $R^2 = 0.99$, respectively.

the mentioned shear strain isocurve when comparing Figure 5.29 and Figure 5.34 and shows the consistency of shear strain and excess pore pressure plots.

Figure 5.36 depicts the resulting shear stress - shear strain paths for symmetric two-way (a) and symmetric one-way (b) loading. The mean shear strain is zero for LTR = 0 so that the sum of the mean and cyclic component is identical to the total path. For LTR = 1 the mean shear strain and cyclic shear strain amplitude shows a more similar trend since the stress path lies on the bisecting line. These curves represent the soil response of an element which was loaded with 30 cycles with the CSR, which can be read from the y-axis, and the element will experience a shear strain which can be read from the x-axis.

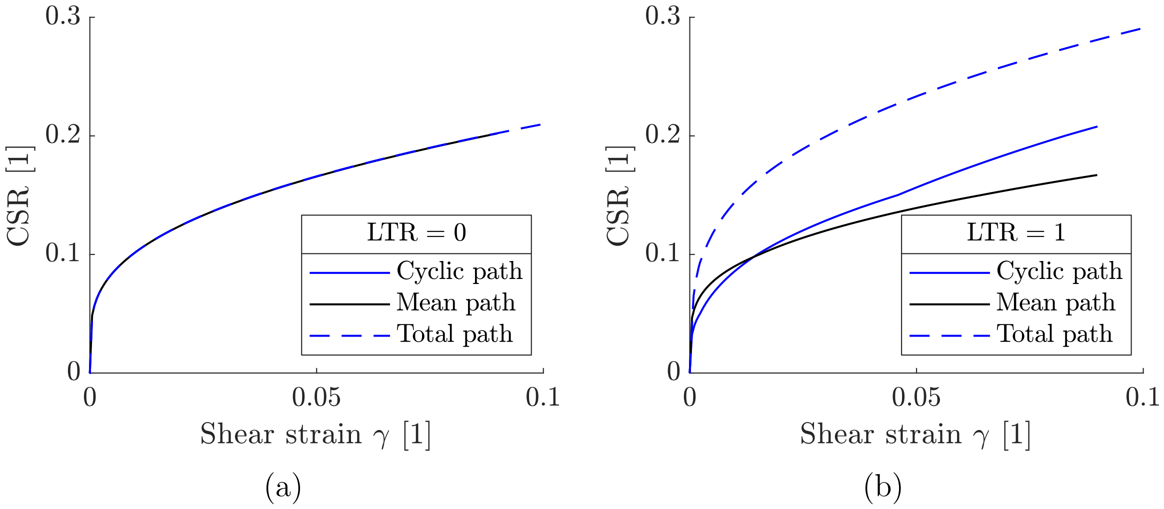

Figure 5.36: CSR over shear strain for LTR = 0 (a) and LTR = 1 (b) for N = 30.

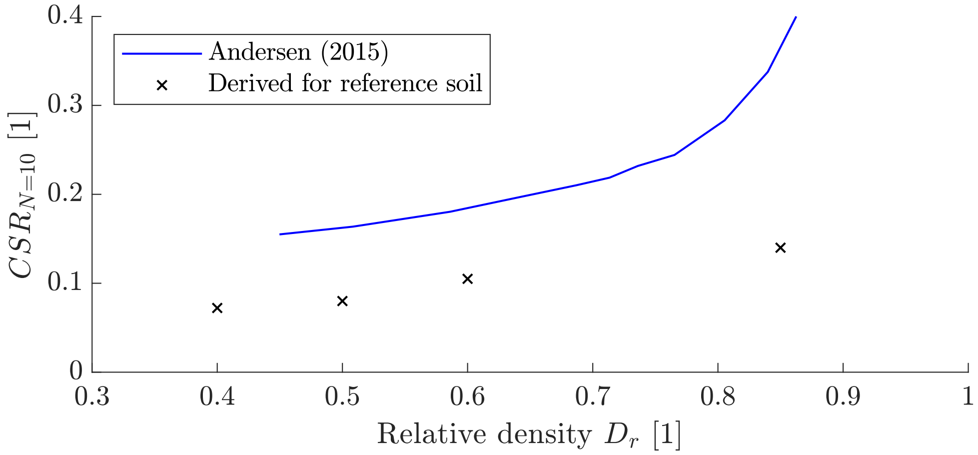

Figure 5.37: Diagram for scaling contour plots for sandy material: ratio of cyclic shear strength for 10 cycles with symmetrical cyclic loading and static shear strength as a function of relative density for DSS conditions with a vertical stress of 100 kPa.

5.3.3 Scaling of contour plots

Contour plots can be constructed based on many cyclic laboratory tests or simplified correlations can be used. This is for instance scaling with empirical correlations in combination with no or only a small number of cyclic test results. In order to scale the cyclic soil response to have a reasonable fit, correlation diagrams in which the cyclic shear stress CSR after 10 cycles at failure is correlated to the relative density can be used (Andersen, 2015). As for all approaches, the accuracy can be increased depending on the amount of laboratory tests. Figure 5.37 shows a diagram presented by Andersen (2015) with additional results for the CSR after 10 cycles for different relative densities of the reference soil used in this work (cf. Figure 5.11 (a)). Generally, the reference sand can sustain less cyclic damage. The trend is also more linear compared to the literature data.

In order to verify these plots, roughly 360 $CSR - N_{liq}$ plots from literature publications were digitized and are shown in Figure 5.38, Figure 5.39 and Figure 5.40 categorized in three different groups by means of relative density and normalized by the value CSR at N = 10. It should be kept in mind that there are different loading conditions, soil preparations, consolidation characteristics and sand types (particle shape and grain size distribution). The fines content is in all cases smaller than 10%. A different definition of liquefaction failure was used and, hence, smaller deviations may arise. There is a dependency on the relative density and also a large bandwidth.

The suggested trend line according to Andersen (2015) was added in all figures. He presents cyclic shear stress at failure as a function of number of cycles in DSS tests for symmetrical cyclic loading on normally consolidated sand for a vertical stress between 85 kPa – 710 kPa and a fines content < 5%. Also results from own investigations were added. Overall, a rough trend can be seen, whereas the approach according to Andersen (2015) is conservative for the case of very dense sand in contrast to the measured data represented with a blue line.

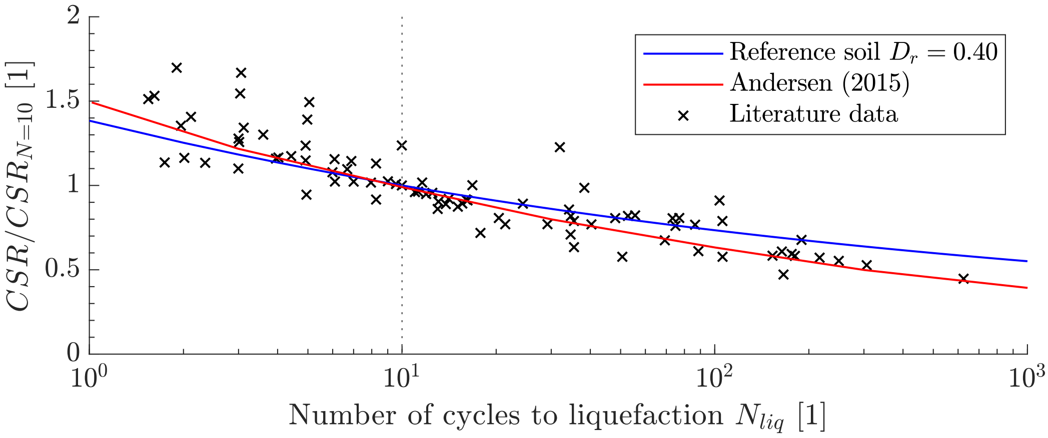

Figure 5.38: Evaluation of various literature data for different CSR and MSR values with $D_{r,max} = 0.35$ for sandy material with fines content $< 10\%$ in comparison with suggestion by Andersen (2015).

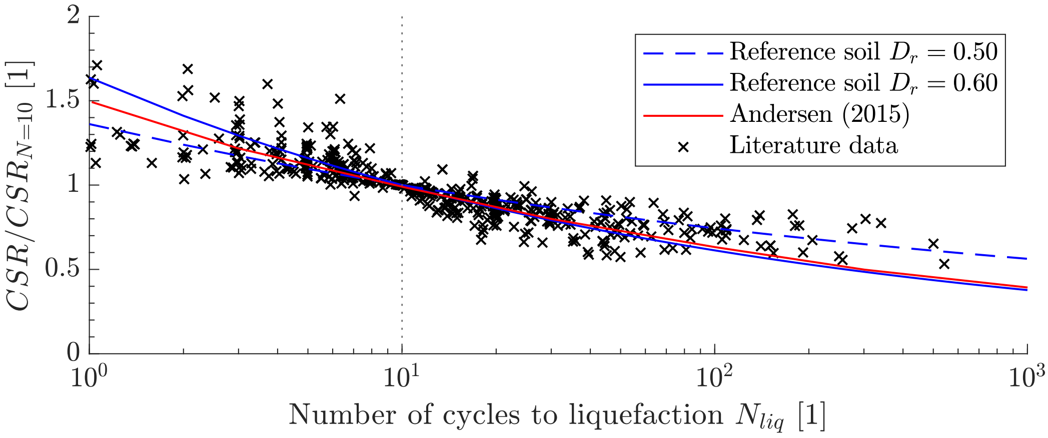

Figure 5.39: Evaluation of various literature data for different CSR and MSR values with $D_{r,max} = 0.65$ for sandy material with fines content $< 10\%$ in comparison with suggestion by Andersen (2015).

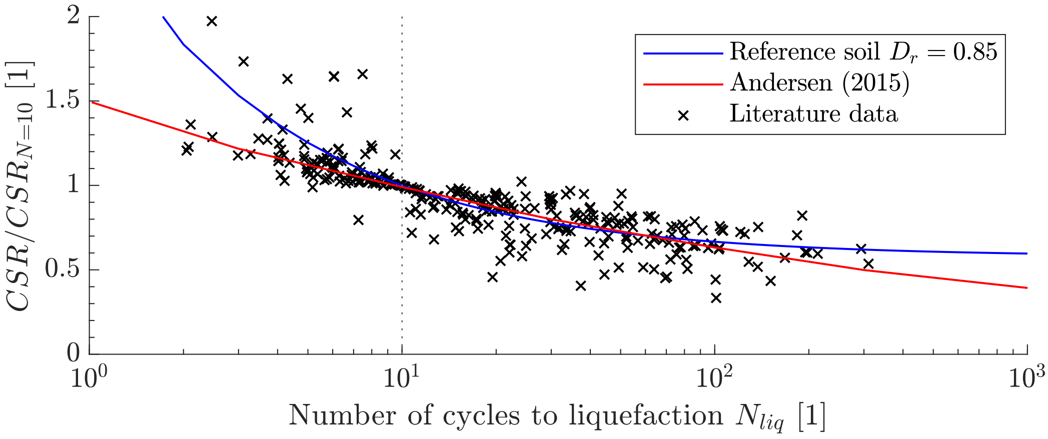

Figure 5.40: Evaluation of various literature data for different CSR and MSR values with $D_{r,max} = 0.85$ for sandy material with fines content $< 10\%$ in comparison with suggestion by Andersen (2015).

For an increasing relative density, there is an increasing deviation between the literature data, the trend curve from Andersen (2015) and the results measured for the reference soil. The largest deviation can be seen for cycle numbers smaller than 10.

Besides symmetric two-way loading conditions with MSR = 0, there may also be a condition with MSR > 0. Figure 5.41 (a) shows the liquefaction curve for different MSR values normalized to the CSR value after 10 cycles from the performed DSS tests. The value $CSR_{N=10}$ used for the normalisation is depicted in Figure 5.41 (b) over the MSR. For MSR = 0 the CSR needed for liquefaction for one cycle is significantly larger compared to the case for larger MSR values (or the approach from the literature). If no data is available, this estimation seems to be a good approximation. The plots can be used for scaling to directly output the liquefaction curve.

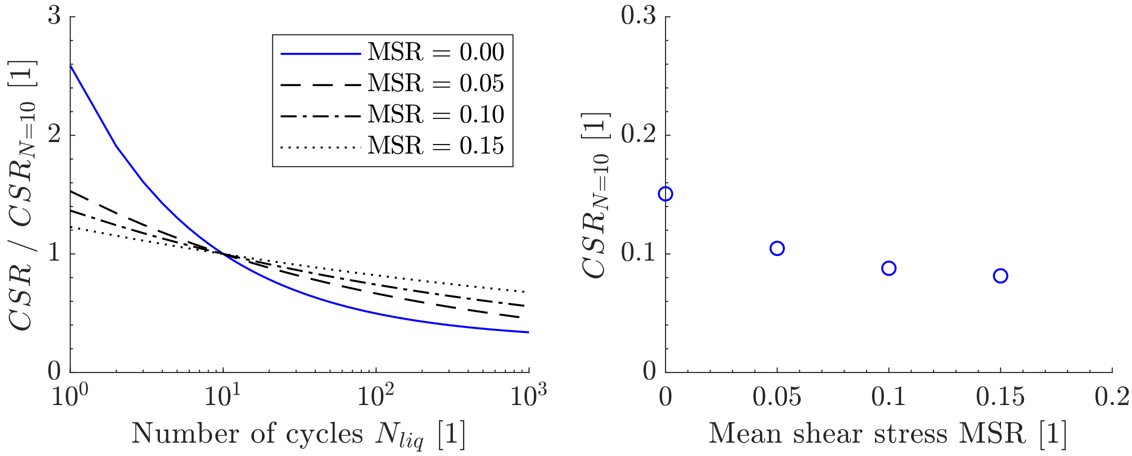

(a) (b)

Figure 5.41: Comparison of number of cycles to liquefaction for different MSR values (a) and $CSR_{N=10}$ over MSR for reference boundary conditions (b).

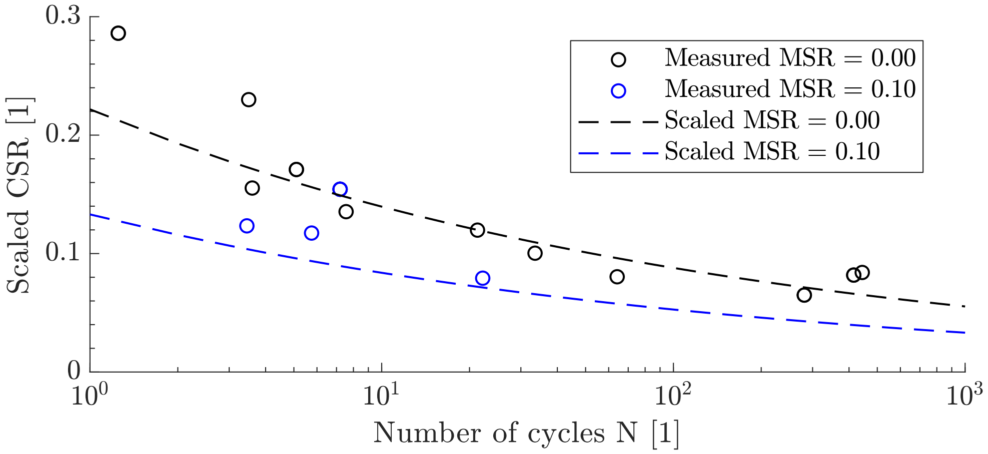

Figure 5.42: Comparison of scaled and measured data for MSR = 0 and MSR = 0.10 with scaling done with normalized approach according to Andersen (2015).

Figure 5.42 shows a comparison between scaled and measured soil response in $CSR - N_{liq}$ space for symmetric two-way loading, which, however, can only be seen as an approximate fitting. Nevertheless, the contours agree very well. In case of scaling, the approach from literature was used, since it yields a good value on average in comparison with Figure 5.41 (a). For other isocurves except the failure one, the semi-empirical approach can be used or an existing contour is scaled vertically.

6 Explicit method for excess pore pressure estimation

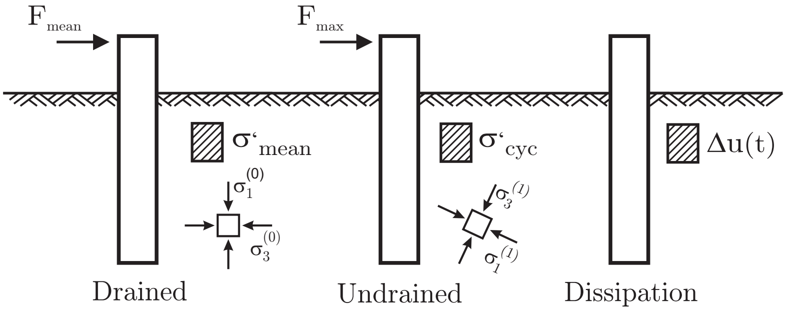

Figure 6.1: Calculation steps of explicit EPPE method.

Cyclic loading leads to a degradation in bearing capacity and accumulation of permanent deformation that must be considered in the design of offshore foundations. The developed explicit method is modular so that all steps can be interchanged for more advanced analyses. The generic approach is able to estimate excess pore pressure accumulation while being simple and comprehensible. It is optimized for practical application due to simple estimation of input parameters and a short calculation time. In practice there are several design loops and one wind farm consists of several locations with a wide range of soil conditions. Nowadays almost all locations are calculated by a finite element approach, thus a slightly faster approach will save immense computational costs. The DNV-RP-C212 proposes to use a quasi-static explicit approach based on the stress path philosophy without consideration of inertia effects. All these criteria are fulfilled by the presented generic approach and it is, hence, in accordance with DNV-RP-C212.

A storm event consists of an irregular load that can be converted into different load bins (cf. Chapter 2). For the geotechnical application, only a few cycles with large loads induce significant strength degradation in contrast to metal fatigue, where many cycles with small loads accumulate damage over time. In the present work, the soil element is to be loaded with an equivalent load and an equivalent load cycle number. A fictitious equivalent single-stage load collective is permitted in accordance with DIN 18088-4:2019-01 and BSH No. 7005 under the conditions listed there. No individual storm packages or derivation of an equivalent load cycle number will be performed below. However, a complementary procedure for this application was derived and is presented in Appendix B.

6.1 EPPE approach

The main concept of the EPPE approach was published in Achmus et al. (2018) and Saathoff and Achmus (2020). The basic idea can be implemented in many different ways and with varying complexity. Hence, a reference procedure is described below and various sub-modelling approaches are separately compared against one another in Chapter 7.

The presented approach consists of four main calculation steps, which are carried out in the numerical simulations. To calculate the cyclic influences, representative soil stresses and strains for each integration point are read from a database. These serve as input to the empirical equations used to estimate cyclic behaviour. The laboratory element test lacks a three-dimensional interaction of the boundary problem, which is accounted for by the finite element model. Herein, first the mean load and then the cyclic load amplitude are applied. This is done in the same finite element model, where the cyclic amplitude can be applied either with or without drainage (Figure 6.1). The individual steps are explained in more detail below.

6.1.1 Step 1: Load application

In the first calculation phase the numerical model is generated based on the site-specific soil conditions and the intended foundation geometry. The foundation is subsequently subjected to the mean load $F_{mean} = 0.5(F_{max} - F_{min})$ corresponding to the cyclic load conditions under consideration. The mean load of the storm is treated as a long-term (drained) load. The stress and strain components at the integration points, such as the effective octahedral stresses, are stored in a database. The numerical model uses drained input variables for the soils' strength and stiffness parameters.

The lateral load is increased by F_{cyc} to reach the maximum load of the first cycle. The stress and strain components are read and stored for all integration points. The model assumption is that the cyclic shear stress amplitude τ_{cyc} is constant over the equivalent number of cycles. The increase of the global load from F_{mean} to F_{cyc} can be done in an undrained or drained manner. Realistically, the load amplitude must be applied in an undrained manner. However, for this, a fully coupled finite element model is required. This type of finite element model is, compared to their uncoupled counterpart, slightly worse in stability and needs larger computational effort. Undrained modelling also introduces some disadvantages when dealing with multi-stage storm loads, since there is a change in the stiffness of the system response between the slowly applied drained mean stress and the rapidly applied undrained amplitude. However, both approaches, a drained or undrained application of F_{cyc}, have the goal to estimate stresses or strains in each integration point and can therefore both be used without any further problems. Nevertheless, an uncoupled model is used in the reference case, because there is only a small influence in the stress and strain estimation, which does not justify the additional effort of a coupled model. A comparison of both modelling approaches is presented in the next chapter to show the justification of this model assumption. The problem and the general procedure for the derivation of an equivalent number of cycles are discussed in more detail in Appendix B (also Section 7.2.2).

6.1.2 Step 2: Extracting equivalent stress and strain measures

In the second step, the stresses (and strains) need to be extracted from the finite element model and processed. The accumulated excess pore pressures at each integration point, corresponding to the applied stresses and the number of load cycles N, need to be calculated based on cyclic laboratory tests. Therefore, either the equivalent shear strains γ_{eq} from the numerical model are evaluated based on cyclic displacement-controlled tests or the equivalent shear stress $\sigma'_{eq,cyc}$ in each integration point is used in conjunction with cyclic load-controlled tests. To keep the explanations simple, the approach is described below using only load-controlled test results. The calculation of excess pore pressure can be based on the approach according to Seed et al. (1975b) or based on derived contour plots.

In order to use the stresses of the finite element model, the cyclic stress ratio (CSR) needs to be derived. The cyclic stress ratio in the finite element model is calculated according to Equation 6.1.

$$CSR_{FE} = \frac{\sigma'_{eq,F_{max}} - \sigma'_{eq,F_{mean}}}{2\,\sigma'_{oct,F_{mean}}} \tag{6.1}$$

The CSR is derived by subtracting the components of the equivalent shear stress at the global mean load and at the end of the calculation at the full cyclic amplitude. It is normalized by the octahedral stress at the global mean load at integration point level (Equation 6.2). The shear component is calculated by using half of the equivalent shear stress difference. In the finite element model, the effective octahedral stress σ'_{oct} is used to account for the rotation of the principal stress axes in and around the failure wedge. The equivalent shear stress $\sigma'_{eq,cyc}$ is used as an indication of prevailing shear stress (Equation 6.3). Equation 6.1 assumes that the mean stress remains constant during the entire time of cyclic loading. Above all, it is important that the conditions from the cyclic laboratory test are transferred to finite element conditions.

$$\sigma'_{oct} = \frac{\sigma'_1 + \sigma'_2 + \sigma'_3}{3} \tag{6.2}$$

$$\sigma'_{eq} = \sqrt{\frac{1}{2}[(\sigma'_{xx} - \sigma'_{yy})^2 + (\sigma'_{yy} - \sigma'_{zz})^2 + (\sigma'_{zz} - \sigma'_{xx})^2] + 6[\tau^2_{xy} + \tau^2_{yz} + \tau^2_{xz}]} \tag{6.3}$$

Figure 6.2 (a-lower) shows that in the cyclic laboratory test, the vertical consolidation stress σ'_v remains constant during the application of the mean load and is only reduced in the cyclic phase by the excess pore pressure (blue point). The stages, separated with blue lines, are consolidation, application of mean shear stress and application of cyclic load amplitude. Figure 6.2 (a-upper) depicts the stress changes over the calculation time in the numerical model. The calculation progress indicates the application up to the maximum cyclic load within the numerical model. The octahedral stress as well as the equivalent shear component are increasing (in most integration points near the pile).

A reference stress for the numerical procedure is chosen at the global mean load (blue point). Figure 6.2 (b) shows this scenario in more detail. The principal stresses are shown in negative direction. The two horizontal stresses ($\sigma'_1 = \sigma'_2$) and the vertical stress (σ'_3) can clearly be seen at the start of the analysis. Afterwards, the stresses increase (also rotation of principal axis). The upper part shows the increase in equivalent and octahedral stress. This implies that the Mohr-Coulomb circle moves to the right to larger octahedral stresses. The boundary conditions between FE and laboratory device can thus only be combined in a best possible way, but are not directly equal for explicit modelling. The value selected for the octahedral stress can have an effect on the CSR value and must therefore be chosen carefully. The use of the stresses after the wished-in-place installation is hence very conservative and may not be a representative stress value. Using the octahedral stress at the end of the calculation would also be justifiable. However, it would not be conservative in most cases, because the octahedral stress at the end of the cyclic loading is larger and would therefore result in a smaller CSR value. For the EPPE procedure the octahedral stress at mean global load is used. An average value of the stress at global mean and global maximum load could be chosen, but lacks theoretical basis.

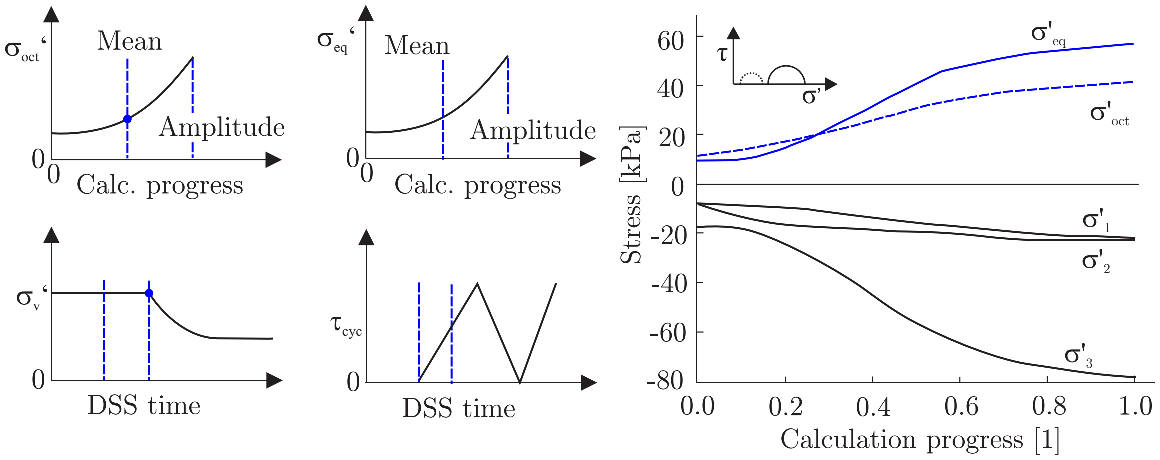

(a) (b)

Figure 6.2: Comparison of stresses in a cyclic laboratory test over time (a) and stresses in integration point in an exemplary finite element model (b).

Transfer of stress states

In the three-dimensional finite element model, different boundary conditions are present compared to laboratory tests. When quasi-one-dimensional cyclic direct simple shear test results are used, they must be transferred to a 3D finite element model state.

$$CSR_{DSS} = \frac{\Delta\tau_{xy,cyc}}{\sigma'_{v,c}} \quad CSR_{Tri} = \frac{\Delta q_{xy,cyc}}{2\sigma'_{oct,c}} \quad CSR_{FE} = \frac{\Delta\sigma'_{eq,cyc}}{2\,\sigma'_{oct}} \tag{6.4}$$

Herein, $\Delta\tau_{xy,cyc}$ and $\Delta\sigma'_{eq}/2$ are the shear component amplitudes. Direct transfer of stress states is difficult, because the exact stress state during the direct simple shear test is unknown. Hence, some assumptions are required. The vertical effective stress from the direct simple shear test can be back-calculated to the octahedral stress using the earth pressure coefficient at rest (Equation 6.5). This earth pressure coefficient at rest k_0 is in turn derived from the internal friction angle according to Jaky (1944) (Equation 6.5).

$$\sigma'_{oct} = \frac{(1 + 2\,k_0)\,\sigma'_v}{3} \qquad k_0 = 1 - sin(\varphi') \tag{6.5}$$

More thoughts must be given to how to interpret the shear component $\Delta\tau_{xy}$ from direct simple shear tests. Some authors only use the transfer procedure described in Equation 6.5 – for instance Ishihara and Li (1972), Cole (1967), Dunlop and Duncan (1969) and Peacock and Seed (1968) (Taiebat, 1999). Some even assume a general earth pressure coefficient at rest of unity $k_0 = 1$ and, hence, an isotropic consolidation which does not happen in most devices (Airey et al., 1985; Atkinson et al., 1991; Randolph and Wroth, 1981; Cole, 1967; De Josselin de Jong, 1971; Le, 2015). Analytical transfer factors vary in literature for earthquake engineering between 0.5 and 1, wherein 0.7 is often used, which agrees well to an earth pressure coefficient at rest $k_0 = 0.5$.

In the following, this problem shall be highlighted in more detail. In the triaxial device, the specimen is consolidated isotropically (CIU test) and then a deviatoric stress is applied. The Mohr-Coulomb circle expands (Figure 6.3 (b)) up to the mean stress deviator (compare Chapter 5). Subsequently, the deviatoric stress amplitude is applied for which the circle is compressed and expanded. In the case of DSS tests, the specimen is consolidated anisotropically and afterwards an additional shear stress is applied. The normal axis rotates and the shear stress increases linearly starting from the largest principal stress during consolidation (Figure 6.3 (a)). This is done until the mean shear stress is fully applied and the circle is extended to a larger τ_{max} (cf. Seed and Peacock (1971)). Herein, the radius of the circle is larger than the applied shear stress within the DSS device. The case of the finite element model was already explained (Figure 6.3 (c)).

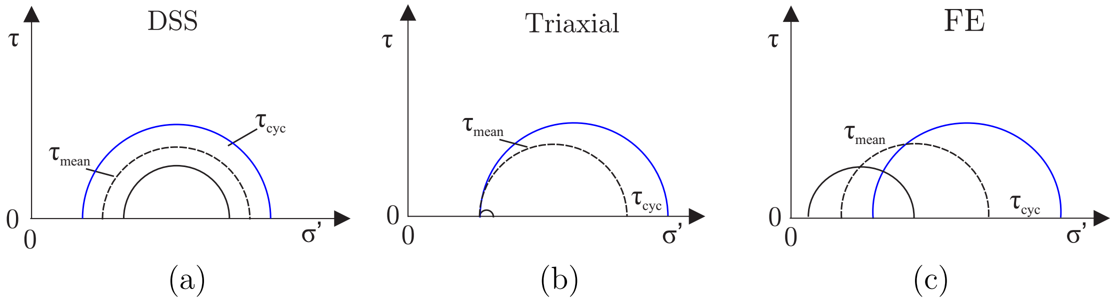

Figure 6.3: Comparison of Mohr-Coulomb circle in direct simple shear test (a), CIU triaxial test (b) and in the finite element model (c).

The radius of the circle and thus the maximum shear stress τ_{max} is interpreted as half of the deviatoric stress. Concerning this matter, the following dependency can be derived:

$$\tau_{max} = \frac{\sigma'_{eq}}{2} = \frac{q}{2} = \sqrt{\left(\frac{(\sigma'_v * (1-k_0)}{2}\right)^2 + \tau_{xy}^2} \tag{6.6}$$

Equation 6.6 calculates the radius of the Mohr-Coulomb circle for the maximum shear stress. However, for the calculation of the CSR value, the amplitude of cyclic loading is of interest, so that the difference between the minimum and maximum shear stress state is needed to calculate the CSR in p'-q space. This is done in Equation 6.7 which is used in the EPPE approach.

$$CSR_{DSS,FE} = \frac{(\tau_{max,max} - \tau_{max,mean})}{\sigma'_v(1+2k_0)/3} = \frac{\Delta\tau_{xy,DSS}}{\sigma'_v(1+2k_0)/3} \tag{6.7}$$

Herein, $CSR_{DSS,FE}$ is the CSR value from DSS test conditions transferred to p'-q space. The value σ'_v represents the vertical effective stress in the DSS test, $\tau_{max,max}$ the deviatoric stress in p'-q space for the maximum shear stress and $\tau_{max,mean}$ the deviatoric stress in p'-q space for the mean shear stress applied in the DSS device. These equations can be used to transfer CSR_{DSS} into the required $CSR_{DSS,FE}$ that is used to derive the excess pore pressure accumulation. Since the final equation uses the difference between the two states, the different consolidation states are not important.

The mean stress ratio (MSR) is derived in the same way. A transfer of stress states is necessary to use the results in p'-q space from the finite element model. The MSR relates the mean load of the cyclic load to the stress level (mean stress/consolidation stress) and is also needed to calculate the load type ratio (LTR) value. For a symmetric two-way loading, the mean shear stress is equal to zero. The particles are physically sheared over to one side and then with the same shear load to the other side. Under direct simple shear conditions there is a rotation of principal stress axis. Hence, due to the anisotropic consolidation state, there is always an initial deviatoric stress. This is also the case for the finite element model in the k_0-step. For the transfer of the MSR from DSS to p'-q space, the initial deviatoric stress from consolidation shall be subtracted in order to yield a MSR = 0 for symmetric two-way loading. With the method presented, the values between DSS, FE and triaxial test are all congruent and therefore easy for an engineer to handle (Equation 6.8). The value $\tau_{max,mean}$ in Equation 6.8 can be derived by using Equation 6.6 with the mean shear stress from DSS test. This formulation is used for the derivation of the MSR in each integration point in the EPPE approach. In case of two-way loading this value is zero.

$$MSR_{DSS,FE} = \frac{\tau_{max,mean} - \left(\frac{(\sigma'_v(1-k_0)}{2}\right)}{\sigma'_v(1+2k_0)/3} = \frac{\tau_{xy,DSS}}{\sigma'_v(1+2k_0)/3} \tag{6.8}$$

The presented transfer of stress conditions does not consider the different stress paths of the testing devices.

6.1.3 Step 3: Dissipation and analytical superposition

Offshore foundations in sandy soil exhibit partially drained conditions. This partial drainage is mainly influenced by the drainage lengths (structure's dimensions) and soil permeability k_f. In the case of low permeability soil layers, concentration will naturally occur at this location. After the CSR and MSR values have been derived for each integration point, the excess pore pressure can be calculated. The excess pore pressure response is evaluated based on a regression analysis from cyclic laboratory tests. Herein, only the derived excess pore pressure response is used, so that no numerically calculated excess pore pressure for N = 1 is needed.

The regression analysis can be based on an excess pore pressure prediction equation for instance according to Seed et al. (1975b). Instead of performing a regression analysis using the results from cyclic laboratory tests, these results can directly be transferred to shear strain and excess pore pressure contour plots. The principles of contour plots have already been explained in chapters 3, 4 and 5.

For contour plots, the excess pore pressure trend is evaluated for a given N_{eq} and an integration point specific CSR value. The contour plot already takes into account the relationship between MSR and CSR. It can be specifically selected from different MSR (or LTR) contour plots, or simplified, it can just be a contour plot for a symmetric two-way loading (MSR = 0, LTR = 0). The excess pore pressure after N_{eq} cycles is estimated based on results of cyclic undrained or constant-volume tests and a superposition of normalized decay curves. Therefore, only the normalized excess pore pressure R_u is read for N = 1 and subjected to a flow-net calculation to derive element-specific dissipation curves. This step can be done with a finite element or a finite volume model; however it is also possible to perform a simplified dissipation analysis by solving a differential equation (see Chapter 4). As an alternative to the excess pore pressure field for N = 1, the field for N = N_{eq} could more intuitively be used as input for the dissipation analysis. For one storm load bin this may even be more accurate; however, if the procedure shall be used for many storm bins, the application of N = 1 is more advantageous. To keep the procedure consistent, the field for N = 1 is used here. However, there is only a small influence between both approaches (discussed in Section 7.2.3).

The derived excess pore pressure field for N = 1 is applied to the numerical model in order to simulate the consolidation process by means of a coupled pore fluid diffusion and stress analysis. The same mesh configuration is used for all calculations. The calculated excess pore pressure is entered as an initial condition in the numerical model, same as the geostatic stress tensor σ reduced by the excess pore pressure to keep equilibrium. The outcome of this analysis is a decay curve (excess pore pressure over time) for each integration point of the numerical model. After the calculation, the decay curve is normalized for each element. The dissipation phase aims to account for the consolidation that takes place during the storm event and adjacent load events. However, the volumetric strains in each integration point, which occur during this phase are not considered within the framework since they are only attributed to one cycle and possible ratcheting effects need to be considered, at most, in the superposition. To make this differentiation clearer, this phase will be mainly referred to as dissipation instead of consolidation. Besides the soil permeability, the storm load period is a governing parameter and is often assumed to be $T = 10\,\mathrm{s}$. This dissipation analysis is only done once and hence considers the three-dimensional drainage paths more realistically than an empirical estimation without the repetitive dissipation analysis during all cycles and the related computational effort. If needed, a repetitive dissipation analysis can be performed (see Section 7.2.3). Different methods can subsequently be used for the cyclic analytical superposition.

To estimate the influence of dissipation, the final excess pore pressure ratio in each element is then back-calculated to an equivalent number of cycles after dissipation $N_{eq,dissi}$ for a constant CSR value (Figure 6.4). The dissipation reduces the accumulated excess pore pressure ratio (from point B to point A) in many cases and leads to a stiffer soil response. This equivalent number of cycles after dissipation can be used to evaluate the shear strain contour plots to find a reduced stiffness modulus. This step is explained in Section 6.1.5.

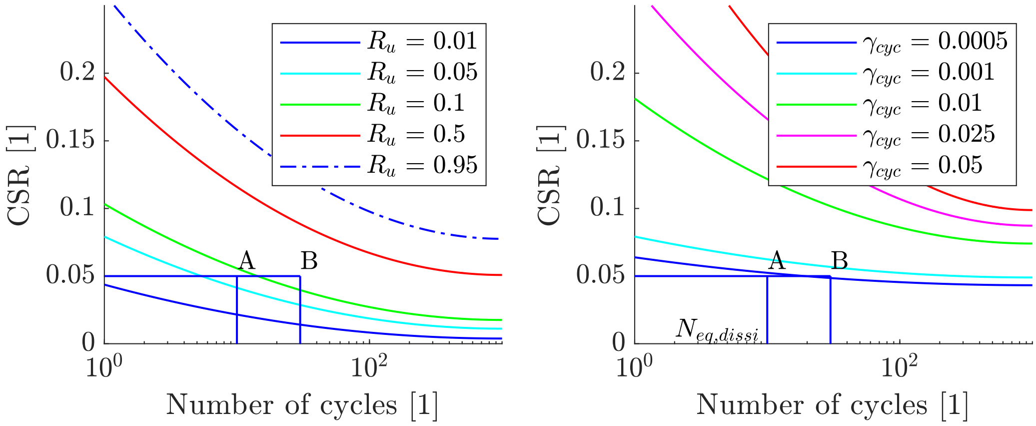

(a) (b)

Figure 6.4: Procedure to derive $N_{eq,dissi}$ in contour plots with excess pore pressure ratio (a) and shear strain (b) contour with point B at $N_{eq} = 30$ and point A for $N_{eq,dissi} < N_{eq}$ after dissipation.

Standard dissipation approach

The first way to deal with partially drained conditions is a conservative dissipation approach. It will always yield residual excess pore pressure and is hence useful for a conservative design of offshore structures. However, this shall not imply that other approaches cannot be used for a design verification, but more that this approach will always give a conservative value. This procedure will be used as a standard procedure by the author. In this approach, the normalized excess pore pressure for N = 1 is first determined and the dissipated value within the decay curve is used for a storm period of T = 10 s. The result is a percentage increase or decrease in excess pore pressure. Figure 6.5 shows the increase for one cycle and a decrease of 50%, which is assumed to be the normalized decay value after one cycle period. The curve is shifted to this point and another cycle is performed. The resulting excess pore pressure is again reduced by 50%. In this way, a smaller increase after each cycle is accounted for, but because of the fixed dissipation amount of, for instance 50%, the general response is increasing to a response in equilibrium.

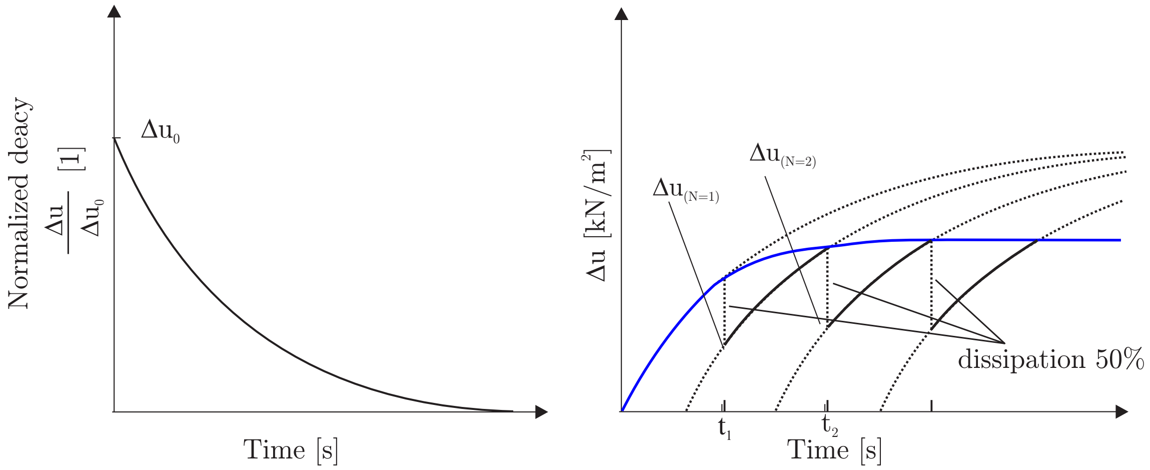

(a) (b)

Figure 6.5: Normalized decay curve (a) and analytical dissipation for partial drained conditions (b).

This procedure uses mainly the stiffness of the first part of the excess pore pressure accumulation curve and is based on the idea that the residual excess pore pressure after dissipation is back-calculated to a new number of equivalent cycles in the very curve. The excess pore pressure build-up starts from where it would be located in the excess pore pressure trend. To the equivalent number of cycles one new cycle is added. This method cannot reach a state in which the dissipation is larger than the generation. The excess pore pressure curve is solely displaced in x-direction for every added cycle. There is always a residual excess pore pressure, which makes the approach conservative.

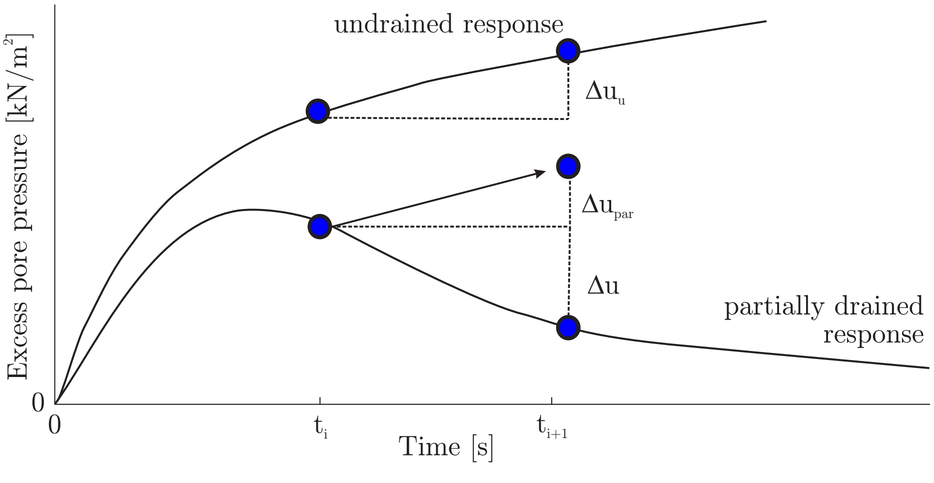

Figure 6.6: Procedure described by Hyodo et al. (1988, 1994).

Complex dissipation approach

Complex dissipation models where presented by e.g. Sakai et al. (2003) (also by Müthing et al. (2016), Davis and Raymond (1965)), but are just too complex to be used for each integration point and later on over a complete design storm. Figure 6.6 shows a procedure described by Hyodo et al. (1992) (Hyodo et al., 1988, 1994). A similar procedure was already used in Achmus et al. (2018). They assume that the increase Δu_p under partially drained conditions is equal to the increase under undrained conditions Δu_u. This is a model assumption since Δu_u is dependent on load history and dissipation behaviour. This compares well with the partially drained tests found in the literature. For results by Kluge (2007) and Ni et al. (2012), there is a softer excess pore pressure accumulation with a peak value in which the generation is larger than the dissipation and afterwards a region in which the dissipation is larger than the generation (after several cycles). This second method for analytical superposition takes the complex soil response into account and is seen as a more advanced dissipation approach. It will be referred to as the "complex dissipation approach" for clarification purposes, although it is difficult to judge if this model is superior.

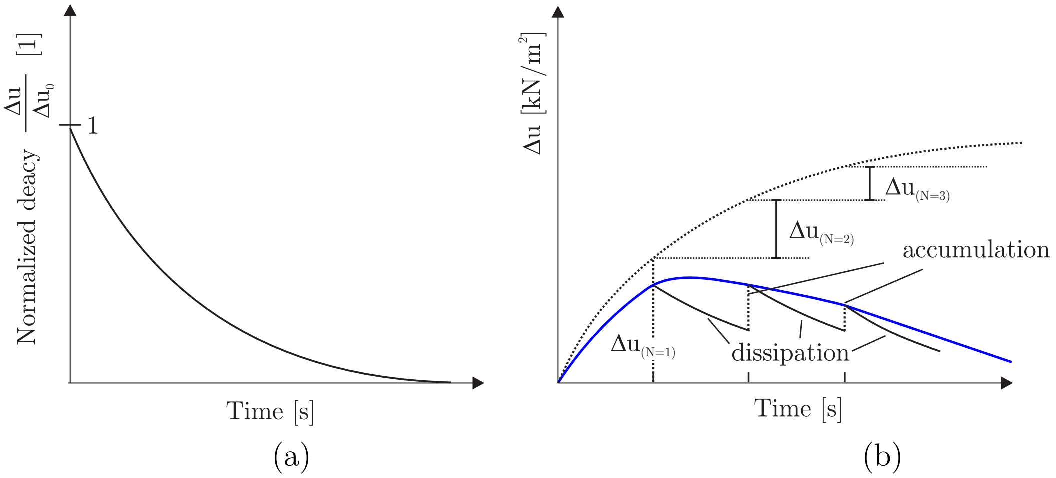

Figure 6.7: Normalized decay curve (a) and analytical dissipation superposition (b).

Figure 6.7 (b) shows a superposition for one integration point. The excess pore pressure after one cycle increases on the one hand with increasing number of cycles (based on DSS results), and, on the other hand, decreases due to the consolidation process. The normalized decay curves are placed with a certain time duration T (storm load period) to each other at which the pore pressure after N-cycles (excess pore pressure increment) is added to the remaining value from the previous load cycle. In the case depicted in Figure 6.7 (b), the overall excess pore pressure decreases with increasing number of cycles, because the increment in excess pore pressure decreases over the number of cycles. This is in contrast to the first presented procedure. This approach assumes a response after N cycles with a decreasing accumulation trend instead of the first procedure with a shifted stiff trend in the first cycles. The result of this procedure agrees better – compared to the first procedure – to results of partially drained triaxial tests. However, in combination with the presented numerical framework it will always tend to a state of zero excess pore pressure, because the interaction between dissipation and (partial) generation is neglected as a model assumption in order to facilitate its use. Furthermore, there is no real test data to validate this approach, although the trend of the curve agrees better with figures from the literature. For an academic back-calculation, not only the excess pore pressure trend for partially drained conditions, but also undrained contour plots are needed as an input for the analytical superposition. Since this approach may lead to a drastical underestimation of the accumulated excess pore pressure, it will not be used as a reference case, but may – after thorough analysis – be used in future.

The excess pore pressure starts to generate and dissipates so that there may be a state during the calculation which shows a larger excess pore pressure compared to the end of the storm. However, it should be taken care that not too much conservatism is used within this step, so the design is not made over-conservative and uneconomical. In all procedures, only the state at the end of the storm is considered and not any mid-states during the storm. For a more conservative approach, this last dissipation is not considered in design applications as a model assumption.

The two approaches lead to different asymptotic values after many cycles. The realistic soil response is hardly described with such a simple procedure and is probably in between both predicted soil responses. Under real conditions, the excess pore pressure build-up is affected by the stress history and additional dissipation effects such as change in fabric or the fact, that for a residual pore pressure an OCR value arises. Although it is possible to incorporate several of these effects, the computational effort is quite large and it will be difficult to handle for the calculation of a complete wind farm with a storm package of over 1000 entries.

Both analytical methods can be improved from a theoretical point of view by accounting a change in σ_{oct}, k_f, OCR or D_r over the cyclic loading. Due to stress history effects, this can be seen as some kind of pre-shearing. Furthermore, the initial σ_{oct} is reduced by the accumulated excess pore pressure Δu of the previous cycle and, thus, also an overconsolidation state arises. A soil with an OCR greater than 1 behaves softer up to the maximum consolidation stress (cf. Chapter 3). This is only the case if some excess pore pressure after a cycle is not completely dissipated and the total initial stress is therefore reduced for the next undrained cycle. For a changed OCR and σ_{oct} a different excess pore pressure behaviour of the number of cycles arises. A decreased stress σ_{oct} results in an increase of CSR. A faster failure occurs. To consider these effects, the trend of the excess pore pressure over the number of cycles needs to be known from cyclic laboratory tests. But as there are generally just enough laboratory tests to generate one specific contour plot, other influences such as D_r (change in fabric) and OCR can often not be separately considered.

Differentiation between stress states

The presented procedure bases mainly on results from cyclic constant-volume direct simple shear tests. However, the shearing stress state is only one of many different possible stress states within the soil and around loaded foundations. The exact stress state can be described by using true triaxial tests or hollow cylinder apparatus test results. The results of these tests and different stress paths can be used within the stress path philosophy (Lambe, 1967; Bjerrum, 1973; Høeg, 1978), since the general soil behaviour for different laboratory tests is different (Zdravkovic et al., 1997; Zdravkovic and Jardine, 2001).

For simplicity reasons and to be able to execute the tests in a practical project, an interpolation between direct simple shear and triaxial stress states is assumed to be accurate enough. By using cyclic triaxial tests it is possible to also consider compression and extension stress states. The exact cyclic response can be derived based on contour plots from these cyclic triaxial tests (Section 5.3.2). By using results from triaxial and direct simple shear tests, the cyclic soil response for each integration point is linearly interpolated between both stress states with the Lode angle (Griffiths, 1990; Lode, 1926). For a general stress state, the Lode angle is derived with normalized third stress invariant according to Equation 6.9 (Han and Chen, 1985). It is calculated by using the second and third invariant of the deviatoric stress tensor (Equation 6.10, Equation 6.11). A similar assessment can be made with Equation 3.9 (right).

$$\Theta = \frac{1}{3} * acos\left(\frac{3\sqrt{3} * J_3}{2 * J_2^{1.5}}\right) \qquad (0° \leq \Theta \leq 60°) \tag{6.9}$$

$$J_2 = \frac{1}{6}[(\sigma'_I - \sigma'_{II})^2 + (\sigma'_{II} - \sigma'_{III})^2 + (\sigma'_{III} - \sigma'_I)^2] \tag{6.10}$$

$$J_3 = (\sigma'_I - \sigma'_{oct})(\sigma'_{II} - \sigma'_{oct})(\sigma'_{III} - \sigma'_{oct}) \tag{6.11}$$

For $\Theta = 0°$ the stress state is in triaxial extension, because $\sigma'_1 = \sigma'_2$ and for $\Theta = 60°$ in triaxial compression with $\sigma'_2 = \sigma'_3$. The direct shear state is reached for $\Theta = 30°$.

$$R_u = \begin{cases} R_{u,\Theta=0} - \dfrac{R_{u,\Theta=0} - R_{u,\Theta=30}}{30°}\,\Theta, & \text{if } \Theta < 30°. \\ R_{u,\Theta=30} - \dfrac{R_{u,\Theta=30} - R_{u,\Theta=60}}{30°}\,(\Theta - 30), & \text{otherwise.} \end{cases} \tag{6.12}$$

6.1.4 Step 4: Post-cyclic calculation

The residual excess pore pressure after the storm event is used to analyse the post-cyclic foundation response. Because of the excess pore pressure the octahedral stress is reduced and, hence, smaller shear stresses can be beared until failure occurs. In a new post-cyclic finite element model the reduced octahedral stresses cannot directly be changed. However, the shear stress at failure can be reduced by using a reduced equivalent angle of internal friction since mainly the reduced bearing behaviour (ULS) is of interest. The calculated excess pore pressures for each integration point are used to derive an equivalent angle of internal friction (Equation 6.13). By applying these friction angles to the related element in the finite element model the shear strength is reduced and the post-cyclic pile capacity can be determined. Besides the angle of friction, the soil-pile friction coefficient is also adjusted accordingly as here the normal stress is decreased by the portion of the excess pore pressure.

$$\varphi'_{red} = atan((1 - R_u)tan(\varphi')) \tag{6.13}$$

The reduced friction angle is entered into the post-cyclic FE model as a field for every integration point and the maximum global load is applied. Changes in soil and foundation stiffness are mainly due to rearrangement and plastic behaviour, but not primarily due to a reduced stiffness. The reduced capacity of the foundation can then be read for instance at a displacement of 0.1D or by using a different criterion. The estimation of the ultimate capacity of laterally loaded monopiles is not trivial. One way is to derive and to integrate the ultimate bedding resistance. However, this is numerically not straight forward and especially for the inhomogeneous post-cyclic degraded soil field not well suited. The lateral capacity can also be estimated with methods of McNulty (1956), Pyke (1984) or Manoliu et al. (1985). Manoliu et al. (1985) state that the lateral bearing capacity can be estimated by using a regression on the initial stiffness (Figure 6.8). The last criterion is exemplary used in the next chapter, but since only a comparison between different approaches is done in Chapter 7, the 0.1D criterion is used in most cases.

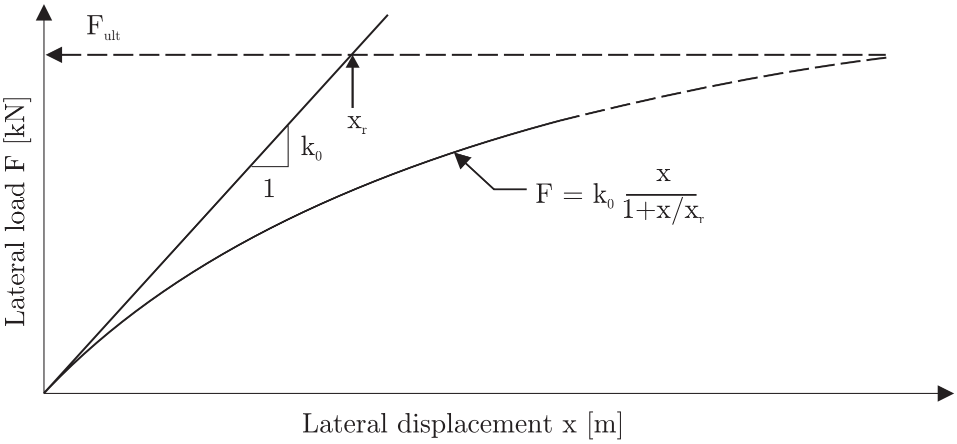

Figure 6.8: Estimation of lateral capacity according to Manoliu et al. (1985).

6.1.5 Optional step: Reduction of stiffness and consideration of cyclic shear strain

In the presented form, no stiffness degradation takes place in model even if this can clearly be seen within the laboratory tests. A reduced oedometric stiffness cannot directly be derived from the excess pore pressure accumulation. A simple procedure for linking oedometric stiffness to normalized excess pore pressure can be used according to Martin (1975). The stiffness modulus is reduced based on the excess pore pressure ratio depending on the relative density and compressibility. However, this approach is only a very rough estimation without considering site-specific soil condition. A more accurate estimation can be used by evaluating the cyclic DSS tests in terms of shear strain. Therefore, the shear strain contour plot results from the cyclic laboratory tests are used within the numerical calculation. With the derived $N_{eq,dissi}$, a calculated load path is used within the associated contour plot by using the quotient of the CSR and MSR. The contour plot summarizes the soil response after N cycles that has acted on the specimen with different combination of the shear components. In a next step, a shear stress - shear strain curve

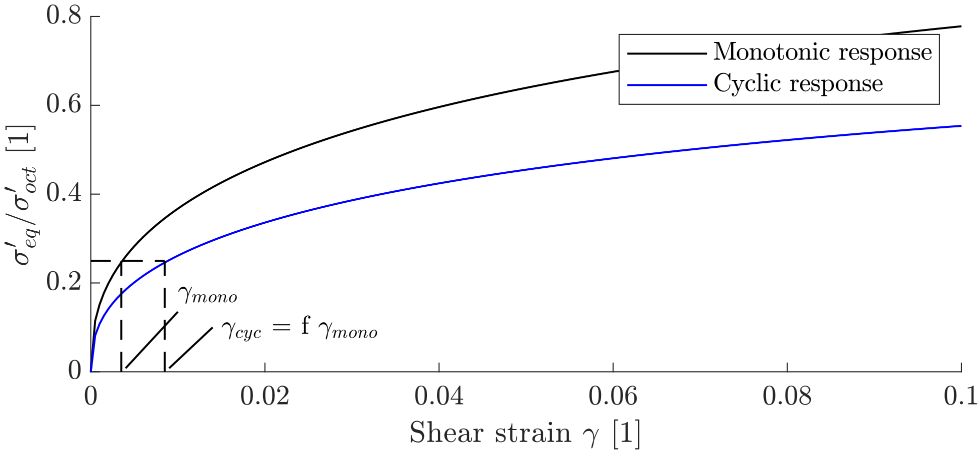

Figure 6.9: Shear stress - shear strain response under monotonic and cyclic conditions with shear strain levels at specific shear stress from finite element model integration point.

can be derived and γ_{cyc} is plotted over τ_{cyc} and γ_{mean} over τ_{mean}. A schematic element response, as well as the decreased stiffness, is depicted in Figure 6.9. The result can be read from the isocurves and the intersection with the inclined load path. The curve gets softer with increasing number of equivalent cycles compared to the monotonic response. A decreased shear modulus derived from the cyclic test results is considered instead of only using a reduced angle of internal friction field. The stiffness modulus is calculated accordingly with the Poisson's ratio.

The stress - strain relation from Figure 6.9 can be considered in two ways. A first way is to use element-specific strain-dependent hardening (Figure 6.10). The strain hardening is done in a three-dimensional state by using an equivalent shear strain (x-axis) and a friction angle interpreted from the normalized shear term (y-axis). This curve is then transferred to a finite element model and the post-cyclic structural response is calculated. Figure 6.10 shows an exemplary stress path for a specific number of cycles. The derived stress path is evaluated by reading the intersecting points with the contour isocurves. A similar approach is done by Jostad and Andresen (2009). For better convergence, the results in terms of shear stress - shear strain relationships of the contour plot are fitted with a hardening curve (Vermeer and De Borst, 1984) (Figure 6.10). By doing so, severe changes in the slope for the given discrete shear strains are avoided. No additional dilatancy is considered for the partial drained response. Dilatancy can lead to generation of negative excess pore pressure and, hence, increase the capacity of the overall structure for very dense sandy soils. Neglect of this effect makes this approach conservative.

$$sin(\varphi^*) = 2\frac{\sqrt{\gamma\gamma^f}}{\gamma+\gamma^f} \quad sin(\varphi^*) = sin(\varphi) \quad for \quad \gamma > \gamma^f \tag{6.14}$$

In Equation 6.14, φ^* is the mobilised friction angle, γ^f is the shear strain at failure and γ is the shear strain. The stress - strain relationship is implemented in ABAQUS in a

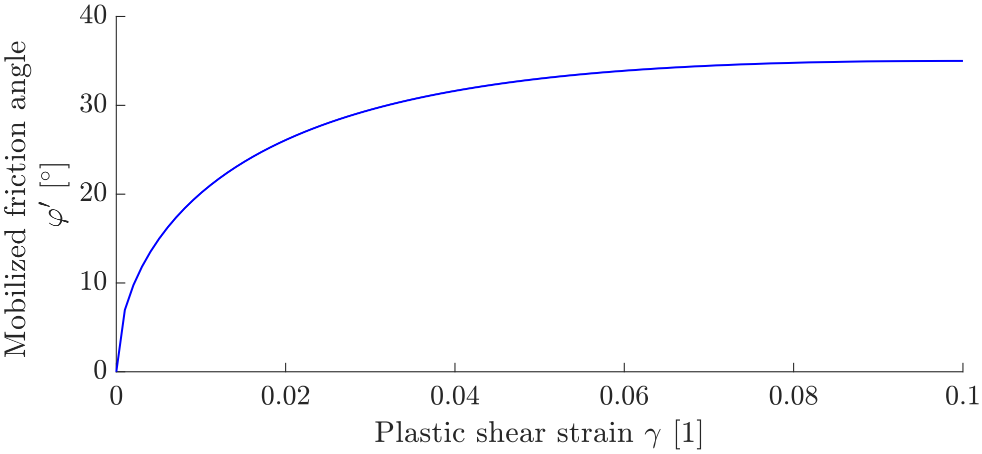

Figure 6.10: Mobilisation of friction angle over plastic shear strain.

subroutine. The initial angle of friction is derived based on the Mohr-Coulomb failure criterion (Equation 6.15).

$$q = p' \frac{6sin(\varphi)}{3 - sin(\varphi)} + c' \frac{6cos(\varphi)}{3 - sin(\varphi)} \tag{6.15}$$

The stress - strain curve from the contour plot is thus understood as a mobilization of the internal friction angle up to the maximum value. The assumption is that the load paths are representative without larger stress redistributions. Thus, the stiffness modulus to be entered becomes relevant only for the initial stiffness and should optimally coincide with the initial stiffness of the curve to be used anyway. This can also be the measured or derived representative G_0. This value is only measured at small shear strains and is especially representative in the far field. The mobilisation of the friction angle occurs over an equivalent shear strain γ_{eq}. Therefore, the three-dimensional shear strain condition needs to be transferred to an equivalent value.

There are different methods to calculate an equivalent shear strain (Wegener and Herle, 2012; Andersen, 2015). Herein, this value is derived with Equation 6.16 which bases on the second deviatoric strain invariant. The chosen equation influences the stiffness of the system and, thus, after which shear strain full mobilisation is already exceeded.

$$\gamma_{eq} = 1.5\sqrt{\frac{2}{9}[(\varepsilon_{xx} - \varepsilon_{yy})^2 + (\varepsilon_{yy} - \varepsilon_{zz})^2 + (\varepsilon_{zz} - \varepsilon_{xx})^2] + \frac{1}{3}[\gamma_{xy}^2 + \gamma_{yz}^2 + \gamma_{xz}^2]} \tag{6.16}$$

It is important to also convert shear strain γ from the cyclic laboratory tests to γ_{eq}. Andersen (2015) uses the shear strain from the cyclic laboratory tests without transferring them to an equivalent shear strain. The model assumption is that the shear strain from the cyclic tests is directly comparable to an equivalent shear strain from finite element models. However, this idea is not followed herein and all tests and results are transferred to the same equivalent value.

The path for shear stress - shear strain cannot be derived based on CSR and MSR. Instead of using a hardening law, the shear modulus can simply be reduced by a cyclic factor. In this way, a simple standard Mohr-Coulomb model can also be used. Of course, this method is only an alternative, which is less accurate, because it evaluates the stress - strain curve at one location (Figure 6.9). Nevertheless, the advantages is the direct use of the simple Mohr-Coulomb soil model. The factor f = $\gamma_{cyc}/\gamma_{mono}$ is obtained by plotting the stress - strain curve for monotonic response and $N = N_{eq,dissi}$. The factor $\gamma_{cyc}/\gamma_{mono}$ should always be less than one. Care should be taken with large CSR values for which the cyclic behaviour is not defined.

6.1.6 Simplified flow chart

The flow chart in Figure 6.11 summarizes the last section very simplified. This procedure is often referred to as the reference procedure in the following. The explanations to each sub-figure are given as follows:

(a) First the equivalent number of cycles needs to be derived.

(b) The mean global load of the related one storm bin is applied in a drained manner and the stresses and strains are read by a Python script.

(c) The global load amplitude of the related one storm bin is applied in a drained manner and the stresses and strains are read by a Python script.

(d) The stresses are transferred to equivalent stresses from which subsequently the CSR and MSR (LTR) are calculated.

(e) The excess pore pressure ratio R_u (and the excess pore pressure) are derived for each integration point for N = 1 based on a pre-specified contour plot. However, this step can also be performed by evaluating cyclic displacement-controlled test results.

(f) The excess pore pressure field for N = 1 is read into a coupled ABAQUS model and the field is dissipated over several seconds (more than the storm period T).

(g) The results is a decay curve for each integration point, which is normalized in order to be used in the analytical superposition.

(h) With the normalized decay curve a superposition is carried out in each integration point. Different procedures may be used herein, but as a reference the conservative design method is used. A primarily accumulation or dissipation may occur.

(i) An equivalent number of cycles after dissipation can be derived from the residual excess pore pressure (after dissipation) with the integration-point specific R_u - N curve.

(j) This figure shows a different presentation of sub-figure (i)in CSR-N space with the corresponding excess pore pressure isocurves.

(k) The excess pore pressure ratio after dissipation as well as the related number of equivalent cycles after dissipation are now known. These can now be used in order to derive the stress - strain relation. With the number of cycles after dissipation, the stress - strain relation may be derived. Therefore a type 2 contour can be used and a path with the related LTR drawn into the contour plot. The shear strain and stress components are added into order to have the maximum load and deformation from the cyclic element tests.

(l) Instead of a type 2, also a type 3 contour may be used and is evaluated at the point of $N_{eq,dissi}$.

(m) The degraded angle of internal friction can be derived based on the residual excess pore pressure ratio.

(n) The stress - strain curve can be implemented by hardening for each integration point or the stiffness modulus is decreased by a factor between monotonic and cyclic shear strain evaluated for the integration-point specific CSR value.

(o) With the degraded input fields, the post-cyclic soil-structure interaction can be assessed.

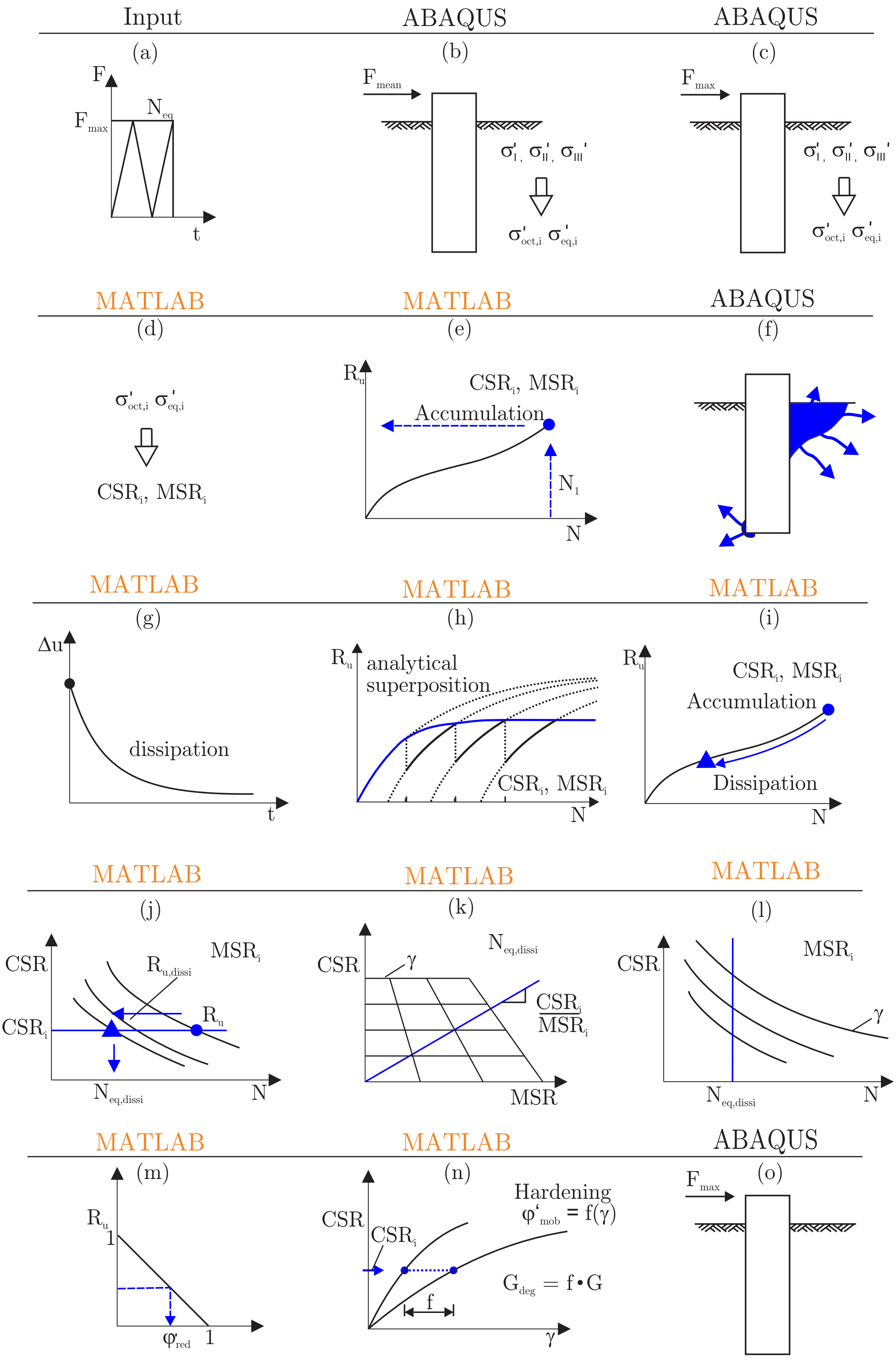

Figure 6.11: Flow chart for EPPE - contour approach.

6.2 Back-calculation with results from field and 1g medium-scale tests

The most important step when dealing with numerical methods is to validate their predictive accuracy. Investigations for validation purposes can be done in 1-g small- or large-scale tests, in centrifuges or with prototype dimension. If a distinction is made between long-term (drained) and short-term (partially drained) tests for cohesionless soils, more results can be obtained with cyclic drained tests than for partially drained conditions (McAdam et al., 2020; Hettler, 1981; Long and Vanneste, 1994). For undrained or partially drained conditions, more tests are performed for clay than for sandy material. Large-scale laboratory tests are more suitable than field tests, because of the controllable boundary conditions, but such tests are very rare. Few data are available for tests that focus on the accumulation of excess pore pressure. The following few test results show that excess pore pressure can occur even in small scale tests such as monopiles with low-frequency loading and small drainage paths. It is difficult to find excess pore pressure measurements on monopile foundations in sand. The soil preparation and sensor placement need to be done with high accuracy and caution in order not to create artificial drainage path or influence the bedding reaction. Furthermore, several pressure sensors are needed to get insight into the subsoil. The smaller the scale, the larger the boundary effects and influences of small drainage paths. Because for the model tests no contour plots are present, the excess pore pressure accumulation is estimated based on the number of cycles to liquefaction. A flow chart is given in Appendix F.1.

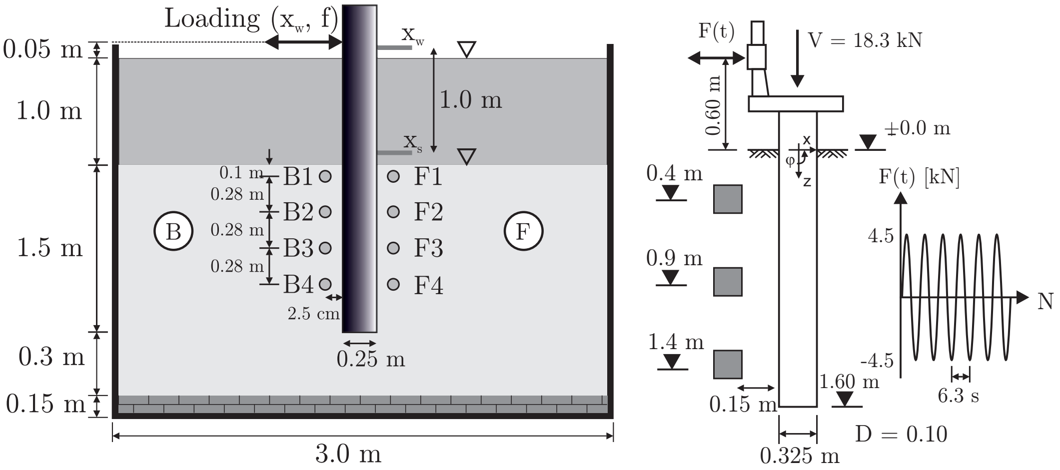

Figure 6.12: Model test performed by Kluge (2007) (a) and model test performed by (Taşan, 2011) (b).

6.2.1 Kluge (2007)

Kluge (2007) (cf. Stahlmann et al. (2007)) performed 1g small-scale laboratory tests for a cyclic displacement-controlled monopile foundation (Figure 6.12 (a)). A focus was set on the development of excess pore pressure over the number of cycles at different locations within the test pit for different loading conditions. One test was performed with a frequency of f = 2 Hz and a displacement amplitude of $x_w = 1\,\text{cm}$ (0.04D) and another test with f = 1 Hz and $x_w = 0.75\,\text{cm}$. The 3 m square test pit has a depth of 2 m. The soil depth within the pit was 1.45 m and the bedding material was a fine sand (grain diameters between 0.063 mm and 0.2 mm with a uniformity index of $C_U = 1.8$). The soil was fully saturated and in a medium dense state ($D_r \approx 0.55$).

The back-calculation was done with the EPPE approach by using results from displacement-controlled tests in combination with a three-dimensional ABAQUS model. Therefore, several displacement-controlled cyclic direct simple shear tests were performed by the author on the used sand in the model tests and a regression was applied. The tested soil used by Kluge (2007) shows a different grain size distribution to the reference sand but a similar soil response. The results of this soil and of the reference soil agree well and since there are more cyclic test results present for the reference soil, the S30T results were used within the calculation. The regression of the S30T is presented in Appendix E. However, the investigated vertical stress bandwidth was not in the region of 5 - 20 kPa but larger than 50 kPa. Additional parameters can be found in Kluge (2007).

Some issues were encountered in the course of back-calculation. Only the trend of the excess pore pressure for several locations are published, but no monotonic or cyclic load-displacement curves. There is a high liquefaction level around the monopile foundation in the 1g tests. The data show liquefaction at the point of rotation in which almost no deformation occurs. A gap could have developed which complicated a back-calculation. Furthermore, the sensors have been put very close to the pile with thick sensor holders. An additional flow along these cannot be ruled out. Lastly, the equation used for the equation approach was initially not meant to be applied for such small vertical stresses. Kluge (2007) could only back-calculate the results by using fully undrained conditions for the first cycles and then assumed fully drained conditions after the peak value. Hence, the soil stiffness and permeability of the soil was adjusted in the finite element back-calculation in order to at least qualitatively be able to perform a back-calculation. Figure 6.13 (a) shows the results of the excess pore pressure trend over the applied number of cycles for three different locations. Only the complex dissipation approach was used herein. The permeability was reduced to $1 \times 10^{-6}\,\text{m/s}$ in order to calculate accumulations. The back-calculation does underestimate the excess pore pressure peak and shows a stiffer response. The results agree not very well, but the trend of the excess pore pressure curve and the realisation of a peak value with a decreasing incremental accumulation can be simulated.

6.2.2 Taşan (2011)

Taşan (2011) performed 1g small-scale tests similar to the ones published by Kluge (2007). The tests were load-controlled on a monopile foundation with different dimension and different load conditions. Taşan performed tests with the same load amplitude but also multi-step tests with different load bins. However, the absolute load level was quite high. In the following, only the regular harmonic loads shall be evaluated (D = 0.325 m, L = 1.6 m, $F_{cyc} = 4.5\,\text{kN}$, e = 0.6 m, f = 0.16 Hz) (Figure 6.12 (b)). The cyclic soil

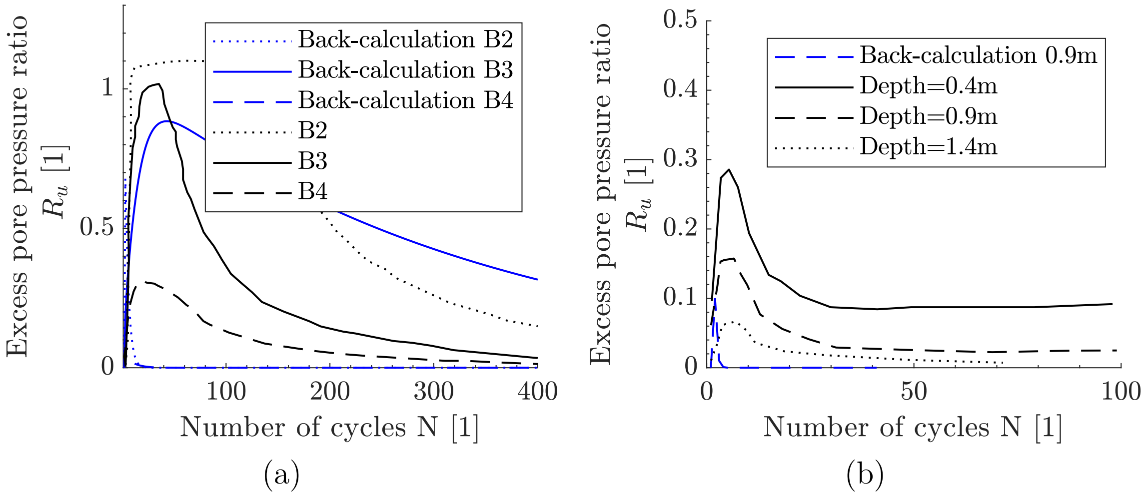

Figure 6.13: Measured mean excess pore pressure by Kluge (2007) (a) for the position depicted in Figure 6.12 (a) and measured excess pore pressure results from Taşan (2011) at three depths with positions depicted in Figure 6.12 (b) with respective back-calculation (b).

properties can be found in Glasenapp (2016) for a sand similar to the used "Berliner Sand". The stated relative density is 0.1. However, the author did not explain how he ensured the consistency of such a small relative density profile in the 1g model tests. The stiffness modulus is derived based on triaxial tests and also the angle of internal friction are published but only for a relative density of 0.7 and not for 0.1. The soil properties are hence assumed. A high accuracy in the back-calculations can not be expected.

In order to evaluate the system response, first the monotonic response was estimated. The load from the model test could not be applied for small angles of friction in a p-y model to estimate the monotonic response. Only when dense conditions are assumed, there is enough bedding reaction present to even bear the load under monotonic conditions. For $\varphi = 30°$ the capacity at 0.1D is 6.2 kN; the acting two-way load is 4.5 kN. Although it is known that for small stresses larger friction angles arise, the angle of friction is larger than expected for the stated relative density to be doubted.

Several excess pore pressure sensors show the evaluation of excess pore pressure over the number of cycles. Figure 6.13 (b) shows the results from the numerical back-calculation with blue lines. The overall trend does qualitatively agree, but the absolute value of excess pore pressure is underestimated. The large dissipation leads to the depicted result which does not agree with the measured values. However, the trend of the number of cycles agrees qualitatively with the published data and also the excess pore pressure accumulation in different locations seem to be reasonable.

It was possible to consider the $CSR-N_{liq}$ curve as well as displacement-controlled conditions into the reference EPPE approach by exchanging some steps of the modulus framework. Although a direct validation was not possible, it seems to be very promising – especially if new high-quality data regarding partially drained conditions around offshore foundations are present.

6.2.3 Ekofisk oil storage tank (Clausen et al., 1975)

Up to now, only regular harmonic loads have been investigated. One of the most famous field tests dealing with liquefaction is the Ekofisk test firstly reported by Clausen et al. (1975). The Ekofisk gravity base foundation located in the North Sea is often used for validation and benchmark purposes because it was one of the first offshore foundations with which accumulation of excess pore pressure and deformation was investigated and studied. The foundation was installed in 1973 and has a diameter of 93 m and is 90 m tall. The cylindrical structure has a permanent vertical force from a dead weight of 1900 MN and an area of 7400 m^2 with a load eccentricity of 36 m (Eide et al., 1981). This results to roughly 280 kPa bedding stress. The water depth is 70 m. Skirts against erosion and piping were attached but will not be modelled.

Soil data and loading conditions

The soil is layered with a 16 m sand layer and a 2 m thin clay layer with low plasticity. Below the clay layer there is fine sand present again. For the design, a 26 m thick very dense sand layer with subsequent stiff clay is assumed (Eide et al., 1981). The relative density is 100% (Lee and Focht Jr., 1975). The angle of internal friction is reported to be 42.5° with an assumed dilatancy angle of zero (Bjerrum, 1973). The permeability is assumed to be 1×10^{-5} m/s with an oedometric stiffness of 48 MPa. Cyclic triaxial tests in the form of $CSR - N_{liq}$ are reported by Lee and Focht Jr. (1975) for a relative density of 100%. A value of $\alpha = 0.7$ was chosen for the Seed and Booker (1976) equation. The design storm load consists of several load parcels with different load magnitudes (Table 6.1) (Lee and Focht Jr., 1975). The 100-year storm has a wave height of 23.8 m. The transition from hydrodynamic (wave height) to lateral load can be found in Taiebat (1999) (Rahman et al., 1977).

Literature review

Several back-calculations have already been done. Measurement results have been presented by Clausen et al. (1975) and Bjerrum (1973). The first explicit back-calculation was done by Rahman et al. (1977).

Rahman et al. (1977) considered stress redistribution with an explicit approach. They used the vertical stress for normalisation of the excess pore pressure for R_u. The soil response was based on DSS test results with pre-shearing. Hence, the soil resistance can be assumed to be slightly increased due to pre-shearing. Rahman et al. (1977) calculated with an axisymmetric model and with D_r of 77% and 85%. They defined the CSR as τ/σ'_v and used an equivalent design storm according to Seed and Rahman (1978).
Verruijt and Song (1991) calculated in a plane strain manner with $D_r = 100\%$. They used u_{max} for the definition of the normalized excess pore pressure R_u.
Taiebat (1999) compared different modelling techniques with different normalisations and calculates larger R_u values over time compared to Rahman et al. (1977). A slightly different approach was published by Taiebat and Carter (2000).

When comparing these different approaches, Rahman et al. (1977) reports a normalized excess pore pressure at the off-edge of 32% and at the centre of 16%. Verruijt and Song

Table 6.1: 15-bin design storm with lateral load F (Taiebat and Carter, 2000).

Bin [1]	Cycles N [1]	Period T [s]	Wave height [m]	F [kN]
1	236	5	0.5	3724
2	235	7.2	2	11134
3	243	10	6	99273
4	235	11.5	10	232832
5	141	12.5	14	384201
6	61	13.2	18	537584
7	16	13.4	22	678262
8	3	13.5	25	777527
9	16	13.4	22	678262
10	61	13.2	18	537584
11	141	12.5	14	384201
12	235	11.5	10	232832
13	243	10	6	99273
14	235	7.2	2	11134
15	236	5	0.5	3724

(1991) calculated off-edge 15 kPa and at the centre 26.5 kPa. Not all authors present the normalized excess pore pressure as well the excess pore pressure value, which makes comparison more difficult. The different results can mainly be explained by different soil data, modelling techniques and other definitions of normalized excess pore pressure. However, the measurement system was not working during the storm in 1973 and, hence, only theoretical back-calculations can be compared.

Finite element model

An ABAQUS model with a Mohr-Coulomb failure criterion was used for the soil. The rigid gravity base foundation was modelled with a linear-elastic material law. The finite element model is a 3D model with C3D8 elements. The clay is modelled with similar cyclic soil properties but lower permeability. The dimensions of the model are chosen in order to minimize boundary effects. Drainage for the flow net calculation was allowed at the top and at side-edges of the model. No contact interface was used.

Back-calculation of Ekofisk tank

The Ekofisk tank back-calculation can be considered the most important back-calculation as it deals with sand layers. However, the contour approach cannot be used as the corresponding contour plots are not present. There are different ways to back-calculate this field test. Two different modelling ways were used in order to back-calculate the Ekofisk tank. Additionally to the reference procedure with a single dissipation calculation, the excess pore pressure was dissipated sequentially for each different storm bin. The stresses however, which are used to calculated the CSR, are assumed to be constant throughout the calculation. A sequential analysis considering stress redistributions can be incorporated, but it comes with larger computational times. Hence, the stresses were estimated based on one calculation and the dissipation was done sequentially.

The design storm consists of different bins with same wave height. According to the presented EPPE method, the calculation is first done for undrained modelling conditions and then dissipation to account for partially drained conditions is considered. The single dissipation model uses a flow net calculation for the maximum storm load and the standard dissipation approach for the analytical superposition. The CSR values for each storm bin were estimated based on a single monotonic calculation, from which the respective shear stress amplitudes were derived. In case of the sequential dissipation analysis, the same CSR values for each integration point and storm parcel were used, but the excess pore pressure was calculated for each parcel separately and then dissipated. The resulting dissipated excess pore pressure field was used in order to derive a new equivalent number of cycles on which the number of cycles of the next storm parcel was added. This N_{eq} was used to calculate the subsequent excess pore pressure field.

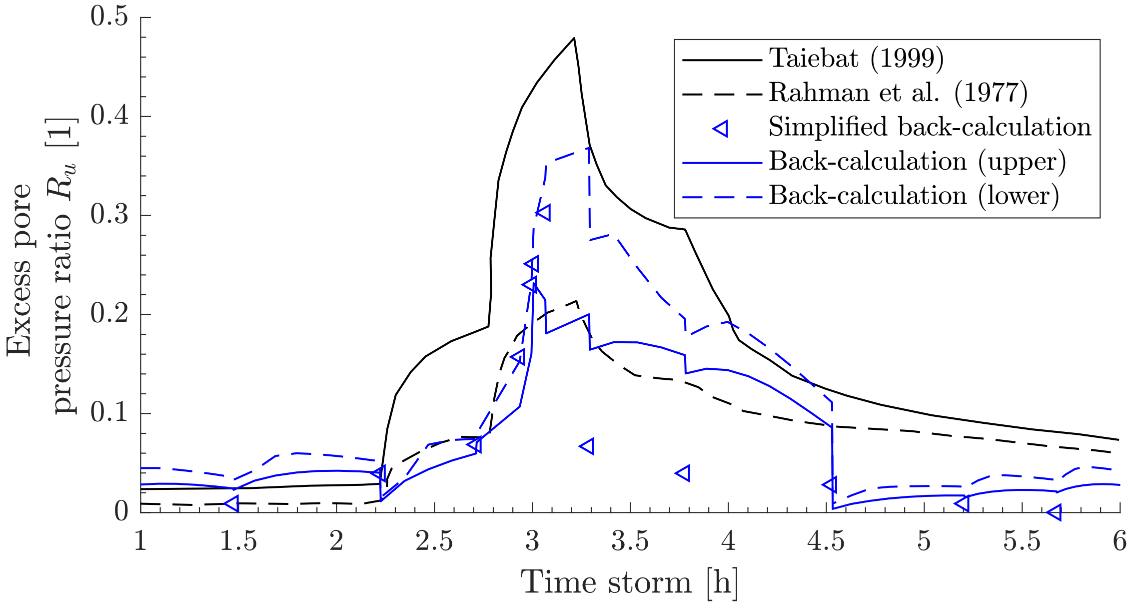

Figure 6.14: Comparison of simplified and sequential EPPE calculation with data according to Rahman et al. (1977) and Taiebat (1999) for the location at the edge of the gravity base foundation in form of normalized excess pore pressure ratio.

Figure 6.14 shows the results at the edge of the structure for the EPPE equation approach with a single dissipation and a sequential dissipation with the results according to Rahman et al. (1977) in dashed-black and Taiebat (1999) with a solid black line. The maximum excess pore pressure of 40 kPa is reached after 3 hours in all cases. The first load parcels only generate a small amount of excess pore pressure. The solid blue line shows the upper excess pore pressure which is subsequently reduced due to dissipation (dashed blue line). The real result may be in between. The simplified calculation with only one single dissipation run (reference procedure) shows a slightly larger peak value but a faster decline in excess pore pressure after the peak value is reached. The results according to Rahman et al. (1977) were transferred to the normalisation with the octahedral stress. Figure 6.15 shows the excess pore pressure without normalisation similar to Figure 6.14. The solid line in Figure 6.14 represents the excess pore pressure prior to and the dashed line after dissipation took place.

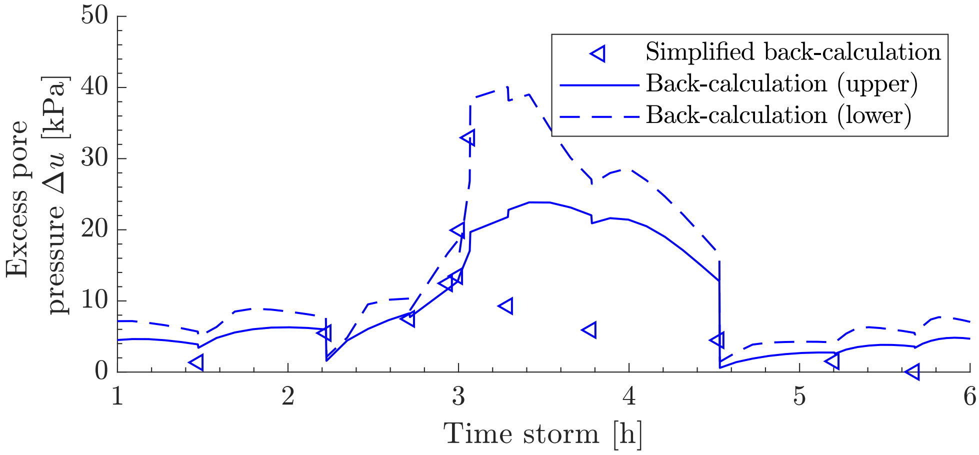

Figure 6.15: Comparison of simplified and sequential EPPE calculation for the location at the edge of the gravity base foundation in form of excess pore pressure.

The back-calculation shows a good agreement with data published by Rahman et al. (1977). It is by far not a complete validation but it shows the effect of excess pore pressure accumulation as well as that the effect can be well estimated with the presented EPPE approach.

6.2.4 Conclusion

Currently, an extensive validation of the EPPE approach is not fully possible. The tests on monopiles have some drawbacks, and the field tests like the Ekofisk tank are not well documented and can only be partially verified. This is mainly because the sensors did not measure during the storm. However, in the presented assessment a first comprehensive comparison of tests and prediction has been shown. Further work regarding a thorough validation is needed.

7 Application of estimation methods on monopile foundations

The developed excess pore pressure estimation concept has been presented in Chapter 6. The general soil response was evaluated for a reference soil from high-quality laboratory results (Chapter 5). Regression analyses have been performed on the results of the cyclic element tests and furthermore contour plots were derived.

In the following, different variations are applied to the developed reference estimation procedure and the influence on the overall bearing behaviour of different modifications to the design process will be shown. A reference monopile will be used with a diameter of D = 9 m and an embedded length of L = 27 m with a load eccentricity of e = 40 m. The wall thickness is assumed to be constant with t = 100 mm. An equivalent number of cycles was set to $N_{eq} = 30$ for all calculations. The sand has a permeability of $k_f = 3.7 \times 10^{-4}$ m/s for a relative density of $D_r = 0.85$. The storm period is assumed to be T = 10 s. The ultimate monotonic bearing capacity was derived from monotonic p-y springs with the approach according to Thieken (2015) ($F_{ult} = 68$ MN from Figure 7.1). The ULS load is assumed to be in the range of 30% of the bearing load. For the cyclic part, the ULS load (or the maximum load from the design storm) is usually applied only a few times. In order to have a larger number of equivalent cycles and to be able to show its influence, the cyclic load was chosen to be roughly 20% of the bearing load with 30 cycles. This is by no means an estimation of structural loads, but more a derivation of a reasonable load level to investigate the structural response and influencing parameters. For comparison, the load at a deformation criterion of 0.1D is 37.4 MN. The monotonic load-displacement curve from the numerical calculation is also depicted in Figure 7.1 and leads to a similar bearing capacity for the 0.1D criterion (Figure 7.1). The monopile is investigated under a symmetric one-way load with a maximum load of 13.6 MN ($F_{min} = 0$ MN, $F_{max} = 13.6$ MN) (i.e. the corresponding maximum moment with respect to soil surface oscillates between $M_{min} = 0$ MNm and $M_{max} = 544$ MNm). Hence, the cyclic values are $\zeta_c = 0$ and $\zeta_b = 0.20$ (or $\zeta_b = 0.367$, depending on the used criterion for the definition of ultimate bearing capacity).

7.1 Numerical model for the reference system

The described analysis was carried out in the finite element program ABAQUS. The three-dimensional numerical model of a monopile consists of approximately 30,000 C3D8(P) elements. Based on the symmetry only one half is modelled to reduce the computational

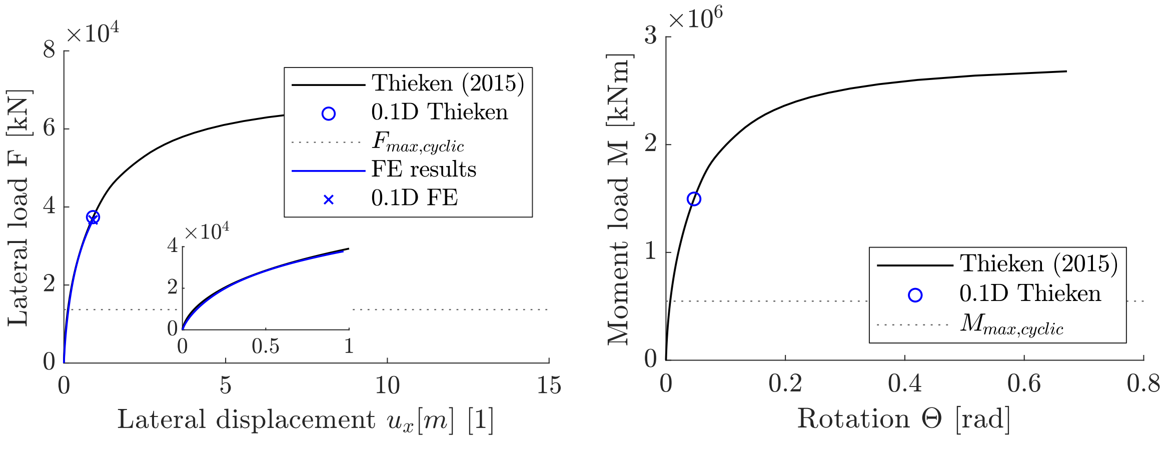

(a) (b)

Figure 7.1: Load-displacement curve (a) and moment-rotation curve (b) for the reference monopile from analytical calculation with results from finite element model.

effort (Figure 7.2). In the preliminary analyses the mesh resolution and the model dimension have been optimized to reach an appropriate balance of computational effort and sufficiently accurate results. The evaluation was done with MATLAB (MathWorks, 2021).

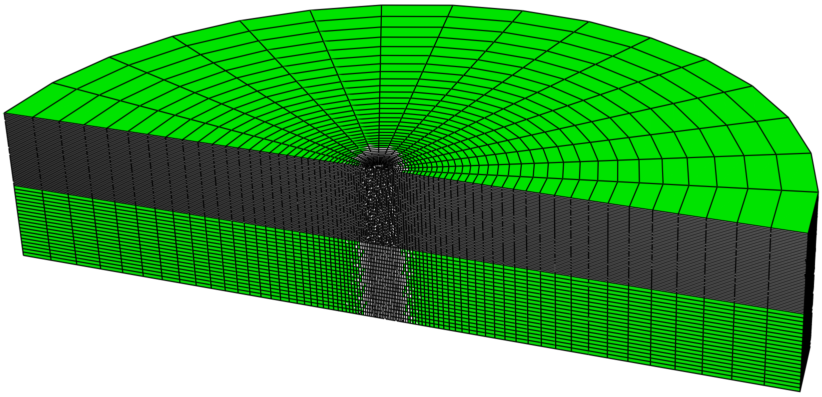

Figure 7.2: Numerical model of the reference system in the finite element software ABAQUS.

The final model has a width of 12-times the diameter and a depth of 1.5-times the pile length. The model is fixed in all degrees of freedom at the bottom, in normal direction at the periphery and in y-direction at the symmetry plane. The monopile is modelled with a linear-elastic behaviour with a Young's modulus $E = 2.1 \times 10^8\,\mathrm{kN/m^2}$, a Poisson's ratio $\nu = 0.27$ and a buoyant steel unit weight $\gamma'_{steel} = 68\,\mathrm{kN/m^3}$. The load is applied on a reference point which is connected to the monopile with a coupling constraint.

The soil parameters are shown in Table 7.1. The initial horizontal earth pressure at rest was calculated according to $k_0 = 1 - sin(\varphi')$ (Jaky, 1944) and the angle of dilatancy with $\psi = \varphi' - 30$ (non-associated flow rule). Regarding the plasticity of the soil, an elasto-plastic material law with Mohr-Coulomb failure criterion and stress-dependent stiffness was used. The linear-elastic, ideal-plastic model with stress dependent stiffness modulus considers all main key mechanism of the soil response. A more sophisticated model with hardening will yield more accurate results, but the increased calibration process is not necessary for the excess pore pressure estimation method. Also the differentiation between the initial stiffness and the un- and reloading stiffness may increase accuracy, but will not lead to substantially different results. The main objective is to estimate the stresses within the soil elements which are then transferred to stress ratios (CSR, MSR, LTR) in order to derive the cyclic response. Especially, in case of this simplified procedure, the Mohr-Coulomb material law is sufficiently accurate and does only need a small number of (five) input parameters, which all have clear physical meanings. Nevertheless, this constitutive model could be interchanged if needed (see Section 7.5). The stress dependent stiffness modulus, i.e. the oedometric stiffness, is considered with the following equation:

$$E_s = \kappa \quad p'_{ref} \left(\frac{\sigma'_{oct}}{p'_{ref}} \right)^m \tag{7.1}$$

Herein, p'_{ref} is the atmospheric reference stress (100 kPa), σ'_{oct} is the current octahedral effective stress in the considered soil element and κ and λ are soil dependent stiffness parameters.

Table 7.1: Soil properties for numerical calculation.

κ [1]	λ [1]	ν [1]	φ' [°]	c [kPa]	δ [°]	k_f [m/s]	ψ [°]	γ' [kN/m^3]
670	0.5	0.25	38	0.1	$2/3\varphi'$	3.7×10^{-4}	8	11

For the contact modelling the elasto-plastic master-slave concept between the monopile and the adjusted soil was used in a way that a connection between the soil and the structure is present as well as their relative displacement is possible. The maximum coefficient of friction in the sand-steel interface is set to $\delta = 2/3\,\varphi'$ and linearly mobilized within an elastic slip value of $du_{el} = 1\,\mathrm{mm}$. The calculation is executed in several steps. First, the initial conditions are set, in which the horizontal stress is calculated with the relation of Jaky (1944). Subsequently, the monopile and the contact are activated with a wished-in-place method. Afterwards, the mean lateral and the related moment and eventually the maximum lateral load are applied. For the consolidation analysis, the ABAQUS model is extended in order to enable a coupled pore fluid and stress analysis. For the hydraulic consolidation analysis the drained model was converted into a simple linear-elastic coupled model by changing the element type to C3D8P. The boundary conditions were adapted for the additional degree of freedom. The weight of the pore fluid is set to $\gamma_{water} = 10\,\mathrm{kN/m^3}$. The bulk modulus of the pore fluid K_w in the coupled analysis was set to $2.092 \times 10^6\,\mathrm{kPa}$ for T = 10°C.

7.2 Application of the EPPE contour approach

The presented EPPE method bases on different model assumptions for which the effect on the global system response will be shown in the following. Only the excess pore pressure plot for different load type conditions will be used; no cyclic stiffness degradation is considered in a first phase. The complete mathematical framework for the derivation of the contour plot for different CSR, MSR and N values was already presented (Chapter 5). The essential equation for the framework was chosen as $CSR_{R_u} = a(3 - log(N))^2 + b$. The input parameters for R_u = f(MSR, CSR, N) and the fitting parameter a = f(MSR, R_u) and b = f(MSR, R_u) for the cyclic input data can be found at the beginning of Section 5.3.

7.2.1 General calculation results

Within the calculation process, first the octahedral stress at mean global load (Figure 7.3 (a)), the equivalent shear stress at mean global and maximum global load are required (Figure 7.3 (b) and (c)). The loading direction is from left to right (positive x-direction). The resulting bedding resistance and the area of large deviatoric stresses can clearly be seen. Both stresses, octahedral and equivalent stress, increase with depth. The largest influence is present on the right side of the pile with the largest deviatoric stress occurring in the upper half of the pile. The resulting CSR field is depicted in Figure 7.3 (d). Large CSR values are obtained on the passive side and in the upper half. The largest CSR is set to 0.35, because above this value liquefaction is expected based on the derived contour plots. This is mainly done for clarification when presenting the results. Regarding the spatial distribution, the CSR value decreases with increasing distance to the pile and increasing depth. Below the point of rotation only small CSR values are calculated. Appendix A.3 shows all calculation steps for one integration point in greater detail. Depending on the location, stress redistributions and unloading occurs within individual elements. In the area of active earth pressure, mainly unloading is present and the active earth pressure coefficient arises. The stresses are, hence, smaller than on the passive side. Thus, the upper active side does not play a key-role in the bearing behaviour. Besides the CSR, also the MSR and LTR are derived. The global load is a symmetric one-way loading. The MSR field looks quite similar to the CSR field (Figure 7.4 (a)) which results in a LTR value of 1 within the main bedding area (Figure 7.4 (b)). On the active pile side, the LTR value is larger and represents a non-symmetric one-way loading up to a point of almost monotonic loading.

The normalized excess pore pressure field is derived based on the presented excess pore pressure ratio contour plots and is depicted in Figure 7.5 (a) for N = 1. The excess pore pressure ratio R_u correlates with the absolute excess pore pressure Δu by the octahedral stress. The absolute excess pore pressure is shown in Figure 7.5 (b). For the area of $R_u = 1$ in front of the pile, the excess pore pressure is equal to the octahedral stress from Figure 7.4 (a), which is approximately 120 kPa. The general distribution changes since the spatial variation of the octahedral stress influences the final result. The excess pore pressure ratio R_u can be interpreted as a damage indicator.

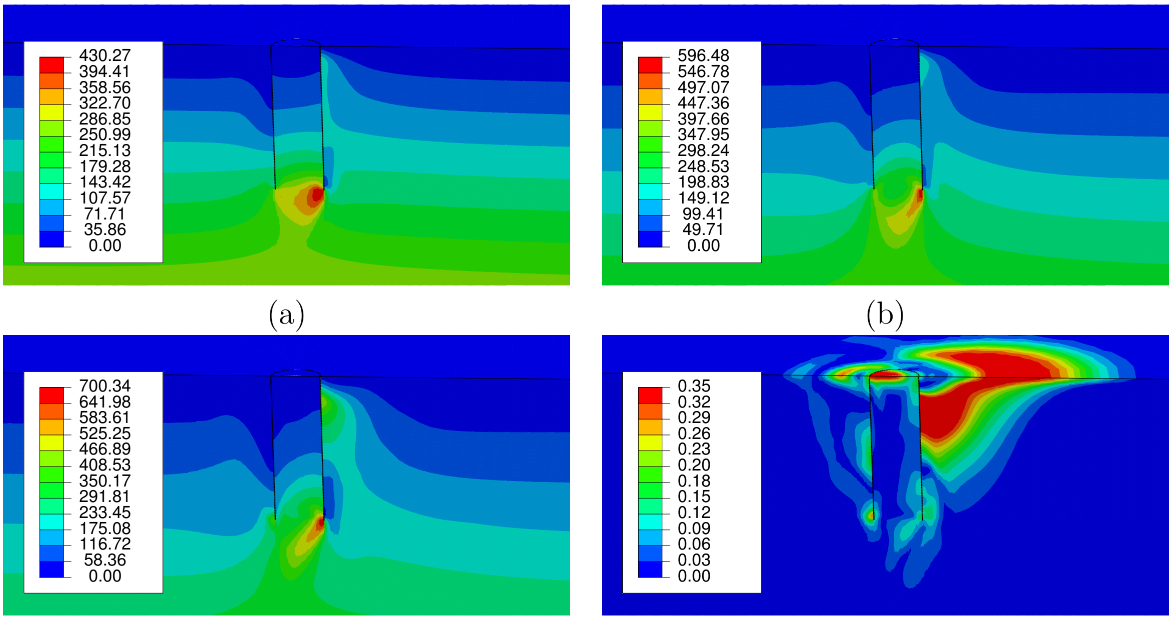

(a) (b)

(c) (d)

Figure 7.3: Input values for MSR and CSR calculation with octahedral stress at mean load (a), equivalent shear stress at mean load (b), equivalent shear stress at maximum load (c) and related CSR field (d).

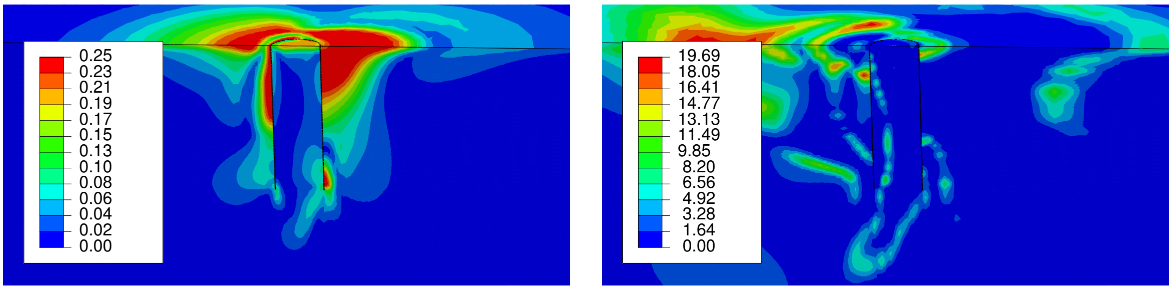

(a) (b)

Figure 7.4: Resulting MSR field (a) and LTR field (b) field for a symmetric one-way loading.

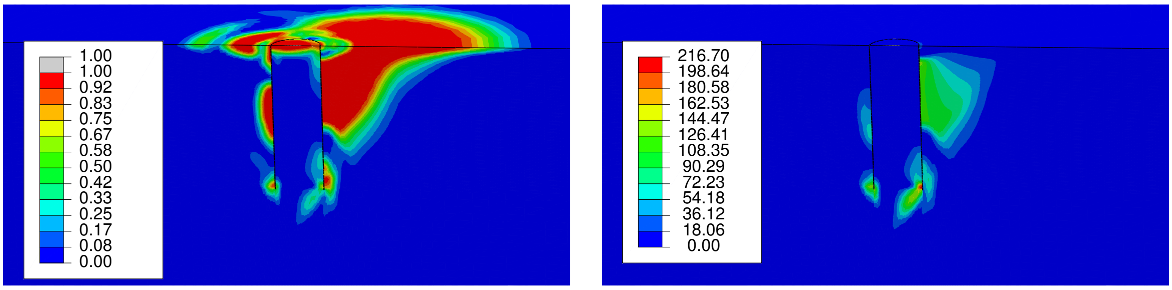

(a) (b)

Figure 7.5: Excess pore pressure ratio R_u (a) and excess pore pressure Δu (b) prior to dissipation for $N_{eq} = 1$.

Hence, a normalized excess pore pressure value of $R_u = 1$ indicates full damage since the element is theoretically liquefied. A dissipation analysis is performed with this excess pore pressure field and an integration point specific decay curve is derived. The dissipation analysis considers the consolidation of excess pore pressure by means of the excess pore pressure travelling through the model over the calculation time. With the normalized integration-point specific decay curve, an analytical superposition is performed.

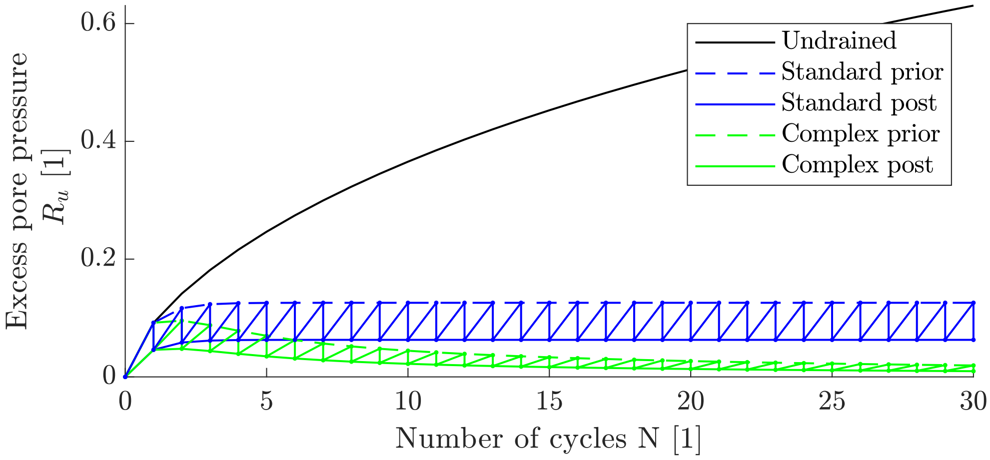

Figure 7.6: Different analytical superposition methods for the dissipation approach for CSR = 0.1 and LTR = 0 for a decay value of 50% (depicted before and after analytical dissipation).

The individual decay curves for each integration point are used in order to derive the final (dissipated) excess pore pressure field. Figure 7.6 shows an example of the analytical superposition for LTR = 0 and CSR = 0.1 for a decay of 50% and both dissipation procedures. The increase as well as the decrease due to dissipation are depicted. The excess pore pressure builds up steadily and then dissipates after more cycles pass. The characteristic trend of the complex approach agrees well with data found in the literature. The complex approach will tend to fully dissipate the excess pore pressure after a sufficient number of cycles, whereas the standard approach will give a conservative larger value. In order to conservatively estimate the excess pore pressure, the standard approach will be used.

The post-dissipated excess pore pressure ratio field R_u is shown in Figure 7.7 (a). The transferred consolidated excess pore pressure field Δu is shown in Figure 7.7 (b). The large potentially liquefied area around the pile was significantly reduced due to dissipation. The largest excess pore pressure ratio R_u cannot be found near the ground surface, because of a small drainage path. Hence, in 5 - 8 m depth, the maximum normalized excess pore pressure is present. In this area, there is an excess pore pressure of approximately 80 kPa based on Figure 7.3 (a). The damage does not concentrate that much any more at the pile toe. Similar to the difference of excess pore pressure and excess pore pressure ratio for N = 1, the excess pore pressure is smaller near the surface, since the octahedral stress is relatively small. Additionally, for the case after dissipation, small dissipation paths have decreased the absolute value of the excess pore pressure ratio. Under the point of rotation small excess pore pressures develop. In the upper part no excess pore pressure accumulates, because of the free drainage boundary condition. The trend over time is almost constant due to the used design dissipation approach. The general excess pore pressure accumulation is not very pronounced due to the homogenous sandy soil layering (without any cohesive layers) and especially because of the comparatively large hydraulic conductivity.

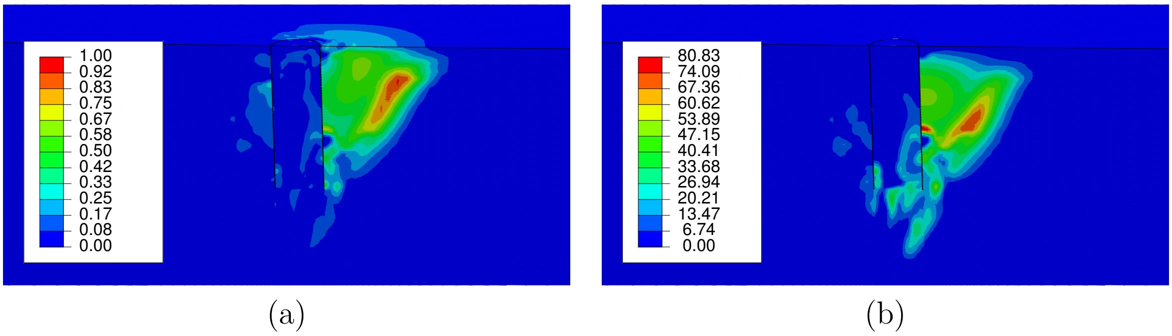

(a) (b)

Figure 7.7: Final excess pore pressure ratio field R_u (a) and results of consolidation analysis in the form of excess pore pressure Δu (b).

Figure 7.8 shows the monotonic and post-cyclic load-displacement curves. However, the cyclic curve should only be analysed regarding a ULS proof, since additional effects such as accumulation of plastic strains and, hence, a softer response in the initial part of the curve are not taken into account in this assessment. For the 0.1D criterion, a degradation of bearing capacity of 53% is expected.

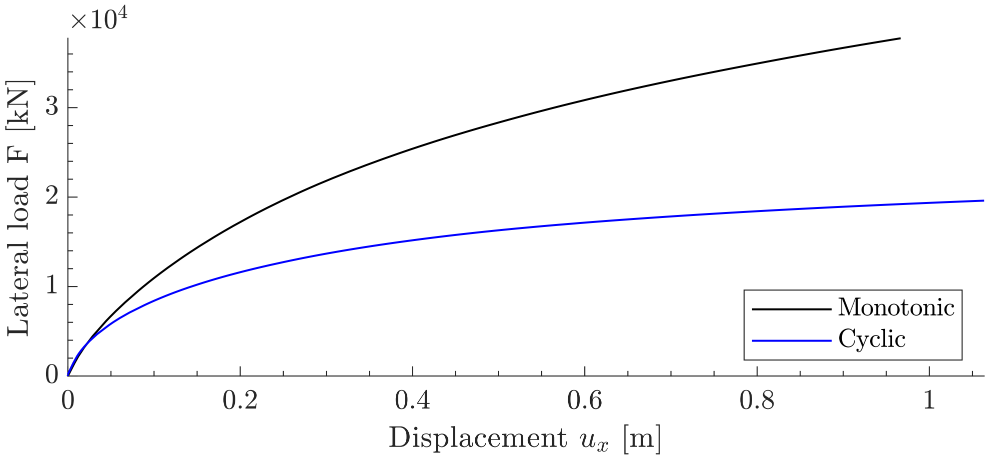

Figure 7.8: Monotonic and cyclic load-displacement curves for reference system.

7.2.2 Variation of stress consideration

The system response is described with the EPPE approach. However, there are several model assumptions whose influence must be quantified to obtain an appropriate conservative approach. Variations of the approach are compared in the following with the CSR field, the final excess pore pressure ratio field R_u as well as the resulting post-cyclic bearing capacity. Although the procedure is modular and depending on the input some results may change, the overall response and influences of variations are expected to be similar. Additionally, it should be kept in mind that the presented problem is highly non-linear since several non-linear effects are sequentially considered.

Figure 7.9 shows the resulting bearing capacity for a deformation criterion at mudline of 0.1D and the approach according to Manoliu et al. (1985) normalized by the post-cyclic value for the reference model. The approach according to Manoliu et al. (1985) will result in slightly larger capacities than the 0.1D criterion. For the reference model a value of 1 is obtained due to normalization. The monotonic capacity is 1.89 times the capacity of the cyclic one. Different model variations are depicted on the x-axis and will be explained briefly in the following. Figure 7.9 depicts the influence of the general input. The bearing capacities are 18.7 MN for the cyclic and 35.4 MN for the monotonic case for the 0.1D criterion. The monotonic results agree well with the results from the analytic calculation.

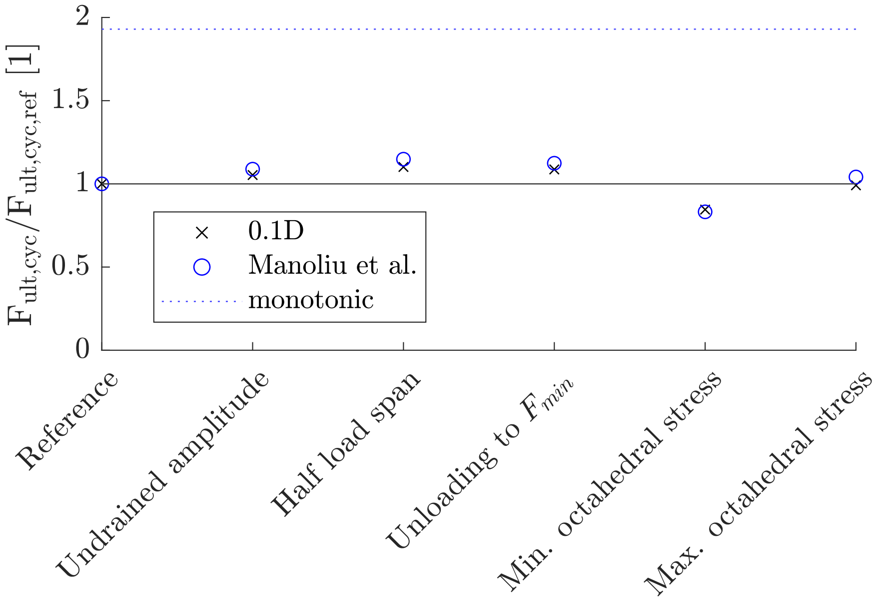

Figure 7.9: Comparison of different modelling approaches in terms of normalized post-cyclic capacity (normalized to reference system).

Application of cyclic load amplitude in an undrained manner

The global cyclic load amplitude can be applied in an undrained or drained manner (cf. Section 6.1.1). For an undrained application, a larger stiffness modulus and a constant volume boundary arise. In the reference model, the global load amplitude is applied in a drained way by means of a simplification to avoid a coupled hydraulic-mechanical model. In this coupled model, the mean load is applied over a long simulation period to avoid the build-up of excess pore pressure and allow for volumetric strains. The global cyclic amplitude is applied much faster in the finite element model. The difference in capacity is an increase of roughly +8% based on the stiffer response (Figure 7.9). The CSR field is depicted in Figure 7.10 (a). The CSR values are generally smaller compared to the reference system, which results in a smaller excess pore pressure degradation field (Figure 7.10 (b)). The reference approach very well estimates the bearing behaviour conservatively and does furthermore bear advantages regarding the derivation of an equivalent number of cycles (see Appendix B).

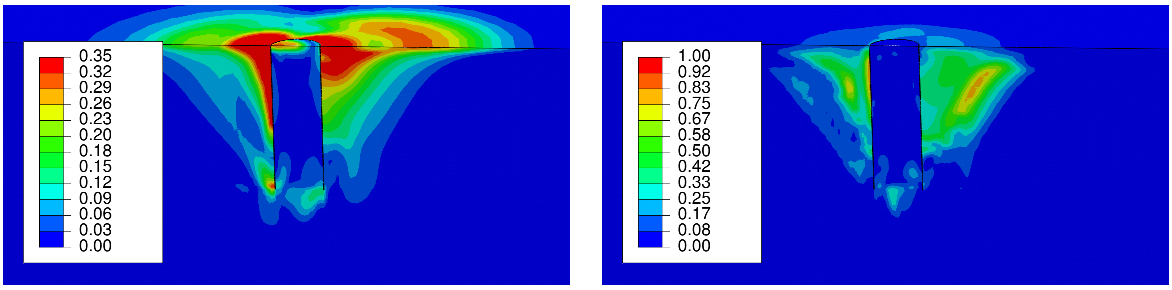

(a) (b)

Figure 7.10: Spatial distribution of CSR (a) and resulting excess pore pressure field R_u (b) for an undrained application of load amplitude.

Calculation of cyclic stress ratio

The equivalent shear stress builds-up non-linearly over the course of the global load application. The CSR is based on the shear stress amplitude within one element. The amplitude can be calculated in the following two ways (Equation 7.2 and see Section 6.1.2). In the reference procedure, the stresses at mean and maximum global load are used. Alternately, the CSR can be based on half of the loading span from minimum to maximum global load.

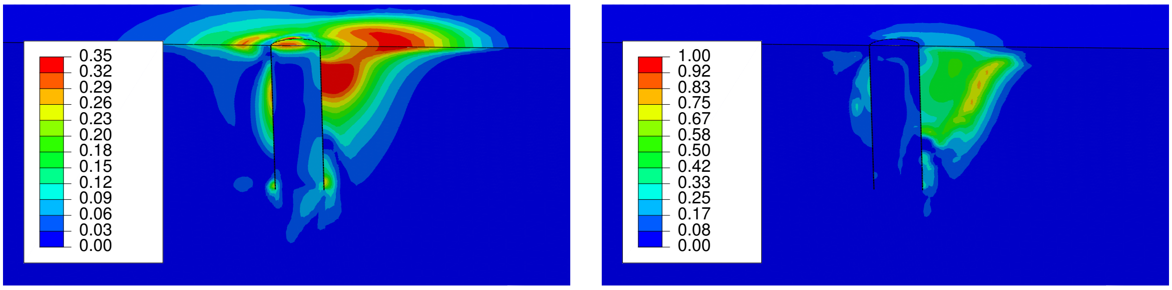

(a) (b)

Figure 7.11: Spatial distribution of CSR (a) and resulting excess pore pressure field R_u (b) for CSR based on half of the deviatoric stress span.

Figure 7.11 shows the resulting smaller CSR field compared to the reference system as well as the damage field (Figure 7.11 (b)). The change in bearing capacity is herein +14% compared to the reference case (Figure 7.9). In the reference procedure the stress amplitude is evaluated in order to evaluate the non-linear stress at the global load amplitude. This procedure is moreover conservative.

$$CSR = \frac{\sigma'_{eq,F_{mean}} - \sigma'_{eq,F_{max}}}{2\sigma'_{oct,F_{mean}}} \quad alternatively: \quad CSR = \frac{0.5(\sigma'_{eq,F_{min}} - \sigma'_{eq,F_{max}})}{2\sigma'_{oct,F_{mean}}} \tag{7.2}$$

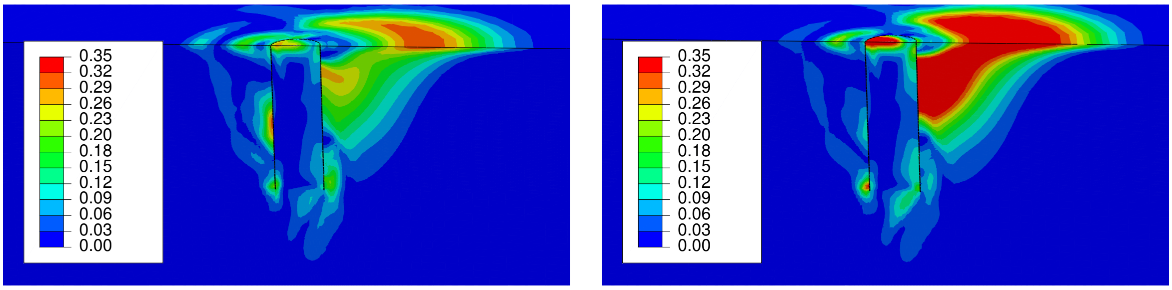

(a) (b)

Figure 7.12: Field of calculated CSR based on octahedral stress at maximum global load (a) and based on the stress at initial conditions (b).

The reference stress within the definition of CSR and MSR can be chosen at initial conditions, at the mean global load (as done by default) or the maximum global load. The influence on the final CSR field is shown in Figure 7.12. The use of the octahedral stress at initial conditions will result in a field with increased CSR values and the stress at maximum global load to decreased CSR values. The change in bearing capacity is -17% and +4% compared to the reference case, respectively (Figure 7.9). There is a difference of about 20% in bearing capacity between the different model assumptions. This indicates how important a correct definition of the input values can be. The non-linear correlations can well be seen in this example, because the CSR and MSR values are smaller for a normalisation with the octahedral stress at global maximum load. Also the spatial distribution changes slightly. This leads to a larger final damage field. The assumption within the reference EPPE procedure is conservative but too uneconomical within the design process.

Unloading of numerical model to global minimum load

Instead of deriving the cyclic input values from one monotonic loading, the stress state can very well be described by performing a calculation with a complete half cycle instead of only loading to the maximum cyclic load level in order to also consider stress-redistributions and above all the stiffer soil response for an un- and reloading stiffness. Even if no un- and reloading modulus is present in the used Mohr-Coulomb model, the effect shall still be presented. Hence, the deviations are based on stress redistribution. The CSR in each integration point is calculated with the difference from global mean load to the global minimum load. The bearing capacity is larger compared to the reference case, because the required shear stress to carry the bedding resistance is already mobilised and only stress redistributions and mainly unloading effects for a symmetric one-way loading case occur. This leads generally to smaller CSR values. The depicted CSR field and excess pore pressure ratio field are depicted in Figure 7.13. The bearing capacity changes by +12% because of the less severe CSR field compared to the reference case (Figure 7.9).

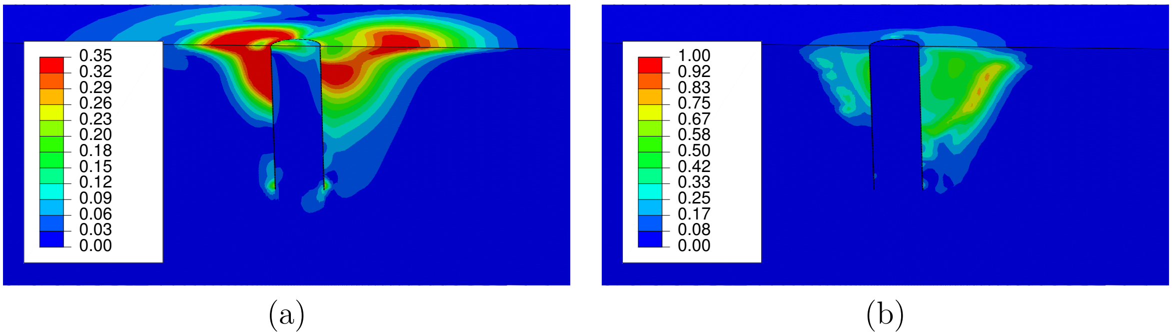

(a) (b)

Figure 7.13: Spatial distribution of CSR (a) and resulting excess pore pressure field (b) based on a monotonic reference calculation with unloading to F_{min} and derivation of CSR by using the amplitude from F_{mean} to F_{min}.

Influence of global mean load

There is a different soil degradation depending on different cyclic load levels and different global mean loads. A focus was put on a constant load amplitude and not on a constant maximum global load (Figure 7.14). Therefore, Figure 7.15 shows results for non-symmetrical, symmetrical two-way loading with $F_{min} = -3.4\,\text{MN}$ / $F_{max} = 10.2\,\text{MN}$ and $F_{min} = -6.8\,\text{MN}$ / $F_{max} = 6.8\,\text{MN}$, respectively; as well as non-symmetrical and symmetrical one-way loading with $F_{min} = 6.8\,\text{MN}$ / $F_{max} = 20.4\,\text{MN}$ and $F_{min} = 0\,\text{MN}$ / $F_{max} = 13.6\,\text{MN}$ in order to evaluate the influence of different load types. Hence, the load amplitude was kept constant as of $F_{cyc} = 6.8\,\text{MN}$. Due to a constant load amplitude and the presented load cases, not only ζ_c, but also ζ_b is varied.

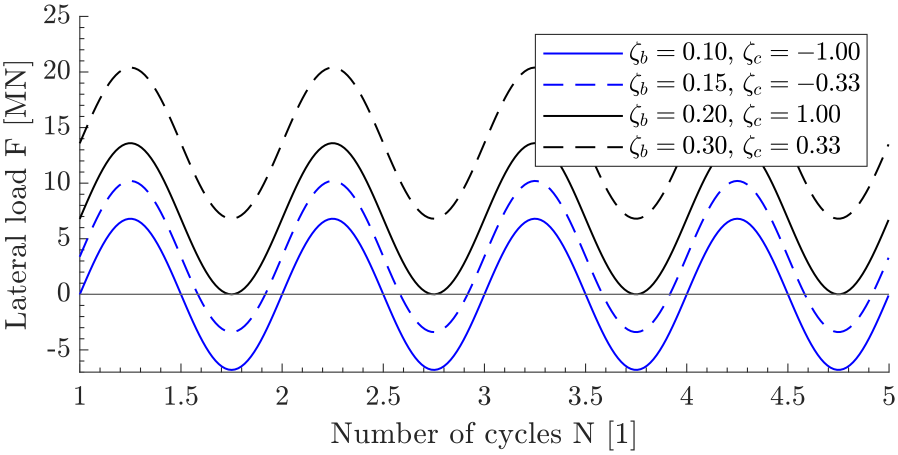

Figure 7.14: Schematic of used load types with constant load amplitude.

Figure 7.15 shows the final excess pore pressure ratio field for different loading scenarios. The damage decreases from ζ_c changing from -1 to 0.3 (Figure 7.16). The overall damage is smaller compared to symmetric one-way loading, but the spatial distribution is similar. The resulting bearing capacities normalized to the reference case are depicted in Figure 7.16. It shows that different load types can be approximated with the EPPE approach and that a one-way loading induces a larger damage compared to a two-way loading. How pronounced the influence is, of course, also depends on the contour representation. The degradation is mainly on the right side of the pile, because the pile was only loaded once in this direction. The degradation could also be calculated for the other pile side, but this would only marginally change the bearing capacity but increase the computational time.

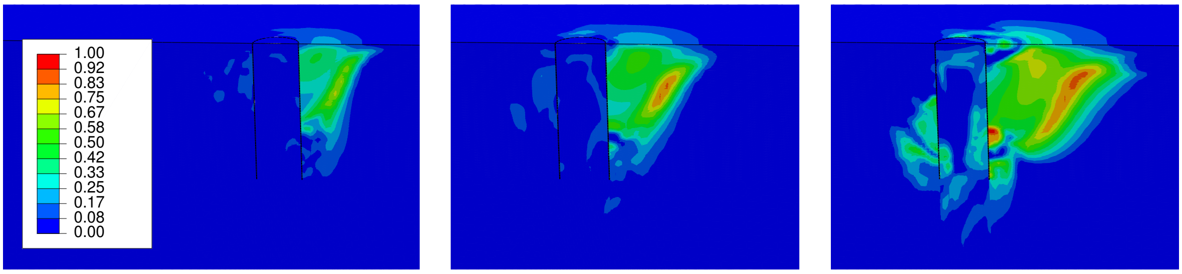

(a) (b) (c)

Figure 7.15: Excess pore pressure ratio field R_u for $\zeta_c = F_{min}/F_{max}$ equal to -1 (a), -0.5 (b) and 0.5 (c).

It should be kept in mind, that as a conservative model assumption the excess pore pressure contour plots were not adjusted to the smaller damage for small CSR and large MSR values. Within the cyclic DSS tests, a smaller excess pore pressure build-up was measured regarding non-symmetric one-way loading and hence the result can be seen as conservative. For a different contour input, this curve may get closer to the monotonic response.

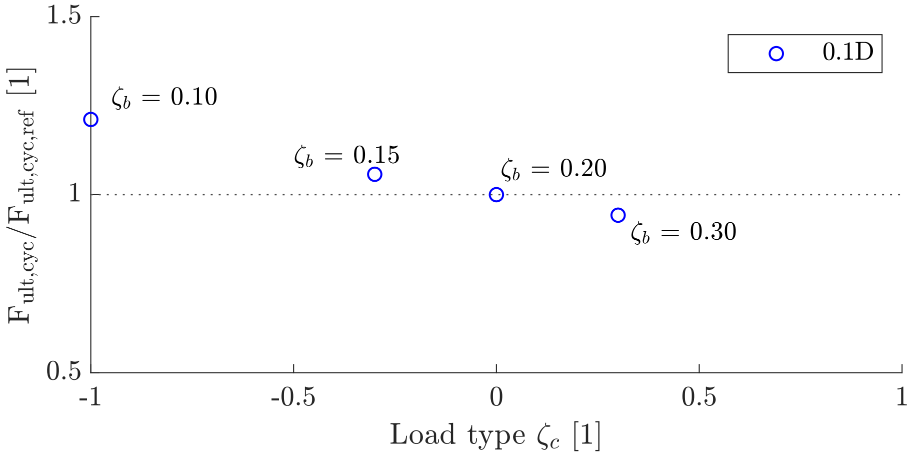

Figure 7.16: Comparison of bearing capacities depicted with $\zeta_c = F_{min}/F_{max}$ for the 0.1D criterion.

Interim summary

The calculation results show, that the model assumption regarding the stress definitions of the reference EPPE method are reasonable. There is no need to apply the load amplitude under undrained conditions. The stress ratios should not be derived based on the stress span since the stresses are averaged and the use of an unloading step does not significantly change the results but implies that the constitutive model can be used for this application, which is strictly speaking not the case. The use of the mean effective octahedral stress for the normalisation of the CSR and MSR is surely a model assumption in order to transfer the stress conditions from finite element to DSS conditions, but also reasonable.

7.2.3 Variation of dissipation modelling

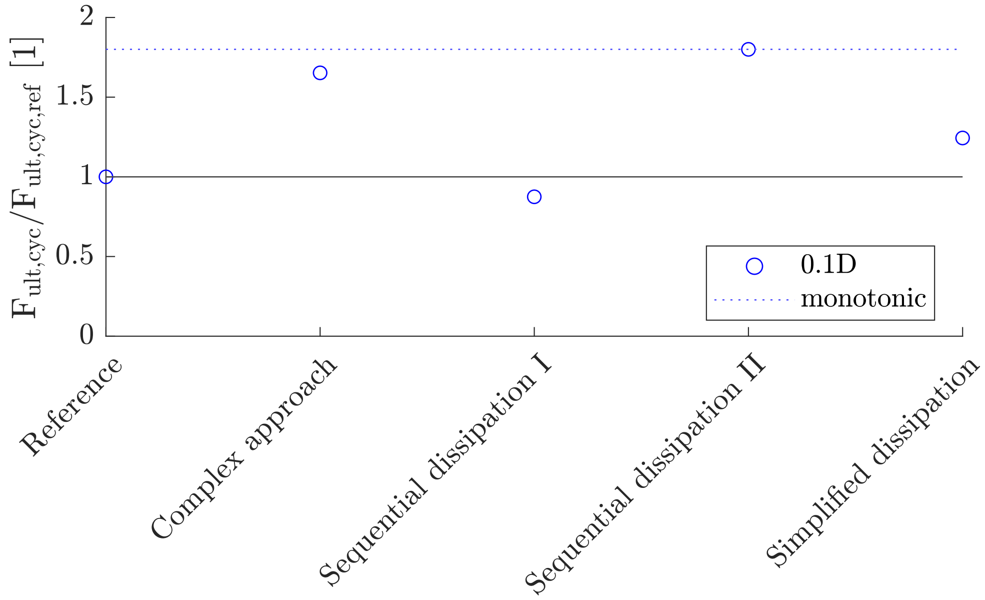

Figure 7.17: Comparison of different modelling approaches by means of total capacity with different dissipation variations.

Several topics need to be addressed regarding cyclic soil response under partially drained conditions. After the effects of the procedure in the finite element modelling were explained, variations in the dissipation analysis shall follow. Since dissipation is a key mechanism when dealing with partially drained conditions, the consideration in the framework can have a large effect on the resulting soil-structure interaction.

Complex dissipation approach

Instead of the standard dissipation approach used in the reference procedure, the complex dissipation approach can be used (Section 6.1.3). Herein, the excess pore pressure can reach a state of zero and the initial part of excess pore pressure curve trend is not solely used leading to a softer response. The resulting excess pore pressure ratio field for the complex dissipation approach is shown in Figure 7.18. The overall damage is smaller compared to the reference approach which results in a larger bearing capacity. For an increasing number of cycles, the residual excess pore pressure will decrease. Figure 7.17 shows the larger bearing capacity for this case since way less damage was induced.

Sequential dissipation calculation

In some cases elements near the structure generate high excess pore pressures after one cycle. This excess pore pressure dissipates to an adjacent element and increases the excess

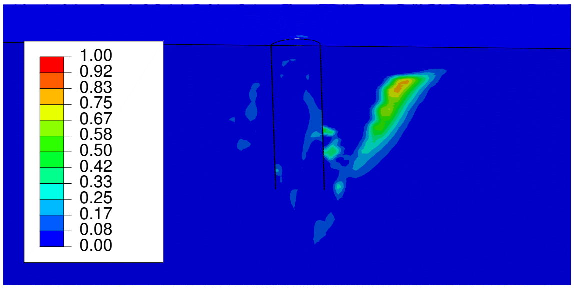

Figure 7.18: Final excess pore pressure ratio R_u field for complex dissipation after 30 cycles.

pore pressure. In the analytical dissipation analysis this percentage increase is used in all cycles which leads to a fast liquefaction failure of this very element. The near-structure element does not induce this high excess pore pressure increment in the next cycles (non-linear trend) and even a flow redirection to this element may occur due to a changed hydraulic gradient. However, all these aspects can only be considered when using an implicit calculation in which all this phenomena find an equilibrium between the generation and dissipation based on the stress states, element interactions and hydraulic gradients. Instead of performing one simple dissipation analysis and an analytical superposition, several dissipation calculations can be done sequentially. This may not be feasible in practical projects, but the deviation to the reference approach can be assessed. The excess pore pressure ratio is calculated and subsequently dissipated. The resulting excess pore pressure after a dissipation period of 10 s is read. This value is then transferred to an equivalent number of cycles, to which a incremental cyclic number dN = 1 is added. The results are depicted in Figure 7.17 (calculation I) and the excess pore pressure field in Figure 7.19 (a).

Compared to the reference procedure, a smaller amount is dissipated which results in less bearing capacity. The spatial distribution agrees very well between both dissipation analyses. Figure 7.20 (a) shows the accumulation of excess pore pressure for one integration point (5 m/0 m/-5 m). The reference method is not strictly speaking conservative in this respect, but this modelling technique is very computationally intensive, and since the standard approach already provides conservative values, validation of the more complex method should be undertaken before suggesting that this method must always be used.

Instead of recalculating the equivalent number of cycles for the dissipated excess pore pressure, the complex method can be used but for sequentially performed calculations. Hence, the incremental increase for the related number of cycles is applied to the excess pore pressure results from the last step. The results are depicted in Figure 7.17 (calculation II), Figure 7.19 (b) and Figure 7.20 (b). Generally, more excess pore pressure dissipates and a capacity almost as large as the monotonic bearing capacity arises. The trend of the excess pore pressure over the number of cycles resembles the general trend of the complex approach. It may be concluded, that the sequential calculation does amplify the tendency from the used method. Due to the complete dissipation of excess pore pressure, this modelling procedure is by no means conservative and should hence not be used within a design calculation.

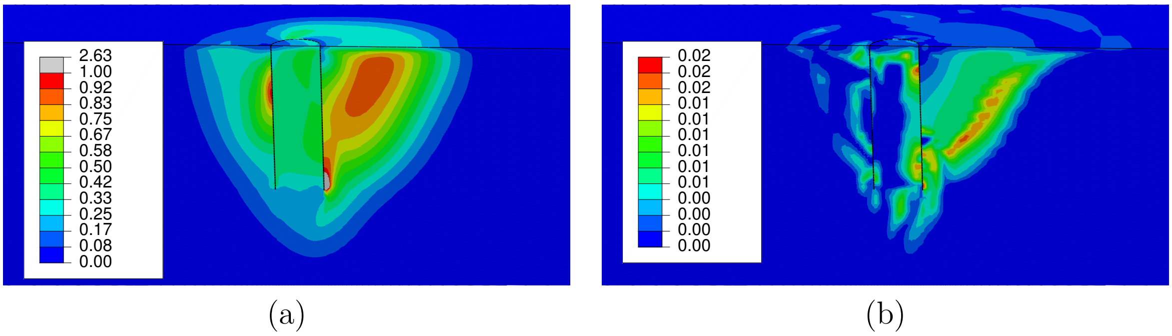

Figure 7.19: Final excess pore pressure ratio R_u field for sequential dissipation calculation for standard (a) and complex dissipation (changed scale) (b).

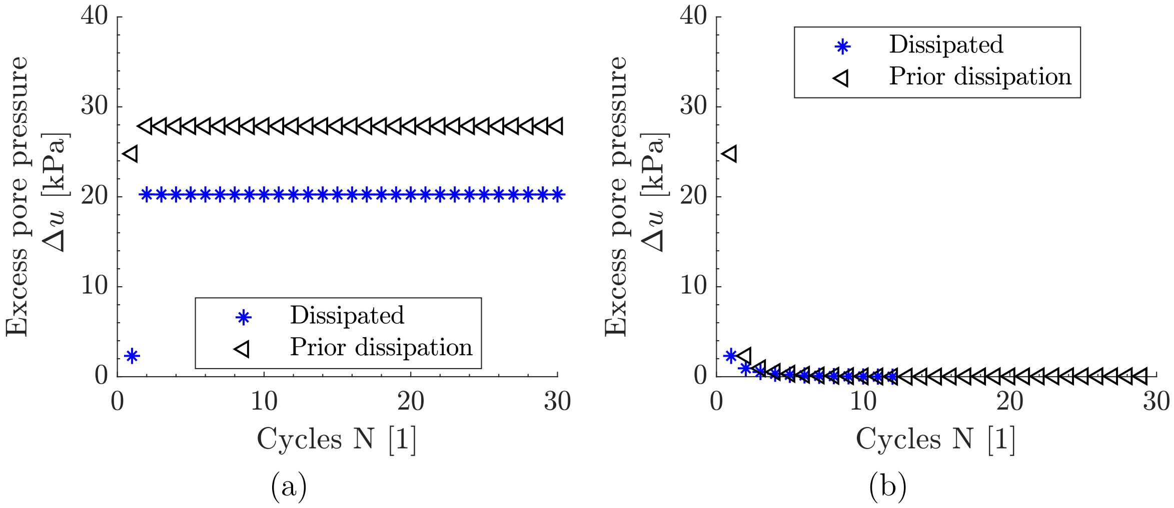

Figure 7.20: Final excess pore pressure Δu for sequential dissipation calculation with standard (a) and complex (b) back-calculation approach of number of cycles N after each new dissipation analysis .

Simplified dissipation with PDE

Even though the three-dimensional dissipation analysis does only take some minutes to calculate and evaluate, a simplification can be made here (cf. Section 4.3.1). Instead of a vertical and horizontal dissipation including an interaction of both, only radial dissipation shall be analytically considered. The drainage can be considered with analytical methods in the form of a finite difference flow net calculation. This approach is more reasonable for a soil profile in which more horizontal than vertical dissipation occurs (sand enclosed from clay layers). For larger layer heights drainage may occur within the layer and excess pore pressure is redistributed. The behaviour is more complex and a flow net analysis is always necessary. For the simplified approach, first the excess pore pressure after specific number of cycles is read from the contour plot for a given cyclic shear stress (and mean shear stress). With the consolidation coefficient the normalized time is derived and the dissipation estimated. It is possible to assume radial or 1D flow. The main differences from a mathematical point of view, is that the radial drainage has a second derivative (additional diffusional term) within the differential equation.

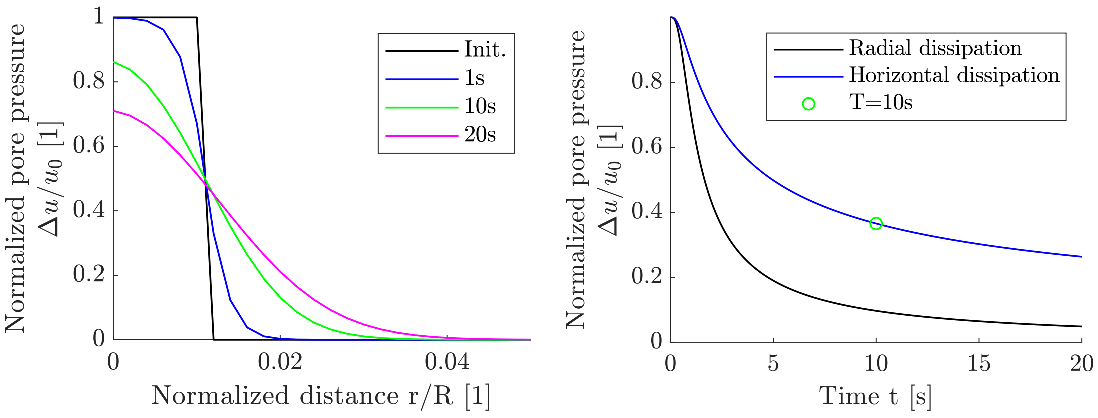

(a) (b)

Figure 7.21: Solution of finite differences in 1D (a) as well as evaluation at point r/R = 0 for radial and horizontal dissipation (b).

Figure 7.21 shows that the radial differential equation will overestimate the consolidation process compared to the three-dimensional finite element model. Hence, the 1D equation is implicitly solved. The total length R was set to 25 m with a discretisation of 500 points over 20 s and 10,000 time increments. Figure 7.21 (a) shows how the initial excess pore pressure dissipates over the normalized distance and over time. Figure 7.21 (b) shows the excess pore pressure over time for the starting point. After a storm period of 10 s the excess pore pressure is reduced to 36%. The resulting excess pore pressure field is shown in Figure 7.22 (a) and leads to an increase in capacity of +24% as shown in Figure 7.17 due to the simplification and overestimation of dissipation.

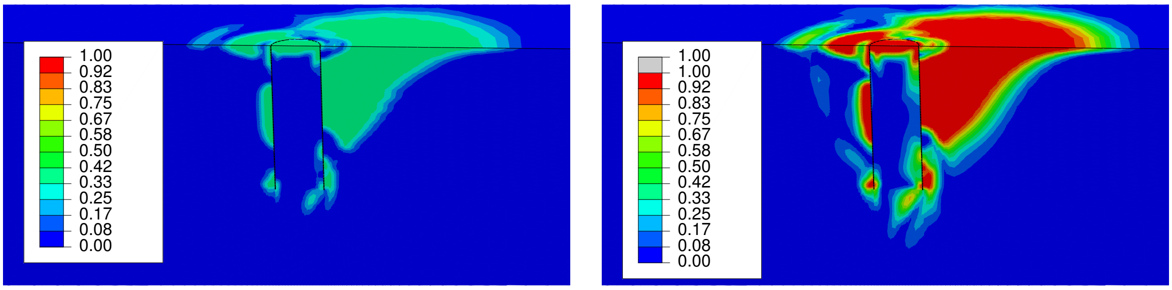

(a) (b)

Figure 7.22: Final excess pore pressure ratio field R_u for simplified dissipation (a) and neglecting dissipation (b).

Neglecting dissipation

One extreme case is to neglect the dissipation at all. The effect on the final excess pore pressure field is shown in Figure 7.22 (b). The damage field is widely spread and, hence, a calculation with this input values is not feasible. The result would not be economical because it neglects one key mechanism when dealing with partially drained conditions.

The figure resembles the excess pore pressure ratio field for N = 1, but is even more severe regarding induced damage.

Derivation in dissipation model input

The decay curves are derived for the excess pore pressure field for a cyclic number of N = 1, although the use of the excess pore pressure field related to the number of equivalent cycles N = 30 is evident. The effect of this modelling assumption needs to be investigated. The effect of a different number of cycles for the input of the dissipation model is shown in Figure 7.23 and Figure 7.24.

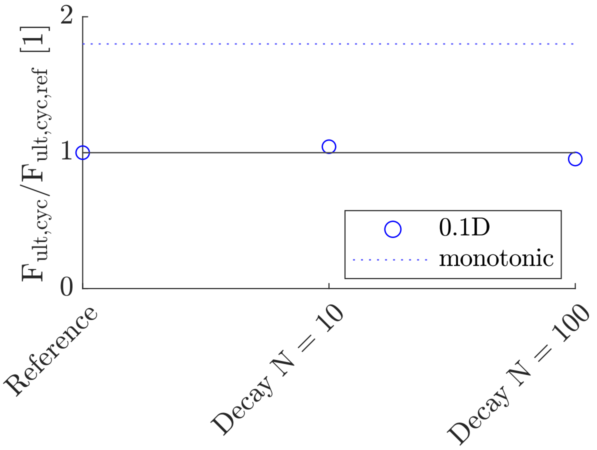

Figure 7.23: Comparison of different dissipation model input.

For N = 10 the capacity is larger and for N = 100 slightly smaller. The degradation field is more severe for N = 100 compared to N = 10 and N = 1 (Figure 7.24). When looking at the load-displacement curve, there is a stiffer response for the soil structure response for the input in the dissipation analysis of N = 1 compared to N = 10 and N = 100; for larger displacement the asymptotic value is not in the expected order. The differences are however reasonable. Overall, the number of cycles influences only marginally the dissipation response for large global loads, because even for one cycle a large area is liquefied due to large CSR values. Hence, this model assumption is reasonable.

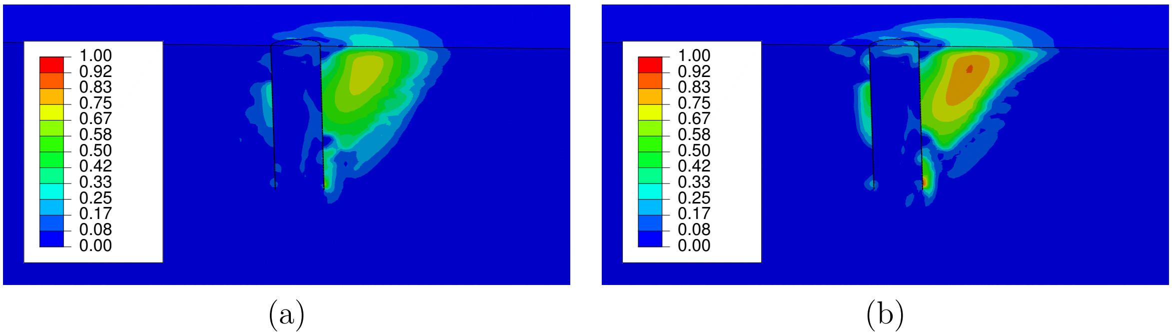

Figure 7.24: Final excess pore pressure ratio field R_u for two different number of cycles for the dissipation model of N = 10 (a) and N = 100 (b).

Interim summary

The results show that the post-cyclic capacity is reasonably estimated with the reference EPPE method. The use of the more complex dissipation method will lead to larger capacities – especially for an increasing number of cycles. The effect of both methods is amplified with a sequential analysis, although a mandatory analysis in such a way does not seem to be necessary. A simplified analysis by using a 1D finite differences model will lead to slightly larger capacities but neglects spatial influences. There is no need to use the equivalent number of cycles for the input of the dissipation model.

7.3 Comparison with different estimation approaches

All presented methods were based on the results of contour plots in accordance to DNV-RP-C212. However, it is also possible to use different approaches to calculate the excess pore pressure in each integration point. The number of cycles, the relative density and the global loads are all identical to the reference case, if not stated differently. The following questions are to be dealt with:

- What happens if there is a deviation within the regression analysis when deriving the contour plot?
- How is the capacity affected if the global load is still a symmetric one-way loading, but the soils' contour input is only based on symmetric two-way loading?
- What happens if additional triaxial test results are considered?
- How can cyclic test results based on displacement-controlled tests be used?
- What happens if the stresses redistribute and the method is used iteratively? Is this even necessary?
- In what order of magnitude are potentially derived post-cyclic volumetric strains due to consolidation if these shall be taken into account? How can this be done?

Figure 7.25 shows the bearing capacities for the following cases normalized to the post-cyclic reference value.

Deviation in contour estimation

Especially the correct approximation of the performed cyclic laboratory tests with the contour plots can have a significant influence on the post-cyclic system response. To simulate the correct approximation, the contour plot was scaled vertically by a factor of 0.9 in order to simulate a different, more conservative regression analysis. The maximum CSR value for liquefaction is hence not e.g. 0.3 for N = 1 but 0.27. This influence is especially pronounced for smaller number of cycles and large CSR values (Figure 7.25). The deviation in bearing capacity is not very pronounced (Figure 7.26 (a)). The CSR value within the bearing area is already large enough so that a small change in the contour plot does not have a large influence on the post-cyclic bearing capacity.

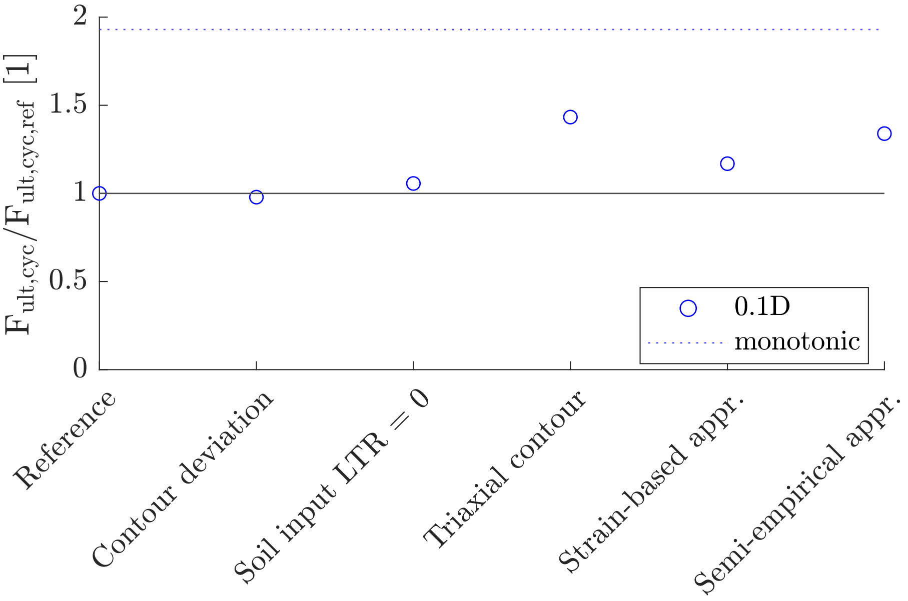

Figure 7.25: Comparison of different modelling approaches by means of total capacity with different variations.

Regarding the contour input, not only a deviation in contour approximation is possible, but also that only symmetric two-way loading DSS test results are present. Hence, Figure 7.26 (b) shows the resulting excess pore pressure ratio field for this condition. The influence on the ULS design proof is very small compared to the reference case (Figure 7.25). The deviation can be explained with the fact that for LTR = 0 a smaller degradation is expected compared to LTR > 0.

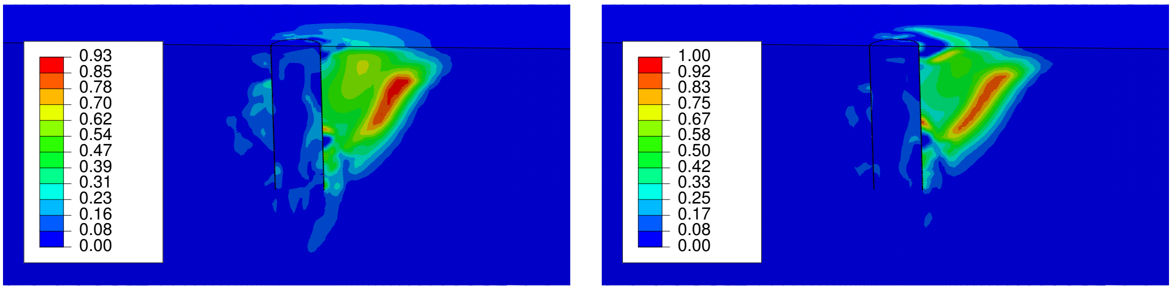

(a)

(b)

Figure 7.26: Resulting excess pore pressure field R_u for scaled contour plot (a) and excess pore pressure field R_u for a global symmetric one-way loading, but contour plot only based on symmetric two-way loading as input (b).

Consideration of cyclic triaxial test results

There is a different soil response for different laboratory devices regarding the anisotropy of the soil specimen and also due to a rotation of principal axis. This is especially the case for triaxial and direct simple shear tests. The differences in cyclic soil response have been presented and implementation for the framework described in Chapter 6. The contour plot was presented in Section 5.3.2. The influence of this distinction shall be shown on the reference system. Since only results for symmetric two-way loading are present for triaxial conditions, the interpolation is only done for this case. The influence on the bearing capacity when changing the contour plot in the mentioned way has already been explained in the last subsection.

The distribution of the Lode angle is shown in Figure 7.27 (b). The region in which triaxial conditions are present is represented by 0° and 60° and DSS conditions for 30°. Since no cyclic extension tests have been performed, the compression contour plots are scaled vertically by a factor of 0.5 in order to qualitatively consider this effect. Hence, a more severe soil response is assumed for triaxial extension conditions. Andersen (2015) shows that this is the case for sandy material for a medium relative density, but for the very dense state, as in the presented study, a factor between DSS and triaxial test extension results of 1 may be assumed. This implies that a factor of 1.0 would have also been reasonable. However, the region of triaxial extension conditions is not very pronounced (Figure 7.27 (b)) which makes the factor choice almost indifferent. Figure 7.27 (a) shows the different excess pore pressure ratio field as well as the influence on the load-displacement curve. The application of cyclic constant-volume DSS tests is faster and leads to a slightly more conservative design. There is only a small effect associated with the change of the contour input regarding the DSS case. Even though compression conditions are present in front of the pile, the general degradation is smaller which leads to larger capacities as shown in Figure 7.25.

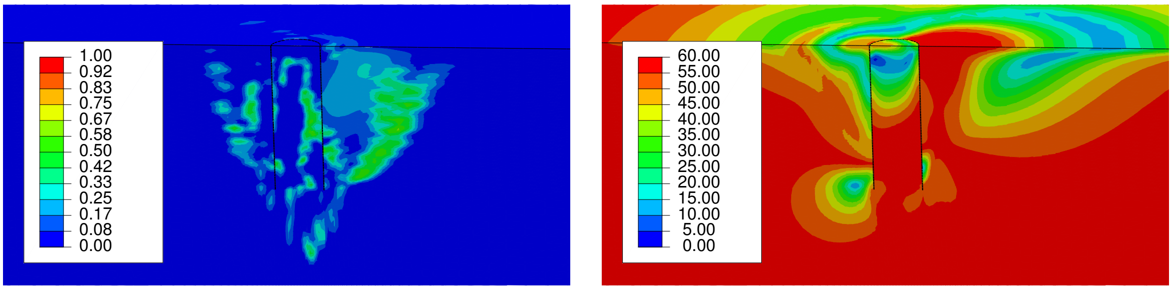

(a) (b)

Figure 7.27: Consideration of cyclic triaxial results with excess pore pressure ratio R_u after N = 1 (a) and Lode angle Θ based on monotonic reference calculation (b).

7.3.1 Displacement-controlled equation approach

Some authors state that due to stress redistributions monopiles are loaded in a displacement-controlled manner (Andersen et al., 1978; Cai et al., 2014). The advantages of displacement-controlled tests have already been explained. Most of the cyclic investigations deal with load-controlled tests, however, no in-depth analysis regarding the most representative load type currently exists to the knowledge of the author. A strain-approach for excess pore pressure estimation was established and is presented in Appendix D (see also Saathoff and Achmus (2021)). The herein used approach bases solely on displacement-controlled test results. Instead of the derivation of an equivalent shear stress, an equivalent shear strain is used. The equation was presented in Chapter 6 (Equation 6.16). Due to the different estimation equation (by using γ_{eq}), the general spatial excess pore pressure distribution for N = 1 is altered. Figure 7.25 shows the resulting bearing capacity. Compared to contour based approaches, the bearing capacity is +17% larger and hence slightly less damage is induced. The value is based on the excess pore pressure ratio field in Figure 7.28 (a) which is derived with the equivalent shear strain distribution depicted in Figure 7.28 (b). The used constitutive model is elastic-ideal plastic and hence, the shear strain distribution may change when using a material law with hardening. Nevertheless, the larger strains by using the Mohr-Coulomb model can be interpreted as conservative in comparison to smaller strains derived with a more sophisticated one.

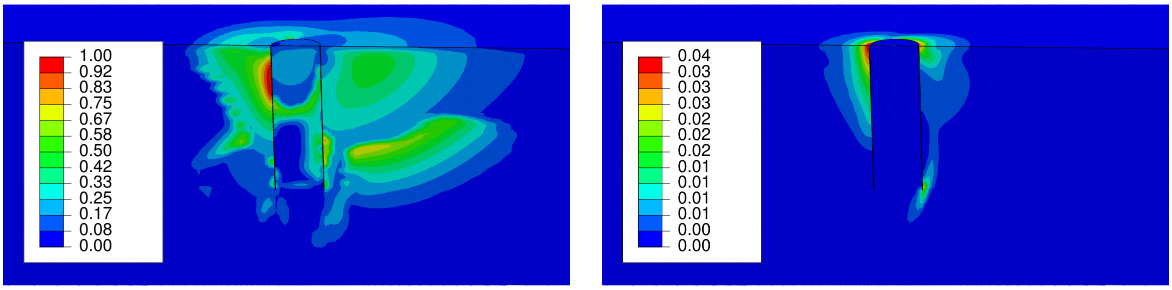

(a) (b)

Figure 7.28: Final excess pore pressure ratio field R_u (a) and equivalent shear strain amplitude $\gamma_{eq,cyc}$ (b).

7.3.2 Alternative load-controlled equation approach according to Seed et al. (1975)

A more simple approach is the one according to Seed et al. (1975b). The CSR curve for different MSR values was shown in Section 5.2.2. The normalized bearing capacity is shown in Figure 7.25. The excess pore pressure field R_u for N = 1 and the R_u field after dissipation is depicted in Figure 7.29. This approach is much simpler and yields a bearing capacity larger to the contour approach. The liquefaction curve is similar, but the trend over the (normalized) number of cycles is different. There is a small initial increase for the case of the semi-empirical equation. This trend is used in the analytical superposition and influences the final excess pore pressure value. Hence, smaller excess pore pressures arise which lead to a larger bearing capacity. An estimation of the capacity degradation can be obtained by using this simplified approach, however, the use of the reference EPPE approach is recommended.

7.3.3 Iterative calculation

A sequential dissipation was already presented and it was concluded that the dissipation effect is slightly amplified, but that this procedure may not be necessary. The next step is to not only calculate the excess pore pressure sequentially within the dissipation model, but the stresses can be calculated sequentially, too. So far, only one calculation was done and the CSR values for each integration point derived. However, due to excess pore

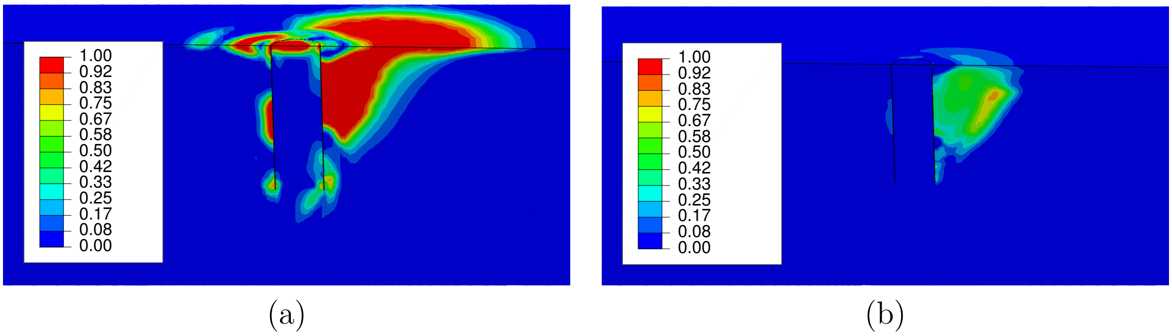

Figure 7.29: Final excess pore pressure ratio field R_u after N = 1 (a) and R_u after superposition (b) with equation approach.

pressures, stress redistributions occur and the local stress values may change. A sequential calculation should be done successively in the finite element model for each cycle due to stress redistribution and, hence, different excess pore pressure responses. The dissipation analysis is performed in each run once. However, the iterative calculation is accompanied with high computational efforts and will not be taken into account within the reference procedure in order to keep the procedure simple. The influence of this model assumption is analysed in the following.

For a sequential calculation, the soil gets softer in the upper part, but the same bedding resistance is required, therefore larger stresses arise in the lower part. There is a gradual decrease in strength and stiffness due to excess pore pressure. In this way other areas are loaded and excess pore pressure is generated in a more distinct manner; a redistribution occurs. The complete behaviour and the areas where the soil softens and how redistributions take place is mainly influenced by the drainage paths. Figure 7.30 shows the bearing capacity over five iterations. Herein, the post-cyclic model was used in order to calculate the input values by means of CSR and LTR to derive the accumulated excess pore pressure ratios. The bearing capacity converges to a value which is slightly larger to the first estimation.

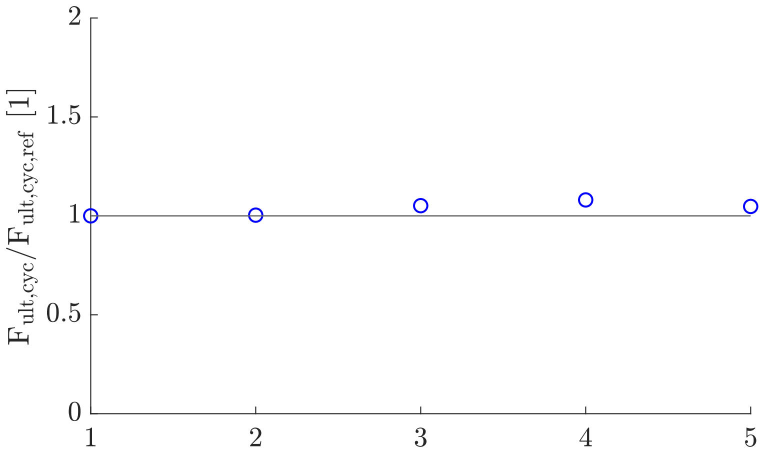

Figure 7.30: Bearing capacity over five iterations normalized to the value of the first run.

The changes of the CSR field over the iteration are depicted in Figure 7.31. There is a clear stress redistribution in which the bedding area is mostly reduced. The spatial dimension has been reduced and the large CSR values occur in the area of active bedding. The distribution depicted in Figure 7.31 (c) would, from a theoretical point of view, be the most accurate. However, because the influence in the bedding reaction of the initial field seems to be already sufficiently calculated in terms of a bearing capacity compared to the one resulting from Figure 7.31 (c).

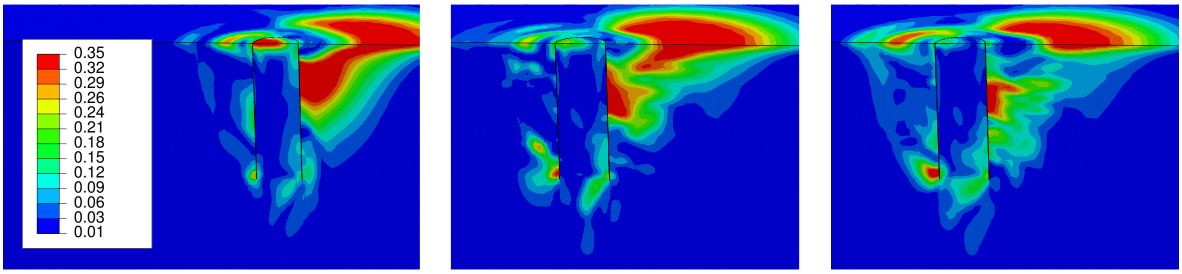

(a) (b) (c)

Figure 7.31: Spatial distribution of CSR field for first (a), third (b) and fifth iteration (c).

7.3.4 Estimation of volumetric strain due to dissipation

The settlement is composed of shear strains from the co-cyclic undrained cyclic soil response and post-cyclic volumetric strains due to dissipation of excess pore pressure (cf. Section 4.3.2). The latter is not considered here. However, with respect to the cyclic accumulation of displacements, the storm may also generate displacements that can only be considered if the volumetric strain is calculated on the basis of the dissipated pore pressure.

Many cycles with full dissipation will – in the current procedure – result in no degradation or accumulation of deformation since the last value of excess pore pressure will be zero. If excess pore pressure accumulates, the soil response gets softer and the shear modulus and angle of friction decrease. The static soil response arises (based on the aforementioned procedures). However, the soil went through N cycles and dissipated the excess pore pressure N times which in turn generated a volumetric strain. With the presented excess pore pressure estimation approaches it is also possible to roughly estimate the drained response of the structure by using undrained cyclic tests. Therefore, it is important to transfer the dissipated excess pore pressure to a volumetric strain, which is then accumulated over time. The consideration of displacements are also important, because the investigation of tilting is part of the SLS proof. Due to the dissipation additional tilting of the structure may arise. The volumetric strain is derived with the dissipated excess pore pressure (which is similar to an increase in effective stresses) by multiplying with the recompression modulus (cf. Section 4.3.2 and Section 5.2.5). Figure 7.32 shows the resulting accumulated volumetric strain. Because this value depends on the current stress conditions, the largest strains are calculated at the pile tip with 7% although there are a volumetric strains of roughly 3% in front of the pile. The volumetric strain was calculated in each cycle with the dissipated excess pore pressure ratio times the stress at mean global load and the recompression modulus of $7 \times 10^{-4}\,1/\mathrm{kPa}$. The resulting additional plastic deformation of the pile was not estimated since only the general applicability of this aspect shall be presented.

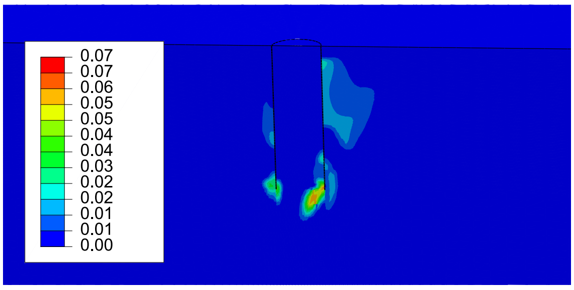

Figure 7.32: Derived volumetric strain field ε_v after 30 cycles.

7.3.5 Interim summary

Based on the presented results, there are some conclusions which can be drawn at this point:

- A small deviation within the regression analysis of the contour curve has no significant influence on the final load-bearing capacity. The influence of a simplified contour input, using only contour plots for LTR = 0, is also not very pronounced.
- There is a larger bearing capacity, if an interpolation between DSS and triaxial test results is done. This was expected since cyclic triaxial compression results will yield smaller cyclic accumulations. The use of cyclic DSS results is recommended since they can be performed much easier and will result in conservative bearing capacity estimations.
- It is not clear if load- or displacement-controlled cyclic tests shall be performed. However, if the latter are used, they lead, in this case, to a slightly larger post-cyclic capacity. The alternative incorporation of cyclic results with the semi-empirical equation according to Seed et al. (1975b) leads to larger degradations.
- An iterative calculation, in which the stresses are used after a degradation in order to calculate the CSR field again, seems not to be necessary, because the results of the first run are accurate enough related to the additional computation effort.
- The volumetric strain can be estimated and the order of magnitude seems reasonable. The incorporation in the framework can easily be done, if required.

7.4 Considering stiffness degradation

Up to this point only an isolated strength degradation for an ULS design verification based on the cyclic assessment was performed. In a next step, also the stiffness degradation will be considered (cf. Section 6.1.5). This consideration allows to account for further mechanisms since the plastic accumulated deformation is additionally considered. Figure 7.33 shows the load-displacement curves which will be discussed in this section. The same boundary conditions as for the reference case were chosen. The number of equivalent cycles is N = 30.

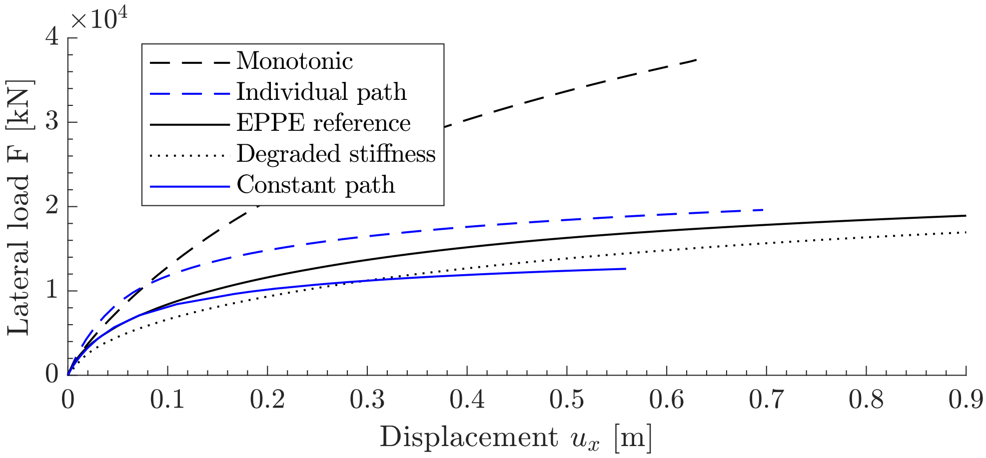

Figure 7.33: Load-displacement curves for different approaches considering the reduction of soil stiffness.

Cyclic assessment based on constant stress paths

Besides excess pore pressure contour plots, also shear strain plots were derived for different MSR, CSR and number of cycles. Jostad et al. (2014) states that for gravity based foundations and for loading from the same direction the quotient of cyclic and mean global loading can approximately be used as the quotient of shear stresses within the soil elements. For the reference system with symmetric one-way loading the global LTR value is 1. The shear stress - shear strain curves are derived for this condition. The evaluation is done based on LTR and not MSR; however, different stress - strain responses arise for the different evaluation approaches. The accuracy of the LTR model assumption can be compared with the LTR field for the reference case in Figure 7.4. A hardening curve for a LTR value of 1 and 30 cycles may be used within all elements without the additional degradation of the friction angle. The asymptotic value is not the arctangent of the friction angle since over the course of the cyclic DSS tests the vertical stress decreases. Starting from the monotonic value the friction angle is reduced for increasing shear strains up to the liquefaction criterion of approximately 2.5%. For larger shear strains, liquefaction occurred with an associated friction angle of nearly zero. In order to incorporate this effect in the FE model, the bearing capacity is reduced independent on the actual friction angle mobilisation. The asymptotic value of the total stress-strain curve indicates a mainly plastic behaviour and is interpreted as mobilised friction angle. For the cyclic curve, the sum of cyclic and mean shear strain and the sum of shear stresses is derived for the load path of LTR = 1. The idea is that in this stress-strain response all effects – including changes in stresses due to excess pore pressures – are included and, thus, any degradation based on the excess pore pressure ratio R_u is obsolete. The same curve is used for all integration points. In order to show the extent of this model assumption, the load-displacement curve is shown in Figure 7.33. No dissipation is considered and especially, the magnitude of global cyclic load is not taken into account, but only the load type. The resulting load-displacement curve (and hence the bearing capacity) agree with the reference approach, although the model assumption should not be neglected and the results should be treated with caution. The assumption of LTR = 1 based on the quotient of global loads agrees with the integration-point specific distribution of the LTR value – at least in the upper half of the passive side. This region is most important for bedding resistance. The derivation of the equivalent number can be done with an accumulation procedure (described in Appendix C), but the accuracy of such an approach is at least debatable. Especially for layered soil, this model assumption may not be accurate enough anymore. The angle of internal friction was derived to $\varphi' = 17°$ at a shear strain value of 10%. By using this value in combination with monotonic p-y curves, a bearing capacity of 11.3 MN can be derived. This value is smaller than the one derived by finite elements. The degradation of each element to such an extent is at first glance too much, however, not all elements bear the load which acts on the monopile. From the equivalent shear stress and the CSR field, the main area of bedding resistance is known. Besides all other elements, which do not directly contribute to the pile capacity, these elements are degraded. A degradation of additional elements may not even be required. Nevertheless, this is a very simple example with homogenous soil which rarely occurs in reality.

Cyclic assessment based on individual stress paths

In order to consider the conditions in each element and be overall more realistic with induced damage, all integration points need to be analysed individually. Therefore, the excess pore pressure ratio R_u is derived based on CSR and LTR as well as N_{eq}. The subsequent dissipation analysis yields a post dissipated excess pore pressure ratio field which can then be transferred again into a post-dissipated field of number of equivalent cycles. Therefore, less damage is induced into each integration point compared to the approach without any dissipation. In the case where all excess pore pressure is dissipated, this value would be zero (N = 0). For monotonic load conditions (large LTR) and for zero equivalent cycles, the monotonic soil response is present. Figure 7.33 shows the resulting load-displacement curve (labelled individual path). For the reference case the LTR varies mainly between 0 and 0.5 and the number of cycles after dissipation is 1 at largest. Hence, in front of the pile fairly monotonic behaviour is expected. In this case, the induced damage seems reasonable compared to the simplified approach of the last paragraph.

Instead of using a mobilised friction angle, the increased plastic strains can also be applied by using a degradation factor applied to the stiffness modulus including the degradation of friction angle based on the derived post-dissipated excess pore pressure ratio. This factor is derived based on the monotonic curve and the integration-point specific cyclic stress-strain curve for the derived CSR value. The reference stiffness was chosen as the oedometric stiffness which was calculated at the end of the monotonic calculation. This is of course a more simple approach than considering the exact hardening curve. The load-displacement curve is also depicted in Figure 7.33. This simplified procedure yields similar results, but

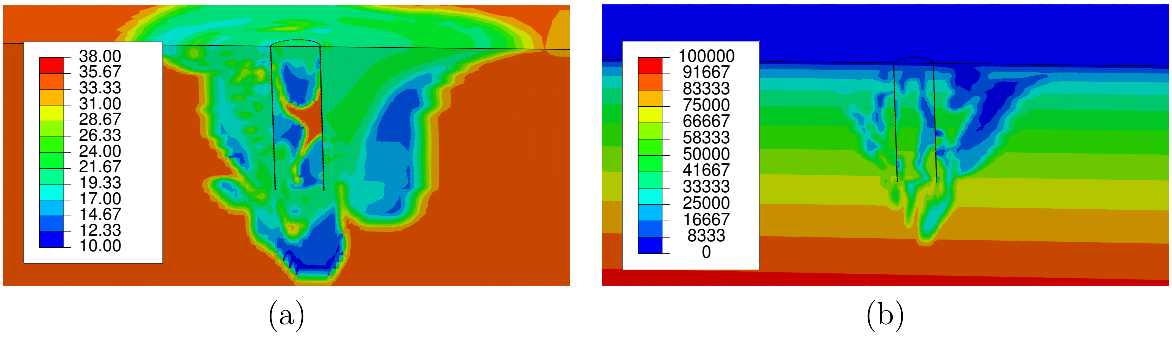

(a) (b)

Figure 7.34: Field of maximum mobilisable friction angle at a shear strain level of 10% (a) and factored (degraded) stiffness modulus field for the total component case (b).

is much easier in implementation and verification. The degraded stiffness modulus field is shown in Figure 7.34 (b). This field is derived from the monotonic and cyclic shear stress-shear strain curve for an integration point specific CSR value. Figure 7.34 (a) shows the friction angle at 10% shear strain for individual shear stress-shear strain curves. A further calculation was done for the evaluation of the mean shear strain, which results in a smaller degradation since less plastic strains occurred and can be used for the long-term structural response.

7.5 Application of SANISAND model

The general system response was presented based on explicit calculations. However, there are still some open questions regarding the correct model assumptions which is the reason why in the following section, the monopile foundation will be calculated with the calibrated SANISAND model.

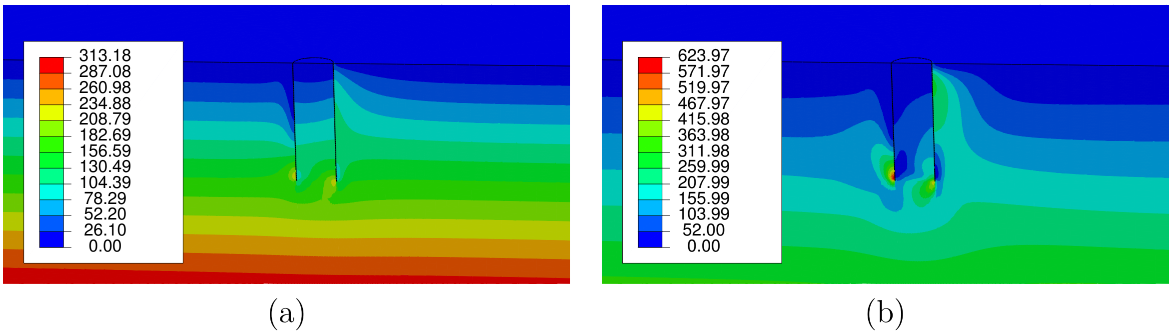

(a) (b)

Figure 7.35: Field of octahedral stress σ'_{oct} at global mean load (a) and equivalent shear stress σ'_{eq} at maximum global load (b) for reference conditions and the SANISAND model.

EPPE combined with SANISAND constitutive model

In a first step, the Mohr-Coulomb model can be exchanged with the SANISAND model in order to show the effects of hardening. The input parameters for the SANISAND model were derived for the monotonic case (Appendix A). A fully drained finite element model is used because no excess pore pressure based on the SANISAND model will be used. The dissipation step within the EPPE procedure is still performed unchanged. The objective of this comparison is to see how the distribution of excess pore pressure ratio field changes due to a more sophisticated soil model. This is of interest because it takes more time to calibrate such a sophisticated model, but it may not be necessary since the key mechanisms for generating and dissipating excess pore pressure are already sufficiently included in the reference EPPE approach.

Figure 7.35 shows the octahedral stress at global mean load (a) and equivalent shear stress at maximum global load (b) for reference conditions and the SANISAND model. The stresses increase over depth and larger stresses concentrate in the upper half of the passive side. From these values, the CSR and MSR can be derived, which are used for the derivation of excess pore pressures from cyclic laboratory tests. Figure 7.36 shows the resulting CSR field. In comparison to the EPPE approach (Figure 7.3 (d)), there is a similar spatial extension in passive pile direction and also a similar distribution around the toe of the pile. In both cases very low CSR values are derived around the point of rotation.

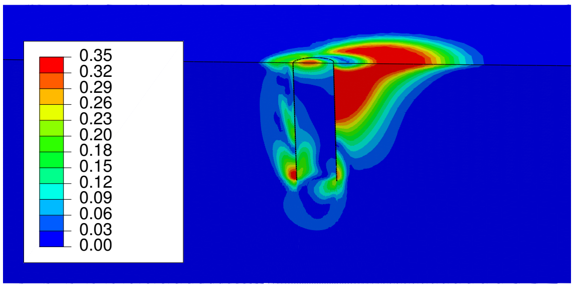

Figure 7.36: CSR field for reference conditions and the SANISAND model.

In a subsequent step, these CSR and MSR fields were used to derive the excess pore pressure ratio for N = 1. The excess pore pressure ratio R_u field is depicted in Figure 7.37 (a) with the corresponding excess pore pressure Δu in Figure 7.37 (b). The induced damage is more severe in terms of its spatial distribution compared to the one derived with the reference EPPE approach (Figure 7.5 (a)) with a large damaged area at the toe of the pile and on the passive side. The presented field is used to derive integration point specific decay curves and perform a superposition. The final post-dissipated R_u field is depicted in Figure 7.37 (c) (with the corresponding Δu in Figure 7.37 (d)). The spatial distribution is similar, but there are still more areas in the lower pile region and inside the pile which are degraded. The resulting damage is more pile-near.

The induced damage is, in this case, smaller with a very similar final spatial distribution compared to the case based on the Mohr-Coloumb model.

Results of implicit cyclic loading calculation

Since the SANISAND model is able to capture cyclic loading, the system response is analysed under repeated loading and the results are compared to the explicit approach with the cyclically calibrated input parameters. The low number of cycles of N = 20

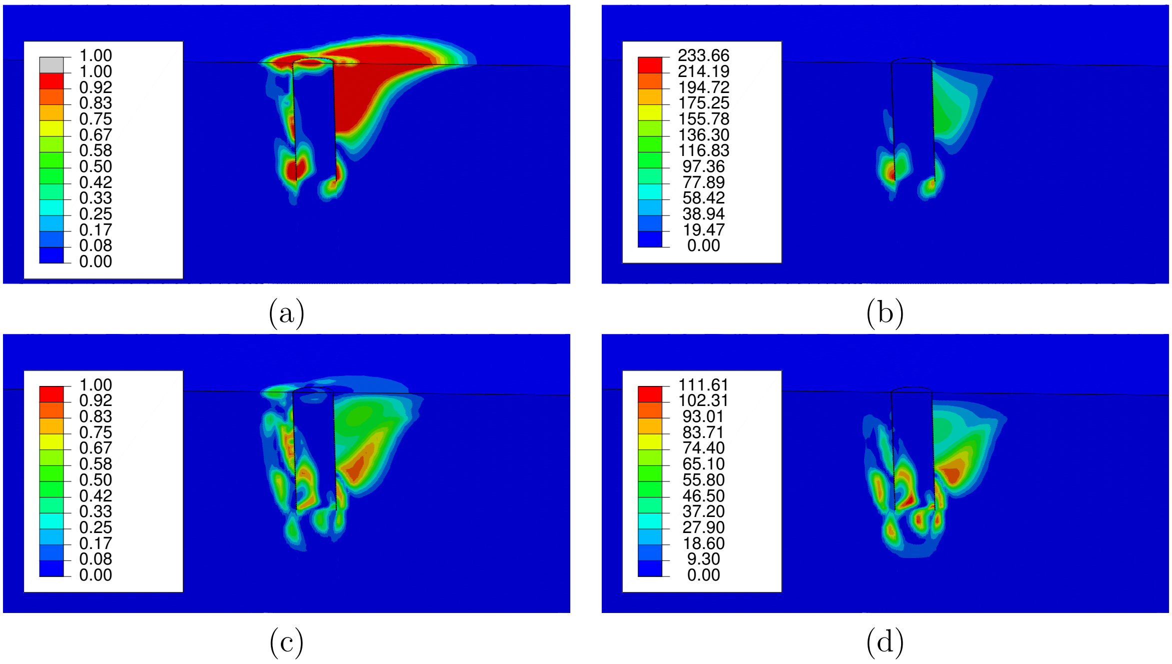

(a) (b)

(c) (d)

Figure 7.37: Excess pore pressure ratio field R_u (a) and excess pore pressure field Δu after N = 1 (b) and excess pore pressure ratio field R_u (c) and excess pore pressure field Δu after dissipation (d) by using monotonic SANISAND model in EPPE approach.

reduces the accumulation of large numerical errors. The maximum load of the symmetric two-way loading was reduced to 4 MN with a load eccentricity of e = 40 m, because the SANISAND model overestimates the induced damage within the soil. The reason that the more sophisticated model does not adequately estimate the induced cyclic damage is that the current version of the model does not describe the dilatant and contractant soil response accurate enough (cf. Appendix Figure A.15). For a comparison with the EPPE approach with a Mohr-Coulomb constitutive model, Figure 7.39 shows the load-displacement curve at mudline. The finite element model was not hydraulic-mechanically coupled. The resulting structure response is stiffer and results for a larger displacement could not be derived due to numerical issues.

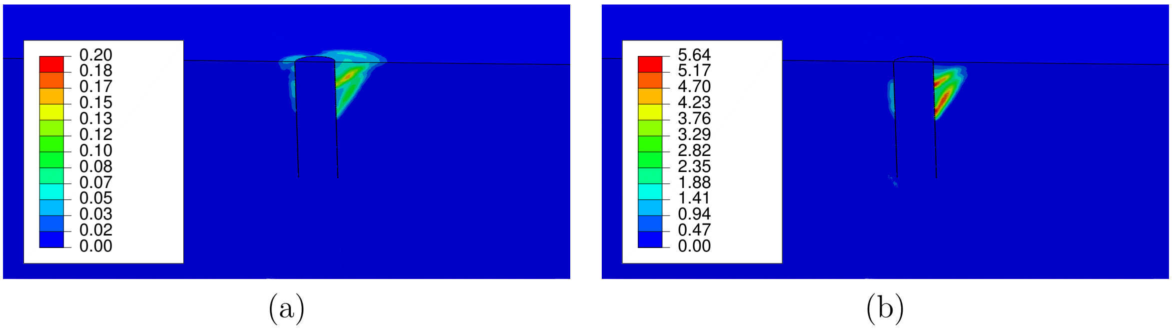

(a) (b)

Figure 7.38: Excess pore pressure ratio field R_u for EPPE approach with a global maximum load of 4 MN (a) and excess pore pressure ratio Δu (b).

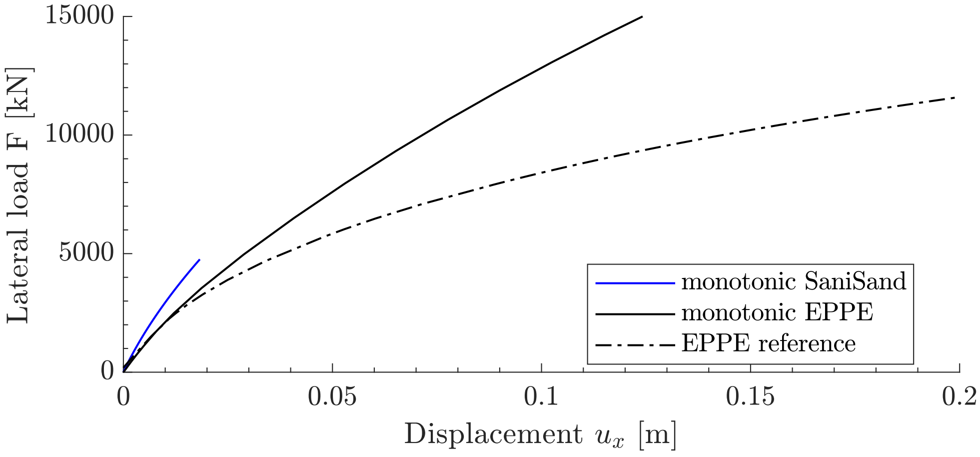

Figure 7.39: Comparison of monotonic response by using SANISAND model for the reference monopile with already presented EPPE results.

Figure 7.38 (a) shows the EPPE procedure applied to the same boundary conditions (reduced load) for a better comparability. Due to the decreased global load there is obviously less damage induced. No element is fully liquefied. The excess pore pressure Δu is depicted in Figure 7.38 (b). The excess pore pressure is quite small, because although there are larger octahedral stresses, only approximately 10% of these are calculated to be excess pore pressure.

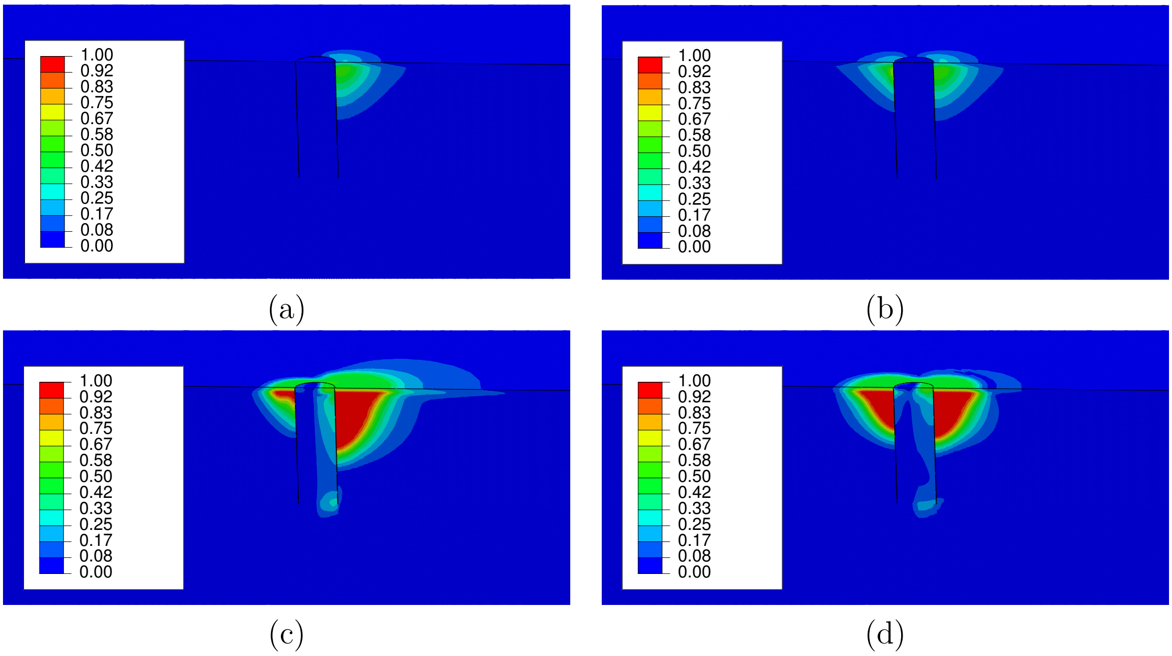

(a) (b)

(c) (d)

Figure 7.40: Excess pore pressure ratio R_u field for symmetric one-way loading (a, c) and symmetric two-way loading (b, d) and for a permeability of 3.7×10^{-4} m/s (a, b) and 1×10^{-6} m/s (c, d).

Figure 7.40 (a) shows the implicitly calculated excess pore pressure normalized to the same octahedral stress (at global mean load) as used in the EPPE approach. The excess pore pressure was read at the last peak of the global harmonic load. The load period was set to 10 s. The damage is mainly induced in the upper part of the pile. There are no additional areas of partial liquefaction around the pile toe or within the pile. Damage is induced in a same area compared to the explicitly calculated case. The excess pore pressure ratio R_u is however significantly larger. This was expected because the SANISAND model overestimated the number of cycles to liquefaction when calibrated. Moreover, liquefaction in this context must be taken with caution, because herein the stresses change over the course of the calculation and do furthermore redistribute. A criterion which bases on the initial octahedral stress is, hence, not a sound criterion for liquefaction.

At this point, the influence of different initial void ratios could be investigated. However, a detailed analysis of an implicit calculation of the reference structure is not in the focus of this thesis. Nevertheless, the influence between symmetric one-way loading as well as symmetric two-way loading is shown in Figure 7.40. The excess pore pressure decreases with increasing distance to the foundation and shows a maximum value right below the surface. Figure 7.40 (c) shows results for a decreased permeability. If the excess pore pressure cannot dissipate, large values accumulate over time and induce larger damage on the loaded pile side. One difference to the EPPE procedure can be seen for a two-way load. Figure 7.40 (c) and (d) show a symmetric two-way loading with the same global load amplitude as used for Figure 7.40 (a). In case of symmetric two-way loading, damage accumulates on both piles sides, whereas in EPPE only one quarter of a cycle is calculated and hence only one side of the pile experiences degradation. However, this effect does not influence the pile capacity, because the same direction is used for both calculation steps. Figure 7.40 shows that also for two-way loading, a decreased permeability leads to larger induced damages.

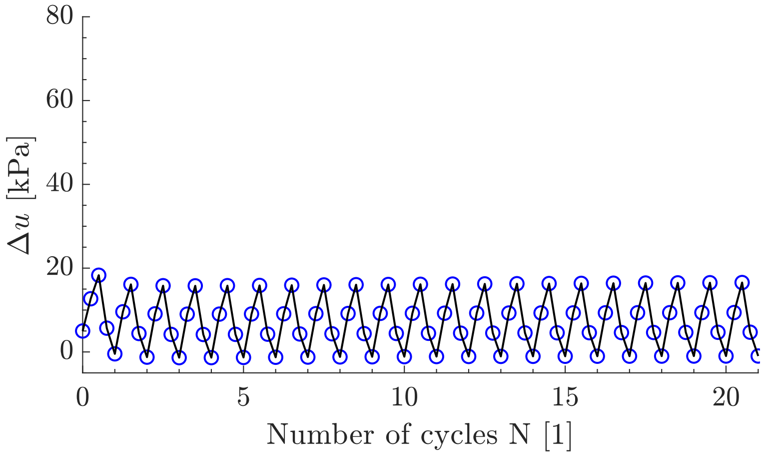

Figure 7.41: Excess pore pressure ratio Δu build-up for point 8 m/0 m/-8 m for symmetric one-way loading.

For an implicit calculation, also the accumulation effect can be plotted for the integration points. Exemplarily, the excess pore pressure Δu over the number of cycles is plotted in Figure 7.41 for one integration point. There is no significant accumulation effect, because of the large permeability. This agrees well with the final excess pore pressure field depicted in Figure 7.40 (a).

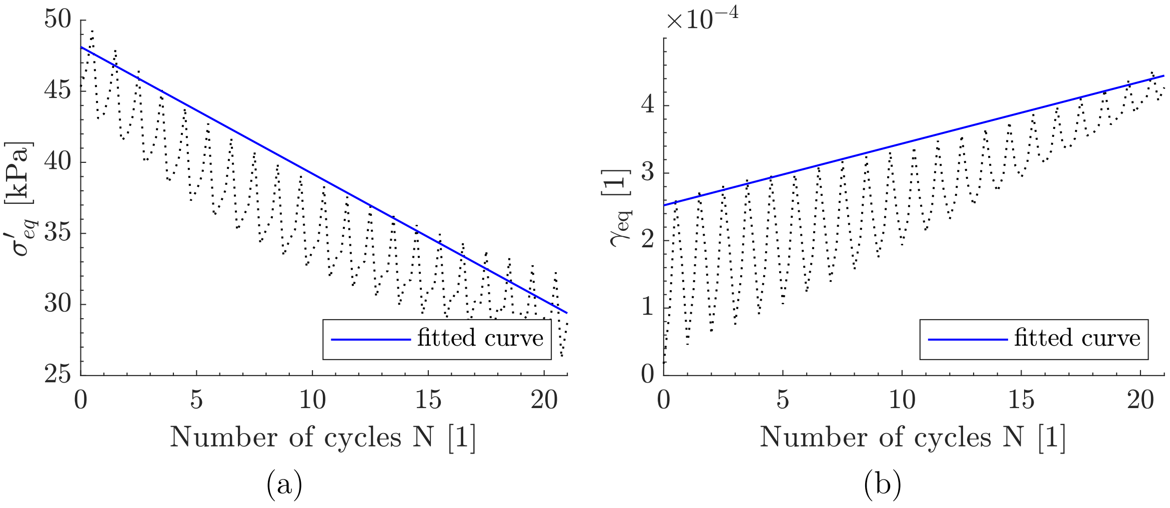

Figure 7.42: Equivalent shear stress σ'_{eq} (a) and equivalent shear strain γ_{eq} (b) over the number of cycles with applied regression for 8 m/0 m/-8 m.

Instead of investigating the soil-structure interaction in greater detail, the results of the finite element model will be used to investigate qualitatively some of the open questions. In order to investigate the different soil element response by means of load-controlled and displacement-controlled boundary conditions, the stress and strain conditions will be evaluated around the monopile. Herein, displacement-controlled conditions can only occur due to stress-redistributions. For this analysis, the equivalent shear stress as well as the equivalent shear strain are plotted over the number of cycles. If load-controlled conditions are present, the equivalent shear stress σ'_{eq} (amplitude and mean value) will be constant over the course of the calculation; the same applies to the equivalent shear strain $\gamma_{eq,cyc}$ (Figure 7.42 (a)). Therefore, the peak values for both indicators for each integration point are evaluated over the 20 cycles, which is the assumed number of cycles for which no significant numerical error may accumulate for this implicit model.

The inclination of the regression line is used as an indicator for the load type (Figure 7.42), which allows three categories to be differentiated. The stress can be constant and the shear strain can change (or vice versa) or there can be elements for which both values change significantly over the calculation. Figure 7.43 shows a comparison of the regression inclination. The blue points have a larger inclination in stress than in strain. This means that either the strain is almost constant and the stress changes or the strain is not constant, but the change in stress is larger compared to the change in strain. Thereby, Figure 7.43 (a) and (b) show results for symmetric one-way loading while symmetric two-way loading is depicted in (c) and (d). The permeability is 3.7×10^{-4} m/s in (a) and (c) and 1×10^{-6} m/s in (b) and (d). Either way for all cases, over the course of the calculation no pattern for displacement-controlled conditions can be seen. Some areas

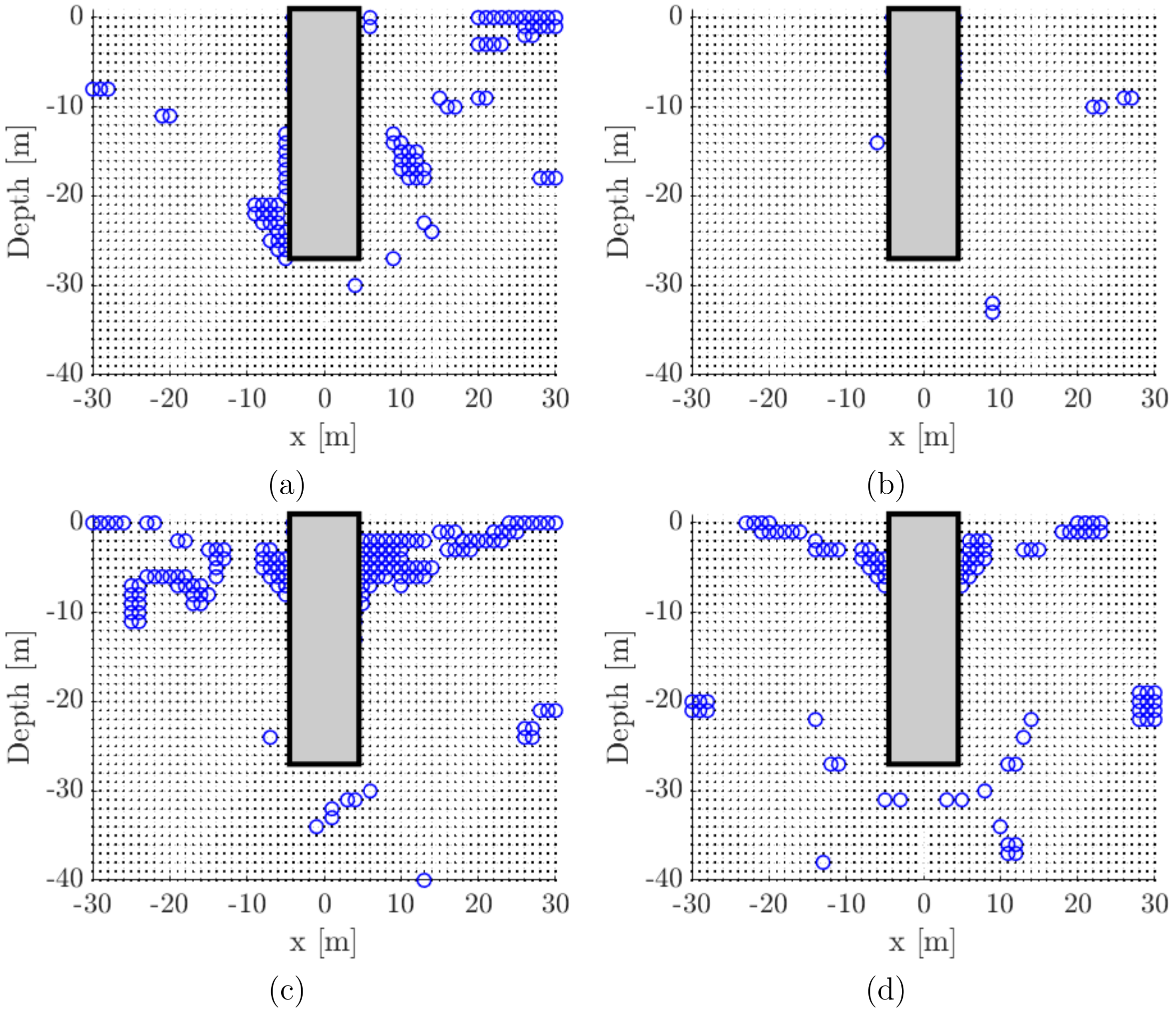

(a) (b) (c) (d)

Figure 7.43: Differentiation between load- and displacement-controlled (blue) test conditions around a monopile foundation for symmetric one-way loading (a, b) and symmetric two-way loading (c, d) and for a permeability of 3.7×10^{-4} m/s (a, c) and 1×10^{-6} m/s (b, d).

arise in case of a smaller permeability in the upper pile region due to a larger excess pore pressure accumulation (Figure 7.43 (c,d)). While this very simplified analysis is not a sufficient criterion, it does suggest that cyclic load-controlled tests are representative for the element conditions. Further investigations are necessary to make a well-founded statement in this regard.

Besides the analysis of the load type, it is also possible to investigate how the cyclic loading characteristics change over the course of the calculation. Therefore, the CSR is calculated by using the octahedral stress prior to each individual cycle and the half of the span of the equivalent shear stress in order to calculate the cyclic shear stress amplitude (Figure 7.44). A changed CSR value is derived for each new cycle. The results for point 8 m/0 m/-8 m are depicted in Figure 7.45 (a) with a comparison of the CSR which is calculated with the EPPE approach (with SANISAND as a constitutive model for a global load of 4 MN). The

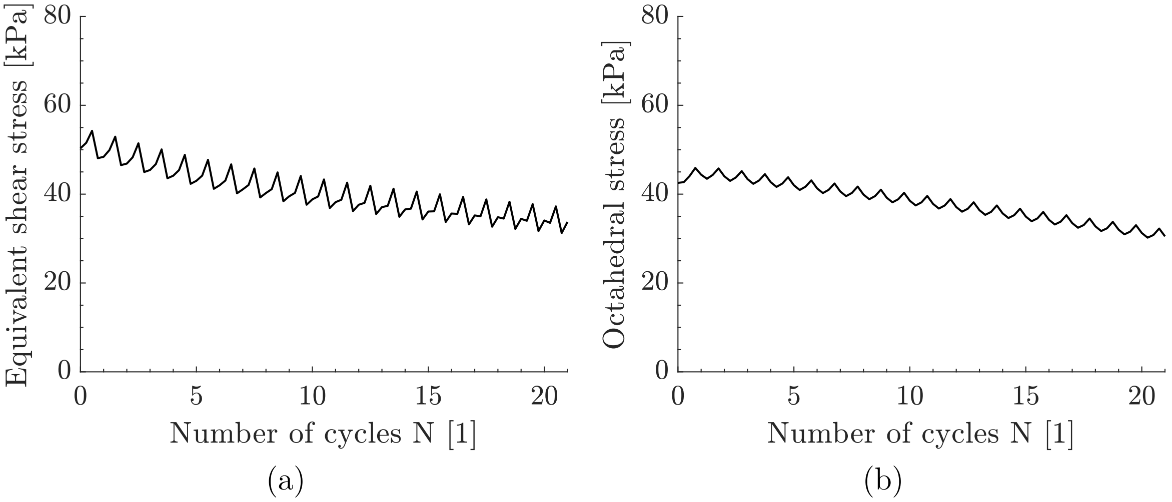

Figure 7.44: Equivalent shear stress σ'_{eq} (a) and octahedral stress σ'_{oct} (b) over number of cycles for point 8 m/0 m/-8 m.

same is subsequently done with the derivation of MSR. Figure 7.45 (b) shows the results for one integration point. The LTR is roughly at 20 and does not change significantly, which means that due to stress redistributions the load type within one soil element is not changed. The CSR for the explicit case is larger compared to the one from the implicit calculation. This can be seen as more conservative. In case of the MSR, the explicit calculation assumes a smaller value, but does not influence the soil response in a way the CSR does. The estimation of MSR in terms of the more influencing parameter CSR in the EPPE procedure is conservative and can, hence, be seen as reasonable.

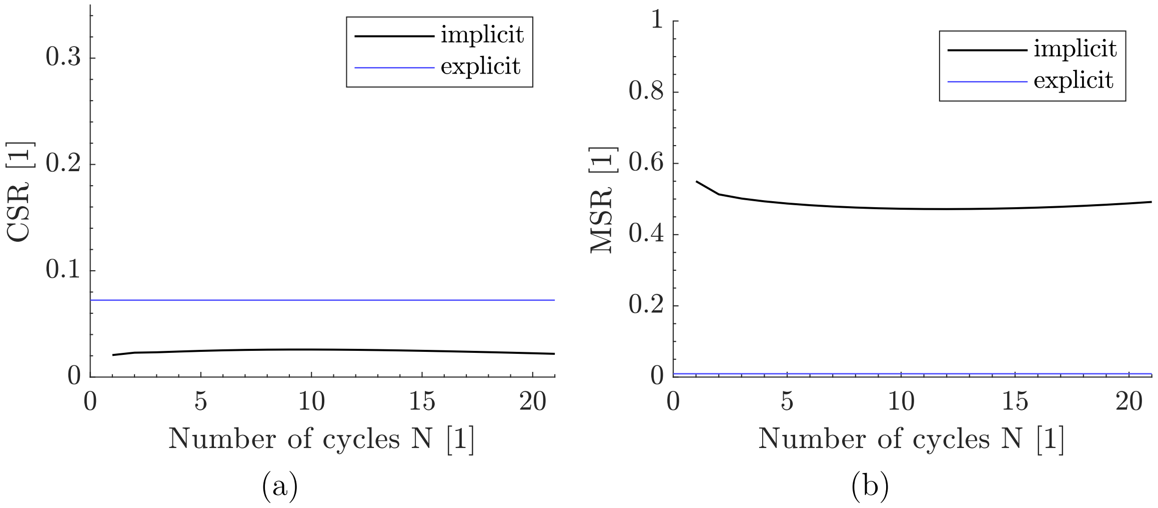

Figure 7.45: CSR (a) and MSR (b) from implicit calculation with comparison of explicit EPPE approach for point 8 m/0 m/-8 m based on an evaluation of a monotonic calculation with the SANISAND model.

Interim summary

An implicit calculation with the reference monopile model was performed and the results for the integration points were analysed in terms of different aspects. The constitutive model was also used in conjunction with the explicit EPPE approach. Some conclusions can be drawn based on the simplified analysis with a homogenous soil layer and the SANISAND model:

- The cyclic back-calculation of the initial reference system is not possible with the available version of the model. The SANISAND model overestimates the cyclic damage and shows some convergence problems. A calculation was possible with a smaller load.
- The monotonic load-displacement curve is stiffer compared to the one of the Mohr-Coulomb model. When using a more sophisticated constitutive model within the EPPE approach, a different excess pore pressure field R_u arises. In this case, the derived damage is less compared to the reference EPPE procedure. If a calculation with a newer SANISAND version is done, there may be a better agreement of induced damage. The results look very promising.
- The excess pore pressure ratio calculated explicitly is less compared to the implicitly calculated R_u field. However, this was to be expected because of the overestimation of the induced damage by the sophisticated soil model.
- When performing an implicit calculation, the resulting excess pore pressure field is, compared to the EPPE approach, more close to the pile and there are less individual areas in which liquefaction occurs, but there is a much more pronounced area on the passive side.
- For a different permeability and a different global load type, there are the expected changes in excess pore pressure build-up.
- The presence of load- or displacement-controlled conditions was investigated and it was shown that the model assumption of this thesis, namely load-controlled tests, is applicable. Even though displacement-controlled tests need to be used or a combination of both, the capacity would only be slightly larger, as presented in the last section.
- The derived CSR and MSR values do change over the course of the calculation, but the derived values for the very same boundary conditions calculated with the EPPE approach yield conservative CSR values. This means that the procedure can be applied in its current form. A more detailed analysis with a SANISAND-MS model is necessary in future .

7.6 Parameter study on monopile foundation

The main influencing parameters for the EPPE approach have repeatedly been addressed and some simplifications and their effects have been explained. The different concepts and the impact of variation within these have been presented so that a parameter study on the boundary conditions of the reference system can follow with consideration of stiffness reduction. Herein, the boundary conditions of the reference system, presented in the beginning of this chapter, are used – if not stated differently.

7.6.1 Effect of number of cycles

Figure 7.46 shows the influence on the load-displacement curve for a different number of cycles for the reference configuration. As already mentioned, after a specific number of cycles a stable response settles in when using the design dissipation. Hence, the largest influence can be seen between the first few cycles. The incremental degradation in bearing capacity increases with increasing number of cycles. Generally, for an increased number of cycles, the capacity degrades.

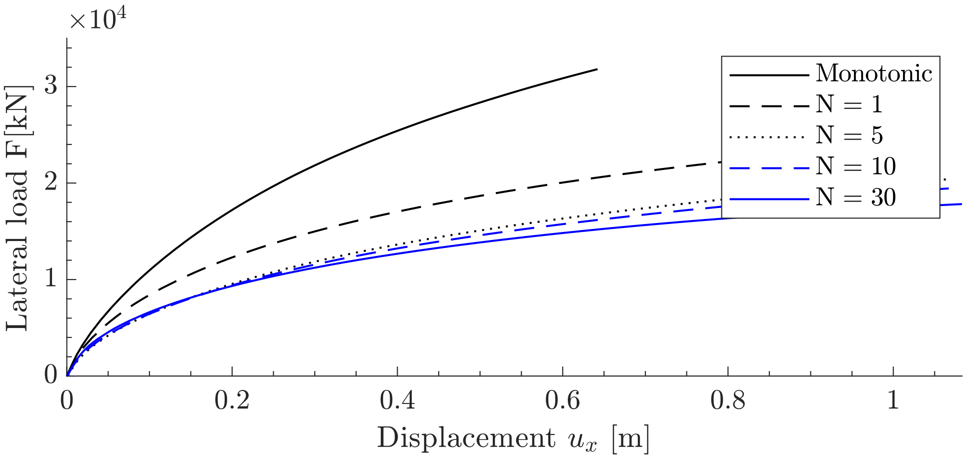

Figure 7.46: Load-displacement curves for different number of cycles for the reference system and EPPE approach with consideration of reduced stiffness.

7.6.2 Effect of loading condition

The load was applied as a symmetric one-way loading. The influence of different load types was already explained. The effect of an altered maximum cyclic lateral load for the reference configuration is shown in Figure 7.47. The number of cycles is kept at 30, but the maximum global load was changed from 20% to values between 5% and 20% related to the monotonic bearing capacity. For an increase in global load, the CSR values increase and subsequently the damage around the structure also increases. This results in a decreased bearing capacity and larger deformation.

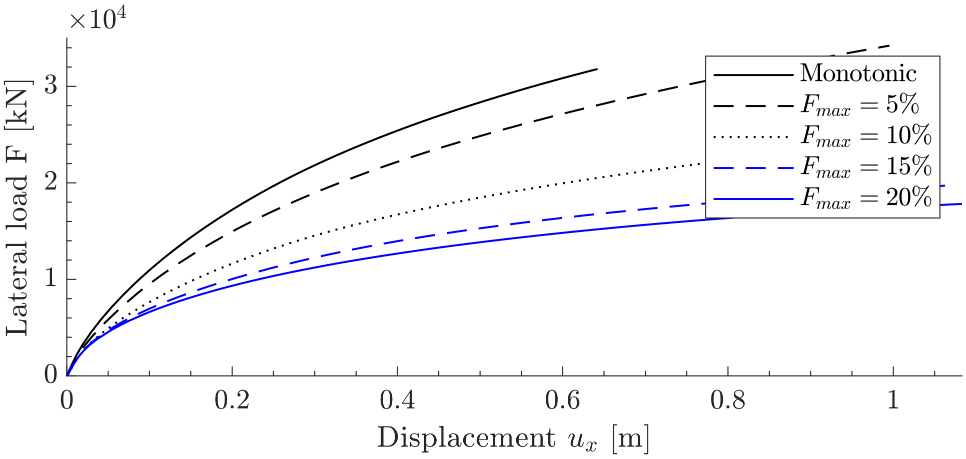

Figure 7.47: Load-displacement curves for different maximum lateral loads for symmetric one-way loading for the reference system and EPPE approach with consideration of reduced stiffness.

7.6.3 Effect of soil permeability

The effect of the soil permeability corresponds with the load frequency. It influences the quotient of excess pore pressure generation and dissipation. In this case, the storm period is kept constant with 10 s and a change in permeability will have a significant influence. Figure 7.48 shows the load-displacement curves for the reference system with permeabilities k_f between 1×10^{-3} m/s and 1×10^{-5} m/s. In addition to load amplitude and number of cycles, permeability has a major influence on the accumulation under partially drained conditions. The general distribution of the CSR is similar, however for a lower permeability, larger degradations occur since a smaller amount dissipates. For a lower permeability, more excess pore pressure accumulates or rather less excess pore pressure dissipates. For a permeability of 1×10^{-5} m/s an almost undrained accumulation response occurs.

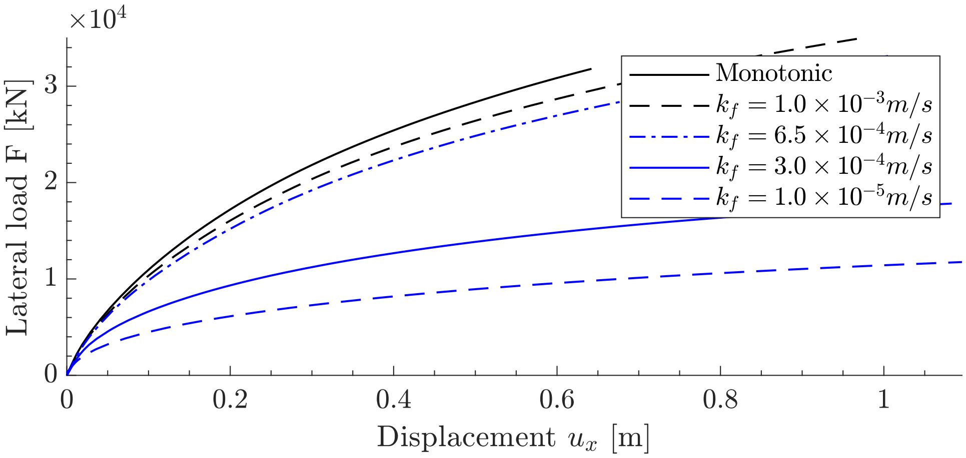

Figure 7.48: Load-displacement curves for different soil permeabilities for the reference system and EPPE approach with consideration of reduced stiffness.

The total excess pore pressure accumulation is influenced by the inherent soil response and the system boundary conditions. One main aspect is the presence of clayey layers for instance a clay or a silt layer in the upper soil stratigraphy. Naturally, a thin clay layer will change the complete dissipation behaviour and, hence, the degradation field which influences the bearing behaviour. One analysis was made in which the influence of a cohesive soil layer with a thickness of 2.0 m (from -5 m to -7 m) was investigated. The influence on the excess pore pressure field is depicted in Figure 7.49. For this purely academic example, the reference contour plots for the excess pore pressure generation were also used for the cohesive layer. The accumulation at this cohesive layer can clearly be seen and underlines the complex non-linear behaviour, which leads to the fact that numerical calculations are inevitable for a design.

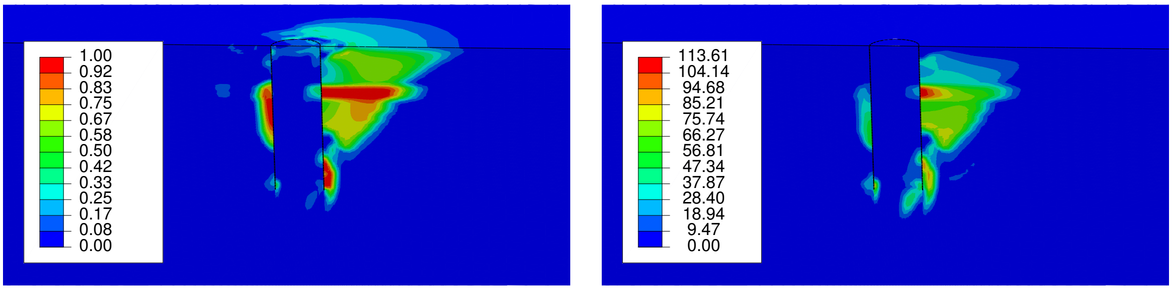

(a) (b)

Figure 7.49: Excess pore pressure ratio R_u (a) and excess pore pressure Δu (b) after dissipation for clay layer ($k_f = 1 \times 10^{-7}$ m/s) from -5 m to -7 m.

Depending on the soil genesis, the permeability is usually assumed to be anisotropic. Booker et al. (1976) showed that the permeability does not change significantly during liquefaction. However, the horizontal permeability can often be assumed to be 10-times larger than the vertical permeability. This can also be incorporated in the finite element model ($k_{f,v} = 3.0 \times 10^{-5}$ and $k_{f,h} = 3.0 \times 10^{-4}$). From Figure 7.48 the almost monotonic response for a permeability of $k_f = 1.0 \times 10^{-3}$ can be seen. Thus, the vertical permeability was scaled to $k_{f,v} = 3.0 \times 10^{-5}$ instead of scaling the horizontal permeability to $k_{f,h} = 3.0 \times 10^{-3}$ in relation to the reference value of $k_f = 3.0 \times 10^{-4}$ to make the influence of the anisotropic permeability in this academic example clearer. Figure 7.50 shows the influence of anisotropic permeability. The spatial expansion in the horizontal direction is evident since less excess pore pressure can be dissipated to the surface in 10 s. Dependent on the site-conditions, this aspect may be incorporated into the EPPE approach. The anisotropic dissipation yields smaller capacities compared to the reference approach (Figure 7.17) since the excess pore pressure can travel less easily through the layers.

7.6.4 Effect of pile geometry

Figure 7.51 shows exemplarily the influence of different pile geometries. The lateral load is kept constant similar to the reference model ($F_{min} = 0$ MN and $F_{max} = 13.6$ MN). This means that the load level is not equal for all investigated cases. The value ζ_b is

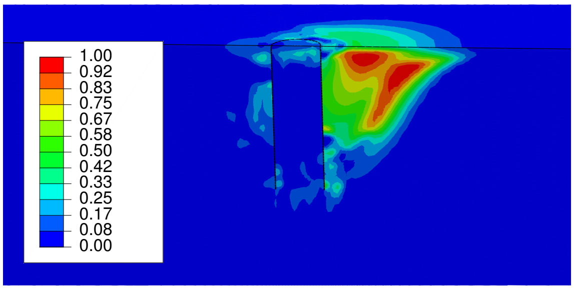

Figure 7.50: Final excess pore pressure ratio field R_u for anisotropic soil permeability with smaller k_f value in vertical direction.

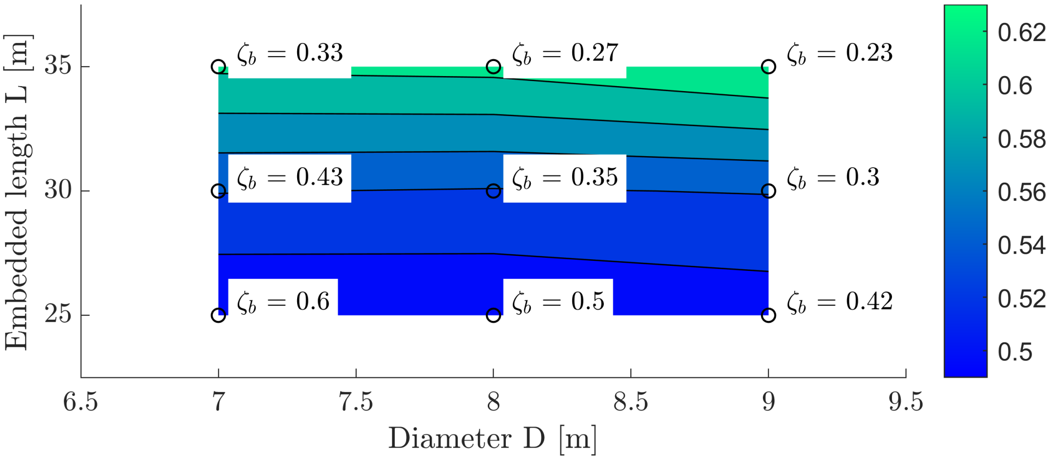

Figure 7.51: Overview of post-cyclic capacity for different diameters and pile lengths for N = 30 cycles and the reference soil with reference load condition.

depicted in Figure 7.51. The load level decreases for a larger pile diameter and a larger embedded length. Regarding the post-cyclic capacity, the cyclic degradation decreases with increasing diameter and pile length. The degradation is directly correlated to the spatial distribution of the CSR field which correlates to the monotonic bearing capacity and the applied maximum global lateral load (cf. Figure 7.16). For the given load there is a degradation of capacity in the worst case of 50%.

The largest post-cyclic capacity is estimated for the smallest load level. Figure 7.52 shows a comparison between different pile lengths for a diameter of D = 8 m regarding the excess pore pressure ratio. Hence, two effects influence the structural response. The first is the bearing behaviour of pile and the second is the load level. The area of liquefaction decreases for increasing embedded length and so does the spatial distribution. For an increasing embedded length, there is less influence at the pile toe and generally in the lower part of the pile. It can clearly be seen, that for larger dimensions less damage is present within the soil for the post-cyclic response.

Figure 7.53 shows related CSR fields for a diameter of 8 m and different embedded lengths. The degradation decreases for an increasing pile length. Also the load bearing behaviour by means of the spatial distribution is changed. Similar to the excess pore pressure ratio,

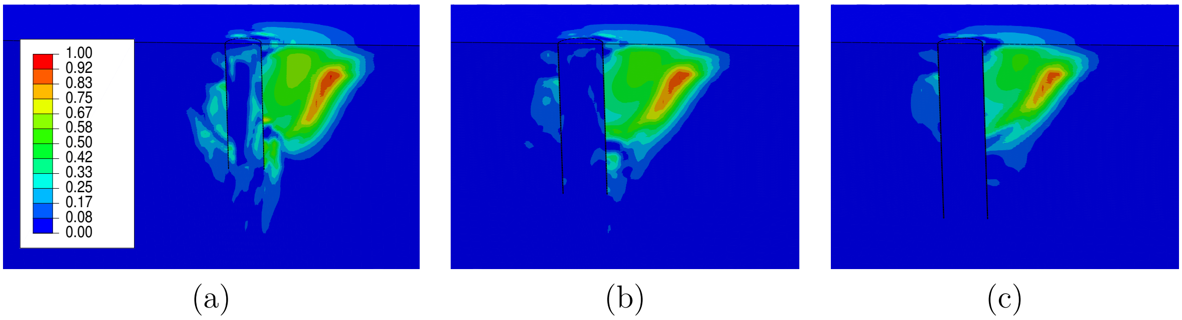

(a) (b) (c)

Figure 7.52: Excess pore pressure ratio field R_u for an embedded length of L = 25 m (a), L = 30 m (b) and L = 35 m (c) for a pile diameter of D = 8 m.

there is less damage in the lower part of the pile for increasing pile length. The location of the largest CSR values moves upwards. The area in which the laterally loaded pile activates its bedding can clearly be seen.

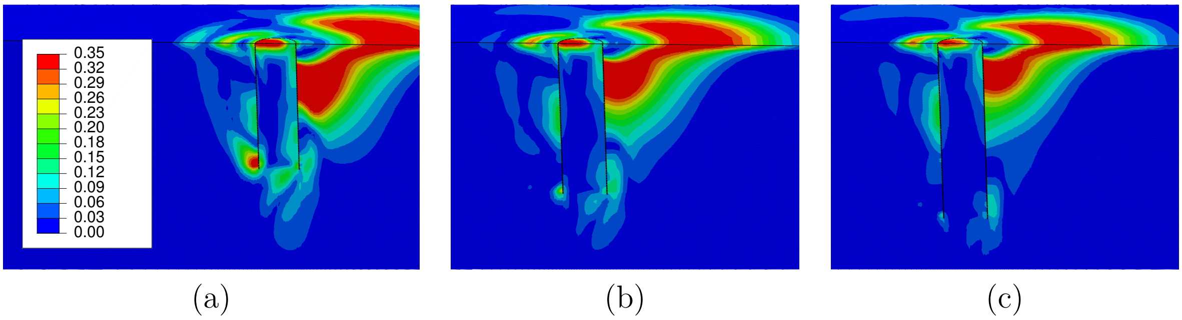

(a) (b) (c)

Figure 7.53: CSR field for an embedded length of L = 25 m (a), L = 30 m (b) and L = 35 m (c) for a pile diameter of D = 8 m.

8 Conclusion and outlook

8.1 Discussion of the results

The proof against cyclic loading is an essential part within the design. This work contributes to the current research on cyclically loaded offshore foundations with the aim of estimating the cyclic degradation of soil-structure interaction under excess pore pressure build-up considering partially drained conditions for sandy soils. Regardless of the applied load type, whether using an irregular storm loading or a simplified equivalent number of cycles, the cyclic effect on the structure must be taken into account according to the standards. However, the standards do not specify a uniform procedure. Only the DNV-RP-C212 specifies an explicit procedure with high-quality cyclic laboratory results. Currently, there is no consistent concept for verification against excess pore pressure accumulation as well as cyclic accumulation of deformation, which is reflected in the mentioned inconsistent procedures within the framework of practical projects. The research presented is particularly concerned with a simple, explicit estimation procedure that can be easily evaluated by engineering judgment.

Cyclic soil response

The general soil behaviour under cyclic loading is presented with load- and displacement-controlled cyclic direct simple shear tests. Even though cyclic soil behaviour is investigated for many years, such a detailed investigation of one sandy material for all different boundary conditions, as given in this thesis, is only present for a few sands which are often used in scientific investigations. With the results of the cyclic laboratory tests, one semi-empirical equation for excess pore pressure estimation is calibrated and additionally contour plots are derived. From the different investigated mathematical frameworks for the derivation of contour plots, one approach could be assessed as advantageous. With this equation, the excess pore pressure accumulation for different mean stresses is derived in order to be used in the numerical explicit framework. Different mathematical frameworks are investigated and one equation is assessed as especially applicable due to its easy use and high controllability.

Besides the contour plots for excess pore pressure, also shear strain contour plots are derived. Since cyclic data is present for different relative densities, a scaling approach is investigated as well. Different relative densities and vertical stresses are examined and the results are compared with a scaling approach for a fast estimation of contour plots. Scaling of existing contour plots can be very helpful if not enough tests for one particular soil are present. The results of the scaling investigations are compared with a large amount of literature data and a good agreement is found.

The performance of cyclic triaxial tests is very time consuming, but in order to show the influence for one specific soil, several symmetric two-way and one-way cyclic loading tests are carried out. The induced damage from cyclic compression triaxial tests under isotropic dissipation is significantly less compared to the cyclic direct simple shear (DSS) tests. Regarding cyclic tests, DSS tests are faster to perform even though triaxial tests will give higher quality results, but also a smaller (non-conservative) degradation. Nevertheless, the cyclic direct simple shear tests showed a large deviation under the same boundary conditions. This could possibly have been prevented by using dry pluviation instead of dry tamping for all tests and also including a pre-shear phase. This is however not done in order to not influence the results in any way, but to have a cyclic database without preconditioning. The consideration of pre-shearing can enhance the cyclic resistance. Also influences between different soil preparation procedures should not be neglected. A pluviated soil sample will fail after a smaller number of cycles than a tamped one.

The external global load is mainly load-controlled but due to stress redistributions or other model assumption displacement-controlled element boundary conditions can arise. This is important because there is a large deviation between both responses when comparing the trend of excess pore pressure over the number of cycles. When analysing the soil response of an implicit model, mainly load-controlled conditions occur. Since cyclic results are present, a transfer from load- to displacement-controlled conditions is performed, but the accuracy is improvable.

Calibration of implicit model

The SANISAND model is able to realistically reproduce many different geotechnical scenarios under cyclic and monotonic loading. With faster computers and better algorithms, the use of more sophisticated models will become more popular. Implicit computation with an appropriate soil model can improve the understanding of soil-structure interaction under complex loading conditions such as cyclic loading. However, the calibration is not trivial, and not all soil properties can be calibrated in one calibration set. Regarding the reference soil, the model is first calibrated with the standard critical state parameters and then an objective function is used in conjunction with a genetic optimization algorithm. This algorithm can also be used in case a newer version is available. When calibrated, the SANISAND model can reproduce a wide range of stresses and void ratios as well as cyclic and monotonic loading. However when comparing the number of cycles to liquefaction for different element tests, the SANISAND tends to underestimate the number of cycles to liquefaction and the calculated results should therefore be treated with caution.

EPPE approach

This thesis highlights how excess pore pressure accumulates under different conditions and how this can be approximated with a simple numerical framework. The main objective of this work is to develop a methodology as simple and transparent as possible for predicting the bearing behaviour of a cyclically loaded foundation based on cyclic element tests, to validate it with experiments, and to make it easier for engineers to implement the procedure. A generic methodology for the estimation of excess pore pressure accumulation around cyclically loaded foundation is developed. There are some model assumptions in order to keep the approach comprehensible. The influences of these simplifications on the bearing capacity have been discussed and all assumptions in the reference procedure can be justified. The concept can also be used without a degradation of the stiffness and with a simplified excess pore pressure estimation, for instance according to Seed et al. (1975b). There is a larger bearing capacity, if an interpolation between cyclic direct simple shear (DSS) and cyclic triaxial test results is done. This is expected since cyclic triaxial compression results will yield smaller cyclic accumulations. The use of cyclic DSS results is recommended since they can be performed much easier and will result in conservative bearing capacity estimations. Although the use of contour plots is favourable, the author stresses that the use of a semi-empirical equation approach is reasonable for instance when only a limited number of tests are available. A small deviation within the regression analysis of the contour curve has no significant influence on the final load-bearing capacity. The influence of a simplified contour input, using only contour plots for LTR = 0, is also not very pronounced.

The main part of this thesis and the related calculations are based on a constant equivalent number of load cycles, although this is not feasible for a practical application. Therefore, for practical applications, a detailed procedure for the consideration of a design storm is presented in Appendix B. Furthermore, multistep DSS tests are used to investigate the accuracy of the accumulation procedure.

Currently, an extensive validation is not fully possible. The existing model tests on monopiles have some drawbacks, and the field tests like the Ekofisk tank are not well documented so they can only be partially verified. This is mainly because the sensors did not measure during the storm. However, in this thesis a first comprehensive comparison of tests and predictions has been shown. For advancements in the sophisticated explicit and implicit models, high-resolution, well-documented model tests are needed.

Investigation with EPPE approach

The method comes along with some model assumptions. All of these have systematically been addressed and showed that especially the ones which come with high computational effort can be simplified. The reference procedure presented seems to be very reasonable. Different load types lead to different capacity degradations from which the symmetric one-way loading shows the largest degradation based on the assumption for the input contour plot. The procedure does also work with a simplified regression analysis of load-controlled cyclic laboratory tests or with the derived strain-based contour plot based on displacement-controlled test results. It is not clear if load- or displacement-controlled cyclic tests shall be performed. However, if the latter are used, it leads, in this case, to a slightly larger capacity.

The dissipation approach to consider partially drained conditions can be used in different ways. From the different dissipation approaches, the standard approach gives the most reasonable results compared to simplified or sequential calculations. The standard dissipation does not accurately describe the dissipation behaviour of a soil, but is a conservative approach compared to the complex dissipation approach. An iterative calculation, in which the stresses are used after a degradation in order to calculate the CSR field again, seems not to be necessary, because the results of the first run are accurate enough related to the additional computation effort. The volumetric strain can be estimated and the order of magnitude seems reasonable. The incorporation in the framework can easily be done, if needed. Small layers (general soil stratigraphy) with a very low permeability can influence the excess pore pressure distribution. This leads to the fact that the soil-structure response for other sites can be different and, therefore, a numerical estimation is essential.

All performed analyses show that the post-cyclic capacity is reasonably estimated with the reference EPPE method. The use of the more complex dissipation method will lead to larger capacities – especially for an increasing number of cycles. The effect of both methods is amplified with a sequential analysis, although a mandatory analysis in such a way does not seem to be necessary. A simplified analysis by using a 1D finite differences model will lead to slightly larger capacities but neglects spatial influences. There is no need to use the equivalent number of cycles for the input of the dissipation model.

The stress - strain response already takes the complete soil response into account. This includes also the reduction of stiffness. To directly consider the stress - strain response, a simplified hardening model is added to the Mohr-Coulomb model. Herein, an idealised stress - strain for all integration points or an integration-point specific curve is introduced. The exact stress-strain curve is based on the excess pore pressure generation and dissipation. A more simplified way of considering a degraded soil response is to consider a reduced stiffness modulus. The concept is also developed and presented in this work. Due to this effect, a softer soil-structure interaction occurs.

With a sensitivity study the general response of the soil structure interaction is investigated. The system response to a varied diameter is obvious. Furthermore, there is a very clear decrease of the capacity for a decreased permeability. The influence of the number of cycles is not pronounced, because of the relatively high permeability and due to the superposition approach. Overall, the method entails a high level of usability.

Application of implicit model

The calibrated SANISAND constitutive model is used to investigate the monopile response from an implicit perspective. Since the model does approximate the stress-strain relations more accurately, the constitutive model is also used in conjunction with the explicit EPPE approach. The monotonic load-displacement curve is stiffer compared to the one of the Mohr-Coulomb model. When using a more sophisticated constitutive model within the EPPE approach, a different excess pore pressure field R_u arises. In this case, the derived damage is less compared to the reference EPPE procedure.

The cyclic back-calculation of the initial reference system is not possible with the available version of the SANISAND model since the model overestimates the cyclic damage and shows some convergence problems. A calculation is possible with a smaller load. This generally agrees with the statements from the literature. The excess pore pressure ratio calculated explicitly is less compared to the implicitly calculated R_u field. However, this is to be expected because of the overestimation of induced damage by the sophisticated soil model. When performing an implicit calculation, the resulting excess pore pressure field is, compared to the EPPE approach, more close to the pile and there are less smaller areas in which liquefaction occurs, but there is a much more pronounced area on the passive side. For a different permeability and a different global load type, there are the expected changes in excess pore pressure build-up.

Instead of trying to solely derive the absolute excess pore pressure field, in a further step the model is used to focus on stress redistributions and investigate some model assumptions. The presence of load- or displacement-controlled conditions is investigated and shows that the model assumption of this thesis, namely load-controlled tests, is applicable. Even though displacement-controlled tests or a combination of both have to be used, the capacity would only be slightly larger, as presented in the last section. Furthermore, the derived cyclic stress ratios (CSR) and mean stress ratios (MSR) values do change over the course of the calculation, but the derived values for the very same boundary conditions calculated with the EPPE approach yield conservative CSR values. This means that the procedure can be applied in its current form. A more detailed analysis with a SANISAND-MS model is necessary in future.

8.2 Recommendations for estimation of excess pore pressure in practical design calculations

For practical applications it is recommended to use the EPPE contour approach in the presented reference configuration. The Mohr-Coulomb constitutive model is sufficiently accurate and favourable due to its small number of input parameters. All parameters have a physical meaning. The excess pore pressure estimation procedure can be based on cyclic DSS tests, which give more conservative results than cyclic triaxial tests. Furthermore, the soil response under field conditions is probably less sensitive to cyclic loading than the response measured in the direct simple shear device. Pre-shearing can be used in order to increase the cyclic resistance and hence not be over-conservative. Anyway, special care needs to be taken when choosing the pre-shear boundary conditions. The contour plot can be derived by scaling of existing ones and check the results with a small number of additional tests with symmetric and non-symmetric two-way loading. By using the standard dissipation, a conservative approach is used to consider partially drained conditions.

The presented method has been evaluated with a constant number of cycles in all integration points without considering any storm parcels. In a practical project these irregular load scenarios need to be taken into account. Due to the non-linear relationships between excess pore pressure and stress state, a field of equivalent number of cycles at the integration points arises. For the calculation of an equivalent number of cycles R_u is interpreted as a memory variable. Additional results are presented in Appendix B. It shows additional considerations of an irregular storm event.

8.3 Recommendations for further research

Although the presented method already covers many topics, there are still some further research aspects that need to be investigated. The specific problems have already been discussed in the related chapters of this thesis.

Andersen (2015) shows a diagram with which contour plots can be scaled. Even if this diagram is used in practice, the application limits and the resulting accuracy are not documented. Therefore, contour plots for other sands and their scaling factors should be derived. A large number of tests are required for an accurate derivation of contour plots, so that an initial estimation based on existing plots would reduce costs in practice.

A different aspect regarding cyclic tests is the general scatter. The cyclic direct simple shear tests scatter under the same boundary conditions. This could possibly have been prevented by using dry pluviation for all tests and including a pre-shear phase. However, the pre-shear phase can influence the cyclic response to a great extent and, hence, the test conditions of this step needs to be well justified. In preliminary tests these methods have shown promising results in terms of reproducibility. This should be investigated further.

In all presented approaches a wished-in-place installation is performed. This procedure is the usual assumption when dealing with numerical calculations. However, with special numerical approaches it is possible to model the complete installation process and analyse the resulting stress redistributions. Depending on the installation procedure there are different stress states due to soil displacement or soil redistribution and disturbance (cf. Staubach et al. (2022)). This consideration can lead to generally smaller cyclic accumulations due to higher normal stresses. The precise behaviour can only be estimated with complex models and a time consuming procedure. In order to enhance the estimation accuracy, these aspects need to be investigated in future.

The greatest influence besides the input contour plot comes from the analytical consideration of dissipation. Two different methods have been presented. In order to investigate this topic further, partially drained triaxial tests should be carried out. The soil response under partially drained conditions can then analytically be back-calculated. The problem when dealing with these kinds of tests is that due to the small specimen with a large hydraulic conductivity for sandy material a fast dissipation occurs. Hence, the frequency needs to be increased which may not be regulated well from the device and is limited at a specific point because of the regulation circuit or inertia effects. One solution within a standard triaxial device could be the use of a substituted pore fluid. The agent changes the viscosity and subsequently the permeability of the soil by keeping the soils' stiffness and strength properties unchanged. Based on this, an improved analytical superposition can be investigated and applied to the EPPE approach.

Finally, a thorough validation of the explicit method with high-quality small-scale or medium-scale tests is necessary. These are, for instance, being carried out in the Collaborative Research Centre 1463 (Schuster et al. (2021)) of the Leibniz University Hannover. Herein, the small-scale tests are first performed in the context of gravity based foundations and subsequently for monopile foundations. In addition to the displacements of the structure, the stresses within the soil are measured by the sensors (stresses and excess pore pressures) without disturbing the soil-structure interaction too much. Within this project there will be small-scale cyclic tests in which the system response under partially drained conditions is investigated under laboratory conditions. These will be used to validate the method in near future.

9 Summary

Offshore wind turbines will be increasingly used for the production of renewable energy in future. Under undrained or partially drained conditions, the corresponding shear stresses in the soil may lead to a build-up and an accumulated of excess pore pressures which in turn cause reductions in shear strength. In addition to Chapter 8, a short summary will be given.

Cyclic loading causes degradation of the bearing capacity which has to be accounted for in the design of cyclically loaded offshore foundations. Although the consideration of a cyclic degradation effect on the bearing capacity due to excess pore pressure is commonly demanded by the involved certification or approval bodies, no general applicable and accepted method for the calculative verification currently exists. The build-up of excess pore pressure and, hence, partial or full liquefaction can influence the integrity of offshore structures. The capacity as well as the serviceability is at risk if liquefaction occurs. This is why there are many studies on the cyclic soil behaviour and several implicit and explicit numerical design approaches. However, there is no comprehensive study conducted on a specific sand and no comparison of different modelling techniques based on the resulting changes in soil-structure interaction.

Cyclic loading can be considered with implicit and explicit approaches, whereas the differences between both depend on many factors. Among others, an important aspect is the quality of the implicit constitutive law and the number of effects incorporated in it. The use of SANISAND model can give significant insights into the soil response, but should not be used in practice. Here, more advanced versions of this very model are more favourable for academia.

In the present thesis, a concept was developed in order to facilitate the inherent complex cyclic loading into a simple estimation procedure. The thesis focuses on a procedure which incorporates the most essential aspects. Some questions were asked in advance of this thesis, which can now all be answered. The present knowledge was fundamentally gained from many laboratory tests in different devices with different boundary conditions. The cyclic response under displacement- as well as load-controlled tests was assessed and was used within the numerical procedure in order to estimate the difference in global response. Different mathematical approaches were investigated to derive contour plots and one was chosen as best suitable. Based on all gathered laboratory data, an implicit model was calibrated. The implicit model gave in-depth insights into the element response around an offshore foundation which could be used to gather a deeper understanding for the optimization of the explicit approach regarding model assumptions.

Different modelling variations have been compared with each other and influences on the bearing capacity assessed. The main objective of the research presented is to provide a simple, understandable concept for estimating excess pore pressure around cyclically loaded offshore foundations that gives sufficiently accurate results but can be used by most engineers. To achieve this goal, mainly monopile foundations were investigated, but the developed generic concept applies to all types of structures. The proposed procedure can be used for the analysis of post-cyclic bearing behaviour, and if shear strain plots are present, also serviceability proofs are possible. This procedure is then extended to the application of multiple storm acts and the general procedure is validated with multi-stage cyclic direct simple shear tests. Partially drained conditions are incorporated in the presented explicit approach with a simplified superposition, which can be exchanged for a more advanced one in a next step. The consideration of volumetric strains due to the dissipation process is also presented.

The Excess Pore Pressure Estimation (EPPE) approach helps to quantify the risk of liquefaction as well as to evaluate an appropriate safety margin. It is possible with the current methodology to evaluate the degradation potential for different sites quite easily and fast. Instead of using conservative analytical methods within the design, it is possible to assess each site with a numerical calculation in the design. The method uses soil-specific contour plots in a simple modular way. Thus, it is very transparent and can be assessed with engineering judgement. By analysing each integration point individually regarding its cyclic element response, the approach can reduce construction costs due to a higher accuracy compared to more generalized approaches. The total computational effort is reasonable, even for large wind farms. Uncertainties are eliminated by simultaneously making numerical methods easier to use in practical offshore applications.

Furthermore, various influences are shown and a clear contribution of this work to the understanding of the cyclic design regarding excess pore pressure accumulation is made. The thesis gives valuable insights for practical application and identifying key cyclic mechanisms for academia. It shows how the soil behaviour under cyclic loading and how to transfer the knowledge to global foundation responses.

Bibliography

M. Achmus, Y.-S. Kuo, and K. Abdel-Rahman. Behavior of monopile foundations under cyclic lateral load. *Computers and Geotechnics*, 36(5):725–735, 2009. URL https://doi.org/10.1016/j.compgeo.2008.12.003.

M. Achmus, J.-E. Saathoff, and K. Thieken. Numerical method for evaluation of excess pore pressure build-up at cyclically loaded offshore foundations. In *Numerical Methods in Geotechnical Engineering IX*, pages 1461–1468, 2018. URL https://doi.org/10.1201/9781351003629-184.

J. K. Ahn and D. Park. Accumulated stress based model for prediction of residual pore pressure. In *Proceedings of the 18th International Conference on Soil Mechanics and Geotechnical Engineering*, pages 1567–1570, 2013.

D. W. Airey and D. M. Wood. Pore pressures in simple shear. *Soils and Foundations*, 26 (2):91–96, 1986. URL https://doi.org/10.3208/sandf1972.26.2_91.

D. W. Airey, M. Budhu, and D. M. Wood. *Some aspects of the behaviour of soils in simple shear*, pages 185–213. Elsevier, 1985.

N. Allotey and M. H. El Naggar. A consistent soil fatigue framework based on the number of equivalent cycles. *Geotechnical and Geological Engineering*, 26:65–77, 2008. URL https://doi.org/10.1007/s10706-007-9147-2.

K. H. Andersen. Behaviour of clay subjected to undrained cyclic loading. In *Behaviour of Off-Shore Structures, Proceedings of the First International Conference*, 1976.

K. H. Andersen. Bearing capacity under cyclic loading - offshore, along the coast, and on land. *Canadian Geotechnical Journal*, 46(5):513–535, 2009. URL https://doi.org/10.1139/T09-003.

K. H. Andersen. Cyclic soil parameters for offshore foundation design. The 3rd McClelland Lecture. In Meyer, editor, *Frontiers in Offshore Geotechnics III, ISFOG'2015*, volume 1, pages 5–82. Taylor & Francis Group, London, 2015.

K. H. Andersen and K. Høeg. *Deformations of soils and displacements of structures subjected to combined static and cyclic loads.* Norges geotekniske institutt, Oslo, 1992.

K. H. Andersen and K. Schjetne. Database of friction angles of sand and consolidation characteristics of sand, silt, and clay. *Journal of Geotechnical and Geoenvironmental Engineering*, 139(7), 2013. URL https://doi.org/10.1061/(ASCE)GT.1943-5606.0000839.

K. H. Andersen, O. E. Hansteen, K. Høeg, and J. H. Prevost. Soil deformations due to cyclic loads on offshore structures. *Norwegian Geotechnical Institute Publication*, 1978.

K. H. Andersen, R. Lauritzsen, R. Dyvik, and P. M. Aas. Cyclic bearing capacity analysis for gravity platforms. In *Proceedings of the International Conference on Behaviour of Offshore Structures, BOSS'88*, 1988.

K. H. Andersen, R. Dyvik, Y. Kikuchi, and E. Skomedal. Clay behaviour under irregular cyclic loading. In *Proceedings of the 6th International Conference on the Behaviour of Offshore Structures*, 1992.

K. H. Andersen, M. A. Allard, and J. Hermstad. Centrifuge model tests of a gravity platform on very dense sand; II: interpretation. In C. Chryssostomidis and others (Elsevier), editors, *Proceedings of the 7th International conference on the behaviour of offshore structures - BOSS'94*, pages 255–282, 1994.

K. H. Andersen, A. A. A. Puech, and R. J. Jardine. Cyclic resistant geotechnical design and parameter selection for offshore engineering and other applications. In *Proceedings of the ISSMGE conference - TC 209 Workshop - Design for cyclic loading: piles and other foundations - Paris*, 2013.

L. Andresen, H. P. Jostad, and K. H. Andersen. Finite element analyses applied in design of foundations and anchors for offshore structures. *International Journal of Geomechanics*, 11(6):417–430, 2011. URL https://doi.org/10.1061/(ASCE)GM.1943-5622.0000020.

ANSI/API RP 2GEO. Geotechnical and foundation design considerations: ANSI/API recommended practice 2GEO; ISO 19901-4:2003 (modified), Petroleum and natural gas industries - Specific requirements for offshore structures part 4. Recommended practice, American Petroleum Institute and American National Standards Institute, Washington, DC, 2014.

L. Arany, S. Bhattacharya, J. Macdonald, and J. Hogan. Design of monopiles for offshore wind turbines in 10 steps. *Soil Dynamics and Earthquake Engineering*, 92:126 – 152, 2017. URL https://doi.org/10.1016/j.soildyn.2016.09.024.

ASTM D4767-11. Standard test method for consolidated undrained triaxial compression test for cohesive soils, 2020. URL https://www.astm.org/d4767-11r20.html.

ASTM D5311-13. Standard test method for load controlled cyclic triaxial strength of soil (withdrawn 2022), 2013. URL https://www.astm.org/d5311_d5311m-13.html.

ASTM D8296-19. Standard test method for consolidated undrained cyclic direct simple shear test under constant volume with load control or displacement control, 2019. URL https://www.astm.org/d8296-19.html.

J. H. Atkinson, W. H. W. Lau, and J. J. M. Powell. Measurement of soil strength in simple shear tests. *Canadian Geotechnical Journal*, 28(2):255–262, 1991. URL https://doi.org/10.1139/t91-031.

R. J. N. Azeiteiro, P. A. L. F. Coelho, D. M. G. Taborda, and J. C. D. Grazina. Energy-based evaluation of liquefaction potential under non-uniform cyclic loading. *Soil Dynamics and Earthquake Engineering*, 92:650–665, 2017. URL https://doi.org/10.1016/j.soildyn.2016.11.005.

A. R. Barrero, M. Taiebat, and Y. F. Dafalias. Modeling cyclic shearing of sands in the semifluidized state. *International Journal for Numerical and Analytical Methods in Geomechanics*, 44(3):371–388, 2020. URL https://doi.org/10.1002/nag.3007.

K. Been and M. G. Jefferies. A state parameter for sands. *Géotechnique*, 35(2):99–112, 1985. URL https://doi.org/10.1680/geot.1985.35.2.99.

Bentley Systems. Plaxis software. 2022.

T. Benz. *Small-Strain Stiffness of Soils and its Numerical Consequences*. PhD thesis, Universität Stuttgart, 2007. URL https://www.igs.uni-stuttgart.de/dokumente/Mitteilungen/55_Benz.pdf.

J. B. Berril and R. O. Davis. Energy dissipation and seismic liquefaction in sands: Revised model. *Soils and Foundations*, 25(2):106–118, 1985. URL https://doi.org/10.3208/sandf1972.25.2_106.

W. Beyer. Hydrogeological investigations in the deposition of water pollutants. *Journal of Applied Geology*, pages 599–606, 1966.

S. Bhattacharya, S. Biswal, M. Aleem, S. Amani, A. Prabhakaran, G. Prakhya, D. Lombardi, and H. K. Mistry. Seismic design of offshore wind turbines: Good, bad and unknowns. *Energies*, 14(12), 2021. URL https://www.mdpi.com/1996-1073/14/12/3496.

L. Bjerrum. Geotechnical problems involved in foundations of structures in the North Sea. *Géotechnique*, 23(3):319–358, 1973. URL https://doi.org/10.1680/geot.1973.23.3.319.

Ø. Blaker and K. H. Andersen. Cyclic properties of dense to very dense silica sand. *Soils and Foundations*, 59(4):982–1000, 2019. URL https://doi.org/10.1016/j.sandf.2019.04.002.

J. R. Booker, M. S. Rahman, and H. B. Seed. GADFLEA: a computer program for the analysis of pore pressure generation and dissipation during cyclic or earthquake loading. Technical report, Earthquake Engineering Research Center, United States, 1976. URL https://www.osti.gov/biblio/7090978.

N. Boukpeti, B. Lehane, and J. A. H. Carraro. Strain accumulation procedure during staged cyclic loading of carbonate sediments. In *Proceedings of the ASME 2014 33rd International Conference on Ocean, Offshore and Arctic Engineering*, 2014. URL https://doi.org/10.1115/OMAE2014-23692.

R. W. Boulanger and I. M. Idriss. Liquefaction susceptibility criteria for silts and clays. *Journal of Geotechnical and Geoenvironmental Engineering*, 132(11):1413–1426, 2006. URL https://doi.org/10.1061/(ASCE)1090-0241(2006)132:11(1413).

R. W. Boulanger and K. Ziotopoulou. Formulation of a sand plasticity plane-strain model for earthquake engineering applications. *Soil Dynamics and Earthquake Engineering*, 53:254–267, 2013. URL https://doi.org/10.1016/j.soildyn.2013.07.006.

R. W. Boulanger and K. Ziotopoulou. PM4Sand Version 3: A sand plasticity model for earthquake engineering applications. Technical Report No. UCD/CGM-15/01, Department of Civil & Environmental Engineering, University of California at Davis, 2015.

R. Brewer. *Fabric and mineral analysis of soils*. Wiley, 1964. ISBN 0882753142.

BSH No. 7005. *Standard design - Minimum requirements concerning the constructive design of offshore structures within the Exclusive Economic Zone (EEZ)*, 2015.

B. W. Byrne, R. A. McAdam, H. J. Burd, G. T. Houlsby, C. M. Martin, W. Beuckelaers, L. Zdravkovic, D. M. G. Taborda, D. Potts, R. J. Jardine, et al. PISA: New design methods for offshore wind turbine monopiles. In *Proceedings of the 8th International Conference for Offshore Site Investigation and Geotechnics*, pages 142–161, 2017.

P. M. Byrne. A cyclic shear-volume coupling and pore pressure model for sand. In *Proceedings of the International Conferences on Recent Advances in Geotechnical Earthquake Engineering and Soil Dynamics*, 1991. URL https://scholarsmine.mst.edu/icrageesd/02icrageesd/session01/1.

F. Cai, G. R. Eiksund, G. Grimstad, and H. P. Jostad. An anisotropic shear strength model for cyclic accumulated plastic strain of overconsolidated clay. *Electronic Journal of Geotechnical Engineering*, 19:4393–4406, 2014. URL http://hdl.handle.net/11250/2381045.

J. A. H. Carraro, P. Bandini, and R. Salgado. Liquefaction resistance of clean and nonplastic silty sands based on cone penetration resistance. *Journal of Geotechnical and Geoenvironmental Engineering*, 129(11):965–976, 2003. URL https://doi.org/10.1061/(ASCE)1090-0241(2003)129:11(965).

A. Casagrande. *Characteristics of cohesionless soils affecting the stability of slopes and earth fills*. Harvard University, 1936.

G. Castro. *Liquefaction of sands*. PhD thesis, Harvard University, Cambridge, MA, 1969.

G. Castro. Liquefaction and cyclic mobility of saturated sands. *Journal of the Geotechnical Engineering Division*, 101(6):551–569, 1975. URL https://doi.org/10.1061/AJGEB6.0000173.

G. Castro and S. J. Poulos. Factors affecting liquefaction and cyclic mobility. *Journal of the Geotechnical Engineering Division*, 103(6):501–516, 1977. URL https://doi.org/10.1061/AJGEB6.0000433.

G. Castro, J. L. Enos, J. W. France, and S. J. Poulos. Liquefaction induced by cyclic loading. Technical report, Geotechnical Engineers, Inc., Winchester, MA, 1982.

K. O. Cetin and H. T. Bilge. Cyclic large strain and induced pore pressure models for saturated clean sands. *Journal of Geotechnical and Geoenvironmental Engineering*, 138 (3):309–323, 2012. URL https://doi.org/10.1061/(ASCE)GT.1943-5606.0000631.

C. S. Chang. Residual pore pressure and deformation behavior of soil samples under variable cyclic loading. In *Proceedings of the International Conferences on Recent Advances in Geotechnical Earthquake Engineering and Soil Dynamics*, 1981. URL https://scholarsmine.mst.edu/icrageesd/01icrageesd/session01b/10.

G. Chen, D. Zhao, W. Chen, and C. H. Juang. Excess pore-water pressure generation in cyclic undrained testing. *Journal of Geotechnical and Geoenvironmental Engineering*, 145(7), 2019. URL https://doi.org/10.1061/(ASCE)GT.1943-5606.0002057.

C. J. F. Clausen, E. J. F. Dibiagio, J. M. Duncan, and K. H. Andersen. Observed behaviour of the Ekofisk Oil storage Tank Foundation. In *Proceedings of the Offshore Technology Conference, Houston, Texas*, pages 399–431, 1975. URL https://doi.org/10.4043/2373-MS.

E. R. L. Cole. *The behaviour of soils in the simple-shear apparatus*. PhD thesis, Downing College, Cambridge University, 1967.

R. Corti. *Hardening memory surface constitutive model for granular soils under cyclic loading conditions*. PhD thesis, University of Bristol, 2016.

W. R. Cox, L. C. Reese, and B. R. Grubbs. Field testing of laterally loaded piles in sand. In *Paper presented at the Offshore Technology Conference*, 1974. URL https://doi.org/10.4043/2079-MS.

P. Cuéllar. *Pile foundations for offshore wind turbines: Numerical and experimental investigations on the behaviour under short-term and long-term cyclic loading*. PhD thesis, Technische Universität Berlin, 2011. URL https://doi.org/10.14279/depositonce-2760.

P. Cuéllar, M. Baeßler, S. Georgi, and W. Rücker. Porenwasserdruckaufbau und Bodenentfestigung um Pfahlgründungen von Offshore-Windenergieanlagen. *Bautechnik*, 89 (9):585–593, 2012. URL https://doi.org/10.1002/bate.201200031.

P. Cuéllar, P. Mira, M. Pastor, J. A. F. Merodo, M. Baeßler, and W. Rücker. A numerical model for the transient analysis of offshore foundations under cyclic loading. *Computers and Geotechnics*, 59:75–86, 2014. URL https://doi.org/10.1016/j.compgeo.2014.02.005.

Y. F. Dafalias. Bounding surface plasticity. I: Mathematical foundation and hypoplasticity. *Journal of Engineering Mechanics*, 112(9):966–987, 1986. URL https://doi.org/10.1061/(ASCE)0733-9399(1986)112:9(966).

Y. F. Dafalias and M. T. Manzari. Simple plasticity sand model accounting for fabric change effects. *Journal of Engineering Mechanics*, 130(6):622–634, 2004. URL https://doi.org/10.1061/(ASCE)0733-9399(2004)130:6(622).

Y. F. Dafalias and E. P. Popov. A model of nonlinearly hardening materials for complex loading. *Acta Mechanica*, 21:173–192, 1975. URL https://doi.org/10.1007/BF01181053.

Y. F. Dafalias and E. P. Popov. Plastic internal variables formalism of cyclic plasticity. *Journal of Applied Mechanics*, 43(4):645–651, 1976. URL https://doi.org/10.1115/1.3423948.

Y. F. Dafalias and M. Taiebat. SANISAND-Z: zero elastic range sand plasticity model. *Géotechnique*, 66(12):999–1013, 2016. URL https://doi.org/10.1680/jgeot.15.P.271.

Y. F. Dafalias, A. G. Papadimitriou, and X. S. Li. Sand plasticity model accounting for inherent fabric anisotropy. *Journal of Engineering Mechanics*, 130(11):1319–1333, 2004. URL https://doi.org/10.1061/(ASCE)0733-9399(2004)130:11(1319).

B. M. Dahl, M. S. Løyland, and H. P. Jostad. Interpretation of cyclic behaviour of a saturated dense sand within an elasto-plastic framework. In *Numerical Methods in Geotechnical Engineering IX*, pages 187–194. Taylor & Francis, 2018.

Danish Energy Agency. Recommendation for technical approval of offshore wind turbines. Technical report, 2001.

S. Dash and S. Bhattacharya. Pore water pressure generation and dissipation near to pile and far-field in liquefiable soils. *International Journal of GEOMATE*, 9(2):1454–1459, December 2015. URL https://doi.org/10.21660/2015.18.4253.

Dassault Systèmes. Abaqus 2016. 2016.

E. H. Davis and J. T. Christian. Bearing capacity of anisotropic cohesive soil. *Journal of Soil Mechanics and Foundations Division*, 97(5):753–769, 1971. URL https://doi.org/10.1061/JSFEAQ.0001594.

E. H. Davis and G. P. Raymond. Non-linear theory of consolidation. *Géotechnique*, 15 (2):161–173, 1965. URL https://doi.org/10.1680/geot.1965.15.2.161.

P. De Alba, C. K. Chan, and H. Seed. *Determination of Soil Liquefaction Characteristics by Large-Scale Laboratory Tests*. 1975.

P. A. De Alba, C. K. Chan, and H. B. Seed. Sand liquefaction in large-scale simple shear tests. *Journal of the Geotechnical Engineering Division*, 102(9):909–927, 1976. URL https://doi.org/10.1061/AJGEB6.0000322.

M. B. de Groot, M. D. Bolton, P. Foray, P. Meijers, A. C. Palmer, R. Sandven, A. Sawicki, and T. C. Teh. Physics of liquefaction phenomena around marine structures. *Journal of Waterway, Port, Coastal, and Ocean Engineering*, 132(4):227–243, 2006a. URL https://doi.org/10.1061/(ASCE)0733-950X(2006)132:4(227).

M. B. de Groot, M. Kudella, P. Meijers, and H. Oumeraci. Liquefaction phenomena underneath marine gravity structures subjected to wave loads. *Journal of Waterway, Port, Coastal, and Ocean Engineering*, 132(4):325–335, 2006b. URL https://doi.org/10.1061/(ASCE)0733-950X(2006)132:4(325).

G. De Josselin de Jong. Discussion to session II. In *Proceedings of the Roscoe Memorial Symposium Stress-Strain Behaviour of Soils, Cambridge, UK*, pages 29–31, 1971.

V. B. DeGregorio. Loading systems, sample preparation, and liquefaction. *Journal of Geotechnical Engineering*, 116(5), 1990. URL https://doi.org/10.1061/(ASCE)0733-9410(1990)116:5(805).

DIN 1054:2021-04. Subsoil - Verification of the safety of earthworks and foundations - Supplementary rules to DIN EN 1997-1. German standard, Deutsches Institut für Normung e.V., Berlin, Germany, 2021.

DIN 18088-4:2019-01. Structures for wind turbines and platforms - Part 4: Soil and foundation elements. German standard, Deutsches Institut für Normung e.V., Berlin, Germany, 2019.

DIN EN 1997-1:2014-03. Eurocode 7: Geotechnical design - Part 1: General rules; German version EN 1997-1:2004 + AC:2009 + A1:2013 . European standard, Deutsches Institut für Normung e. V., Berlin, Germany, 2014.

DIN EN 1998-1:2010-12. Eurocode 8: Design of structures for earthquake resistance - Part 1: General rules, seismic actions and rules for buildings; German version EN 1998-1:2004 + AC:2009. European standard, Deutsches Institut für Normung e.V., Berlin, Germany, 2010.

DIN EN IEC 61400-3-1:2020-11. Wind energy generation systems - Part 3-1: Design requirements for fixed offshore wind turbines (IEC 61400-3-1:2019); German version EN IEC 61400-3-1:2019. European standard, Deutsches Institut für Normung e.V., Berlin, Germany, 2020.

DIN EN ISO 17892-9:2018-07. Geotechnical investigation and testing - Laboratory testing of soil - Part 9: Consolidated triaxial compression tests on water saturated soils (ISO 17892-9:2018); German version EN ISO 17892-9:2018. International standard, International Organization for Standardization, Geneva, Switzerland, 2018.

DIN EN ISO 19901-4:2017-01. Petroleum and natural gas industries - Specific requirements for offshore structures - Part 4: Geotechnical and foundation design considerations. International standard, International Organization for Standardization, Geneva, Switzerland, 2017.

DIN EN ISO 19902:2021-03. Petroleum and natural gas industries - Fixed steel offshore structures. International standard, International Organization for Standardization, Geneva, Switzerland, 2021.

H. Dingle, C. Humpheson, and A. Pillai. 3D finite element modelling of the cyclic behaviour of offshore gravity base foundations on sands. In *Proceedings of the 8th Offshore Site Investigation and Geotechnics International Conference*, pages 441–448, 2017. URL https://doi.org/10.3723/OSIG17.441.

DNV-OS-J101. Design of Offshore Wind Turbine Structures. Offshore standard, Det Norske Veritas, 2014.

DNV-RP-C212. Offshore soil mechanics and geotechnical engineering. Standard, Det Norske Veritas, 2019.

DNV-ST-0126. Support structures for wind turbines. Standard, Det Norske Veritas, 2019.

R. Dobry, R. S. Ladd, F. Y. Yokel, R. M. Chung, and D. Powell. *Prediction of Pore Water Pressure Buildup and Liquefaction of Sands during Earthquakes by the Cyclic Strain Method*. U.S. Department of Commerce, National Bureau of Standards, 1982. URL http://doi.org/10.6028/NBS.BSS.138.

R. Dobry, W. G. Pierce, R. Dyvik, G. E. Thomas, and R. S. Ladd. *Pore pressure model for cyclic straining of sand*. Department of Civil Engineering, Rensselaer Polytechnic Institute, 1985a.

R. Dobry, A. Vasquez-Herrera, R. Mohamad, and M. Vucetic. Liquefaction flow failure of silty sand by torsional cyclic tests. In *Proceedings of a Session of ASCE Convention in Detroit, Michigan: Advances in the Art of Testing Soils Under Cyclic Conditions*, 1985b.

V. P. Drnevich and F. E. Richart. Dynamic prestraining of dry sand. *Journal of Soil Mechanics and Foundations Division*, 96:453 – 469, 1970.

P. Dunlop and J. M. Duncan. Behaviour of soils in simple shear tests. In *Proceedings of the 7th International Conference on Soil Mechanics and Foundation Engineering*, 1969.

R. Dyvik, T. Berre, S. Lacasse, and B. Raadim. Comparison of truly undrained and constant volume direct simple shear tests. *Géotechnique*, 37(1):3–10, 1987. URL https://doi.org/10.1680/geot.1987.37.1.3.

J. A. Díaz-Rodríguez and J. A. López-Molina. Strain thresholds in soil dynamics. In *Proceedings of the 14th World Conference on Earthquake Engineering*, 2008.

J. Dührkop. *Zum Einfluss von Aufweitungen und zyklischen Lasten auf das Verformungsverhalten lateral beanspruchter Pfähle im Sand*. Technische Universität Hamburg-Harburg, Institut für Geotechnik und Baubetrieb, 2009. ISBN 9783936310214.

J. Dührkop, K. Siegl, E. Heins, and T. Pucker. Bemessung von XXL-Monopiles – Aktuelle Erfahrungen und Herausforderungen im Geotechnischen Design. In *Pfahl-Symposium 2019*. Institut für Grundbau und Bodenmechanik, Technische Universität Braunschweig, 2019.

O. Eide, K. H. Andersen, and T. Lunne. Observed foundation behaviour of concrete gravity platforms installed in the North Sea 1973-1978. *Applied Ocean Research*, 3(3): 134–144, 1981. URL https://doi.org/10.1016/0141-1187(81)90102-4.

C. S. El Mohtar. Evaluation of 5% double amplitude strain criterion. In *Proceedings of the 17th International Conference on Soil Mechanics and Geotechnical Engineering*, pages 80–83, 2009. URL https://doi.org/10.3233/978-1-60750-031-5-80.

A. Elgamal, Z. Yang, E. Parra, and A. Ragheb. Modeling of cyclic mobility in saturated cohesionless soils. *International Journal of Plasticity*, 19(6):883–905, 2003. URL https://doi.org/10.1016/S0749-6419(02)00010-4.

P. K. Esfeh and A. M. Kaynia. Earthquake response of monopiles and caissons for offshore wind turbines founded in liquefiable soil. *Soil Dynamics and Earthquake Engineering*, 136, 2020. URL https://doi.org/10.1016/j.soildyn.2020.106213.

J. Feda. Constant volume shear tests of saturated sand. *Archiwum Hydrotechnika*, pages 349–367, 1971.

W. D. L. Finn and S. K. Bhatia. Prediction of seismic porewater pressures. In *Proceedings of the 10th International Conference on Soil Mechanics and Foundation Engineering, Stockholm*, pages 201–206, 1981.

W. D. L. Finn and Y. P. Vaid. Liquefaction potential from drained constant volume cyclic simple shear tests. In *Proceedings of the 6th World Conference on Earthquake Engineering, New Delhi, India*, 1977.

W. D. L. Finn, P. L. Bransby, and D. J. Pickering. Effect of strain history on liquefaction of sand. *Journal of the Soil Mechanics and Foundations Division*, 96(6):1917–1934, 1970. URL https://doi.org/10.1061/JSFEAQ.0001478.

W. D. L. Finn, G. R. Martin, and P. M. Byrne. Seismic response and liquefaction of sands. *Journal of the Geotechnical Engineering Division*, 102(8):841–856, 1976. URL https://doi.org/10.1061/AJGEB6.0000310.

W. D. L. Finn, K. W. Lee, and G. R. Martin. An effective stress model for liquefaction. *Journal of the Geotechnical Engineering Division*, 103(6):517–533, 1977. URL https://doi.org/10.1061/AJGEB6.0000434.

W. Fuentes and T. Triantafyllidis. *ISA: A constitutive model for deposited sand.* Springer Vieweg, Berlin, Heidelberg, 2015. URL https://doi.org/10.1007/978-3-662-45991-1_10.

German Geotechnical Society. *Empfehlungen des Arbeitskreises „Pfähle“: EA-Pfähle.* Wilhelm Ernst & Sohn, 2012. ISBN 9783433601112. URL https://doi.org/10.1002/9783433601112.

R. Glasenapp. *Das Verhalten von Sand unter zyklischer irregulärer Belastung.* PhD thesis, Technische Universität Berlin, 2016. URL https://doi.org/10.14279/depositonce-5402.

Global Wind Energy Council. Global wind report 2021. 2021. URL https://gwec.net/global-wind-report-2021/.

D. E. Goldberg. *Genetic algorithms in search, optimization, and machine learning.* Addison-Wesley Longman Publishing Co., Inc., 1989. ISBN 978-0-201-15767-3.

A. Gotschol. *Veränderlich elastisches und plastisches Verhalten nichtbindiger Böden und Schotter unter zyklisch-dynamischer Beanspruchung.* PhD thesis, Universität Kassel, Fachgebiet Geotechnik, 2002. URL https://kobra.uni-kassel.de/handle/123456789/2009010525537.

J. Grabe, J. Dührkop, and K.-P. Mahutka. Monopilegründungen von Offshore-Windenergieanlagen - Zur Bildung von Porenwasserüberdrücken aus zyklischer Belastung. *Bauingenieur*, 79:418–423, 2004.

J. Grabe, K.-P. Mahutka, and J. Dührkop. Monopilegründungen von Offshore-Windenergieanlagen - Zum Ansatz der Bettung. *Bautechnik*, 82(1):1–10, 2005. URL https://doi.org/10.1002/bate.200590020.

R. A. Green and G. A. Terri. Number of equivalent cycles concept for liquefaction evaluations - revisited. *Journal of Geotechnical and Geoenvironmental Engineering*, 131(4): 477–488, 2005. URL https://doi.org/10.1061/(ASCE)1090-0241(2005)131:4(477).

D. V. Griffiths. Failure criteria interpretation based on Mohr-Coulomb friction. *Journal of Geotechnical Engineering*, 116(6):986–999, 1990. URL https://doi.org/10.1061/(ASCE)0733-9410(1990)116:6(986).

G. Grimstad, L. Andresen, and H. P. Jostad. NGI-ADP: Anisotropic shear strength model for clay. *International Journal for Numerical and Analytical Methods in Geomechanics*, 36(4):483–497, 2012. URL https://doi.org/10.1002/nag.1016.

G. Gudehus. A comprehensive constitutive equation for granular materials. *Soils and Foundations*, 36(1):1–12, 1996. URL https://doi.org/10.3208/sandf.36.1.

D. J. Han and W. F. Chen. A nonuniform hardening plasticity model for concrete materials. *Mechanics of Materials*, 4(3-4):283–302, 1985. URL https://doi.org/10.1016/0167-6636(85)90025-0.

A. Hettler. *Verschiebungen starrer und elastischer Gründungskörper in Sand bei monotoner und zyklischer Belastung*. PhD thesis, Universität Karlsruhe, Institut für Bodenmechanik und Felsmechanik, 1981.

P. Hinz. *Beurteilung des Langzeitverhaltens zyklisch horizontal belasteter Monopile-Gründungen: Mitteilungen 37 aus dem Fachgebiet Grundbau und Bodenmechanik*. VGE Verlag GmbH, 2009. ISBN 9783867970662.

T. Hodgson, N. Sampathkumar, and I. Cortizo. Approach to wind wave correlation in coupled analysis of offshore WTG substructures. In *Proceedings of the Wind Europe summit*, 2016.

K. Høeg. Deformation computations in geotechnical engineering. 1978. URL http://ngf.no/wp-content/uploads/2022/01/1977-Hoeg-K-2nd-Lecture.pdf.

Y. Hosono and M. Yoshimine. *Liquefaction of sand in simple shear condition*, pages 129–136. Taylor & Francis, 2004.

M. Hyodo, K. Yashuhara, and H. Murata. Earthquake induced settlements in clays. In *Proceedings of the Ninth World Conference on Earthquake Engineering*, 1988. URL https://www.iitk.ac.in/nicee/wcee/article/9_vol3_89.pdf.

M. Hyodo, K. Yasuhara, and K. Hirao. Prediction of clay behaviour in undrained and partially drained cyclic triaxial tests. *Soils and Foundations*, 32:117–127, 1992. URL https://doi.org/10.3208/sandf1972.32.4_117.

M. Hyodo, Y. Yamamoto, and M. Sugiyama. Undrained cyclic shear behaviour of normally consolidated clay subjected to initial static shear stress. *Soils and Foundations*, 34(4): 1–11, 1994. URL https://doi.org/10.3208/sandf1972.34.4_1.

I. Ishibashi and M. A. Sherif. Soil liquefaction by torsional simple shear device. *Journal of the Geotechnical Engineering Division*, 100(8):871–888, 1974. URL https://doi.org/10.1061/AJGEB6.0000074.

K. Ishihara. Stability of natural deposits during earthquakes. In *Proceedings of the 11th International Conference on Soil Mechanics and Foundation Engineering*, 1985.

K. Ishihara. Liquefaction and flow failure during earthquakes. *Géotechnique*, 43(3):351–451, 1993. URL https://doi.org/10.1680/geot.1993.43.3.351.

K. Ishihara and S. Li. Liquefaction of saturated sand in triaxial torsion shear test. *Soils and Foundations*, 12(2):19–39, 1972. URL https://doi.org/10.3208/sandf1972.12.19.

K. Ishihara and S. Okada. Effect of stress history on cyclic behavior of sand. *Soils and Foundations*, 18(4):31–45, 1978. URL https://doi.org/10.3208/sandf1972.18.4_31.

K. Ishihara and S. Okada. Effects of large preshearing on cyclic behavior of sand. *Soils and Foundations*, 22(3):109–125, 1982. URL https://doi.org/10.3208/sandf1972.22.3_109.

K. Ishihara and H. Takatsu. Effects of overconsolidation and K0, conditions on the liquefaction characteristics of sands. *Soils and Foundations*, 19(4):59–68, 1979. URL https://doi.org/10.3208/sandf1972.19.4_59.

K. Ishihara, F. Tatsuoka, and S. Yasuda. Undrained deformation and liquefaction of sand under cyclic stresses. *Soils and Foundations*, 15(1):29–44, 1975. URL https://doi.org/10.3208/sandf1972.15.29.

T. Ivsić. A model for presentation of seismic pore water pressures. *Soil Dynamics and Earthquake Engineering*, 26(2-4):191–199, 2006. URL https://doi.org/10.1016/j.soildyn.2004.11.025.

W. D. Iwan. On a class of models for the yielding behavior of continuous and composite systems. *Journal of Applied Mechanics*, 34(3):612–617, 1967. URL https://doi.org/10.1115/1.3607751.

J. Jaky. The coefficient of earth pressure at rest. *Journal for Society of Hungarian Architects and Engineers*, 78(22):355–358, 1944.

S. Jalbi, L. Arany, A. Salem, L. Cui, and S. Bhattacharya. A method to predict the cyclic loading profiles (one-way or two-way) for monopile supported offshore wind turbines. *Marine Structures*, 63:65–83, 2019. URL https://doi.org/10.1016/j.marstruc.2018.09.002.

R. J. Jardine and J. R. Standing. Field axial cyclic loading experiments on piles driven in sand. *Soils and Foundations*, 52(4):723–736, 2012. URL https://doi.org/10.1016/j.sandf.2012.07.012.

H. P. Jostad and L. Andresen. A FE procedure for calculation of displacements and capacity of foundations subjected to cyclic loading. In *Proceedings of the 1st International Symposium on Computational Geomechanics – GOMGEO I*, 2009.

H. P. Jostad, K. H. Andersen, and T. I. Tjelta. Analyses of skirted foundations and anchors in sand subjected to cyclic loading. 1997.

H. P. Jostad, G. Grimstad, K. H. Andersen, M. Saue, Y. Shin, and D. You. A FE procedure for foundation design of offshore structures – Applied to study a potential OWT monopile foundation in the Korean Western Sea. *Geotechnical Engineering*, 45 (4):63–72, 2014.

H. P. Jostad, G. Grimstad, K. H. Andersen, and N. Sivasithamparam. A FE procedure for calculation of cyclic behaviour of offshore foundations under partly drained conditions. In *Frontiers in Offshore Geotechnics III*, 2015a.

H. P. Jostad, Ø. Torgersrud, and H. K. Engin. A FE procedure for calculation of fixity of jack-up foundations with skirts using cyclic strain contour diagrams. In *International Conference: The Jack-Up Platform 2015*, 2015b.

H. P. Jostad, B. M. Dahl, A. Page, N. Sivasithamparam, and H. Sturm. Evaluation of soil models for improved design of offshore wind turbine foundations in dense sand. *Géotechnique*, 70(8):682–699, 2020. URL https://doi.org/10.1680/jgeot.19.TI.034.

H. P. Jostad, P. Carotenuto, S. Yusuke, and N. Sivasithamparam. Measuring and modelling cyclic response of dense sand under partially drained conditions. In *IACMAG 2021: Challenges and Innovations in Geomechanics*, 2021. URL https://doi.org/10.1007/978-3-030-64514-4_43.

T. Kagawa. Cyclic and loading-rate effects on pile responses. In *Proceedings of the 3rd International Conference on Numerical Methods in Offshore Piling*, 1986.

W. S. Kaggwa, J. R. Booker, and J. P. Carter. Residual strains in calcareous sand due to irregular cyclic loading. *Journal of Geotechnical Engineering*, 117(2):201–218, 1991. URL https://doi.org/10.1061/(ASCE)0733-9410(1991)117:2(201).

A. Kavli, L. Grande, S. Nordal, and H. P. Jostad. A coulombian soil model applied to an offshore platform. In *Proceedings of the 12th International Conference on Soil Mechanics and Foundation Engineering*, 1989.

H. D. V. Khoa and H. P. Jostad. Application of a cyclic accumulation model UDCAM to FE analyses of offshore foundations. In *Proceedings of the 4th Congrès International de Géotechnique - Ouvrages -Structures*, 2017. URL https://doi.org/10.1007/978-981-10-6713-6_65.

R. T. Klinkvort, H. Sturm, A. M. Page, Y. Zhang, and H. P. Jostad. A consistent, rigorous and super fast monopile design approach. In *Proceedings of the 4th International Symposium on Frontiers in Offshore Geotechnics*, 2020.

K. Kluge. *Soil liquefaction around offshore pile foundations - scale model investigations.* PhD thesis, Faculty of Architecture, Civil Engineering and Environmental Sciences, University of Braunschweig, 2007. URL https://doi.org/10.24355/dbbs.084-200808280200-5.

D. Kolymbas. *Eine konstitutive Theorie für Böden und andere körnige Stoffe.* PhD thesis, Institut für Bodenmechanik und Felsmechanik der Universität Fridericiana, 1988.

S. L. Kramer. *Geotechnical earthquake engineering.* Pearson, 1996. ISBN 978-0133749434.

KTA 2201.2 (2012-11). Design of Nuclear Power Plants Against Seismic Events Part 2: Subsoil. Safety standard, Nuclear Safety Standards Commission, Salzgitter, Germany, 2012.

K. Kudo, H. Nagatomo, and S. Sato. Effect of microscopic characteristics of sand grain on its liquefaction resistance. In *Proceedings of the Regional Conference of West Japan Society of Civil Engineers*, pages 200–501, 1993.

R. S. Ladd. Specimen preparation and liquefaction of sands. *Journal of the Geotechnical Engineering Division*, 100(10):1180–1184, 1974. URL https://doi.org/10.1061/AJGEB6.0000117.

R. S. Ladd. Specimen preparation and cyclic stability of sands. *Journal of the Geotechnical Engineering Division*, 103(6):535–547, 1977. URL https://doi.org/10.1061/AJGEB6.0000435.

R. S. Ladd, R. Dobry, P. Dutko, F. Y. Yokel, and R. M. Chung. Pore-water pressure buildup in clean sands because of cyclic straining. *Geotechnical Testing Journal*, 12(1): 77–86, 1989. URL https://doi.org/10.1520/GTJ10677J.

T. W. Lambe and W. A. Marr. Stress path method: Second edition. *Journal of the Geotechnical Engineering Division*, 105(6):727–738, 1979. URL https://doi.org/10.1061/AJGEB6.0000821.

W. T. Lambe. Stress path method. *Journal of the Soil Mechanics and Foundations Division*, 93(6):309–331, 1967. URL https://doi.org/10.1061/JSFEAQ.0001058.

V. H. Le. *Zum Verhalten von Sand unter zyklischer Beanspruchung mit Polarisationswechsel im Einfachscherversuch.* PhD thesis, Technische Universität Berlin, 2015. URL https://doi.org/10.14279/depositonce-4896.

C. Leblanc, G. T. Houlsby, and B. W. Byrne. Response of stiff piles in sand to long-term cyclic lateral loading. *Géotechnique*, 60(2):79–90, 2010. URL https://doi.org/10.1680/geot.7.00196.

C. Y. Lee and H. G. Poulos. Influence of excess pore pressures on axial offshore pile response. *International Journal of Rock Mechanics and Mining Sciences & Geomechanics Abstracts*, 26(5), 1988. URL https://doi.org/10.1016/0148-9062(89)91229-1.

K. L. Lee and A. Albaisa. Earthquake induced settlements in saturated sands. *Journal of the Geotechnical Engineering Division*, 100(4):387–406, 1974. URL https://doi.org/10.1061/AJGEB6.0000034.

K. L. Lee and J. A. Focht Jr. Liquefaction potential at Ekofisk Tank in North Sea. *Journal of Geotechnical Engineerin Division*, 101(1):1–18, 1975. URL https://doi.org/10.1061/AJGEB6.0000138.

K. L. Lee and H. B. Seed. Cyclic stress conditions causing liquefaction of sand. *Journal of the Soil Mechanics and Foundations Division*, 93(1):47–70, 1967. URL https://doi.org/10.1061/JSFEAQ.0000945.

G. Lefebvre, D. LeBoeuf, and B. Demers. Stability threshold for cyclic loading of saturated clay. *Canadian Geotechnical Journal*, 26(1):122–131, 1989. URL https://doi.org/10.1139/t89-013.

S. Lenart. The response of saturated soils to a dynamic load. *Acta geotechnica Slovenica*, 5(1):37–49, 2008.

S. Li, Y. Zhang, and H. P. Jostad. Drainge conditions around monopiles in sand. *Applied Ocean Research*, 86:111–116, 2019. URL https://doi.org/10.1016/j.apor.2019.01.024.

X. S. Li and Y. F. Dafalias. Dilatancy for cohesionless soils. *Géotechnique*, 50(4):449–460, 2000. URL https://doi.org/10.1680/geot.2000.50.4.449.

X. S. Li and Y. Wang. Linear representation of steadystate line for sand. *Journal of Geotechnical and Geoenvironmental Engineering*, 124(12):1215–1217, 1998. URL https://doi.org/10.1061/(ASCE)1090-0241(1998)124:12(1215).

S.-S. Lin and J.-C. Liao. Permanent strains of piles in sand due to cyclic lateral loads. *Journal of Geotechnical and Geoenvironmental Engineering*, 125(9):798–802, 1999. URL https://doi.org/10.1061/(ASCE)1090-0241(1999)125:9(798).

H. Liu, F. Zygounas, A. Diambra, and F. Pisanò. Enhanced plasticity modelling of high-cyclic ratcheting and pore pressure accumulation in sands. In *Proceedings of the 9th European Conference on Numerical Methods in Geotechnical Engineering*, 2018a.

H. Liu, A. Diambra, J. A. Abell, and F. Pisano. Memory-enhanced plasticity modelling of sand behaviour under undrained cyclic loading. *Journal of Geotechnical and Geoenvironmental Engineering*, 146(11), 2020. URL https://doi.org/10.1061/(ASCE)GT.1943-5606.0002362.

H. Liu, E. Kementzetzidis, J. A. Abell, and F. Pisanò. From cyclic sand ratcheting to tilt accumulation of offshore monopiles: 3D FE modelling using SANISAND-MS. *Géotechnique*, 72(9):753–768, 2021. URL https://doi.org/10.1680/jgeot.20.P.029.

H. Y. Liu, J. A. Abell, A. Diambra, and F. Pisanò. Modelling the cyclic ratcheting of sands through memory-enhanced bounding surface plasticity. *Géotechnique*, 69(9):783–800, 2018b. URL https://doi.org/10.1680/jgeot.17.P.307.

W. Lode. Versuche über den Einfluß der mittleren Hauptspannung auf das Fließen der Metalle Eisen, Kupfer und Nickel. *Zeitschrift für Phyisk*, 36:913–939, 1926.

J. H. Long and G. Vanneste. Effects of cyclic lateral loads on piles in sand. *Journal of Geotechnical Engineering*, 120(1):225–225, 1994. URL https://doi.org/10.1061/(ASCE)0733-9410(1994)120:1(225).

C. Madshus and L. Harvik. Solutions to the consolidation equation for some different geometries and initial pore pressure distributions. *NGI Internal Report*, 514150-1, 1988.

I. Manoliu, D. V. Dimitriu, N. Radulescu, and G. Dobrescu. Load-deformation characteristics of drilled piers. In *Proceedings of the 11th International Conference on Soil Mechanics and Foundation Engineering*, 1985.

M. T. Manzari and Y. F. Dafalias. A critical state two-surface plasticity model for sands. *Géotechnique*, 47(2):255–272, 1997. URL https://doi.org/10.1680/geot.1997.47.2.255.

X. Mao, M. Fahey, and M. F. Randolph. Cyclic loading behaviour of fine-grained calcareous soils: Effect of mean and cyclic stress level. In *Proceedings of the Ninth International Offshore and Polar Engineering Conference*, 1999.

T. Marcher, P. A. Vermeer, and P.-A. Von Wolffersdorff. *Hypoplastic and elastoplastic modelling - a comparison with test data*, pages 353–374. Springer, Berlin, Heidelberg, 2000. ISBN 978-3-642-63115-3. URL https://doi.org/10.1007/978-3-642-57018-6_17.

W. A. Marr Jr. and J. T. Christian. Permanent displacements due to cyclic wave loading. *Journal of the Geotechnical Engineering Division*, 107(8):1129–1149, 1981. URL https://doi.org/10.1061/AJGEB6.0001179.

G. R. Martin, H. B. Seed, and W. D. L. Finn. Fundamentals of liquefaction under cyclic loading. *Journal of Geotechnical Engineering Division*, 101(5), 1974. URL https://doi.org/10.1061/AJGEB6.0000164.

G. R. Martin, I. Lam, and C.-F. Tsai. Pore-pressure dissipation during offshore cyclic loading. *Journal of the Geotechnical Engineering Division*, 106(9):981–996, 1980. URL https://doi.org/10.1061/AJGEB6.0001040.

P. Martin. *Nonlinear methods for dynamic analysis of ground response.* PhD thesis, Department of Engineering, University of California, 1975.

N. Matasovic. *Seismic response of composite horizontally-layered soil deposits.* PhD thesis, University of California, 1993.

MathWorks. Matlab. R2021b. 2021.

M. Matsuishi and T. Endo. Fatigue of metals subjected to varying stress. *Presented to the Japan Society of Mechanical Engineers*, 1968.

R. A. McAdam, B. W. Byrne, G. T. Houlsby, W. J. A. P. Beuckelaers, H. J. Burd, K. G. Gavin, D. J. P. Igoe, R. J. Jardine, C. M. Martin, A. Muir Wood, D. M. Potts, J. S. Gretlund, D. M. G. Taborda, and L. Zdravkovic. Monotonic laterally loaded pile testing in a dense marine sand at Dunkirk. *Géotechnique*, 70(11):986–998, 2020. URL https://doi.org/10.1680/jgeot.18.PISA.004.

B. McClelland and J. A. Focht Jr. Soil modulus for laterally loaded piles. *Transactions of the American Society of Civil Engineers*, 123(1):1049–1063, 1958. URL https://doi.org/10.1061/TACEAT.0007599.

J. F. McNulty. Thrust loading on piles. *Journal of the Soil Mechanics and Foundations Division*, 82(2), 1956. URL https://doi.org/10.1061/JSFEAQ.0000009.

P. Meijers and D. Luger. On the modelling of wave-induced liquefaction, taking into account the effect of preshearing. In *Proceedings of the Twenty-second International Offshore and Polar Engineering Conference*, 2012.

P. Meijers, T. Raaijmakers, and D. Luger. The effect of a random wave field on wave induced pore pressure generation. In *Proceedings of the Twenty-fourth International Ocean and Polar Engineering Conference*, 2014.

M. A. Miner. Cumulative damage in fatigue. *Journal of Applied Mechanics*, 12(3):A159–A164, 1945. URL https://doi.org/10.1115/1.4009458.

R. J. Mitchell and B. I. Dubin. Pore pressure generation and dissipation in dense sands under cyclic loading. *Canadian Geotechnical Journal*, 23(3):393–398, 1986. URL https://doi.org/10.1139/t86-055.

Z. Mrǒz, V. A. Norris, and O. C. Zienkiewicz. An anisotropic hardening model for soils and its application to cyclic loading. *International Journal for Numerical and Analytical Methods in Geomechanics*, 2(3):203–221, 1978. URL https://doi.org/10.1002/nag.1610020303.

J. P. Mulilis, H. B. Seed, C. K. Chan, J. K. Mitchell, and K. Arulanandan. Effects of sample preparation on sand liquefaction. *Journal of the Geotechnical Engineering Division*, 103(2):91–108, 1977. URL https://doi.org/10.1061/AJGEB6.0000387.

N. Müthing, S. S. Razouki, M. Datcheva, and T. Schanz. Rigorous solution for 1-D consolidation of a clay layer under haversine cyclic loading with rest period. *SpringerPlus*, 5, 2016. URL https://doi.org/10.1186/s40064-016-3660-9.

F. Nelson and M. Okamura. Influence of strain histories on liquefaction resistance of sand. *Soils and Foundations*, 59(5):1481–1495, 2019. URL https://doi.org/10.1016/j.sandf.2019.06.011.

J. Ni. *Application of geosynthetic vertical drains under cyclic loads in stabilizing tracks*. PhD thesis, University of Wollongong, School of Civil Mining and Environmental Engineering, 2012. URL https://ro.uow.edu.au/theses/3604.

J. Ni, B. Indraratna, X.-Y. Geng, J. P. Carter, and C. Rujikiatkamjorn. Radial consolidation of soft soil under cyclic loads. *Computers and Geotechnics*, 50:1–5, 2012. URL https://doi.org/10.1016/j.compgeo.2012.11.011.

A. Niemunis and I. Herle. Hypoplastic model for cohesionless soils with elastic strain range. *Mechanics of Cohesive-frictional Materials*, 2(4):279–299, 1998. URL https://doi.org/10.1002/(SICI)1099-1484(199710)2:4<279::AID-CFM29>3.0.CO;2-8.

A. Niemunis, T. Wichtmann, and T. Triantafyllidis. A high-cycle accumulation model for sand. *Computers and Geotechnics*, 32(4):245–263, 2005. URL https://doi.org/10.1016/j.compgeo.2005.03.002.

K. Norén-Cosgriff, H. P. Jostad, and C. Madshus. Idealized load composition for determination of cyclic undrained degradation of soils. In *Proceedings of the 3rd International Symposium on Frontiers in Offshore Geotechnics*, pages 1097–1102, 2015.

M. Oda and K. Iwashita. *Mechanics of Granular Materials: An introduction*. CRC Press, 1st edition, 1999. URL https://doi.org/10.1201/9781003077817.

M. Oda, K. Kawamoto, K. Suzuki, H. Fujimori, and M. Sato. Microstructural interpretation on reliquefaction of saturated granular soils under cyclic loading. *Journal of Geotechnical and Geoenvironmental Engineering*, 127(5):416–423, 2001. URL https://doi.org/10.1061/(ASCE)1090-0241(2001)127:5(416).

N. Ohno and J.-D. Wang. Kinematic hardening rules with critical state of dynamic recovery, part I: formulation and basic features for ratchetting behavior. *International Journal of Plasticity*, 9(3):375–390, 1993. URL https://doi.org/10.1016/0749-6419(93)90042-O.

M. Okamura, F. Nelson, and S. Watanabe. Pre-shaking effects on volumetric strain and cyclic strength of sand and comparison to unsaturated soils. *Soil Dynamics and Earthquake Engineering*, 124:307–316, 2018. URL https://doi.org/10.1016/j.soildyn.2018.04.046.

M. W. O'Neill and J. M. Murchison. *An evaluation of p-y relationships in sands*. University of Houston, 1983.

N. J. O'Riordan and J. W. Seaman. *Optimization of underbase drainage systems for gravity structures on sand*. Springer, 1993. URL https://doi.org/10.1007/978-94-017-2473-9_21.

A. Pak, P. Ayoubi, and H. Shahir. A performance-based approach to the design of shallow foundations resting on heterogeneous subsoil prone to liquefaction hazards. In *Proceedings of the Fourth Geo-China International Conference*, 2016. URL https://doi.org/10.1061/9780784480076.006.

A. G. Palmgren. Die Lebensdauer von Kugellagern. *Zeitschrift des Vereines Deutscher Ingenieure (ZVDI)*, 14:339–341, 1924.

K. Pan and Z. X. Yang. Effets of initial static shear on cyclic resistance and pore pressure generation of saturated sand. *Acta Geotechnica*, 13:473–487, 2018. URL https://doi.org/10.1007/s11440-017-0614-5.

M. Pastor, V. Drempetic, J. A. Fernández Merodo, and P. Mira. Modelling marine structures foundations: A rational approach. In *Proceedings of the 1st Euro-Mediterranean Symposium on Advances in Geomaterials and Structures*, pages 203–208, 2006.

M. Paul, R. B. Sahu, and G. Banerjee. Undrained pore pressure prediction in clayey soil under cyclic loading. *International Journal of Geomechanics*, 15(5), 2014. URL https://doi.org/10.1061/(ASCE)GM.1943-5622.0000431.

W. H. Peacock and H. B. Seed. Sand liquefaction under cyclic loading simple shear conditions. *Journal of the Soil Mechanics and Foundations Division*, 94(3):689–708, 1968. URL https://doi.org/10.1061/JSFEAQ.0001135.

A. Petalas and V. Galavi. Plaxis liquefaction model UBC3D-PLM. Technical report, 2012.

A. L. Petalas, Y. F. Dafalias, and A. G. Papadimitriou. SANISAND-F: Sand constitutive model with evolving fabric anisotropy. *International Journal of Solids and Structures*, 188-189:12–31, 2020. URL https://doi.org/10.1016/j.ijsolstr.2019.09.005.

D. J. Pickering. Drained liquefaction testing in cyclic shear. *Journal of the Soil Mechanics and Foundations Division*, 99(12):1179–1184, 1973.

C. P. Polito. *The Effects Of Non-Plastic and Plastic Fines On The Liquefaction Of Sandy Soils*. PhD thesis, Faculty of the Virginia Polytechnic Institute and State University, 1999.

C. P. Polito, R. A. Green, and J. Lee. Pore pressure generation models for sands and silty soils subjected to cyclic loading. *Journal of Geotechnical and Geoenvironmental Engineering*, 134(10):1490–1500, 2008. URL https://doi.org/10.1061/(ASCE)1090-0241(2008)134:10(1490).

D. Porcino, V. Marcianò, and V. N. Ghionna. Influence of cyclic pre-shearing on undrained behaviour of carbonate sand in simple shear tests. *Geomechanics and Geoengineering*, 4(2):151–161, 2009. URL https://doi.org/10.1080/17486020902855662.

S. J. Poulos. The steady state of deformation. *Journal of the Geotechnical Engineering Division*, 107(5):553–562, 1981. URL https://doi.org/10.1061/AJGEB6.0001129.

M. C. Powers. A new roundness scale for sedimentary particles. *Journal of Sedimentary Research*, 23, 1953. URL https://doi.org/10.1306/D4269567-2B26-11D7-8648000102C1865D.

J.-H. Prevost. Mathematical modelling of monotonic and cyclic undrained clay behaviour. *International Journal for Numerical and Analytical Methods in Geomechanics*, 1(2):195–216, 1977. URL https://doi.org/10.1002/nag.1610010206.

J. H. Prevost. A simple plasticity theory for frictional cohesionless soils. *International Journal of Soil Dynamics and Earthquake Engineering*, 4(1):9–17, 1985. URL https://doi.org/10.1016/0261-7277(85)90030-0.

J. H. Prevost, T. J. R. Hughes, and M. F. Cohen. Analysis of gravity offshore structure foundations. *Journal of Petroleum Technology*, 32(02):199–209, 1980. URL https://doi.org/10.2118/7239-PA.

K. Price and R. Storn. Differential evolution–A simple evolution strategy for fast optimization. *Dr. Dobb's Journal*, 22(4):18–24, 1997.

H. Puebla, P. M. Byrne, and R. Phillips. Analysis of CANLEX liquefaction embankments: prototype and centrifuge models. *Canadian Geotechnical Journal*, 34(5):641–657, 1997. URL https://doi.org/10.1139/t97-034.

A. Puech and J. Garnier, editors. *Design of Piles Under Cyclic Loading: SOLCYP Recommendations*. Wiley, 2017. URL https://doi.org/10.1002/9781119469018.

R. Pyke. *Settlement and liquefaction of sands under multi-directional loading*. PhD thesis, University of California, 1973.

R. Pyke. Panel discussion, laterally loaded deep foundations. In *Laterally loaded deep foundations: analysis and performance*, pages 239–243. ASTM, Philadelphia, Pa, 1984.

M. S. Rahman, J. R. Booker, and H. B. Seed. Pore pressure development under offshore gravity structures. *Journal of the Geotechnical Engineering Division*, 103(12):1419–1436, 1977. URL https://doi.org/10.1061/AJGEB6.0000537.

M. F. Randolph and C. P. Wroth. Application of the failure state in undrained simple shear to the shaft capacity of driven piles. *Géotechnique*, 31(1):143–157, 1981. URL https://doi.org/10.1680/geot.1981.31.1.143.

L. C. Reese and H. Matlock. *Non-dimensional solutions for laterally-loaded piles with soil modulus assumed proportional to depth*. Association of Drilled Shaft Contractors, Dallas, Texas, 1956.

L. C. Reese, W. R. Cox, and F. D. Koop. Analysis of laterally loaded piles in sand. In *Proceedings of the Offshore Technology Conference, Houston, Texas*, 1974. URL https://doi.org/10.4043/2080-MS.

F. E. Richart, J. R. Hall, and R. D. Woods. *Vibrations of soils and foundations*. Prentice-Hall, Inc., Englewood Cliffs, New Jersey, 1970.

P. K. Robertson. Suggested terminology for liquefaction. In *Proceedings of the 47th Canadian Geotechnical Conference*, 1994.

P. K. Robertson. Evaluation of flow liquefaction and liquefied strength using the cone penetration test. *Journal of Geotechnical and Geoenvironmental Engineering*, 136(6):842–854, 2010. URL https://doi.org/10.1061/(ASCE)GT.1943-5606.0000286.

K. O. Ronold. *Reliability of Marine Clay Foundations in Cyclic Loading.* PhD thesis, Stanford University, Department of Civil Engineering, 1993. URL https://doi.org/10.13140/2.1.1506.6405.

K. H. Roscoe, A. N. Schofield, and C. P. Wroth. On the yielding of soils. *Géotechnique*, 8(1):22–53, 1958. URL https://doi.org/10.1680/geot.1958.8.1.22.

P. W. Rowe. Stress-dilatancy relation for static equilibrium of assembly of particles in contact. In *Proceedings of the Royal Society A*, volume 269, pages 500–527, 1962. URL https://doi.org/10.1098/rspa.1962.0193.

C. Rudolph, J. Grabe, and I. Albrecht. Simple shear tests with a varying shearing direction during cyclic shearing. *Géotechnique Letters*, 4(2):102–107, 2014. doi: 10.1680/geolett.13.00088.

M. Ruffatto. Calibration of material parameters and model performance analysis for two proposed soil models. 2012.

J.-E. Saathoff and M. Achmus. Practical approach for the evaluation of cyclically induced excess pore pressure around offshore foundations in sand. In *Proceedings of the 4th International Symposium on Frontiers in Offshore Geotechnics*, 2020.

J.-E. Saathoff and M. Achmus. Excess pore pressure estimation based on cyclic laboratory tests. In *Proceedings of the 7th International Young Geotechnical Engineers Conference*, 2021.

J.-E. Saathoff, K. Thieken, and M. Achmus. Evaluation of un- and reloading stiffness and damping of monopile foundations in sand soils. In *Proceedings of the 29th International Ocean and Polar Engineering Conference*, 2019.

A. Sadrekarimi and S. M. Olson. Defining the critical state line from triaxial compression and ring shear tests. In *Proceedings of the 17th International Conference on Soil Mechanics and Geotechnical Engineering*, pages 36–39, 2009. URL https://doi.org/10.3233/978-1-60750-031-5-36.

S. Safinus, G. Sedlacek, and U. Hartwig. Cyclic response of granular subsoil under a gravity base foundation for offshore wind turbines. In *Proceedings of the 30th International Conference on Ocean, Offshore and Arctic Engineering*, pages 875–882, 2011. URL https://doi.org/10.1115/OMAE2011-49391.

A. Sakai, L. Samang, and N. Miura. Partially-drained cyclic behavior and its application to the settlement of a low embankment road on silty-clay. *Soils and Foundations*, 43 (1):33–46, 2003. URL https://doi.org/10.3208/sandf.43.33.

J. C. Santamarina and G. C. Cho. Determination of critical state parameters in sandy soils - simple procedure. *Geotechnical Testing Journal*, 24(2):185–192, 2001. URL https://doi.org/10.1520/GTJ11338J.

S. Savidis, T. Richter, F. Kirsch, and W. Rücker. *Entwurf und Bemessung von Gründungen für Offshore-Windenergieanlagen.* Wilhelm Ernst & Sohn, 2018. URL https://doi.org/10.1002/9783433607350.ch5.

A. Sawicki and W. Swidzinski. Mechanics of a sandy subsoil subjected to cyclic loadings. *International Journal for Numerical and Analytical Methods in Geomechanics*, 13(5): 511–529, 1989. URL https://doi.org/10.1002/nag.1610130505.

D. Schaefer, M. Achmus, and K. Abdel-Rahman. Effect of sand type on capacity degradation of cyclic axially loaded piles. In *Coastal Structures 2019*, pages 942–951. Karlsruhe: Bundesanstalt für Wasserbau, 2019. URL https://doi.org/10.18451/978-3-939230-64-9_094.

A. Schofield and P. Wroth. *Critical State Soil Mechanics*. McGraw-Hill, 1968. ISBN 978-0641940484.

D. Schuster, C. Hente, C. Hübler, and R. Rolfes. Integrierte Entwurfs- und Betriebsmethodik für Offshore-Megastrukturen. *Bautechnik*, 98(8):563–570, 2021. URL https://doi.org/10.1002/bate.202100044.

H. B. Seed. *Representation of irregular stress time histories by equivalent uniform stress series in liquefaction analyses*. College of Engineering, University of California, 1975.

H. B. Seed. Soil liquefaction and cyclic mobility evaluation for level ground during earthquakes. *Journal of the Geotechnical Engineering Division*, 105(2):201–255, 1979. URL https://doi.org/10.1061/AJGEB6.0000768.

H. B. Seed and J. R. Booker. Stabilization of potentially liquefiable sand deposits using gravel drains. *Journal of Geotechnical Engineering Division*, 103(7), 1976. URL https://doi.org/10.1061/AJGEB6.0000453.

H. B. Seed and I. M. Idriss. Analysis of soil liquefaction: Niigata earthquake. *Journal of the Soil Mechanics and Foundations Division*, 93(3):83–108, 1967. URL https://doi.org/10.1061/JSFEAQ.0000981.

H. B. Seed and K. L. Lee. Liquefaction of saturated sands during cyclic loading. *Journal of the Soil Mechanics and Foundations Division*, 92(6):105–134, 1966. URL https://doi.org/10.1061/JSFEAQ.0000913.

H. B. Seed and W. H. Peacock. Test procedures for measuring soil liquefaction characteristics. *Journal of the Soil Mechanics and Foundations Division*, 97(8):1099–1119, 1971. URL https://doi.org/10.1061/JSFEAQ.0001649.

H. B. Seed and M. S. Rahman. Wave-induced pore pressure in relation to ocean floor stability of cohesionless soils. *Marine Geotechnology*, 3(2):123–150, 1978. URL https://doi.org/10.1080/10641197809379798.

H. B. Seed, I. Arango, and C. K. Chan. Evaluation of soil liquefaction potential for level ground during earthquakes. a summary report. Technical report, 1975a. URL https://doi.org/10.2172/7146067.

H. B. Seed, P. P. Martin, and J. Lysmer. *The generation and dissipation of pore water pressures during soil liquefaction*. College of Engineering, University of California, 1975b.

H. B. Seed, K. Mori, and C. K. Chan. Influence of seismic history on liquefaction of sands. *Journal of the Geotechnical Engineering Division*, 103(4):257–270, 1977. URL https://doi.org/10.1061/AJGEB6.0000399.

B. B. Sheil and B. A. McCabe. Biaxial loading of offshore monopiles: Numerical modeling. *International Journal of Geomechanics*, 17(2), 2016. URL https://doi.org/10.1061/(ASCE)GM.1943-5622.0000709.

T. Shibata, H. Yukitomo, and M. Miyoshi. Liquefaction process of sand during cyclic loading. *Soils and Foundations*, 12(1):1–16, 1972. URL https://doi.org/10.3208/sandf1960.12.1.

R. Siddharthan. Wave-induced displacements in seafloor sands. *International Journal for Numerical and Analytical Methods in Geomechanics*, 11(2):155–170, 1987. URL https://doi.org/10.1002/nag.1610110205.

M. L. Silver and H. B. Seed. Deformation characteristics of sands under cyclic loading. *Journal of the Soil Mechanics and Foundations Division*, 97(8):1081–1098, 1971a. URL https://doi.org/10.1061/JSFEAQ.0001648.

M. L. Silver and H. B. Seed. Volume changes in sands during cyclic loading. *Journal of the Soil Mechanics and Foundations Division*, 97(9):1171–1182, 1971b. URL https://doi.org/10.1061/JSFEAQ.0001658.

M. L. Silver, C. K. Chan, R. S. Ladd, K. L. Lee, D. A. Tiedemann, F. C. Townsend, J. E. Valera, and J. H. Wilson. Cyclic triaxial strength of standard test sand. *Journal of the Geotechnical Engineering Division*, 102(5), 1976.

K. S. Skau, Y. Chen, and H. P. Jostad. A numerical study of capacity and stiffness of circular skirted foundations in clay subjected to combined static and cyclic general loading. *Géotechnique*, 68(3):205–220, 2017. URL https://doi.org/10.1680/jgeot.16.P.092.

F. P. Smits, K. H. Andersen, and G. Gudehus. Pore pressure generation. In *Proceedings of the International symposium on soil mechanics research and foundation design for the Oosterschelde storm surge barrier*, 1978.

E. X. Song. *Elasto-plastic consolidation under steady and cyclic loads.* PhD thesis, Delft University of Technology, 1990.

J. Stahlmann, J. Gattermann, and K. Kluge. FINO 3 - Forschungsansätze für Offshore Windenergieanlagen. *Mitteilung des Instituts für Grundbau und Bodenmechanik, Technische Universität Braunschweig*, 84:207–224, 2007.

P. Staubach, J. Machacek, B. Bienen, and T. Wichtmann. Long-term response of piles to cyclic lateral loading following vibratory and impact driving in water-saturated sand. *Journal of Geotechnical and Geoenvironmental Engineering*, 148(11), 2022.

H. E. Stewart. Permanent strains from cyclic variable-amplitude loadings. *Journal of Geotechnical Engineering*, 112(6):646–660, 1986. URL https://doi.org/10.1061/(ASCE)0733-9410(1986)112:6(646).

J. A. Studer, J. Laue, and M. Koller. *Bodendynamik - Grundlagen, Kennziffern, Probleme und Lösungsansätze*. Springer-Verlag, Berlin, Heidelberg, New York, 2007. ISBN 978-3-540-29625-6. URL https://doi.org/10.1007/978-3-540-29625-6.

M. Suzuki and T. Yamamoto. Liquefaction characteristic of undisturbed volcanic soil in cyclic triaxial test. In *Proceedings of the 13th World Conference on Earthquake Engineering*, 2004.

T. Suzuki and S. Toki. Effects of preshearing on liquefaction characteristics of saturated sand subjected to cyclic loading. *Soils and Foundations*, 24(2):16–28, 1984. URL https://doi.org/10.3208/sandf1972.24.2_16.

Y. Suzuki, P. Carotenuto, R. Dyvik, and H. P. Jostad. Experimental study of modeling partially drained dense sand behavior in monotonic triaxial compression loading tests. *Geotechnical Testing Journal*, 43(5), 2020. URL https://doi.org/10.1520/GTJ20190097.

H. Y. Sze and J. Yang. Failure modes of sand in undrained cyclic loading: Impact of sample preparation. *Journal of Geotechnical and Geoenvironmental Engineering*, 140 (1):152–169, 2014. URL https://doi.org/10.1061/(ASCE)GT.1943-5606.0000971.

H. E. Taşan. *Zur Dimensionierung der Monopile-Gründungen von Offshore-Windenergieanlagen*. PhD thesis, Technische Universität Berlin, 2011.

H. E. Taşan. Behaviour of free and fixed-head offshore piles under cyclic lateral loads. *Uludağ Üniversitesi Mühendislik Fakültesi Dergisi*, 22(1):219–234, 2017. URL https://doi.org/10.17482/uumfd.310966.

H. E. Taşan, F. Rackwitz, and S. Savidis. Porenwasserdruckakkumulation bei zyklisch horizontal belasteten Monopiles mit großen Durchmessern. *Bautechnik*, 87(8):449–461, 2010. URL https://doi.org/10.1002/bate.201010032.

H. A. Taiebat. *Three dimensional liquefaction analysis of offshore foundations*. PhD thesis, Department of Civil Engineering, University of Sydney, 1999.

H. A. Taiebat and J. P. Carter. A semi-empirical method for the liquefaction analysis of offshore foundations. *International Journal for Numerical and Analytical Methods in Geomechanics*, 24(13):991–1011, 2000. URL https://doi.org/10.1002/1096-9853(200011)24:13<991::AID-NAG108>3.0.CO;2-5.

M. Taiebat and Y. F. Dafalias. SANISAND: Simple anisotropic sand plasticity model. *International Journal for Numerical and Analytical Methods in Geomechanics*, 32(8):915–948, 2008. URL https://doi.org/10.1002/nag.651.

M. Taiebat, B. Jeremić, Y. F. Dafalias, A. M. Kaynia, and Z. Cheng. Propagation of seismic waves through liquefied soils. *Soil Dynamics and Earthquake Engineering*, 30 (4):236–257, 2010. URL https://doi.org/10.1016/j.soildyn.2009.11.003.

F. Tatsuoka, K. Ochi, S. Fujii, and M. Okamoto. Cyclic undrained triaxial and torsional shear strength of sands for different sample preparation methods. *Soils and Foundations*, 26(3):23–41, 1986. URL https://doi.org/10.3208/sandf1972.26.3_23.

D. W. Taylor. *Fundamentals of soil mechanics.* John Wiley & Sons, 1948.

J. Teparaksa and J. Koseki. Silica sand behavior under repeated liquefaction in cyclic triaxial test. In *Proceedings of the 19th International Conference on Soil Mechanics and Geotechnical Engineering*, 2017.

K. V. Terzaghi. The shearing resistance of saturated soils and the angle between the planes of shear. In *Proceedings of the 1st International Conference on Soil Mechanics and Foundation Engineering*, 1936.

K. Thieken. *Geotechnical design aspects of foundations for offshore wind energy converters.* PhD thesis, Institut für Geotechnik, Leibniz Universität Hannover, 2015.

K. Thieken, M. Achmus, J.-E. Saathoff, J. Albiker, and M. Terceros. Stiffness of monopile foundations under un- and reloading conditions. In *Numerical Methods in Geotechnical Engineering IX*, pages 1469–1476. Taylor & Francis, 2018.

K. Tokimatsu and Y. Hosaka. Effects of sample disturbance on dynamic properties of sand. *Soils and Foundations*, 26(1):53–64, 1986. URL https://doi.org/10.3208/sandf1972.26.53.

A. Tsegaye. Plaxis liquefaction model (UBC3D). Technical report, PLAXIS knowledge base, 2010.

S. Tsotsos, M. Georgiadis, and A. Damaskinidou. Numerical analysis of liquefaction potential of partially drained seafloors. *Coastal Engineering*, 13(2):117–128, 1989. URL https://doi.org/10.1016/0378-3839(89)90019-7.

Y. P. Vaid and J. C. Chern. Effect of static shear on resistance to liquefaction. *Soils and Foundations*, 23(1):47–60, 1983. URL https://doi.org/10.3208/sandf1972.23.47.

P. A. Vermeer and R. De Borst. Non-associated plasticity for soils, concrete and rock. *HERON*, 29(3), 1984.

A. Verruijt and E. X. Song. Finite element analysis of pore pressure build-up due to cyclic loading. In *Proceedings of the 10th European Conference on Soil Mechanics and Foundation Engineering*, pages 277–280, 1991.

P. A. Von Wolffersdorff. A hypoplastic relation for granular materials with a predefined limit state surface. *Mechanics of Cohesive-frictional Materials*, 1(3):251–271, 1996. URL https://doi.org/10.1002/(SICI)1099-1484(199607)1:3<251::AID-CFM13>3.0.CO;2-3.

M. Vucetic. Cyclic threshold shear strains in soils. *Journal of Geotechnical Engineering*, 120(12):2208–2229, 1994. URL https://doi.org/10.1061/(ASCE)0733-9410(1994)120:12(2208).

M. Vucetic and R. Dobry. *Pore pressure buildup and liquefaction at level sandy sites during earthquakes.* Rensselaer Polytechnic Institute, Troy, New York, 1986.

M. Vucetic and A. Mortezaie. Cyclic secant shear modulus versus pore water pressure in sands at small cyclic strains. *Soil Dynamics and Earthquake Engineering*, 70:60–72, 2015. URL https://doi.org/10.1016/j.soildyn.2014.12.001.

D. Wegener and I. Herle. Ermittlung von Scherdehnungen durch Schwingungsmessungen und numerische Berechnungen. *BAWMitteilungen*, 95:59–70, 2012. URL https://hdl.handle.net/20.500.11970/102560.

S. Werkmeister. *Permanent deformation behaviour of unbound granular materials in pavement constructions.* PhD thesis, Fakultät Bauingenieurwesen der Technischen Universität Dresden, 2004.

D. Wichtmann. *Explicit accumulation model for non-cohesive soils under cyclic loading.* PhD thesis, Fakultät für Bauingenieurwesen, Ruhr-Universität Bochum, 2005.

T. Wichtmann. Soil behaviour under cyclic loading - experimental observations, constitutive description and applications. *Habilitationsschrift, Veröffentlichungen des Institutes für Bodenmechanik und Felsmechanik am Karlsruher Institut für Technologie*, 2016.

T. Wichtmann and T. Triantafyllidis. Prognose bleibender Verformungen infolge zyklischer Belastung mit veränderlicher Amplitude: Eine Diskussion unterschiedlicher Ansätze. *Veröffentlichungen des Grundbauinstitutes der Technischen Universität Berlin*, (56), 2011.

T. Wichtmann and T. Triantafyllidis. Effect of uniformity coefficient on G/Gmax and damping ratio of uniform to well-graded quartz sands. *Journal of Geotechnical and Geoenvironmental Engineering*, 139(1):59–72, 2013. URL https://doi.org/10.1061/(ASCE)GT.1943-5606.0000735.

T. Wichtmann, A. Niemunis, and T. Triantafyllidis. Setzungsakkumulation in nichtbindigen Böden unter hochzyklischer Belastung. *Bautechnik*, 82(1):18–27, 2005. URL https://doi.org/10.1002/bate.200590023.

T. Wichtmann, A. Niemunis, and T. Triantafilidis. Prediction of long-term deformations for monopile foundations of offshore wind power plants. In *Proceedings of the 11th Baltic Sea Geotechnical Conference: Geotechnics in Maritime Engineering*, 2008.

T. Wichtmann, A. Niemunis, and T. Triantafyllidis. Validation and calibration of a high-cycle accumulation model based on cyclic triaxial tests on eight sands. *Soils and Foundations*, 2009. URL https://doi.org/10.3208/sandf.49.711.

T. Wichtmann, A. Niemunis, and T. Triantafallidis. On the “elastic” stiffness in a high-cycle accumulation model for sand: a comparison of drained and undrained cyclic triaxial tests. *Canadian Geotechnical Journal*, 47(7):791–805, 2010. URL https://doi.org/10.1139/T09-142.

T. Wichtmann, B. Rojas, A. Niemunis, and T. Triantafyllidis. Prediction of drained and undrained cyclic behaviour of a fine sand using a high-cycle accumulation model. In *Proceedings of the 5th International Conference on Earthquake Geotechnical Engineering*, 2011.

T. Wichtmann, W. Fuentes, and T. Triantafyllidis. Inspection of three sophisticated constitutive models based on monotonic and cyclic tests on fine sand: Hypoplasticity vs. Sanisand vs. ISA. *Soil Dynamics and Earthquake Engineering*, 124:172–183, 2019. URL https://doi.org/10.1016/j.soildyn.2019.05.001.

S. Wiesener, B. Schaedlich, T. Richter, and F. Kirsch. Ansatz zur Erfassung der Porenwasserdruckakkumulation bei Offshore-Monopilegründungen/ A method for predicting the accumulation of excess pore pressure at offshore monopile foundations. *Bauingenieur*, 91:26–33, 2016. URL https://doi.org/10.37544/0005-6650-2016-01-60.

Wind Europe. Wind energy in Europe : 2021 statistics and the outlook for 2022-2026. Technical report, 2021. URL https://windeurope.org/intelligence-platform/product/wind-energy-in-europe-2021-statistics-and-the-outlook-for-2022-2026/.

E. Winkler. *Die Lehre von der Elastizität und Festigkeit mit besonderer Rücksicht auf ihre Anwendung in der Technik: für polytechnische Schulen, Bauakademien, Ingenieure, Maschinenbauer, Architecten, etc.* Dominicus, 1867.

D. M. Wood. *Soil Behaviour and Critical State Soil Mechanics.* Cambridge University Press, 1990.

N. M. Wride, X.-Y. Geng, W. H. Zhou, and Y.-J. Cui. Partially drained response of cohesive soils subjected to cyclic loading. In *Proceedings of the XVII European Conference on Soil Mechanics and Geotechnical Engineering*, 2019. URL https://doi.org/10.32075/17ECSMGE-2019-0320.

J. Wu, A. Kammerer, M. F. Riemer, R. B. Seed, and J. M. Pestana. Laboratory study of liquefaction triggering criteria. In *Proceedings of the 13th World Conference on Earthquake Engineering*, 2004.

Y. Yamada and K. Ishihara. Yielding of loose sand in three-dimensional stress conditions. *Soils and Foundations*, 22(3):15–31, 1982. URL https://doi.org/10.3208/sandf1972.22.3_15.

S. Yamashita and S. Toki. Effects of fabric anisotropy of sand on cyclic undrained triaxial and torsional strengths. *Soils and Foundations*, 33(3):92–104, 1993. URL https://doi.org/10.3208/sandf1972.33.3_92.

J. Yang and H. Y. Sze. Cyclic behaviour and resistance of saturated sand under non-symmetrical loading conditions. *Géotechnique*, 61(1):59–73, 2011. URL https://doi.org/10.1680/geot.9.P.019.

M. Yang, A. R. Barrero, and M. Taiebat. Application of a SANISAND model for numerical simulations of the LEAP 2017 experiments. In *Model Tests and Numerical Simulations of Liquefaction and Lateral Spreading.* Springer, 2020. URL https://doi.org/10.1007/978-3-030-22818-7_30.

M. Yang, M. Taiebat, and Y. F. Dafalias. SANISAND-MSf: a sand plasticity model with memory surface and semifluidised state. *Géotechnique*, 72(3):227–246, 2022. URL https://doi.org/10.1680/jgeot.19.P.363.

K. Yasuhara and K. H. Andersen. Recompression of normally consolidated clay after cyclic loading. *Soils and Foundations*, 31(1):83–94, 1991. URL https://doi.org/10.3208/sandf1972.31.83.

T. L. Youd. Compaction of sands by repeated shear straining. *Journal of the Soil Mechanics and Foundations Division*, 98(7):709–725, 1972. URL https://doi.org/10.1061/JSFEAQ.0001762.

H. S. Yu. Multi-surface and bounding surface plasticity. In *Plasticity and Geotechnics. Advances in Mechanics and Mathematics*, volume 13. Springer, 2006. URL https://doi.org/10.1007/978-0-387-33599-5_7.

H. Zachert and T. Wichtmann. *Approaches for the design of foundations for offshore wind turbines*. Springer, 2020. URL https://doi.org/10.1007/978-3-030-28516-6_7.

L. Zdravkovic and R. J. Jardine. The effect on anisotropy of rotating the principal stress axes during consolidation. *Géotechnique*, 51(1):69–84, 2001. URL https://doi.org/10.1680/geot.2001.51.1.69.

L. Zdravkovic, E. Porovic, and R. J. Jardine. Panel contribution: Anisotropic consolidation including principal stress axis rotation: Experiments, results and practical implications. In *Proceedings of the 14th International Conference on Soil Mechanics and Foundation Engineering*, 1997.

Y. Zhang, K. H. Andersen, and P. Jeanjean. Cyclic p-y curves in clays for offshore structures. In *The Offshore Technology Conference*, 2019. URL https://doi.org/10.4043/29346-MS.

O. C. Zienkiewicz and P. Bettess. Soil and other saturated porous media under transient, dynamic conditions. general formulation and the validity of various simplifying assumptions. In G. Pande and O. C. Zienkiewicz, editors, *Soils under Cyclic and Transient Loading*, pages 1–16. Wiley, 1982.

D. Zografou, N. Boukpeti, S. Gouvernec, and C. D. O'Loughlin. Definition of failure in cyclic direct simple shear tests on normally consolidated kaolin clay and presentation of shear strain contour diagrams. In *Proceedings of the 5th International Conference on Geotechnical and Geophysical Site Characterisation*, 2016.

D. Zografou, S. Gourvenec, C. O'Loughlin, and M. Banimahd. Applicability of the strain accumulation procedure for the geotechnical foundation design of zero-radius bend triggers. *Ocean Engineering*, 186, 2019a. URL https://doi.org/10.1016/j.oceaneng.2019.05.044.

D. Zografou, S. Gourvenec, and C. D. O'Loughlin. Response of normally consolidated kaolin clay underirregular cyclic loading and comparison with predictions from the accumulation procedure. *Géotechnique*, 69(2):106–121, 2019b. URL https://doi.org/10.1680/jgeot.16.P.340.

G. Zorzi, F. Kirsch, T. Richter, M. U. Ostergaard, and S. P. H. Sorensen. Validation of explicit method to predict accumulation of strain during single and multistage cyclic loading. In *Proceedings of the XVII European Conference on Soil Mechanics and Geotechnical Engineering*, 2019. URL https://doi.org/10.32075/17ECSMGE-2019-0255.

G. Zorzi, A. Mankar, J. Velarde, J. D. Sorensen, P. Arnold, and F. Kirsch. Reliability analysis of offshore wind turbine foundations under lateral cyclic loading. *Wind Energy Science*, 5:1521–1535, 2020.

A Appendices to individual chapters

Additional information on individual chapters and further research findings are provided below.

A.1 Chapter 4.1: SANISAND constitutive model

The SANISAND model is a stress-ratio controlled critical state compatible bounding-surface plasticity model by Dafalias and Manzari (2004) with a non-associative flow rule. The dilatancy depends on both stress state and void ratio. Dilatancy describes the development of shear induced volumetric strain and it is considered by the phase transformation line. A fabric-dilatancy tensor was added in this work based on Manzari and Dafalias (1997). The fabric change describes the altering of micro structure due to changes in particle arrangements. A change in fabric (or dilatancy behaviour) by means of a transforming of a dilatant to a contractant behaviour due to a small volumetric strain can only be incorporated with implicit models and can have a huge effect in the overall soil response.

Besides the most popular SANISAND version presented by Dafalias and Manzari (2004), there have been many additional versions that have for instance a closed wedge-typed yield surface in order to capture plastic behaviour for a constant stress ratio within the yield surface (cf. Taiebat and Dafalias (2008)). The model according to Taiebat and Dafalias (2008) considers the limiting compression curve (LCC) and, hence, partial grain crushing can be considered (Taiebat et al., 2010). There are also other enhanced versions for instance by Petalas et al. (2020). Other SANISAND implementations are the SANISAND-Z (Dafalias and Taiebat, 2016) for which for any loading direction plastic strains occur as the yield surface is zero and is represented by the stress point itself. The SANISAND-Sf (Barrero et al., 2020) contains a strain liquefaction factor for a semi-fluidized state (with a lower mean threshold stress value p_{th}) especially for liquefaction and post-liquefaction analysis (MSf-version with additional memory surface in Yang et al. (2020)). The dilatancy and plastic shear stiffness can be controlled with the new strain liquefaction scaling factor.

The most promising development bases on a multi-surface approach. The multi-surface framework was presented e.g. in Iwan (1967). Mrŏz et al. (1978) used nested yield surfaces in an effective stress based framework, similar to the work of Prevost (1977). It can be used to model and discretize the field of plastic moduli for softening, hardening and ratcheting. The soil response is modelled with several surfaces. The response within the first surface is purely elastic and does not change its position. The position of the centre of the yield surface is given by α, the back-stress tensor. The slope of the stress-strain curve changes when the current stress state crosses the first surface as the behaviour becomes plastic and kinematic hardening occurs. Both surfaces translate to the next surface. When unloading at the reversal point occurs, elastic behaviour inside the first surface is present until the stress state reaches the next surface where the slope changes again (Figure A.1). The disadvantage is the non-trivial calibration and the high amount of laboratory tests to calibrate different soil responses.

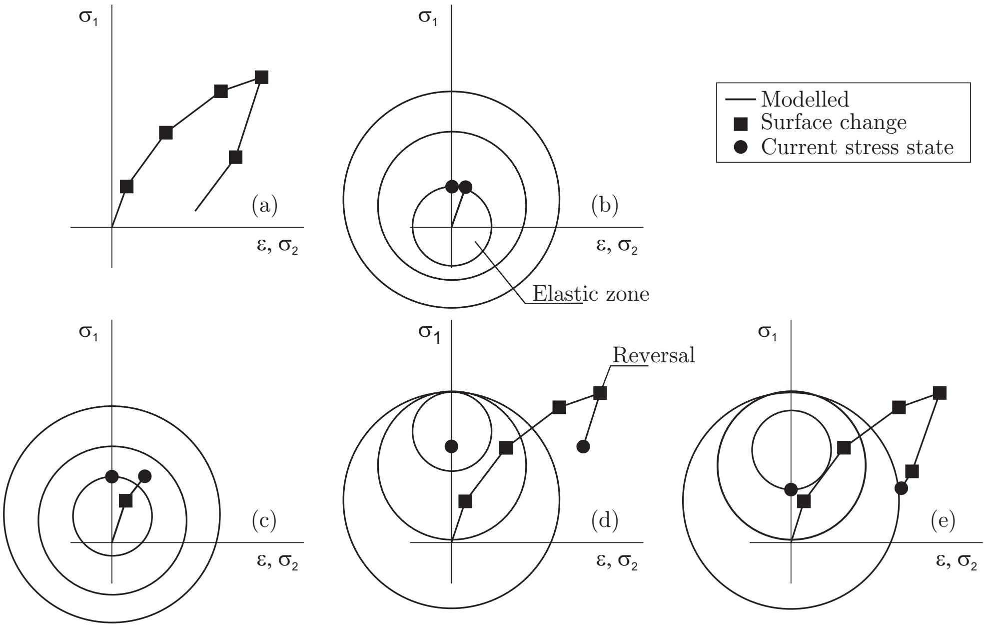

Figure A.1: Example of multi surface approach (Yu, 2006).

The SANISAND model considers most of the monotonic soil response mechanism, but is not capable of realistically reproducing the exact response for the specific number of cycles to liquefaction. The modification by Liu et al. (2018a) (Liu et al., 2020, 2021) with a memory surface is able to consider correct gradual sand stiffening. Especially, in order to capture ratcheting a third surface termed memory surface was introduced. Ratcheting is the gradual accumulation of plastic strains under cyclic loading and is induced by micro-mechanical and fabric change. Even for high cyclic loading, the transition from shakedown to ratcheting can very well be captured. Within the memory surface a smaller accumulation rate arises and therefore to the hardening factor h an additional term is added which introduces the memory concept in the Dafalias and Manzari (2004) approach. Without a memory surface, strain and excess pore pressure cannot be accurately simulated. This concept bases among others on Corti (2016), who combined a memory surface with the bounding surface approach which can change in size and position.

When dealing with the initial implementation of Dafalias and Manzari (2004), there are some limitations presented by Dahl et al. (2018). The model underestimates the initial dilation and contraction of the soil, because of a solely linear trend of the dilatancy term. There is an increasing plastic shear strain under cyclic loading. Dahl et al. (2018) show the need for an decreasing trend of h_0 over the number of cycles to increase the accuracy of SANISAND for a better representation of total shear strains.

The SANISAND model bases on critical state mechanics and bounding surface plasticity which allows for cyclic and reverse loading. The following equations are formulated in triaxial stress space with all components as effective stress. The principal stresses and strains are defined in axisymmetric triaxial space. The stress ratio η is defined as the ratio of deviatoric stress to mean effective stress.

Elastic and plastic strain components

The nonlinear elastic response is modelled in a hypoelastic manner. The strain consists of elastic and plastics parts composed in deviatoric and volumetric components (Equation A.1). The development of plastic strain is directly correlated to the changes in stress ratio (Equation A.2).

$$d\varepsilon_q^e = \frac{dq}{3G} \quad d\varepsilon_v^e = \frac{dp}{K} \tag{A.1}$$

$$d\varepsilon_q^p = \frac{d\eta}{H} \quad d\varepsilon_v^q = d|d\varepsilon_q^p| \tag{A.2}$$

G is the hypoelastic shear modulus, K is the hypoelastic bulk modulus, η is the stress ratio, H is the plastic hardening modulus and d is the dilatancy parameter. The elastic shear modulus and the elastic bulk modulus are dependent on the mean effective stress and the void ratio (Richart et al., 1970; Li and Dafalias, 2000) (Equation A.3).

$$G = G_0 p_{ref} \frac{(2.97-e)^2}{(1+e)} \frac{p'}{p_{ref}}^{0.5} \quad K = 2\frac{(1+\nu)}{3(1-2\nu)} \tag{A.3}$$

G_0 is a material constant; ν is the Poisson's ratio, e the void ratio and p_{ref} is the atmospheric pressure.

Plastic flow

The increasing stress ratio η is bounded by the bounding stress ratio M^b. The bounding surface is a straight line with a specific slope. The plastic modulus decreases for an increasing current stress ratio up to the bounding surface. The hardening modulus H relates to the evolution of plastic strain $d\varepsilon_q^p$ and depends on the distance from the current stress ratio η to the bounding surface M^b (Equation A.4 and Equation A.5). Hence, H controls the plastic deviatoric strain, dependent on the distance between bounding surface and current stress ratio. The bounding stress ratio varies with the state parameter.

$$H = h(M^b - \eta) \quad h = \frac{b_0}{|\eta - \eta_{in}|} \tag{A.4}$$

$$b_0 = G_0 h_0 (1 - c_h e)(p/p_{ref})^{-0.5} \tag{A.5}$$

Herein, M^b is the bounding stress ratio and h a function of the stress ratio η and the state variable b_0. The values h_0 and c_h are scalar parameters and η_{in} the initial stress ratio (Dafalias, 1986).

Dilatancy

The dilatancy parameter d depends on the relative distance between the current stress ratio η to the dilatancy stress ratio M^d (or phase transformation line) and bases on the idea according to Rowe (1962) (Equation A.6).

$$d = A_d(M^d - \eta) \tag{A.6}$$

A_d is a function of state. For d > 0 contractant behaviour and for d < 0 dilatant behaviour is obtained.

Critical state line

Casagrande (1936) observed that independently from the initial void ratio, soils achieve a constant void ratio after large shearing. This value was later termed critical void ratio (Taylor, 1948). The concepts was refined by Roscoe et al. (1958) to the definition that in a drained test further shearing does not lead to further change in void ratio and in an undrained test to no additional excess pore pressure. Hence, the steady state (Castro, 1969) or critical state (Roscoe et al., 1958; Schofield and Wroth, 1968) is a flow state associated with large deformations for a constant deviatoric stress under undrained or drained conditions. The steady state is an intrinsic soil parameter and uniquely relatable to void ratio for different stress states over e-log(p') and p'-q (Castro et al., 1982). It is defined as the state of deformation for a mass of particles in which the mass is continuously deforming at constant volume, constant normal effective stress, constant shear stress, and constant velocity (Poulos, 1981). The continuous deformation is accompanied by a constant volume in which initial structure is altered to a flow state (Wood, 1990). When the stress path η reaches the critical state line (CSL) with the slope M, no dilatancy occurs due to a critical flow state (d = 0). The critical stress ratio M for triaxial compression can be derived from Figure A.2 (a). Due to the inherent anisotropy of the soil and more contractive behaviour the steady state strength is lower for extension. The parameter c correlates the soil response in triaxial extension to triaxial compression (Dafalias et al., 2004). The critical state line in the void-ratio stress space is depicted in Figure A.2 (b) and bases on the concept of critical state (Roscoe et al., 1958). In the upper right part there is a contractive behaviour with a state parameter larger than zero. In the lower left dilatancy with a state parameter smaller than zero.

Based on Li and Wang (1998) a powerlaw is used to describe the critical state line (Schofield and Wroth, 1968). This law however results in a void ratio smaller zero for a stress tending to infinity (Equation A.7 and Equation A.8).

$$e_c = e_{c0} - \lambda_c(p'/p_{ref})^{\xi} \tag{A.7}$$

$$\psi = e - e_c \tag{A.8}$$

Herein, p_{ref} is the reference stress, e_{c0} is the void ratio for $\mathrm{p} = 0\,\mathrm{kPa}$ and λ, ξ are material parameters which describe the position of the CSL in the (p'/p_{ref}) ξ -e plane. ξ is for most sands roughly 0.7. The distance between the critical state line and the current state for the same mean effective stress of the soil is described with the state parameter ψ which represents the distance between both (Been and Jefferies, 1985). For ψ<0 a dilative behaviour and for $\psi > 0$ a contractive behaviour is calculated. For the contractive behaviour a densification with a positive volumetric strain due to an external shear load is calculated.

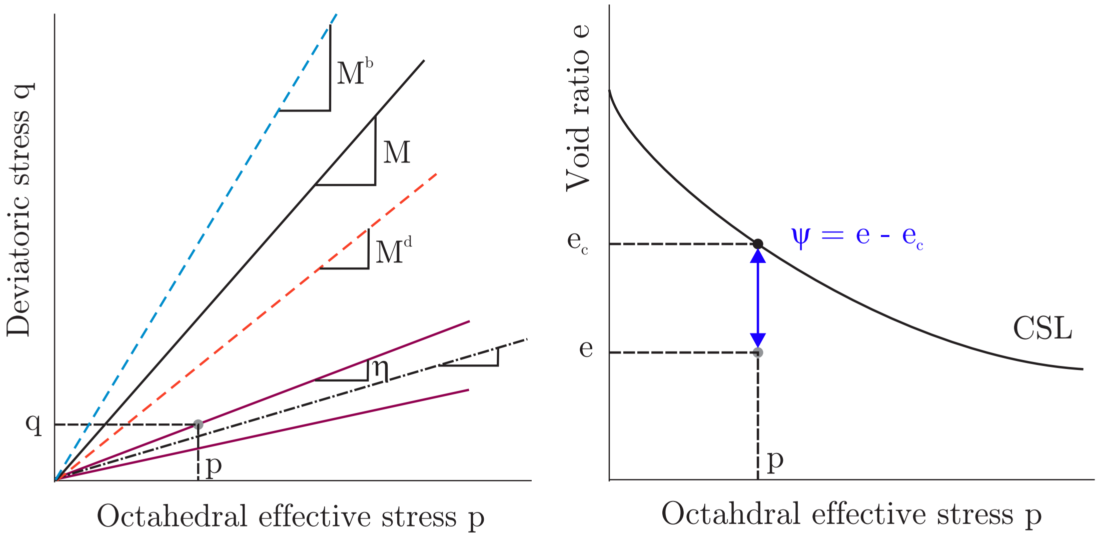

(a) (b)

Figure A.2: Bounding, critical and dilatancy surface as well as yield surface (a) and powerlaw in e-p' space (b).

Yield surface

The yield surface is a small wedge (in p'-q space) (Equation A.9). Thereby, the material constant m represents the opening and the deviatoric back stress ratio α the orientation of the yield surface (Manzari and Dafalias, 1997; Dafalias and Manzari, 2004). The elastic regime of the size $2mp$ moves with a changing stress ratio. The material constant m is often assumed to be between 0.02 - 0.05.

$$f = |\eta - \alpha| - m = 0 \tag{A.9}$$

Due to narrow open wedge type yield surface, there is no additional cap within the wedge and, hence, no induced plastic strain under a constant stress ratio.

Dilatancy, bounding and critical surfaces

There are different homologous, concentric surfaces, namely bounding, dilatancy and critical surface. They depend on the current material state (state parameter) (Dafalias and Manzari, 2004). M^d and M^b are the inclinations of the dilatancy and bounding surface, respectively (Equation A.10 and Equation A.11). With the parameter $c = M_c/M_e$ the difference in critical state line between extension and compression can be incorporated.

$$M^d = Mexp(n^d\psi) \tag{A.10}$$

$$M^b = Mexp(-n^b\psi) \tag{A.11}$$

The values n^b and n^d are positive material constants. If the soil approaches the critical state, the distance between the current void ratio and the critical state (ψ) tends to zero and converges finally to the critical surface M. For $\psi < 0$, $M^d < M < M^b$ for $\psi = 0$, $M^b = M^d = M$ arises.

The phase transformation line (dilatancy surface) can be evaluated for the stresses and strain at the point of the maximum volumetric strain. It separates the dilative from the contractive soil behaviour. The acting shear stress and normal stress can be read and correspondingly plotted in the p'-q space. For dilative soils there is a larger maximum shear stress since the specimen dilates and reduces the build excess pore pressure. The bounding surface is evaluated at the peak shear stress and, hence, gives the boundary for all stress states.

Fabric change

The dilatancy is influenced by the fabric-dilatancy internal variable z, whereby z depends on the plastic volumetric strain. Initially, this variable is zero and evolves for dilatant behaviour. For contractant behaviour this value is zero. The value z_{max} is the limiting value for this internal variable. The constant c_z is a multiplier for the rate of the fabric increase.

A.2 Chapter 5.2: Calibration of SANISAND model

In the following, the SANISAND model is calibrated to drained and undrained monotonic and cyclic test results. The SANISAND model performs very well under different boundary conditions and can be used for static and cyclic problems which need sophisticated constitutive models.

A.2.1 Laboratory program

The void ratio was varied for all tests from a medium dense to very dense relative density state (e = 0.5, 0.55, 0.6, 0.65 and 0.7). Drained and undrained, monotonic and cyclic, load-controlled triaxial tests have been performed. Furthermore, one dimensional compression tests, cyclic direct simple shear and resonant column tests have been conducted.

A.2.2 Monotonic calibration

The procedure for the calibration of the 12 main parameters is described in great detail in Ruffatto (2012), Taiebat et al. (2010) and Taiebat and Dafalias (2008). The needed parameters are shown in Table A.1.

Table A.1: Main calibrated input parameters for monotonic loading.

Parameter	Symbol	Parameter	Symbol
Elasticity	G_0	Yield surface	m
	ν	Plastic modulus	h_0
Critical state	M	Yield surface	c_h
	λ	Yield surface	n_b
	e_0	Dilatancy	A_0
	ξ		n_d

Elasticity parameters

The reference value for the elastic shear modulus G_0 (Figure A.3) can be calculated with the elastic response within the stress-strain curves to 120 kPa. However, resonant column tests have been performed which can be used for a more accurate calibration.

The elastic bulk modulus K_0 (Equation A.3) can be derived from unloading test on isotropic triaxial tests by assuming isotropic load reversal behaviour. Herein, the compressibility behaviour of the soil to hydrostatic compression is analysed. Based on the results, the value K_0 can be derived to 140 kPa.

From K_0 and G_0 a constant Poisson's ratio ν is derived (Equation A.12). For an accurate fitting an unrealistic small Poisson's ratio arises.

$$G = 3\,K\frac{(1-2\nu)}{2\,(1+\nu)} \tag{A.12}$$

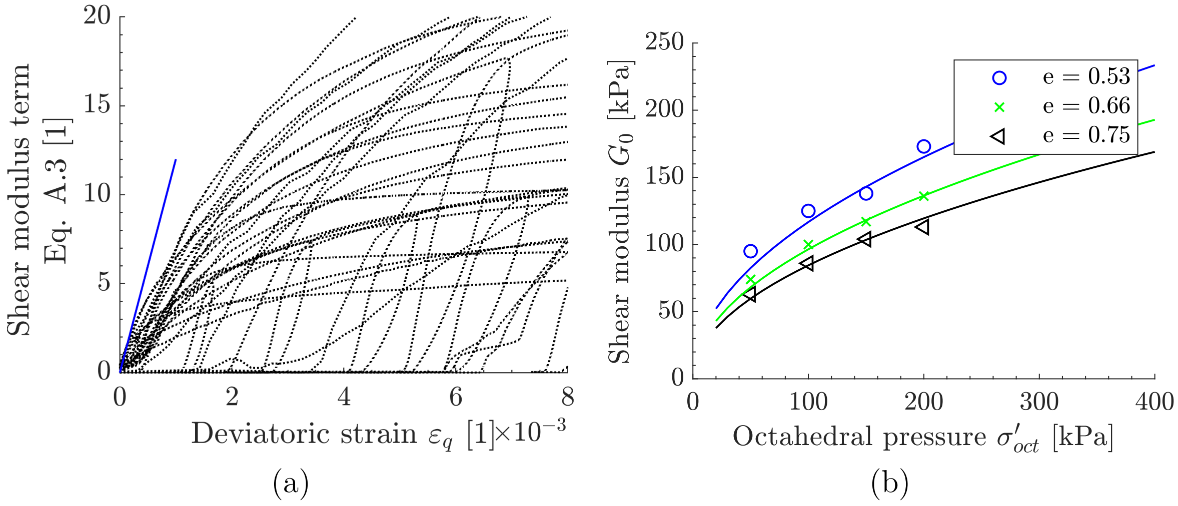

(a)

(b)

Figure A.3: Calibration of G_0 from monotonic triaxial ($G_{0,ref} = 120\,\text{kPa}$) (a) and RC tests in $G_0 - \sigma'_{oct}$ ($G_{0,ref} = 300\,\text{kPa}$) (b) on reference soil for different relative densities.

Critical state parameters

The triaxial device is commonly used for the estimation of the critical state line (CSL). The slope of the CSL can also be derived from oedometer, isotropic compression or ringshear test results (Sadrekarimi and Olson, 2009). The slope is used in combination with drained and undrained monotonic triaxial tests in order to derive e_0, which is assumed to be in the range of e_{max}. In triaxial CID tests the void ratio changes and in triaxial CIU tests the void ratio remains constant. However, often critical state cannot be achieved with 20% strain in a standard triaxial test (Santamarina and Cho, 2001). The value ξ is assumed to be 0.7.

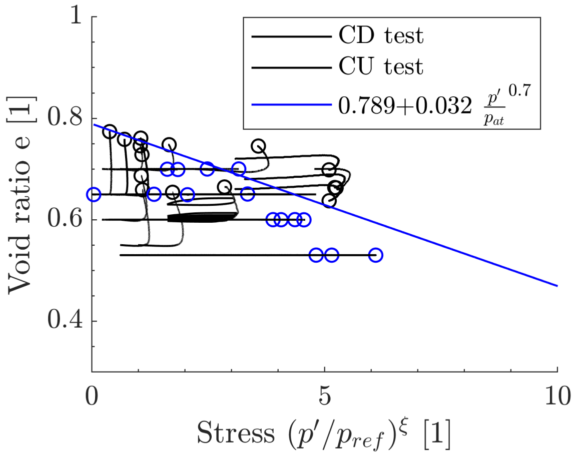

Figure A.4: Critical state line in e-p space from triaxial test results.

The failure line in p’-q space can be estimated from the triaxial results, critical angle of friction from shear box tests and from the angle of repose (Equation A.13). Figure A.5

shows the evolution of deviatoric stress for a relative density of $D_r = 0.85$. The inclination M_c can be estimated to 1.15. The inclination M_c can also be derived with ($\varphi_c = 30.9°$):

$$M = 6\,sin(\varphi_c)/(3 - sin(\varphi_c)) \tag{A.13}$$

The value $c = M_e/M_c$ is assumed to be 0.75.

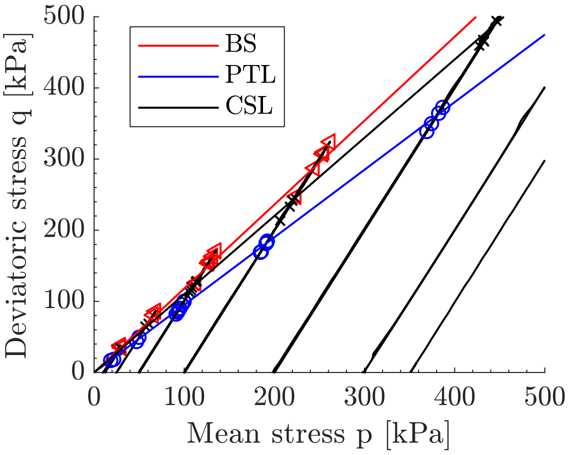

Figure A.5: Calibration of critical stress ratio M_c and critical state line in e-p space with boundary surface (BS), phase transformation line (PTL) and critical state line (CSL).

Dilatancy parameters

The parameter n^d needs to be evaluated at the phase transformation line (D = 0); hence, ψ^d and α^d are evaluated from drained or undrained tests at the phase transformation line (PTL) (Figure A.6). The PTL is the change from contractant to dilatant behaviour (Ishihara et al., 1975). It is assumed to be at the peak of volumetric strain or excess pore pressure. Therefore, α^d/α^c is plotted against ψ^d of the individual tests, where $\psi^d = e_{PTL} - e_{CSL}$. The linear interpolation in semi-log scale starts at the origin for $\psi = 0$, equalling the critical state (Equation A.14). Figure A.6 (a) shows the results with $n^d = 2.5$.

$$n_d = \frac{1}{\psi^d}\,ln(\frac{\alpha^d}{\alpha^c}) \tag{A.14}$$

Kinematic hardening parameters

The hardening parameter n^b is calibrated similarly to n_d, but ψ^b and α^b are derived from drained or undrained tests at peak stress ratio (bounding surface) (b = 0) (Figure A.6 with inclination of line representing n^b and n_d) to $n^b = 1.2$, with $\psi^b = e_{PS} - e_{CSL}$ and $\alpha^c = M - m$. The kinematic hardening parameter can be estimated by Equation A.15.

$$n^b = \frac{1}{\psi^b}\,ln(\frac{\alpha^c}{\alpha^b}) \tag{A.15}$$

For $\psi = 0$ the critical state is reached and this represents again the y-interception of the linear regression equation. For both n_d and n_b different values arise if only CIU or CID tests are used.

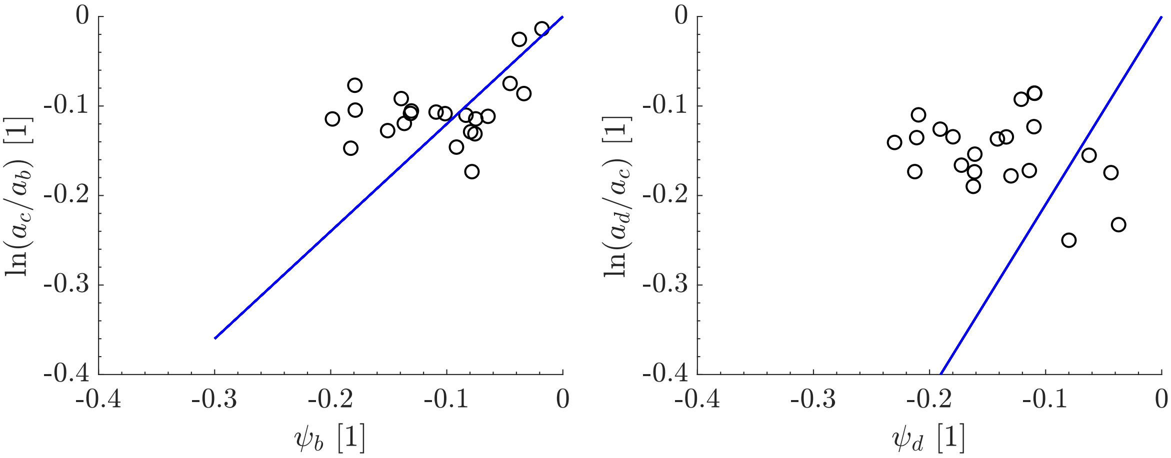

(a) (b)

Figure A.6: Calibration of n_d (a) and n_b (b) parameter on drained and undrained monotonic triaxial test results.

Calibration with genetic optimization algorithm

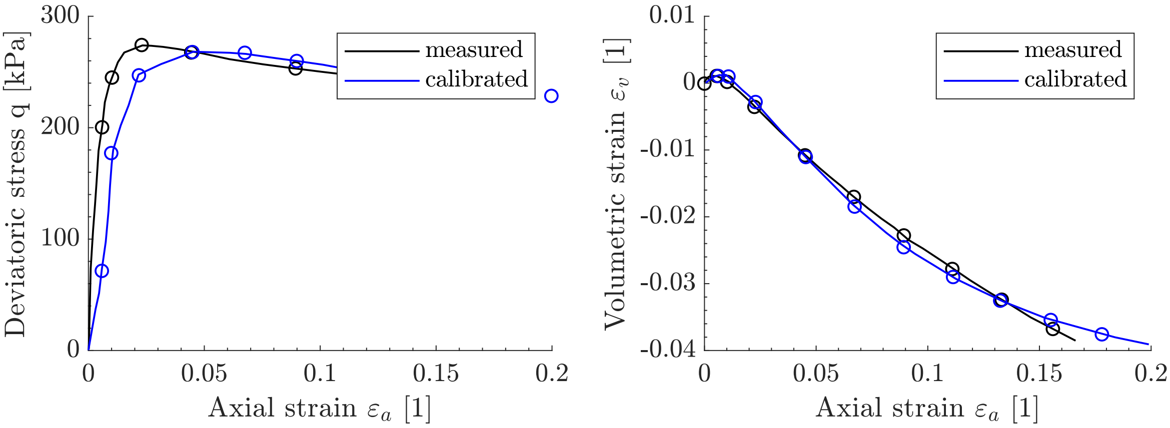

(a) (b)

Figure A.7: Exemplary comparison of calibrated and measured results from a monotonic CD triaxial test.

The value z_{max} is evaluated for loading-unloading tests in the triaxial device. The values h_0 and c_h can be evaluated over different void ratios and plotted as a straight line with $h_0(1-c_h e)$ which is a term in the definition of b_0. However, they are related to the distance to the bounding surface by trial and error. In order to faster evaluate different combinations due to the trial-and-error parameters and mutual influence a particle swarm and a genetic optimization algorithm were implemented in order to perform a least-square regression. From both, the genetic algorithm gave the better results. In a next step, the bandwidth of input parameters were estimated based on the aforementioned calibration. Figure A.7 shows the measured values from monotonic CD triaxial tests with the back-calculation of SANISAND. The genetic algorithm (Goldberg, 1989) bases on differential evolution (Price and Storn, 1997) and optimizes an objective function which gives the difference between laboratory results and model results (mutation, cross over, recombination). This is done on five characteristic points in order to have a small weighting. A population of 20 was chosen with 60 - 100 runs. The calculation was performed for element models (triaxial and DSS model) in ABAQUS and the regression was controlled via a Python script. The fitness was checked via the error in volumetric strain and deviatoric stress (Figure A.7). Figure A.8 shows exemplary trends of different input parameters over the course of the optimization. For all input parameters a specific bandwidth was chosen as well as a representative initial value based on the manual calibration. The input values for the constitutive model converge towards one value, which gives the least square error within the objective function. There is also a very good agreement between calculated and measured values. The algorithm did calibrate trial-and-error values well and improved the accuracy of the input parameter set.

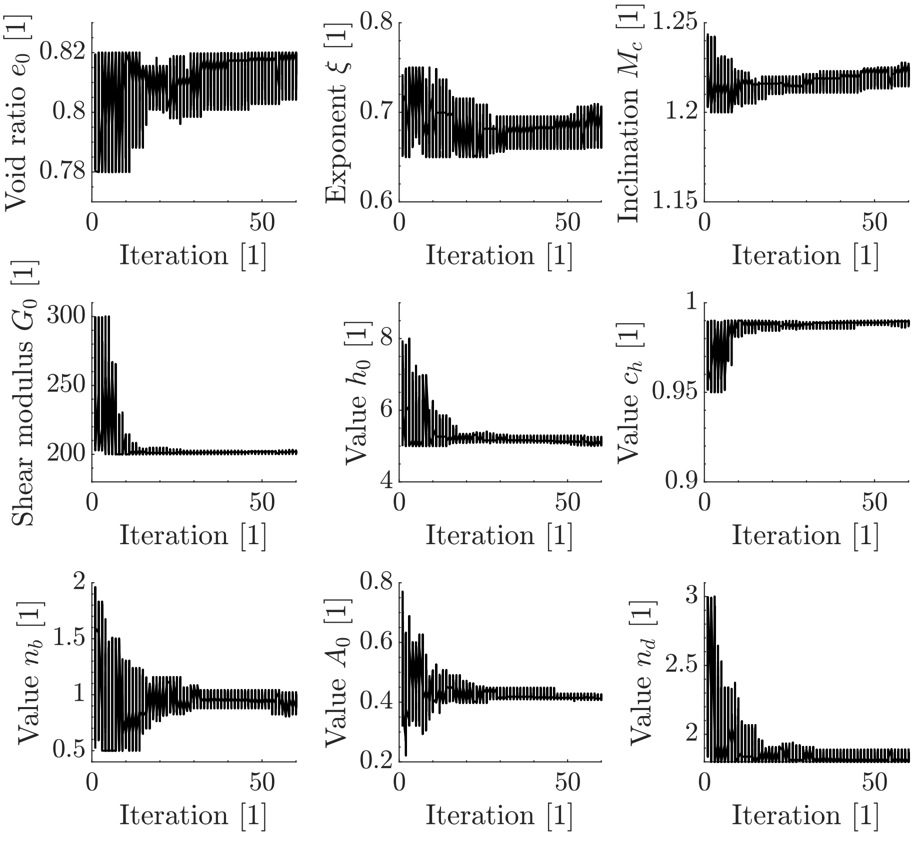

Figure A.8: Calibration with genetic algorithm.

It is unlikely that one model is calibrated to give an accurate representation of the full monotonic and cyclic soil response under drained and undrained conditions. However, the strength as well as the volumetric behaviour of the soil is calibrated quite well. Figure A.9 and Figure A.10 show the results for the final parameter set for different relative densities

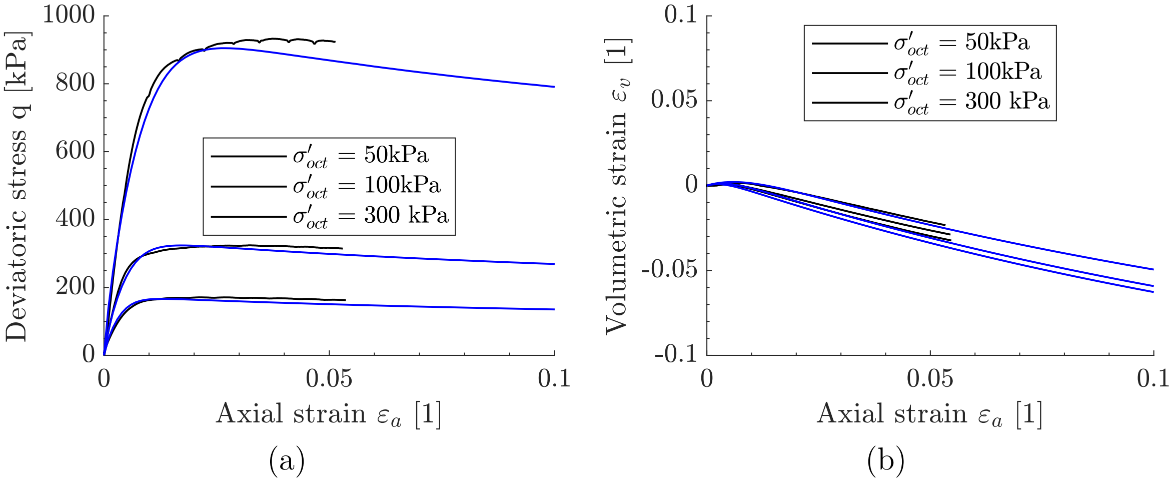

(a) (b)

Figure A.9: Results for drained monotonic triaxial test (SANISAND in blue and measured results in black) for e = 0.53 and three different stresses.

and different consolidation stresses for the monotonic case. The trend of the volumetric strain agrees better for the case of denser sand than for the more loose soil.

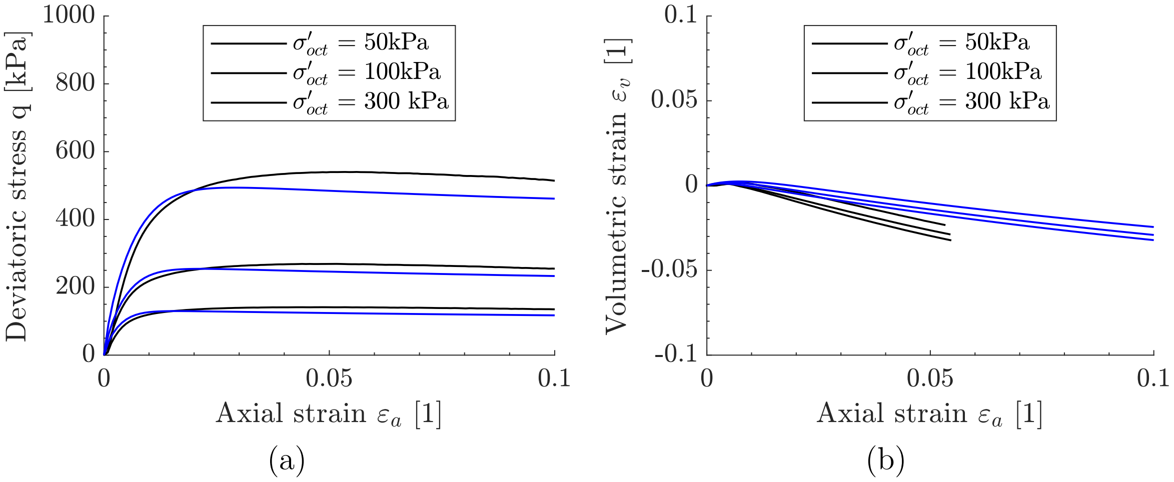

(a) (b)

Figure A.10: Results for drained monotonic triaxial test (SANISAND04 in blue and measured results in black) for e = 0.64 and three different stresses.

A.2.3 Cyclic calibration

The characteristic monotonic soil behaviour can very well be reproduced. In a next step, the model is calibrated to cyclic undrained (CIU) and drained (CID) triaxial test as well as cyclic constant-volume direct simple shear tests for different confining pressures and void ratios. Figure A.11 to Figure A.14 show the results for two different CSR values (LTR = 0) and for constant-volume cyclic DSS tests with adjusted (cyclic) input parameters. The SANISAND can realistically reproduce a wide variation in soil response under different confining pressures and dilatant as well as contractant responses. However, the dilatancy in denser sample is overestimated and the incremental increase in plastic deformation is comparatively large. When dealing with cyclic tests the influence of dilatancy and fabric change of non-cohesive soils plays a key role to the overall complex behaviour.

With one parameter set the soil model is able to realistically reproduce the soil response under different stress states for drained and undrained conditions (Table A.2). The monotonic behaviour and the dilatancy are reproduced well. Some shortcomings were already explained in Chapter 4. Only with a modification such as a memory surface a more realistic soil response can be modelled.

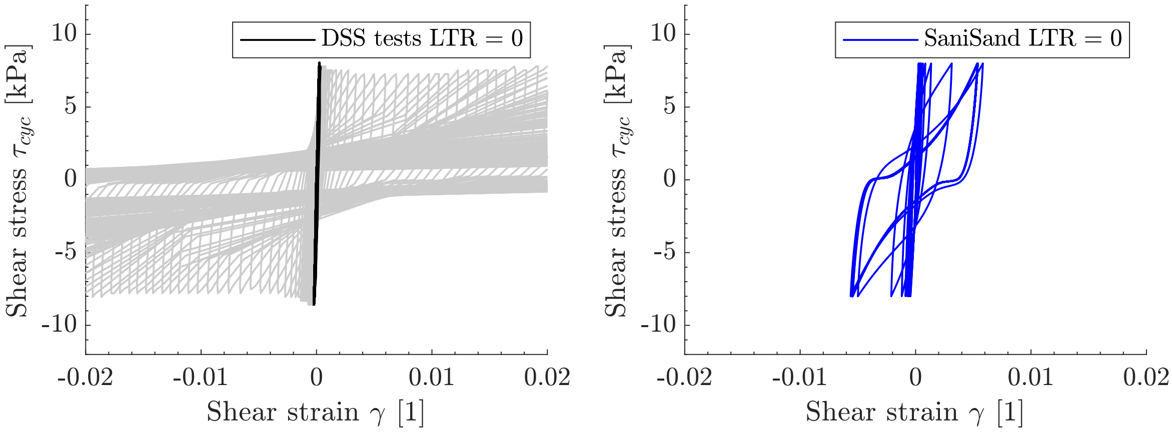

(a) (b)

Figure A.11: Results for constant volume cyclic direct simple shear with test results (a) and SANISAND back-calculation (b) for reference relative density with shear-stress over shear-strain.

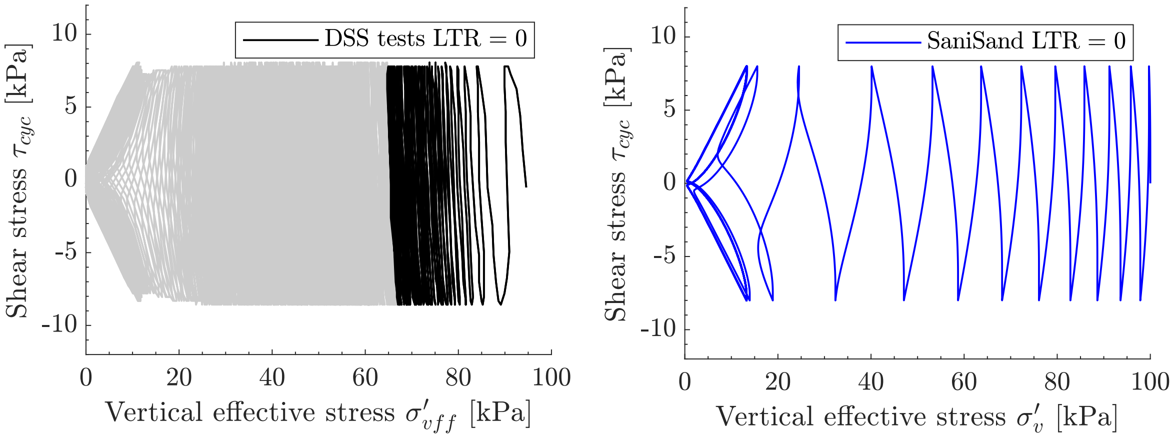

(a) (b)

Figure A.12: Results for constant volume cyclic direct simple shear with test results (a) and SANISAND back-calculation (b) for reference relative density with shear-stress over vertical stress.

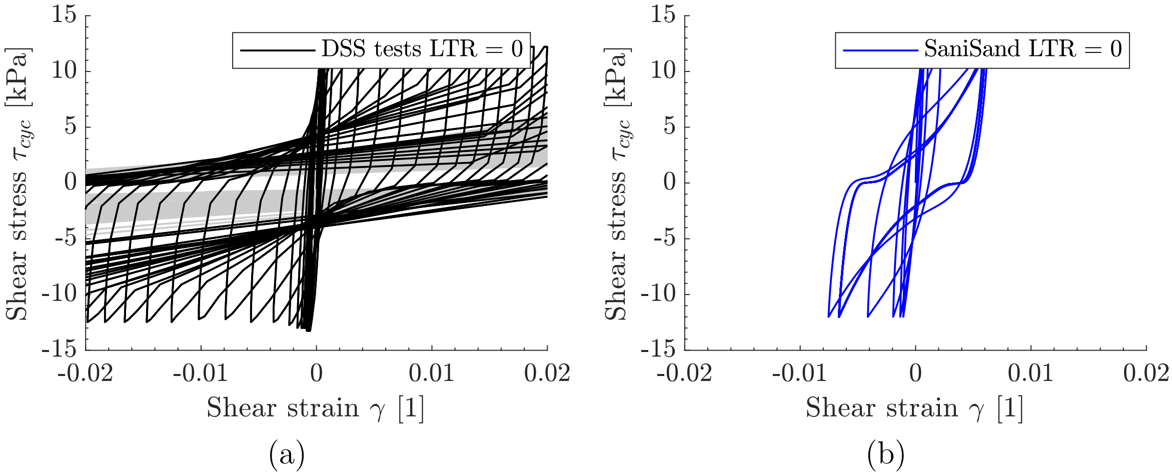

Figure A.13: Results for constant volume cyclic direct simple shear with test results (a) and SANISAND back-calculation (b) for reference relative density with shear-stress over shear-strain.

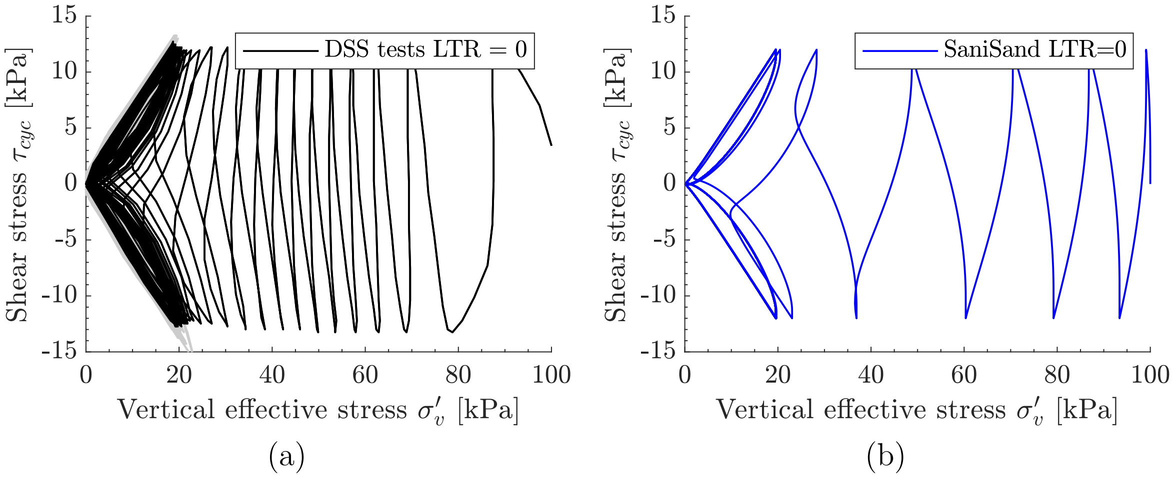

Figure A.14: Results for constant volume cyclic direct simple shear with test results (a) and SANISAND back-calculation (b) for reference relative density with shear-stress over vertical stress.

A.2.4 Cyclic element response

Both, drained and undrained tests have been back-calculated. One main key feature in common liquefaction analysis is the graphical representation of shear loading (CSR) against the number of cycles to liquefaction. This figure is mainly used by Seed and Booker (1976) and is derived from stress-controlled cyclic direct simple shear or triaxial tests. Figure A.15 shows a comparison between measured results for LTR = 0 and $D_r = 0.85$ and the back-calculation. The damage in terms of number of cycles to liquefaction from the back-calculation is significantly overestimated. The resulting trend of the CSR - N_{liq} curve, however, is mainly shifted parallelly. The asymptotic CSR value is also smaller.

Table A.2: Final input parameters for SANISAND model.

Parameter	*Symbol*	*Monotonic*	*Cyclic*
Elasticity	G_0	120	120
Elasticity	ν	0.05	0.05
Critical state	M	1.20	*1.1
Critical state	c	0.90	0.90
Critical state	λ	0.015	0.015
Critical state	e_0	0.79	0.79
Critical state	ξ	0.70	0.70
Yield surface	m	0.03	0.03
Plastic modulus	h_0	9.00	*3.70
Plastic modulus	c_h	0.986	*1.20
Plastic modulus	n_b	1.20	1.20
Dilatancy	A_0	0.70	0.70
Dilatancy	n_d	2.50	*2.3
Fabric dilatancy	z_{max}	10.0	10.0
Fabric dilatancy	c_z	700	700

The reason can be the insufficient modelling of the dilative soil response which leads to too large excess pore pressures for a small number of cycles. All points fail after a limited number of cycles for which none shows a stable response in terms of excess pore pressure accumulation.

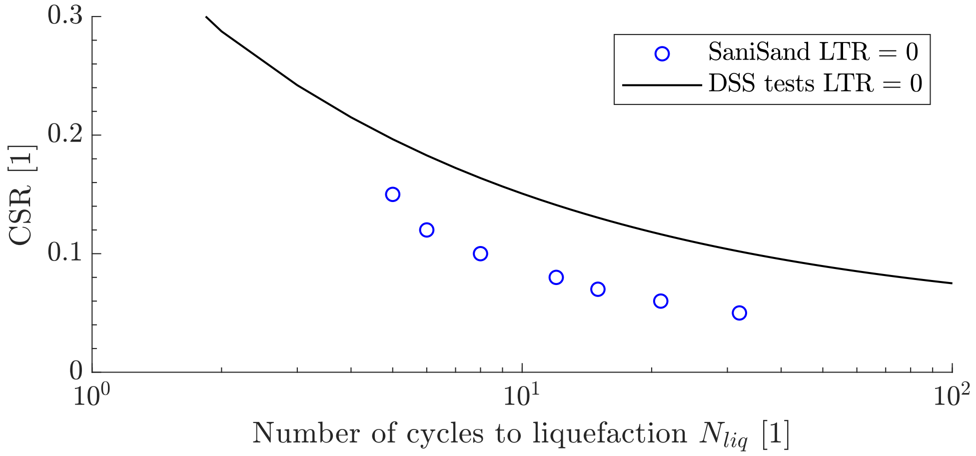

Figure A.15: CSR over N_{liq} for $D_r = 0.85$ and for symmetric two-way loading with back-calculation and results from cyclic DSS tests.

A.3 Chapter 7: Step-wise explanation of numerical procedure

In order to enhance the transparency, more detailed results will be given in the following to Chapter 7. A back-calculation is done for one specific integration point. The point used is located 5 m in front of the pile and 5 m below mudline (on the symmetry axis). The number of equivalent cycles is chosen to 30. The stresses at this point are depicted in Table A.3. The principal stress is depicted in Figure A.16. The upper part shows the equivalent stresses and the lower part the principal stress components. The equivalent shear stress is hereby larger than the octahedral stress. The three principal stresses start at an anisotropic consolidation condition and increase steadily over the course of the calculation. This must not be the case for all elements, but since this element is in the active bedding area, the stress increases steadily over the load application. The octahedral stress is calculated with Equation 6.2 and the equivalent stress with Equation 6.3.

Table A.3: Stresses at point 5 m/0 m/-5 m.

Step [-]	σ'_I [kPa]	σ'_{II} [kPa]	σ'_{III} [kPa]	σ'_{oct} [kPa]	σ'_{eq} [kPa]
Installation-step	25.99	25.99	63.59	38.30	37.96
Mean load applied	52.67	75.22	225.61	117.83	162.86
Cyclic amplitude applied	143.16	163.49	606.84	304.5	453.93

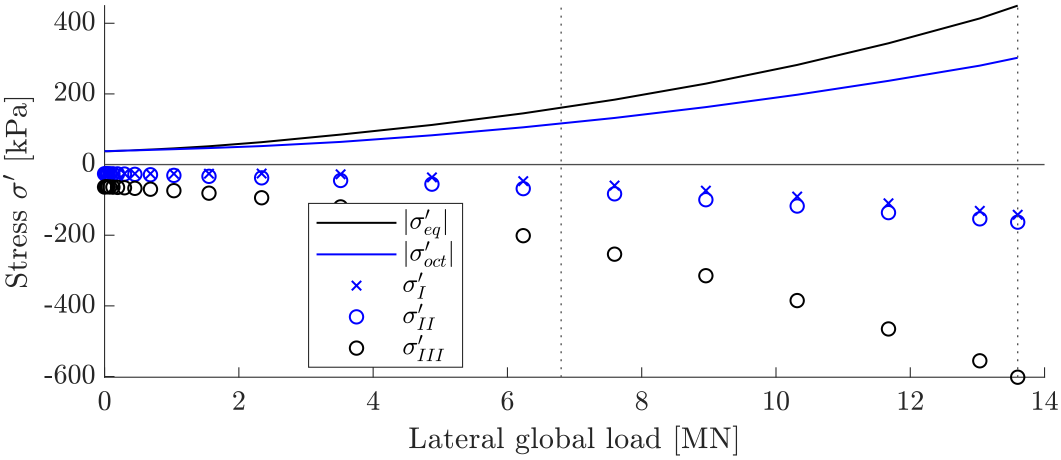

Figure A.16: Principal stresses over course of calculation.

The CSR is derived from the presented stresses. The equivalent effective stress increment between global mean load and global maximum load is calculated and divided by the octahedral stress at global mean load (Equation A.16). The MSR is calculated in a similar way by using the stresses at global mean and minimum load (Equation A.17). Both values are subsequently transferred to DSS conditions with a $k_0 = 0.38$ to a factor of 0.586 (Equation A.16 and Equation A.17). As a result, the transferred CSR and MSR values are smaller and are used in the contour plots.

$$CSR_{FE} = \frac{453.93\,kPa - 162.86\,kPa}{2\ \ 117.83\,kPa} = 1.2357 \quad CSR_{FE,DSS} = 0.728 \tag{A.16}$$

$$MSR_{FE} = \frac{162.86 - 37.96\,kPa}{2\ \ 117.83\,kPa} = 0.53 \quad MSR_{FE,DSS} = 0.313 \tag{A.17}$$

$$LTR = \frac{0.313}{0.728} = 0.71 \tag{A.18}$$

Figure A.17 shows a contour plot for the related LTR value. Full liquefaction is reached immediately after one cycle because of a large CSR value.

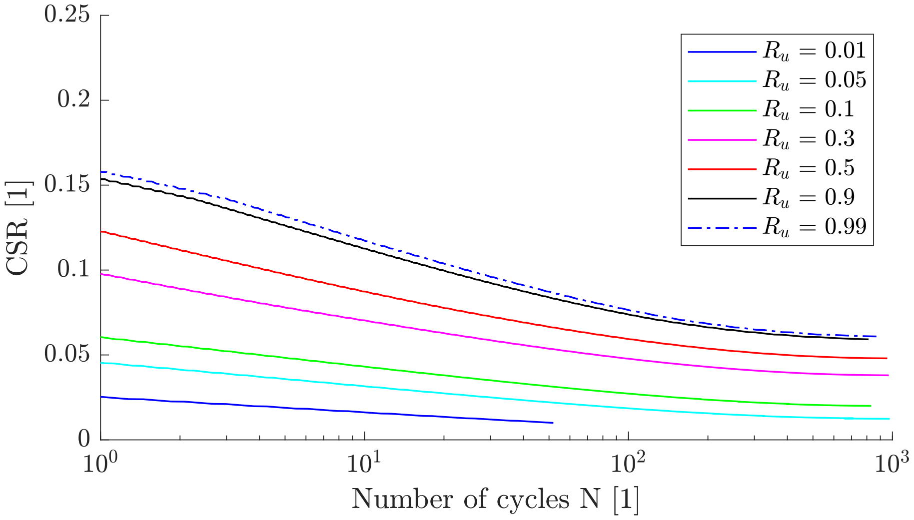

Figure A.17: Type 3 contour plot for LTR = 0.

$$R_{u,N=30} = 1.0 \tag{A.19}$$

$$\Delta u = R_{u,N=30}\ \sigma'_{oct,Fmean} = 1.0 \times 117.83\,kPa = 117.83\,kPa \tag{A.20}$$

Figure A.18 shows the dissipation procedure in order to derive the dissipated excess pore pressure ratio. The excess pore pressure ratio reaches full liquefaction after one cycle. The design method reduces this value to 34% and adds one cycle to the number of cycles related to the residual excess pore pressure ratio. This procedure is repeated. In the case of the alternative approach, the complete excess pore pressure trend is used, but because full liquefaction is reached after only one cycle, the additional increment is zero. Hence, the depicted decrease only bases on the residual excess pore pressure which is multiplied with 34% in each cycles.

$$R_{u,diss} = 0.34 \tag{A.21}$$

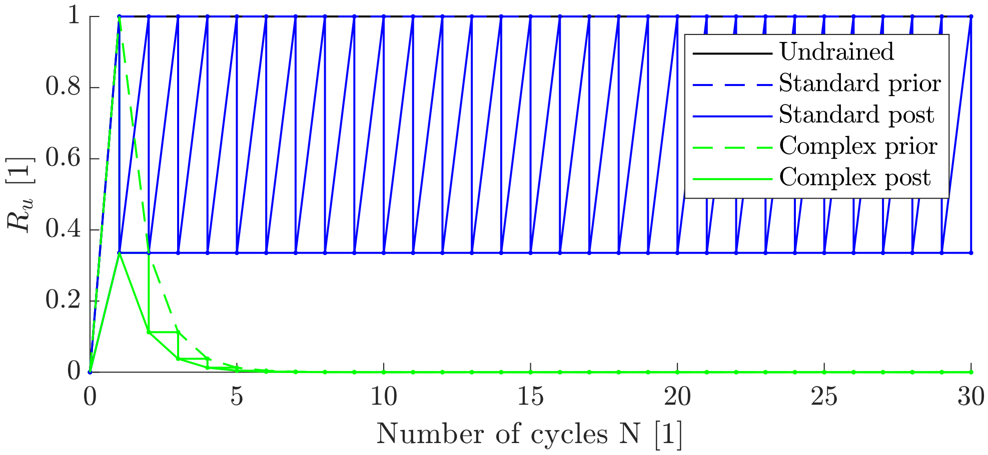

Figure A.18: Analytical superposition with design dissipation approach.

$$\Delta u_{diss} = R_{u,diss,N=30}\ \sigma'_{oct,Fmean} = 0.34 \times 117.83\,kPa = 40.06\,kPa \tag{A.22}$$

B Derivation of an equivalent number of cycles

Since a cyclic loading event consists of irregular cyclic loads of different magnitudes and load types, a concept for superposition is needed. This concept shall be implemented into the EPPE approach in order to enhance its applicability. The irregular storm can be transformed into a regular storm load using rainflow counting (Matsuishi and Endo, 1968). The irregular storm load and the corresponding equivalent number of cycles must have the same effects on the soil-structure interaction as the irregular storm load. However, the trend over time may not be the same. Instead of an equivalent number of cycles, a numerical model can also be used and all storm bins can be calculated sequentially. A much greater computational effort is required in this way.

A storm consists of load bins with constant mean and cyclic loads and a number of cycles related to the mudline (see Chapter 2). These storm bins are then converted to an equivalent number of cycles. The superposition of the cyclic loads should take the beneficial aspect of the excess pore pressure dissipation into account that occurs between adjacent cyclic load events.

B.1 Estimation of an equivalent number of cycles

To perform design proofs, the regular bins must be evaluated for an equivalent number of cycles. Most of the published concepts regarding the derivation of an equivalent number of cycles deal with a superposition of deformation for global or local variables. The most commonly used approach is the time-hardening concept based on triaxial tests by Stewart (1986). He published a strain superposition, which was later also used on a global scale, presented by Lin and Liao (1999) and Leblanc et al. (2010). Herein, the displacement (or a different cyclic memory variable) after the first number of cycles is evaluated and this very value is transferred to the response of the next loading bin. The equivalent number of cycles is evaluated and the number of cycles for the related current load bin is added (Figure B.1 (a)). There are also other approaches which use, for instance, a normalized CSR curve (Seed, 1975; Green and Terri, 2005; Chang, 1981; Allotey and Naggar, 2008). A detailed overview of the calculation procedures can be found in Glasenapp (2016) and Wichtmann and Triantafyllidis (2011).

The approach according to Chang (1981) and the German Geotechnical Society (2012) is similar to the time-hardening approach. It transfers the memory variable of the individual bins to the reference load without consideration of any load history (Figure B.1 (b)).

Herein, mainly the stiffer first soil behaviour of each bin is used without transferring them sequentially. The procedure needs an ascending order of loads to be conservative. The strain accumulation procedure according to Andersen (1976) is explained and used in Appendix C (Andersen, 1976; Andersen et al., 1988, 1992).

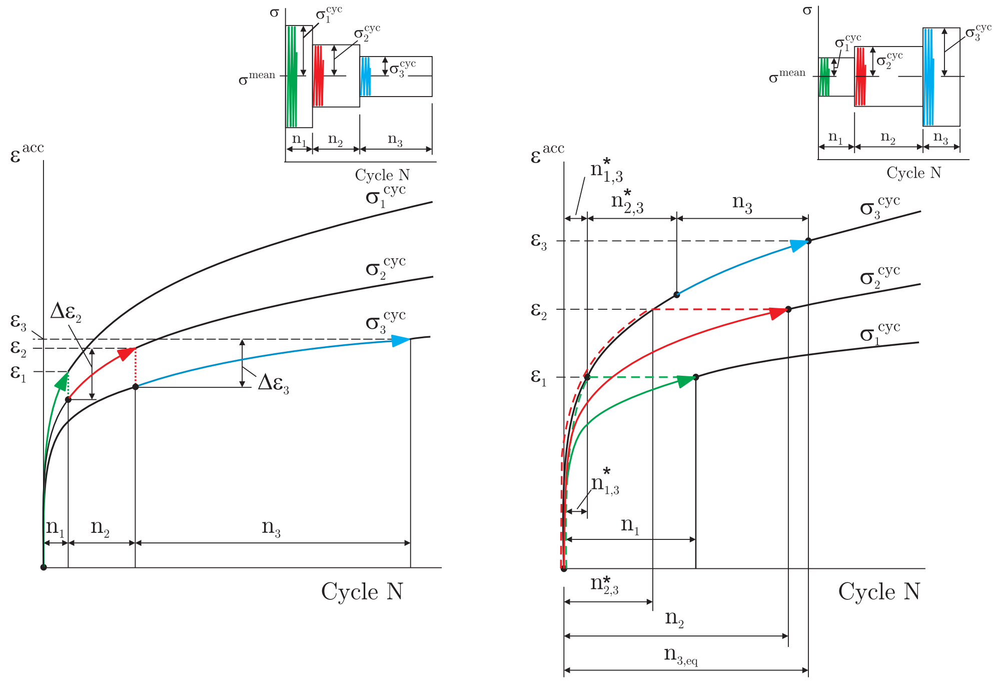

(a) (b)

Figure B.1: Time-hardening concept concept based on Stewart (1986) for an increasing load amplitude (a) approach according to Chang (1981) (b) following Wichtmann and Triantafyllidis (2011).

B.2 Miner rule

In addition to the superposition method, the effect of reordering the loads must also be considered. A storm consists of different mean loads and cyclic load amplitudes. The regular storm bins are ordered with increasing CSR or increasing maximum load. This bases on the assumption that there are no order effects. However, O'Riordan and Seaman (1993) state that it is too conservative to use an ascending order of wave loads and better to use a randomized distribution (Dingle et al., 2017).

Palmgren-Miner dealt with irregular load and predicted fatigue damage for metals under cyclic non-uniform load (for high cycle number of loads with small amplitude) (Miner, 1945; Palmgren, 1924). They stated that the order of the bins has no influence on the final induced damage. This also seems to be the case for a constant mean stress, but is doubted for changing mean stress. Different authors state that there is a moderate reordering effect when dealing with drained triaxial tests – which may be transferable to undrained conditions (Stewart, 1986; Kagawa, 1986; Wichtmann, 2005). Wichtmann et al.

(2010) used the HCA model for a validation of the Miner rule with a back-calculation of cyclic triaxial tests consisting of three load bins. The test program was done with medium dense sand in a drained manner with pluviated preparation. They found a very good agreement between the different results and confirmed the validity of Miners rule. This was similar to the work of Stewart (1986), Kaggwa et al. (1991) and Glasenapp (2016). They experimentally confirmed Miners rule in drained cyclic triaxial tests with constant mean stresses. For a changing mean load, the Miner rule may not be applicable anymore (Wichtmann and Triantafyllidis, 2011), but further research is needed.

A detailed discussion can be found in Wichtmann and Triantafyllidis (2011).

B.3 Concept for estimating cyclic response by integrating storm bins

Different load bins could be calculated one after the other to consider the complete storm load. Instead of this complex calculation procedure, however, compatibility can also be ensured by using the excess pore pressure as a memory variable in combination with the derived contour plots. The excess pore pressure at the end of a cycle is equal to the excess pore pressure at the beginning of the next cycle. It can hence be used to calculate the number of equivalent cycles. However, for sandy material drainage needs to be considered. For an offshore foundation this should be done on element level, for which a finite element model is necessary. Thereby, not only monotonic results are directly present but also the soil stratigraphy and element specific CSR values. The approach presented consists of several calculation steps. The maximum reference load is applied in a finite element model to read the stress components for each integration point. The developed calculation steps to consider regular storm bin instead of a fixed number of equivalent cycles is presented in the following.

Step 0a: Integration point response

In the first calculation phase, the numerical model is generated based on the site-specific soil conditions and the intended foundation geometry. The finite element model is loaded with the predefined maximum storm load. The numerical model uses only drained input variables for the soil profiles. From this calculation, the shear component and mean stress can be read for all conditions within the regular storm bins. For each entry of the regular storm bins, the associated mean and maximum stresses can be interpolated. The shear component and the octahedral stress is read for every integration point over the increasing global load. Instead of calculating several finite element models with different mean and cyclic loads, the procedure is optimized by using only one finite element model and successively accumulating the influence of the storm from the smallest to the largest load bin.

In the design procedure, the equivalent stress is used as an indicator for shear loading (cf. Chapter 6). The use of the equivalent stress relates its quotient directly to the second invariant of the deviatoric stress. The CSR represents the ratio of the element's deviatoric stress to the mean stress. Thus, a high CSR value is an indicator of high stress on the element (cf. Chapter 6). The mean stress has a stabilizing effect and an increased octahedral stress reduces the CSR value. The shear stress amplitude is derived from the equivalent shear stress by subtracting the components at the global mean stress and the end of the calculation at the full cyclic amplitude. It is normalized by the octahedral stress at the global mean stress at integration point level. The MSR is derived by using the shear stress at mean global load and the mean pressure (cf. Chapter 6).

Step 0b: Re-ordering

The storm matrix is usually ordered from the smallest to largest load. For the procedure the matrix can be ordered via the maximum occurring load or the maximum load amplitude. The largest amplitude will generate the largest CSR values and, thus, the largest damage. However, influences such as N or LTR are not considered. Hence, the reordering based on induced damage (R_u) considers these additional aspects. The damage in the form of the excess pore pressure ratio is evaluated for a reference point for each bin. Based on the induced damage, the regular storm bins are reordered. The largest value induces the most damages to the soil surrounding the structure. For this reference load, a number of equivalent cycles is needed, which combines all individual load bins to the reference load. A reordering assumes the validity of the Miner rule.

Step 0c: Flow net calculation

The calculated excess pore pressure of the upcoming step 2 must be subjected to a consolidation analysis. Therefore, the reference load is used and the excess pore pressure field evaluated for N = 1. To reduce the computational effort, the dissipation analysis is performed only once for the reference load. The related excess pore pressure field is based on the largest storm load and therefore, representative for the conditions which induce the most damage. A coupled ABAQUS model is used and the excess pore pressure is initialized with an associated stress field in which the excess pore pressure is subtracted from the principal stress. The same mesh configuration is used for all calculations. Regarding the decay curve, for the whole procedure, the same decay curve for the reference load and N = 1 is used. Even though redistributions of excess pore pressure and accumulations occur near soil layers with low permeability, this assumption is conservative for the near field around the structures, which has the greatest influence on the bedding resistance and load-deformation behaviour. The individual bins are connected with the excess pore pressure of the previous bin.

Step 1: Exclude integration points smaller than a limit value

As explained, for each integration point the stresses are plotted against the global load. For one integration point, the soil reaction can be derived over the course of the calculation (see Figure B.2 (a)). The cyclic stress ratio is calculated from the variation of the shear component over the increased global load by subtracting the point at the global maximum load and the global mean load corresponding to the investigated load bin of the cyclic load spectrum (Figure B.2 (a)). The model assumption is that the cyclic shear stress for each storm entry is considered as a constant over the number of cycles for the corresponding storm bin. The CSR and LTR value are read for each integration point for the reference case. From the integration-point specific LTR, the corresponding contour plot can be evaluated. A CSR limit value is specified as an asymptotic value. Elements loaded with a cyclic load amplitude below this limit will not liquefy for the representative number of cycles for which the laboratory results are valid. A CSR_{lim} profile can be derived and the computational time reduced.

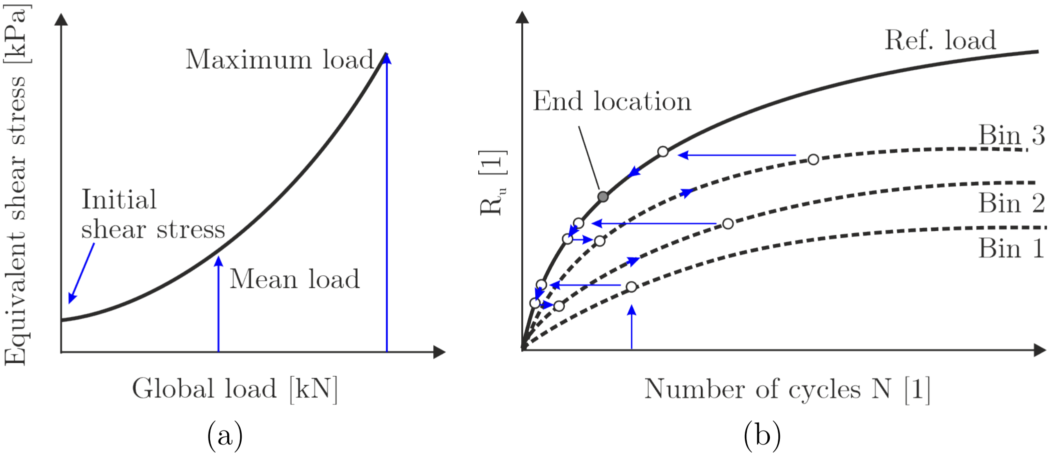

Figure B.2: Overview of calculation concept with stresses over global load (increasing ζ_b) for one integration point (a) and transfer of excess pore pressure from individual storm entry to reference curve (b).

Step 2: Read CSR and LTR for storm bin

The CSR and LTR values are read for each integration point for the first entry (or in the second loop for the very next storm entry) (Figure B.2 (b)). CSR values, which are smaller than the limit value are excluded. This is the case for many of the first storm entries since the loads are very small, resulting in low CSR values and, hence, many integration points can be excluded. The limiting CSR value is derived based on an excess pore pressure ratio of $R_u = 0.15$ after 1000 cycles. This value does not represent any physical threshold, but was purely chosen to reduce the computational time, since most of the elements far from the structure do not experience any accumulation effects.

Step 3: Read excess pore pressure from the contour plot

The excess pore pressure is evaluated for a given N and an integration point specific CSR value. It is specifically selected from different LTR contour plots. The degradation factor R_u is determined for the number of cycles of the corresponding load bin based on the induced shear (CSR) from step 2. If cycles within one storm bin are greater than the maximum number of cycles from laboratory tests, these bins can be divided into two or more bins (see also UDCAM-S in PLAXIS (Bentley Systems, 2022)).

Step 4: Transfer to reference load

The degradation factor R_u from the analysed bin is transferred into an equivalent number of load cycles corresponding to the reference load. The excess pore pressure curve over the number of cycles was derived in step 1 (cf. Figure B.2 (b)).

Step 5: Dissipate excess pore pressure

To account for dissipation, the calculated excess pore pressure ratio is subjected to a flow calculation and element-specific dissipation curves are evaluated (see step 0b). The integration point-specific normalized decay curve is used. The storm period T is assumed to be 10 s; although the storm period changes over the build-up of the storm. However, the influence is not very pronounced for a changing storm period from e.g. 30 s for the first entries to 10 s for the last storm entries, since mainly the last entries govern the general soil response. Hence, 10 s as a constant storm period seems to be acceptable. In many cases, dissipation (analytical superposition) reduces the accumulated excess pore pressure and results in a stiffer soil response. The initial large degradation of the static response due to induced excess pore pressure ratio is thus reduced. A higher capacity results with a lower number of equivalent cycles.

Step 6: Superposition

In the sixth step, the superposition is performed. The normalized excess pore pressure for $N = 1$ (depending on the octahedral and equivalent stress state) is first determined and the dissipated value within the decay curve is used for a storm period of $T = 10\,\text{s}$. The result is a percentage increase or decrease in excess pore pressure.

This method uses mainly the large increase in the first part of the curve and is based on the idea that the remaining excess pore pressure after dissipation is calculated back to a new number of equivalent cycles in the curve itself. A new cycle is added to the equivalent number of cycles. For each cycle added, the excess pore pressure curve is only shifted in the y-direction. Changes in the build-up trend are not taken into account.

The excess pore pressure ratio of the individual storm bin is transferred to the reference curve and a respective number of equivalent cycles. The number of cycles determines the number of superposition steps. Within the superposition the starting value from the previous dissipation is used and an additional cycle is applied. The excess pore pressure increases. Afterwards the resulting excess pore pressure is reduced by the value based on the dissipation analysis. If the number of cycles is smaller than 1 only this fraction is applied. The procedure is repeated for the number of equivalent cycles. The excess pore pressure increases due to an additional number of cycles and decreases due to dissipation. After some cycles a stable equilibrium is reached and no increase occurs. The final excess pore pressure value is transferred to the next storm bin.

Step 7: Transfer to next bin

The remaining excess pore pressure ratio of the reference curve is transferred into an equivalent number of load cycles corresponding to the next load bin of the cyclic load collective (cf. Figure B.2 (b)).

Step 8: Add next number of cycles

The number of load cycles of the next load bin is added to the load cycles corresponding to the dissipation analyses (see Figure B.2 (b)).

$$R_{N+\Delta N} = R_N + R_{\Delta N} \tag{B.1}$$

$R_{N+\Delta N}$ is the excess pore pressure ratio after an additional number of cycles and R_N the excess pore pressure ratio for the current shear component after dissipation. $R_{\Delta N}$ is the increase due to an additional number of cycles.

Step 9: Loop through design storm, transfer to reference load

The next calculation loop is performed. This procedure is performed for all storm entries up to the last entry where the maximum cyclic shear stress is equal to the maximum cyclic load. The analysis is repeated until all load bins of the analysed cyclic load collective have been considered (a procedure similar to Stewart (1986)). The load cycles are sorted in a sense that the most detrimental cycle is considered to the end of the procedure (evaluated for one reference integration point and related CSR, LTR values as well as the N value for the storm bin). In this case, the worst-case situation corresponding to the largest excess pore pressures in the soil around the monopile occur to the end of the considered cyclic event. Figure B.2 shows a summary of the procedure presented.

Last Step:

After all storm entries have been evaluated, a shear stress - shear strain curve can be derived and γ_{total} is plotted over CSR_{total} for the final number of equivalent cycles. The curve gets softer with an increasing number of equivalent cycles compared to the monotonic response. The contour plot summarizes the soil response after N cycles that have acted on the specimen with different combinations of the shear components.

The residual excess pore pressure after the storm event is used to analyse the post-cyclic foundation response. Because of the excess pore pressure, the octahedral stress is reduced and, hence, smaller shear stresses can be beared until failure occurs. In the (new post-cyclic) finite element model the stresses cannot be changed according to the resulting excess pore pressures in a way that would be possible in the case of an implicit analysis. However, the shear stress can be reduced by using a reduced equivalent angle of internal friction. Besides the angle of friction, the soil-pile friction coefficient is also adjusted accordingly as here also the normal stress is decreased by the portion of the excess pore pressure. The friction angle is entered into the post-cyclic FE model as a field for every integration point and the global load is applied.

Simplified flow chart

Although a detailed description has been given, the flow chart in Figure 6.11 summarizes simplified these explanations with the following remarks:

(a) The irregular storm load is transferred to storm bins with constant mean load and load amplitude with a related number of cycles.

(b) The maximum global load of the related storm is applied in a drained manner and the stresses as well as strains are read by a Python script for all calculation steps.

(c) The stresses are transferred to equivalent stresses from which subsequently the CSR and MSR (LTR) are calculated. These are derived form the stresses in each integration point. The CSR and MSR value are different in each storm bin.

(d) The storm is reordered based on a calculated damage. The excess pore pressure ratio R_u is interpreted as a damage indicator and is calculated for each storm bin with the related CSR, MSR and N.

(e) The excess pore pressure ratio R_u (and the excess pore pressure) are derived for each integration point for N = 1 based on a pre - specified contour plot and based on the CSR and MSR of the maximum load in the newly sorted storm. The excess pore pressure field for N = 1 is read into a coupled ABAQUS model and the field is dissipated over several seconds (more than the storm period T). The result is a decay curve for each integration point, which is normalized in order to be used in the analytical superposition.

(f) The excess pore pressure for the first storm bin is evaluated in each integration point based on the specific CSR and MSR value as well as the predefined number of cycles from the first storm bin.

(g) The excess pore pressure ratio from the first bin is transferred to the reference curve (R_u-N) and the related equivalent number of cycles for this entry is estimated.

(h) The analytical superposition is carried out in each integration point.

(i) An equivalent number of cycles after dissipation can be derived from the residual excess pore pressure (after dissipation, marked with a red dot) with the integration-point specific R_u-N curve. The residual excess pore pressure ratio is transferred to the next storm bin and the number of equivalent cycles within this curve is derived. The number of cycles from the next storm bin is added to the number of cycles of the last storm entry.

(j) The excess pore pressure ratio of the storm entry is again transferred to the reference curve (not the largest load, but the storm entry with the largest induced damage) and an analytical dissipation is performed. The procedure is done for all subsequent storm entries.

(k) The excess pore pressure ratio after dissipation as well as the related number of equivalent cycles after dissipation are now known. These can now be used in order to derive the stress - strain relation. With the number of cycles after dissipation, the stress - strain relation may be derived. Therefore, a type 2 contour plot can be used and a path with the related LTR drawn into the contour plot. The shear strain and stress components are added into order to have the maximum load and deformation from the cyclic element tests.

(l) With the degraded soil properties, the post - cyclic bearing capacity can be evaluated.

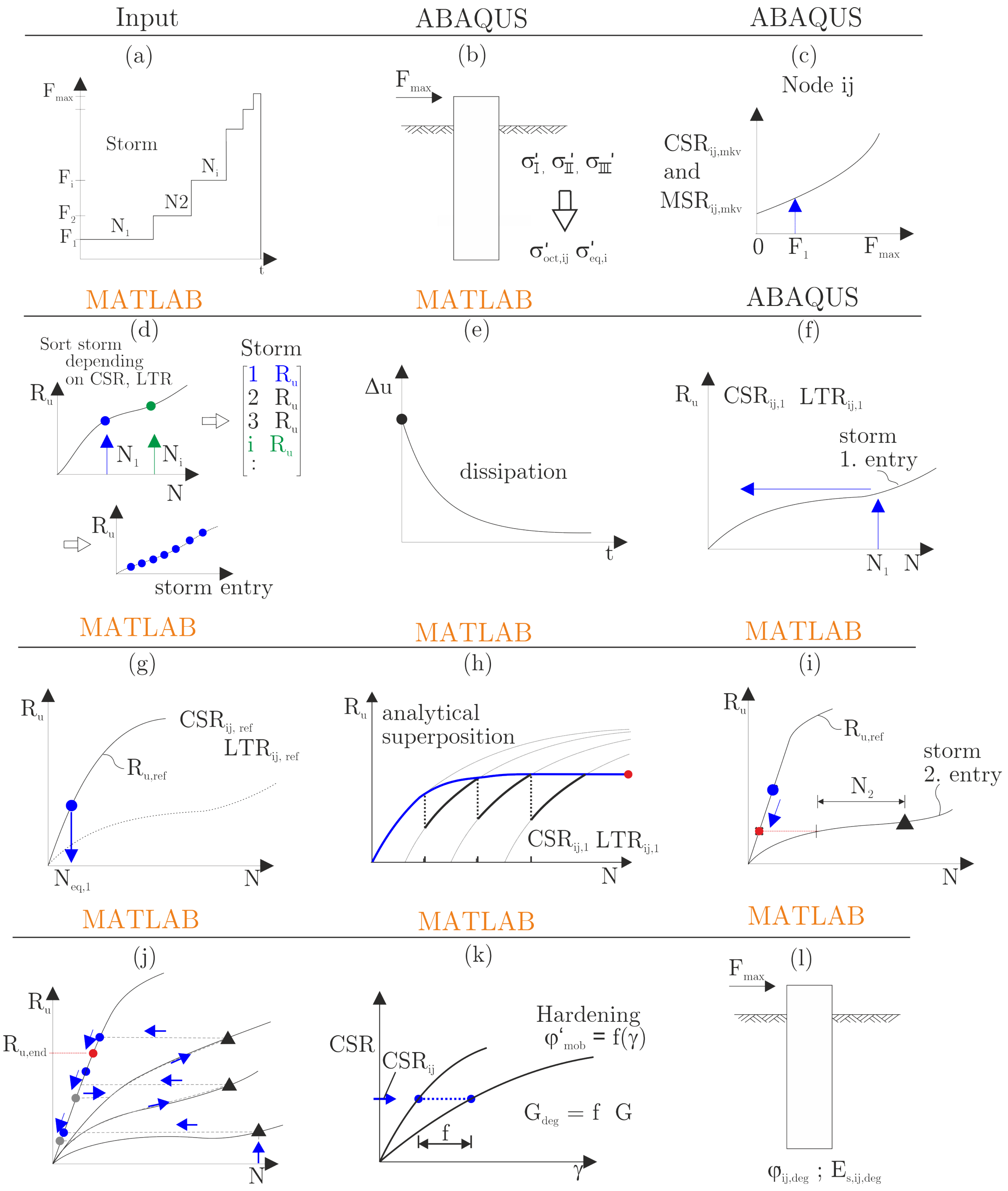

Figure B.3: Flow chart for EPPE - N_{eq} approach.

B.4 Results of numerical model and reference soil

The presented procedure shall be used with the reference monopile foundation. The results cannot directly be compared with the soil-structure response from Chapter 7 since the global load and the equivalent number of cycles changes due to the consideration of a design storm. The reference system with the depicted storm from Chapter 2 shall be used. The contour plot for a relative density of $D_r = 0.85$ is used (Chapter 5). In a first step the regular storm bin need to be reordered. Figure B.4 shows the equivalent shear stress and the octahedral stress over the application of the global load. For each storm bin, the related stress values can be interpolated. With both CSR and MSR, the value of LTR can be derived. One example is depicted in Figure B.4. The monopile foundation was loaded with 16.4 MN in order to have a load larger than the largest global load within the design storm. An example is depicted in Figure B.4 for a symmetric one-way load of 13.4 MN. For this value a $\Delta\sigma'_{eq,cyc}$ and a σ'_{oct} can be evaluated. The starting value of the equivalent shear stress plot is due to the anisotropic consolidation and can be calculated to 30.75 kPa with $\sigma'_v - \sigma'_h$.

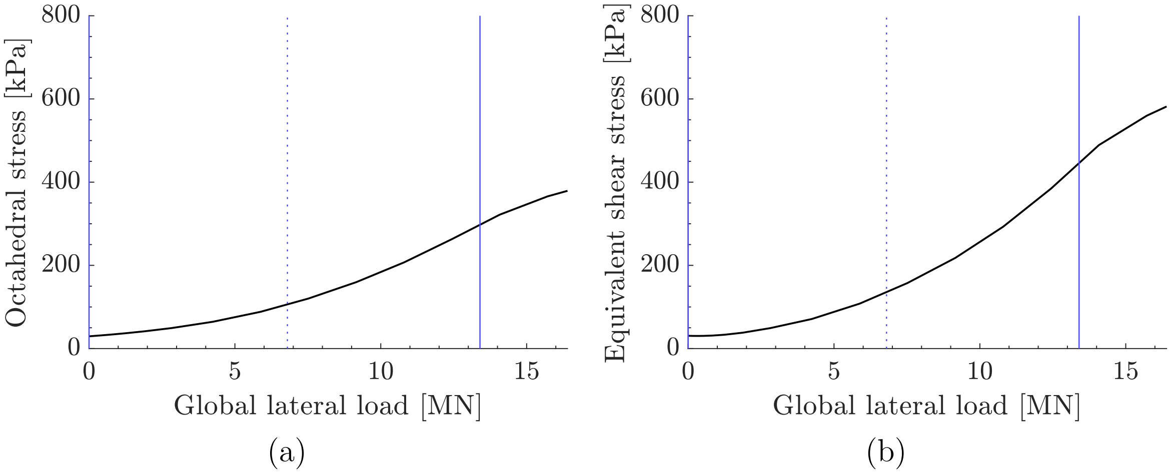

(a) (b)

Figure B.4: Octahedral stress σ'_{oct} (a) and equivalent shear stress σ'_{eq} (b) over global load application for a point 5 m/0 m/-5 m from monotonic FE calculation for a maximum global cyclic load of 13.4 MN.

Figure B.4 shows the evaluation of stress for one integration point with an exemplary cyclic global load of 13.6 MN as a solid blue line. The stress increments can be derived based on the marked mean and maximum global load, instead of performing individual calculations for each storm bin. The same procedure is done for all storm entries in order to derive CSR and LTR values. Afterwards the excess pore pressure ratio is calculated based on the related contour plot and the number of cycles from the individual storm bin. Based on this result, the storm is then reordered. Figure B.5 (a) shows the increasing CSR values over the storm load bins. Herein, the CSR values are not strictly increasing. This is because not only the CSR influences the damage within the element, but also the number of cycles N and the load type LTR. Figure B.5 (b) shows the related excess pore pressure ratio for this representative node. Because the R_u value would be equal to one for very large CSR values, the CSR values from Figure B.5 (a) are only half of the actual calculated values from the FE model in order to be able to sort every storm entry and avoid multiple (fully liquefied) entries. This scaling was only done for sorting the storm entries and not for the calculation of the excess pore pressure in the subsequent step. Figure B.6 (a) shows the global number of cycles in the sorted order. Generally, the number of cycles is decreasing, but there are also some peaks in between. The same applies for the normalized global load amplitude of the storm bin depicted in Figure B.6 (b).

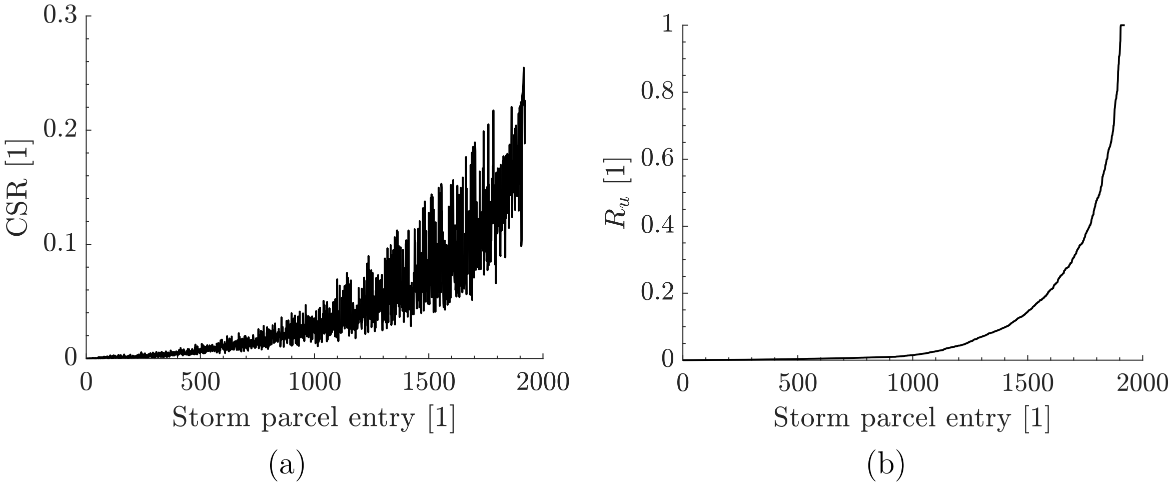

(a) (b)

Figure B.5: CSR value for point 5 m/0 m/-8 m over storm bins.

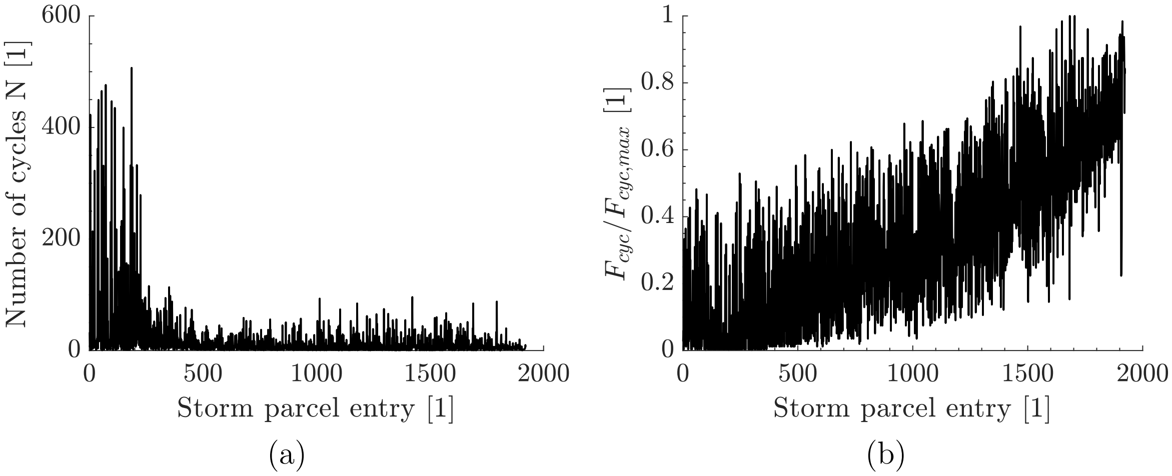

(a) (b)

Figure B.6: Number of global cycles (a) and global lateral load (b) over storm bins.

The CSR values related to the reference load of the storm are plotted in Figure B.7 (a). The area of influence is around the pile and correlates with the trend of bedding resistance along the pile. There are large CSR values near the surface as well as at the pile tip. Some of the CSR values are very small and since the figure shows the CSR field related to the largest global load, there are many elements for other storm entries which are even smaller. In order to speed the calculation up, a limiting CSR value is introduced. Figure B.7 (b) shows the CSR_{lim} as well as indirectly the loading condition, because each LTR relates to an individual CSR_{lim} value. The CSR_{lim} value decreases from symmetric two-way loading to symmetric one-way load. The upper part in front of the pile shows LTR values of 1 (symmetric one-way loading) and the yellow area LTR values from 0 to 1, which indicates approximately non-symmetric two-way loading. It can be seen that in the area of the most bedding resistance up to the failure wedge two-way loading is expected. This means that there is a large increase in equivalent shear stress over the load application.

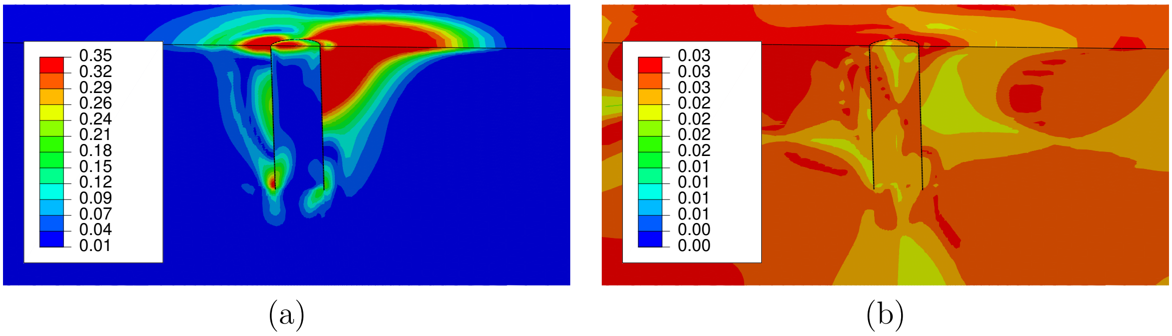

Figure B.7: CSR value for reference load (a) and CSR limit values (b).

Many of the entries result in CSR values smaller than the calculated CSR_{lim} for the reference load and are skipped within the calculation routine, because of a very small global load or since the integration points are too far away from the structure. The number of integration points, which need to be evaluated, increases over the analysis of storm bins since the total damage to the structure correlates to the global load, which also increases over the reordered storm bins.

The excess pore pressure can be evaluated based on the given CSR field and a number of cycles of N = 1 to show the induced damage without any dissipation or other effects (Figure B.8 (a)). The normalized excess pore pressure field correlates directly with the CSR field. This field is subjected to a flow net analysis in order to derive the individual consolidation behaviour. The decay for one element is shown in Figure B.9. After dissipation and analytical superposition, the excess pore pressure field in Figure B.8 (b) arises.

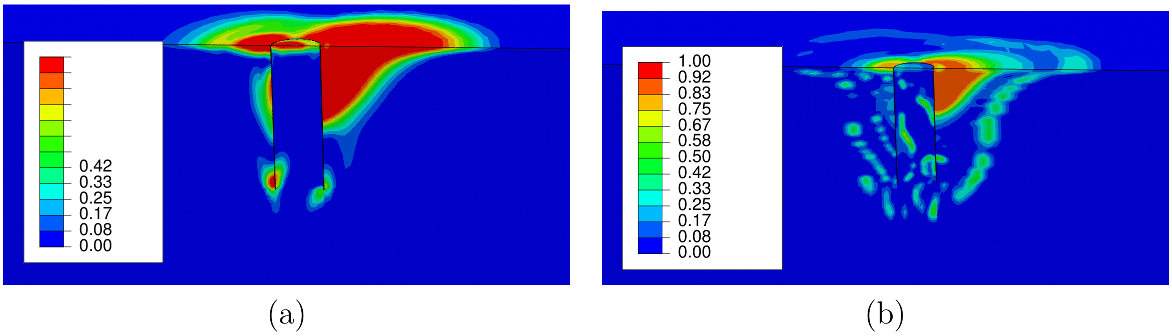

Figure B.8: Excess pore pressure ratio field R_u for N = 1 for reference load conditions (a) as well as dissipated and superposed excess pore pressure ratio R_u field (b).

For the final number of cycles after dissipation, a shear stress - shear strain curve can be plotted. Within this curve, the associated CSR value can be added and a factor between the reference value and the shear strain response for the calculated number of equivalent cycles can be derived (Figure B.10). This value is applied as a factor to the shear modulus of the integration point within the numerical analysis. An alternative approach is to use the shear stress-shear strain curve directly for the number of cycles directly by using a hardening extension for the standard Mohr-Coulomb model.

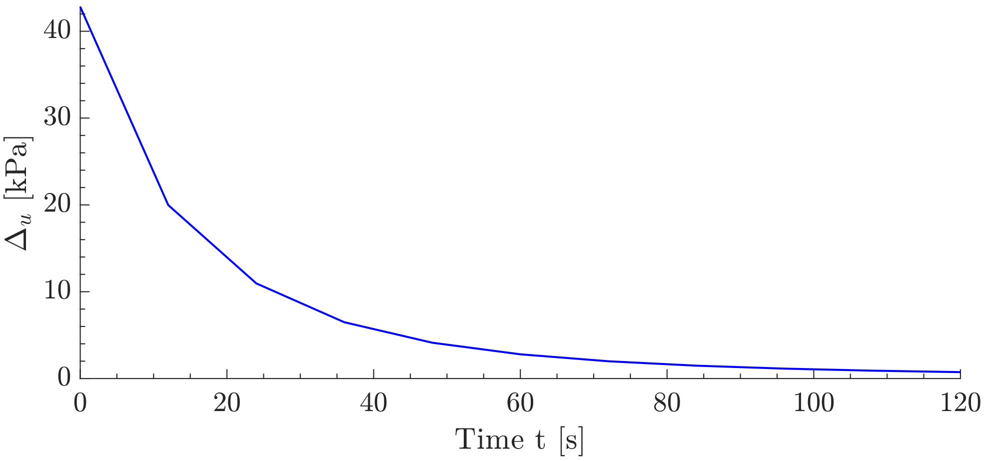

Figure B.9: Decay curve for excess pore pressure Δu from dissipation analysis for one integration point.

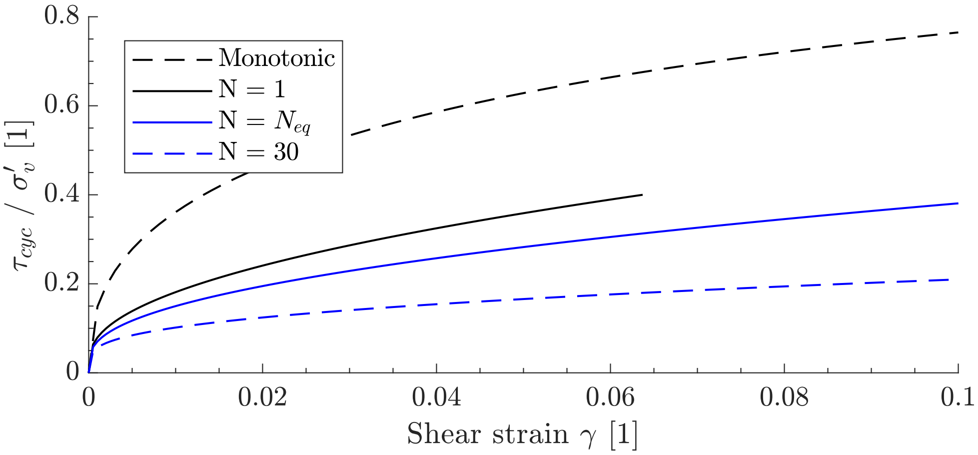

Figure B.10: Shear stress-shear strain curve for N = 1 as well as for the number of equivalent cycles in point 5 m/0 m/-8 m for the reference case.

Figure B.11 shows the results after the shear modulus degradation was evaluated for all integration points. The number of equivalent cycles in log-scale Figure B.11 (a) and the shear modulus degradation factor Figure B.11 (b) are shown for the end of the storm. The maximum number of equivalent cycles is 1000 and, thus, in the defined region of the mathematical framework derived from the DSS test results. A factor of unity indicates no stiffness degradation. Larger degradation occurred in front of the pile, but not directly at the surface since here the excess pore pressure could dissipate easily.

The resulting load-displacement curve is shown in Figure B.12. In comparison to the monotonic case, the cyclic storm load led to a decrease of bearing capacity of approximately 55% to 20.3 MN for the 0.1D criterion. Different approaches are also depicted and are explained in the following.

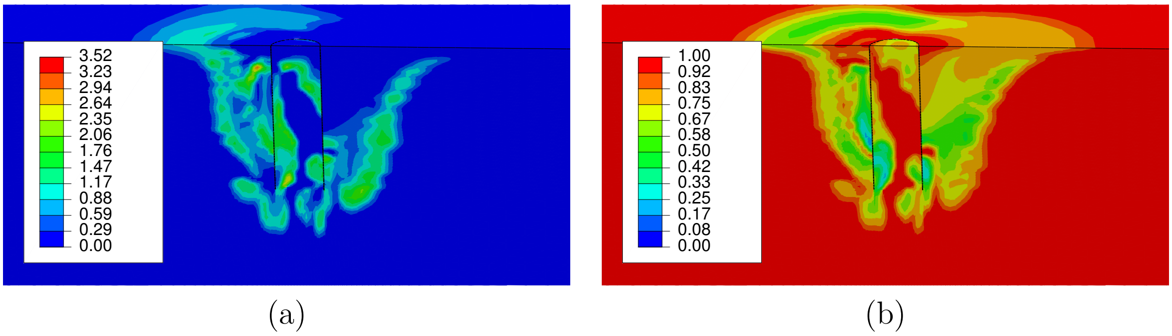

(a) (b)

Figure B.11: Resulting fields of equivalent number of cycles ($log_{10}(N_{eq})$) (a) and the shear modulus degradation factor (b) at the end of the storm.

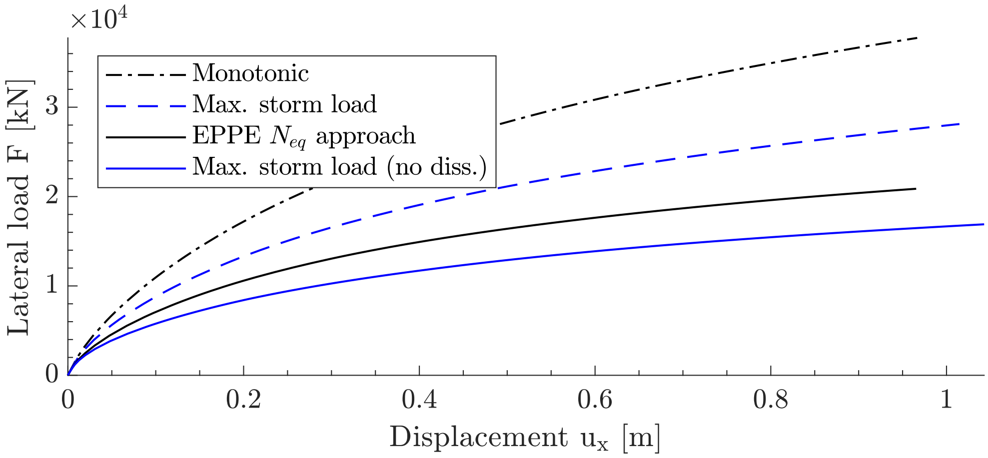

Figure B.12: Load-displacement curve for monotonic and cyclic analysis as well as for other simplified approaches.

B.5 Comparison with different literature procedures

The non-linear influence of the soil stratigraphy is the reason each location has to be calculated with the presented method individually. However, through various optimizations, a site can be calculated numerically within less than two hours. The advantage over other procedures is the consideration of drainage and the use of integration point specific CSR and LTR values. The calculation of an equivalent number of cycles for each integration point takes a good amount of this calculation time. Two different methods from the literature are used for comparison purposes. However, it is very difficult to approximate the influence of the stratigraphy herein accordingly.

B.5.1 Constant N_{eq} from storm bins on global level

In order to reduce the computational effort, only the load cases with substantial influence shall be evaluated. Hence, in the following, the storm load is ordered based on one representative integration point and only the last entry is evaluated with $F_{min} = -13\,\text{MN}$ and $F_{max} = 9\,\text{MN}$ with the related number of cycles entry of N = 0.9 (exactly as explained in chapters 6 and 7). All entries except the last one are deleted. In this way, no storm build-up is considered. Effects from stress redistribution and soil stratigraphy are considered since the CSR and LTR are derived based on one monotonic calculation; accumulation effects from previous storm entries with smaller global loads and smaller damages are neglected.

Figure B.12 shows a comparison of the load-displacement curve resulting from the procedure described above with the monotonic response. The load-displacement curve shows a larger bearing capacity since most of the excess pore pressure is dissipated due to the larger hydraulic permeability. Therefore, a second calculation was done with disregarding dissipation and also only considering the last storm entry. The resulting structural response shows a lower capacity in comparison to the result based on the EPPE approach with a full storm consideration (and dissipation is included). This is because the largest global lateral load induces the largest and most substantial damage and also, because most of the storm history was dissipated due to the comparatively large hydraulic conductivity of the sand. However, this does not necessarily have to be the case with stratified subsoil due to its non-linear behaviour.

Figure B.13 shows the excess pore pressure ratio field R_u for the three numerical models. If the monopile is loaded with the maximum storm load (including dissipation), there is a medium severe damage field and only a minor capacity degradation. For the academic scenario of neglecting dissipation of the very last cycle, there is a larger degradation. In between both scenarios, there is the model which includes the storm effects. Hence, the difference to Figure B.13 (a) can be related to storm history effects.

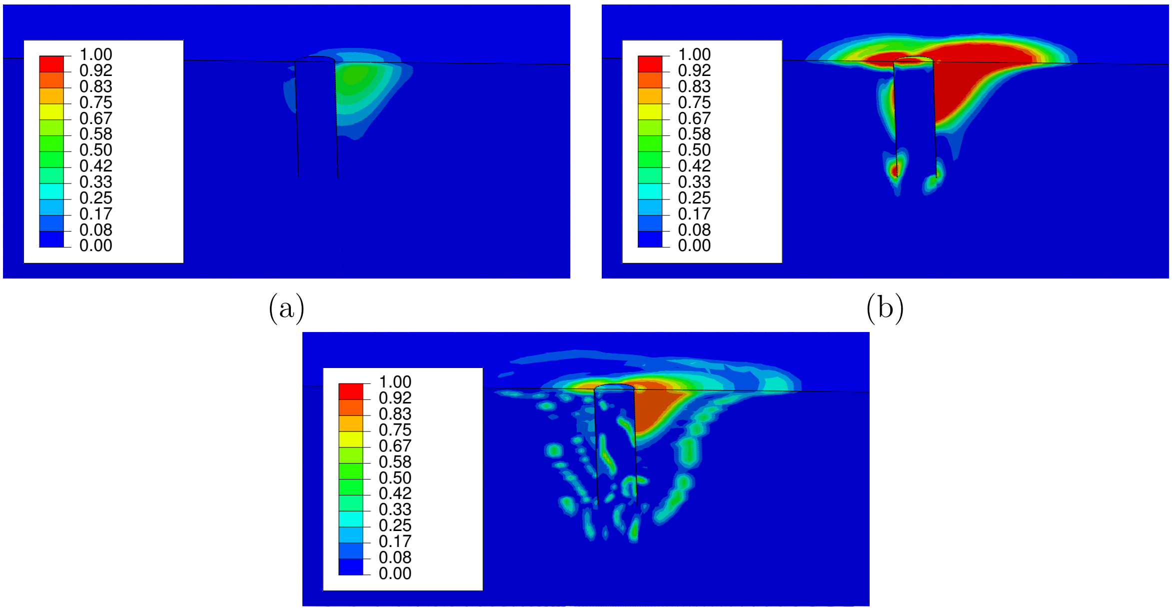

(a)

(b)

(c)

Figure B.13: Final excess pore pressure field R_u for maximum load (a), maximum load without dissipation (b) and complete storm consideration (c).

B.5.2 Constant N_{eq} from excess pore pressure accumulation procedure

Another way of reducing the computational time is to exclude all CSR effects and use the procedure, which is explained in Appendix C (Andersen, 2015) and has also been used by Klinkvort et al. (2020). It neglects spatial variations as well as the stress conditions within the soil. Compared to the reference procedure above, this procedure is, hence, less accurate and saves almost no time since all main implementations of the reference EPPE approach with consideration of full storm are also needed. For the calculation, the same input as before is used, only that it is done globally as a pre-processor with a scaled factor on the global storm load. Simplified dissipation is considered by using a decay of 20%. Figure B.14 depicts the excess pore pressure accumulation for different scaling factors. The black points mark the storm entries with the last scaling factor to touch the failure line. The blue circles track the end points of the smaller scaling factors. The green and black circles represent the end points of the storm for smaller scaling factors for simplified dissipation between adjacent storm bins. The influence even of this simplified dissipation can clearly be seen. The global number of equivalent cycles is N = 55. If a very simplified dissipation is considered in each step, the equivalent number of cycles is reduced to N = 3.

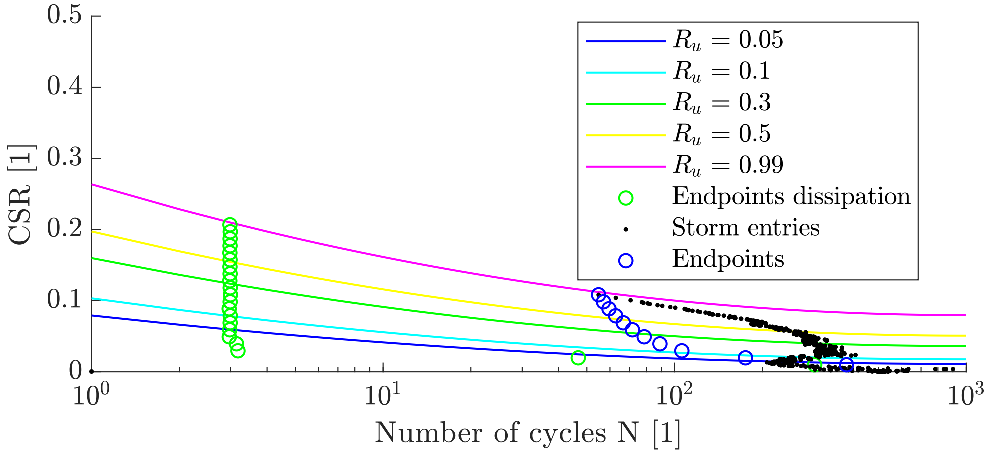

Figure B.14: Excess pore pressure accumulation for LTR = 1 for different scaling factors and different dissipations. The black points mark the storm entries with the last scaling factor to touch the failure line of $R_u = 0.99$. The blue circles track the end points of the smaller scaling factors. The green and black circles represent no and dissipation of 20%.

Figure B.15 shows the resulting normalized excess pore pressure field for N = 55. The induced damage is so large, that a calculation of the bearing behaviour is not required. Hence, the load-displacement curve is not depicted in Figure B.12.

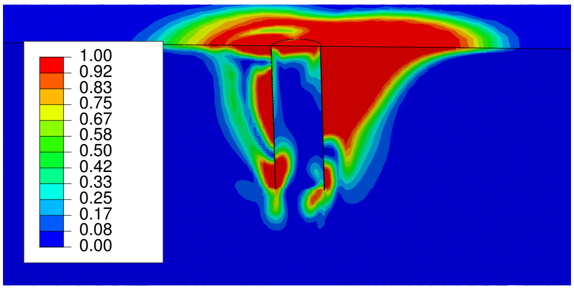

Figure B.15: Final excess pore pressure ratio field for N = 55.

B.6 Summary

A simple procedure to consider a storm loading instead of a single number of equivalent cycles N_{eq} is presented. The method evaluates all integration points of the finite element model for all storm entries. The method is more accurate than the assumption of a constant number of cycles due to spatial variations around the pile and is not too conservative in order to establish an economical design. However, by considering the storm build-up the damage cannot drastically be reduced.

If the storm build-up shall be considered by means of a damage-reducing effect, preconditioning should be taken into account on the cyclic element tests instead on finite element level. Therefore, a pre-shear phase can be performed prior to the main constant-volume shear phase. However, the exact boundary conditions in laboratory testing can significantly influence the result. Parameters are, for instance, the vertical stress, the LTR, the CSR and the number of cycles, and even if the preconditioning phases are done under drained or undrained conditions. The influence of the experimental boundary conditions on the final contour plots will change the numerical results more than considering the storm build-up more accurately within the explicit method mentioned above.

C Estimation of equivalent number of cycles with accumulation procedure

A superposition procedure is necessary for the estimation of an equivalent number of cycles. The procedure described in Appendix B is similar to the excess pore pressure accumulation procedure for completely undrained conditions according to Andersen (1976).

In order to investigate the accuracy of the estimation of an equivalent number of cycles based on the excess pore pressure ratio as a memory variable multi-step cyclic DSS tests were performed. Similar work has been done by Zografou et al. (2019a) for clay and with the HCA model by Wichtmann et al. (2010). For this thesis, first a contour plot for two-way loading was established and subsequently staged cyclic direct constant-volume tests have been performed. An equivalent number of cycles was derived from an assumed storm load and compared with the related multistep cyclic DSS test results. The results verify the EPPE approach which uses storm packages and is explained in the following.

C.1 Excess pore pressure accumulation method

The excess pore pressure estimation can be used for the derivation of the equivalent number of cycles similar to the approach according to Stewart (1986) (Andersen et al., 1978; Andersen, 1976; Jostad et al., 2015b) (Figure C.1). Therefore, different load bins are successively calculated. The excess pore pressure at the end of a cycle is equal to the excess pore pressure at the beginning of the next cycle. For monopiles a strain compatibility is not generally given and especially in case of sandy soils the excess pore pressure compatibility should be used. The procedure can be performed in a simplified way by only using contour plots based on symmetrical two-way loading (Figure C.1). This implies the assumption that the non-linear soil behaviour is well represented by one contour plot and that there are only marginal influences induced by other mean shear stresses.

The accumulation procedure ensures the compatibility between two or more load parcels with different shear stresses. Therefore, the governing loads are sorted in ascending order with the related numbers of cycles for each specific load parcel. It is assumed that the global load is linearly correlated to the shear stress acting in the soil element. A scaling factor is introduced and the cyclic shear stress can be calculated. Jostad et al. (2015b) propose that the mean and cyclic load can be assumed to be directly proportional to the mean and cyclic shear stress within the elements (if in same loading direction). The procedure is done for different scaling factors until the last bin touches the failure line (Equation C.1). The procedure is first done for small scaling factors which are then increased up to the point of failure. The last scaling factor is used to scale the quotient of global loads to element level (Appendix B).

$$\frac{\tau}{\tau_{max}} = \chi \frac{F}{F_{max}} \tag{C.1}$$

The procedure bases on the following equation:

$$R_{N+\Delta N} = R_N + \Delta R_i + R_{\Delta N} \tag{C.2}$$

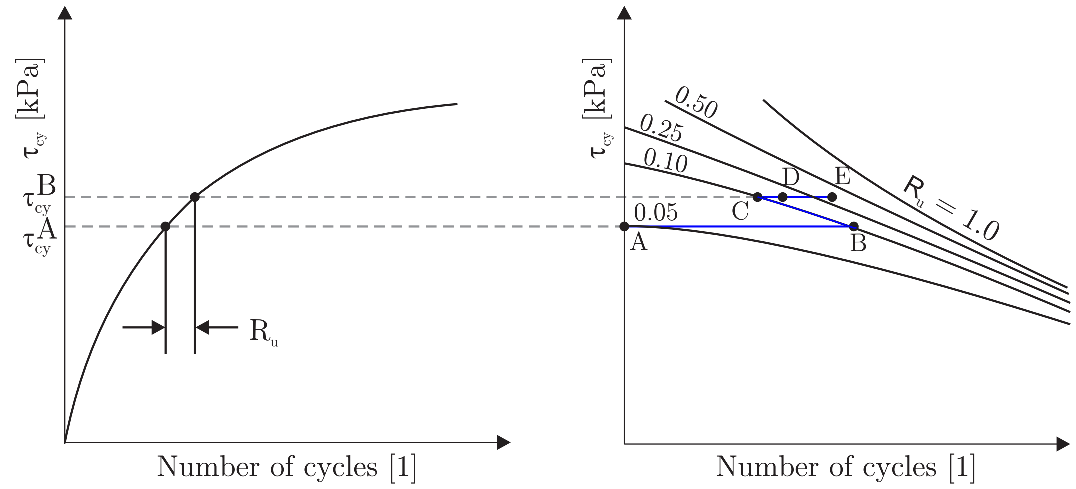

Figure C.1: Accumulation procedure according to Andersen et al. (1978).

The value $R_{N+\Delta N}$ is the excess pore pressure after an additional number of cycles and R_N the excess pore pressure for the current shear component. ΔR_i represents the intermediate change in excess pore pressure due to an increase in cyclic shear stress (here undrained conditions are assumed). $R_{\Delta N}$ is the increase due to an additional number of cycles.

The procedure shall be explained on a simple example. The load sequence in Figure C.1 starts in point A for a load (multiplied by the scaling factor). The number of cycles of the first load parcel is applied in order to reach point B. The resulting excess pore pressure is given by the isoline point B. For the next load parcel, which is higher and denoted with E, the same excess pore pressure is expected but for fewer number of cycles. From point B the isoline is followed up to the crossing point C with the shear stress at C, D and E. Point C describes the equivalent number of cycles from the first to the new load parcel. Due to the increase in shear stress an additional excess pore pressure increment needs to be applied. This increment can be derived from the cyclic shear stress - excess pore pressure ratio curve for N = 1. The increase for the curve for N = 1 is added and leads to point D. Subsequently, the number of cycles for the second parcel is added to point E. In case of partly drained analysis, dissipation has to be considered. For the same shear stress level, a small part is assumed to dissipate and the resulting end point is reached for a smaller number of cycles. After the last load parcel was applied, the procedure is repeated with a different scaling factor and the intersection between end of locus and the failure enveloped are used as the indicator for the equivalent number of cycles.

The dissipation can be integrated with a flow net calculation or empirical approach. For more complex boundary conditions a flow net analysis may be necessary. This procedure is done for all entries in the storm parcel up to the last entry where the maximum cyclic shear stress is equal to the normalized maximum cyclic load. Afterwards the procedure is repeated with a different (larger) scaling factor. The ratio between cyclic and mean shear stress as well as cyclic and mean global load is assumed to be equal. As a result the locus of the end point of the accumulation procedure will move upwards to a larger CSR value. The scaling factor is initially chosen rather small and subsequently increased until the end point reaches the cyclic strain failure criterion. The result of this last calculation estimates the equivalent number of cycles.

C.2 Application to reference sand

The method is used to back-calculate cyclic constant-volume multi-step direct simple shear tests. The general applicability of the procedure will be shown with the results of these element tests. No dissipation is considered and no scaling factor (factor = 1.0) is needed since the CSR values in the DSS tests are known and the problem does not deal with soil-structure interaction. There is no need for a differentiation between the application of the mean shear stress in an drained or undrained manner since the tests were performed as symmetric two-way loading test (with a mean shear stress of zero). The test conditions are depicted in Table C.1. The mean load is kept constant, so that additional multi-step cyclic constant-volume DSS tests should be performed with changing mean shear stress for a further validation.

Table C.1: Multi-step cyclic constant-volume direct simple shear tests with LTR = 0.

Number [1]	*CSR* [1]	*N* [1]	*CSR* [1]	*N* [1]	*CSR* [1]	*MSR* [1]	*N* [1]
1	0.001	300	0.050	100	0.075	0.00	30
2	0.050	500	0.062	400	0.074	0.00	100
3	0.012	500	0.025	400	0.050	0.00	100
4	0.025	300	0.050	100	0.075	0.00	30
5	0.050	400	0.062	500	0.075	0.00	100
6	0.025	450	0.050	310	0.075	0.00	250

Figure C.2 shows this exemplary for a simulated storm event consisting of three load parcels with increasing CSR value (0.051, 0.062, 0.074) and decreasing number of cycles (500, 400, 100). As the shear stress increases, so does the shear strain and the excess pore pressure. A large increase of shear strain can be seen when liquefaction occurs (Figure C.3).

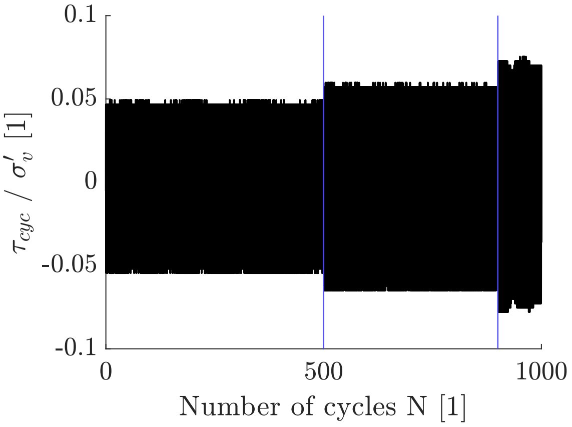

Figure C.2: CSR for three different storm steps in constant-volume DSS tests.

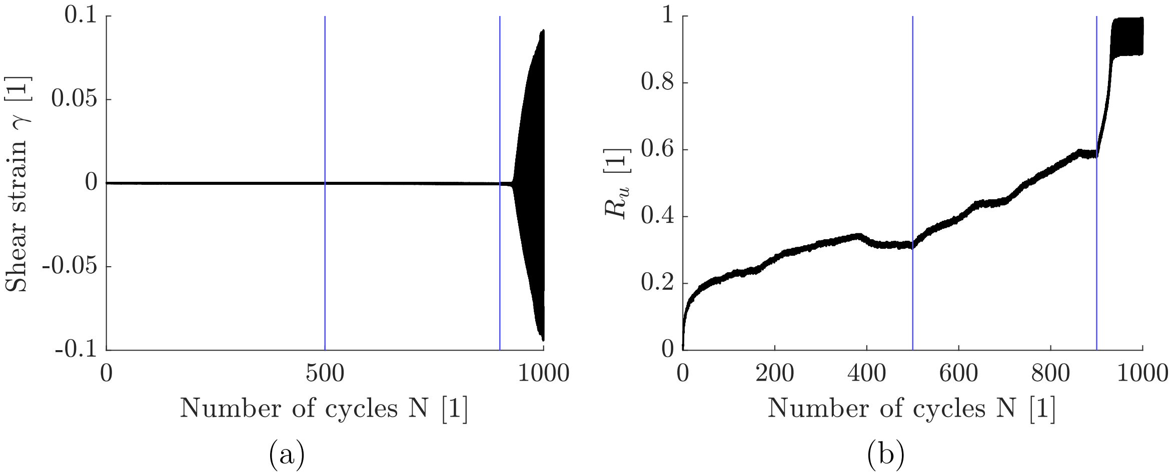

Figure C.3: Shear strain (a) and normalized excess pore pressure (b) for three different storm steps in cyclic constant-volume DSS.

Figure C.4 shows the accumulation procedure for different multi-step tests. The equivalent number of cycles at the end of the step is depicted in red. The final equivalent number of cycles can be read on the axis for the last storm entry. Figure C.5 presents the same data in a different way. The CSR is plotted over the excess pore pressure generation. The result of the accumulation method can visually be compared to equivalent laboratory tests. The dotted blue curve shows the accumulation method using contour plots. The curve follows the response of the soil at N = 1 with discrete increases in excess pore pressure when the CSR of the load parcel is reached. The blue curve represents multi-step DSS test results and the black curve the equivalent one-step DSS test for the equivalent number of load cycles (N_{eq}). Comparing the end point of the dotted and solid blue line, the calculated excess pore pressure build-up trend seems very reasonable. Moreover, the end of each step represents the excess pore pressure up to this point within the cyclic test. This value does also agree well between the procedure, the curve for N_{eq} and the measured data.

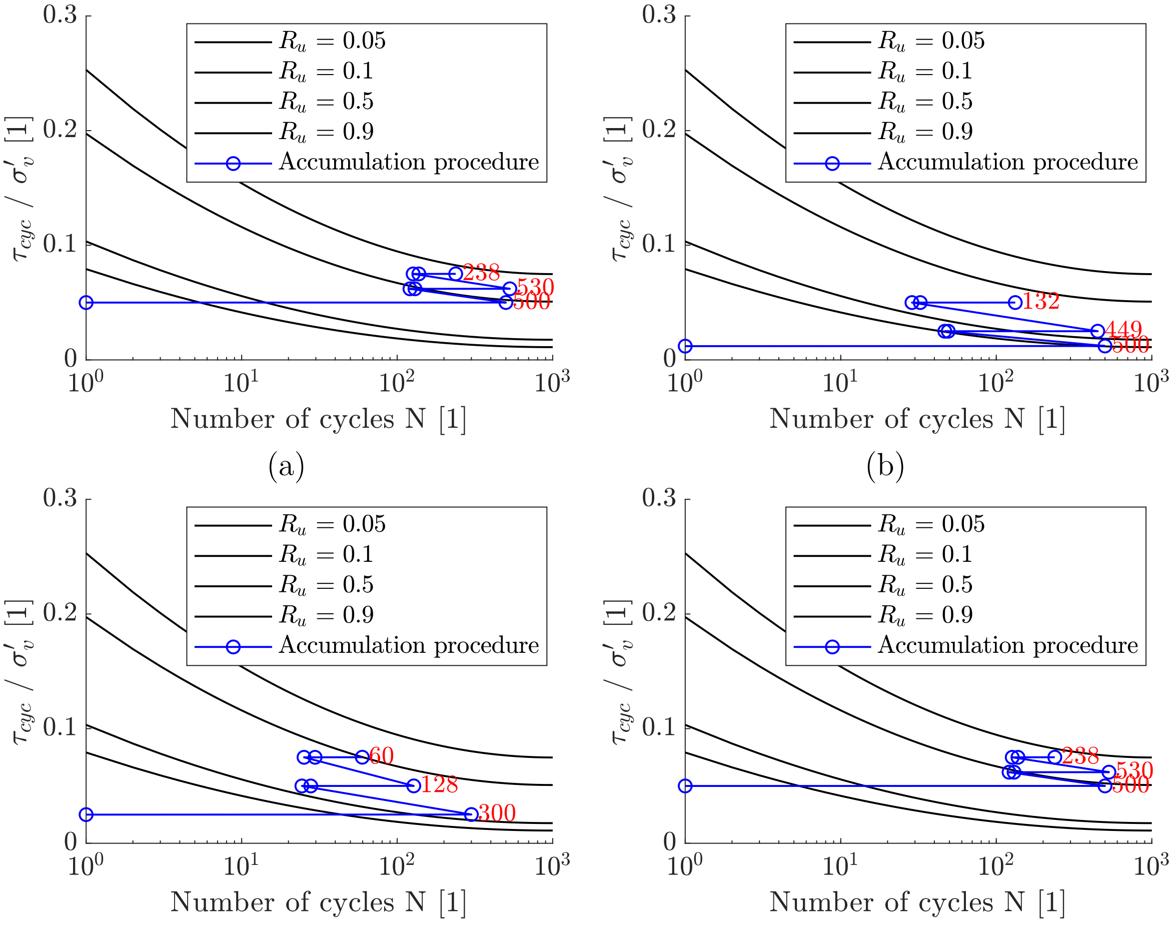

(a) (b) (c) (d)

Figure C.4: Excess pore pressure contour plot with CSR over number of cycles for LTR = 0 with results from excess pore pressure accumulation procedure without dissipation and equivalent number of cycles in red.

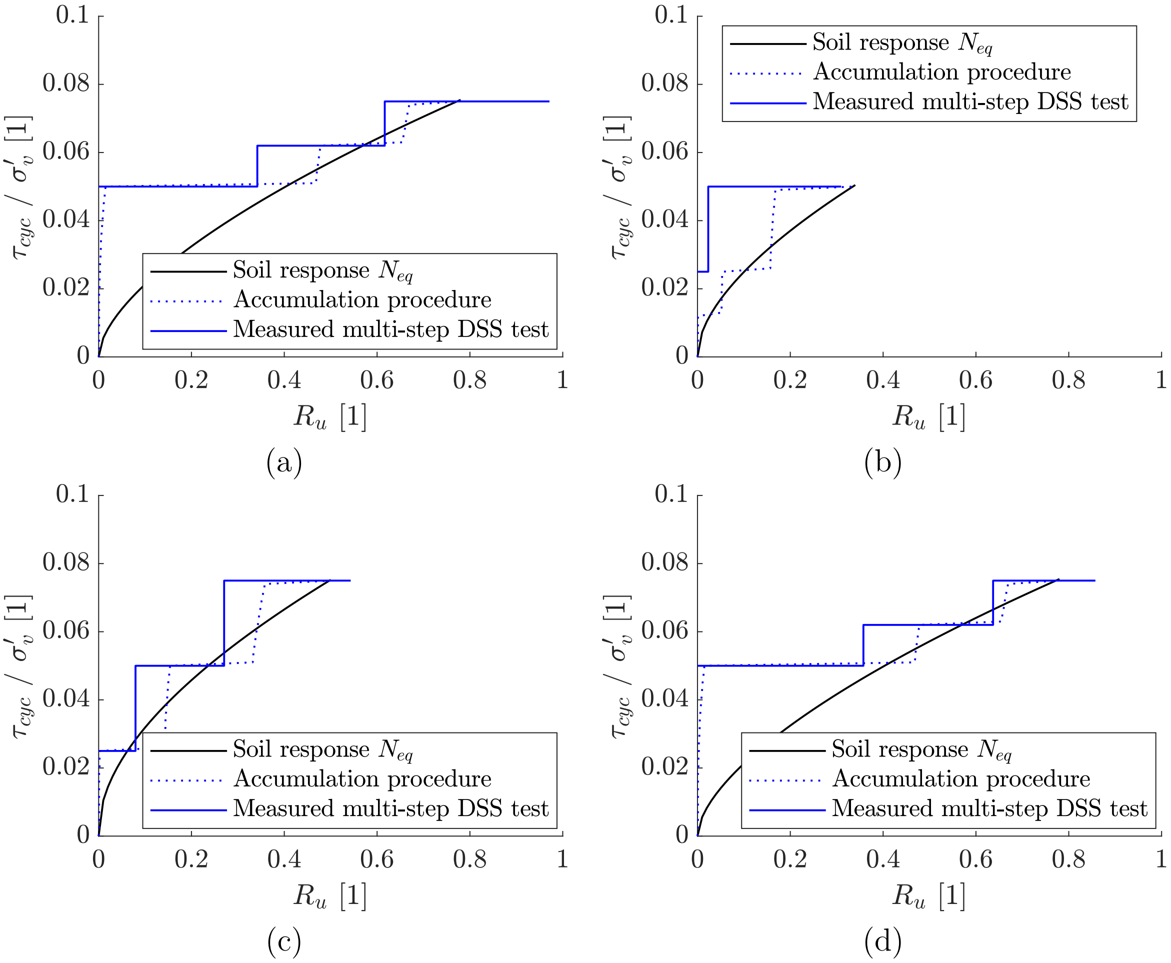

Figure C.5: CSR plotted over excess pore pressure generation; comparison of results from stress-accumulation-method (blue dotted), multi-step DSS tests (blue) and response of the soil at N_{eq} (black).

D Comparison of load- with displacement-controlled cyclic direct simple shear tests

Cyclic laboratory tests can be performed load- or displacement-controlled. There are some applications in which the loading state resembles more of displacement-controlled situation on macro level due to a redistribution of stresses. In this case displacement-controlled tests are needed. However, mainly load-controlled tests are performed and the question arises if it is possible to transfer the results from one to another in order to incorporate these into the EPPE approach.

D.1 Transfer procedure

The soil response by means of the stress - strain relation is completely different for the two boundary conditions, even if the soil still generally degrades. The rate of degradation and the stress states are different. For a load-controlled test, the shear strain increases and for a displacement-controlled test the shear stress decreases. In both cases, there is a degradation of the shear modulus. The difference can be explained by the different cyclic stress paths and the energy development over the cycles. For a displacement-controlled test the energy per cycle decreases. However, this behaviour depends on the cyclic amplitude, as both boundary conditions give similar results for small loads. The load-controlled based contour plots can be back-calculated to displacement-controlled element responses. This is not possible vice-versa. The reason for the difference in the response is that in a displacement-controlled test the specimen was loaded N cycles with a specific shear strain; the shear stress is reduced quite fast. In a load-controlled test, the specimen is only loaded with this high shear strain at the end of the test; the shear strain builds up not as fast as the shear stress is reduced in case of a displacement-controlled test. More information and a procedure for the back-calculation is presented by Andersen et al. (1978). In the following, this procedure is briefly described.

In case of displacement-controlled tests, the shear strain remains constant and the shear stress decreases over the number of cycles. During a cyclic load of ΔN the shear stress is reduced for the case of load-controlled tests but the cyclic shear strain must remain constant in order to meet the displacement boundary conditions. The calculation procedure can be explained with Figure D.1 with a cyclic shear strain amplitude of $\gamma_{c,1}$. A displacement controlled test with $\gamma_{c,1}$ will show a decreased shear stress after ΔN_1 (from point 1 to point 2). On the left side, the cyclic shear strain $\Delta\gamma_{c,i,1}$ can be read from the curve for N = 1 resulting to $\gamma_{c,2}$ for the now reduced shear stress (point 3 with the same shear stress as point 2). The number of cycles ΔM_1 is needed to get from point 3 again to point 2 and meet the boundary conditions for displacement-controlled tests.

For a second load parcel with ΔN_2 the shear stress decreased again from point 2 and results in a drop of shear strain of $\Delta\gamma_{c,i,2}$ (point 4). The difference in shear stress is used in the right hand side image to derive the decrease in shear strain. When considering this decrease in shear strain point 5 arises for the shear strain of $\gamma_{c,3}$. In order to get back to the constant shear strain (point 4) the number of cycles ΔM_2 is needed. When plotting the derived displacement-controlled results, the number of cycles ΔM_i is used. Point 6 arises, for instance, for the resulting end of the second storm parcel with $M = \Delta M_1 + \Delta M_2$. The complete curve and comparison between constructed and measured data is depicted in Figure D.2 (Andersen et al., 1978).

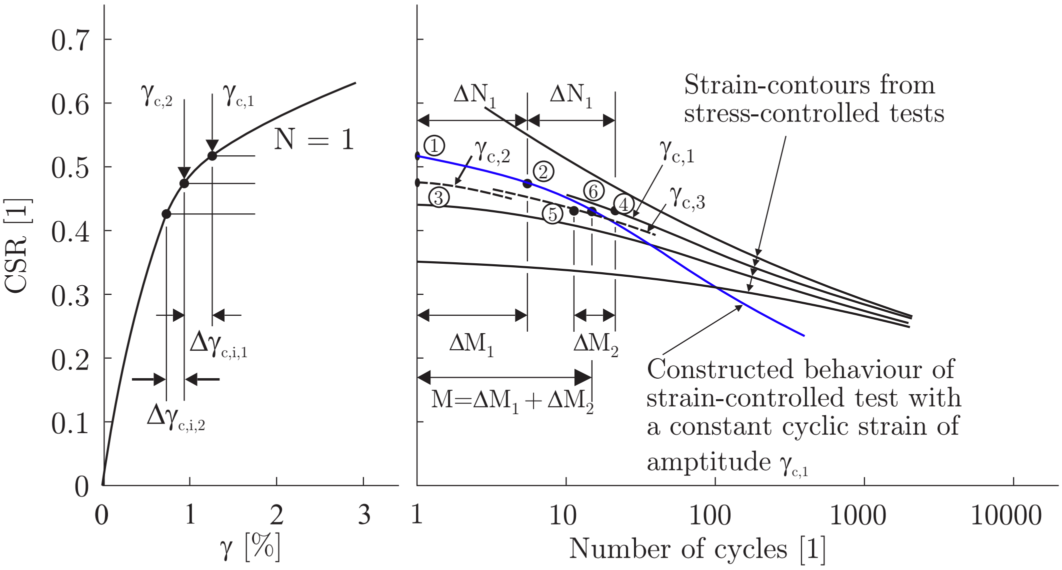

Figure D.1: Transfer procedure according to Andersen et al. (1978).

D.2 Transfer to displacement-controlled test conditions for reference sand

Displacement-controlled tests have been performed for different vertical stress and cyclic strain amplitudes (cf. Chapter 5 and Appendix E). A transfer of the data is done in order to show the general applicability. The contour plot for a relative density of $D_r = 0.85$ and for a vertical stress of 100 kPa was used. Figure D.3 shows the input for the aforementioned procedure in form of cyclic shear strain contour plots. Figure D.4 (a) shows the same contour plot but with the results of a displacement-controlled test with a shear strain amplitude of 0.01. Figure D.4 (b) shows an excess pore pressure contour plot with the position of the derived equivalent displacement-controlled cyclic direct simple shear test. Figure D.5 shows the comparison over the number of cycles for four different shear strain amplitudes for excess pore pressure ratio over number of cycles with the results of true

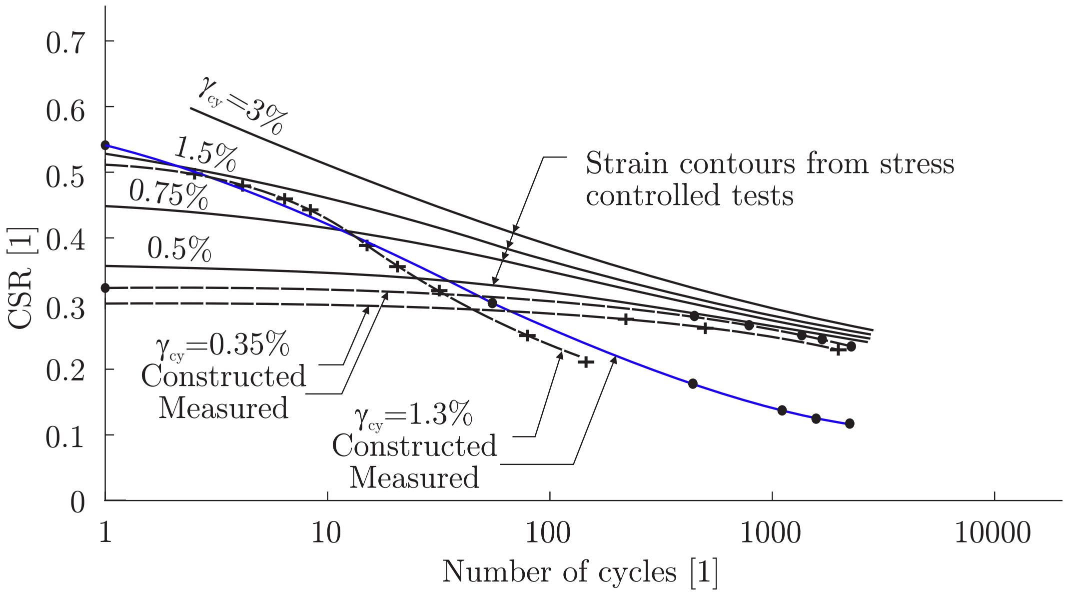

Figure D.2: Overview of general soil response according to Andersen et al. (1978).

displacement-controlled tests with 100 kPa and 400 kPa vertical stress. For small shear strain amplitudes, the transfer from load- to displacement-controlled tests seems to be acceptable, but for increasing shear strains the deviation increases. Based on the results of this comparison, such a transfer from load-controlled test results to displacement-controlled test conditions should be used carefully.

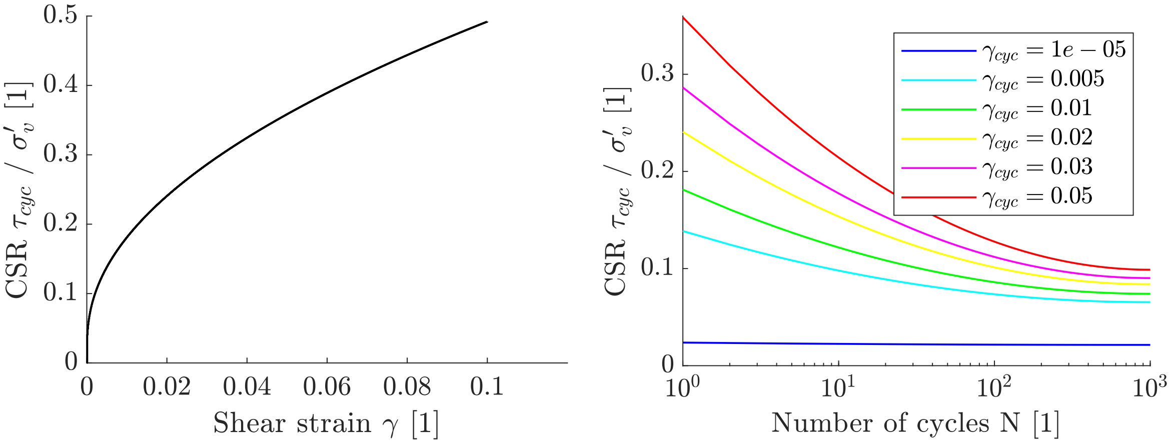

(a) (b)

Figure D.3: CSR over shear strain for N = 1 (a) and cyclic shear strain contour plot for LTR = 0 (b).

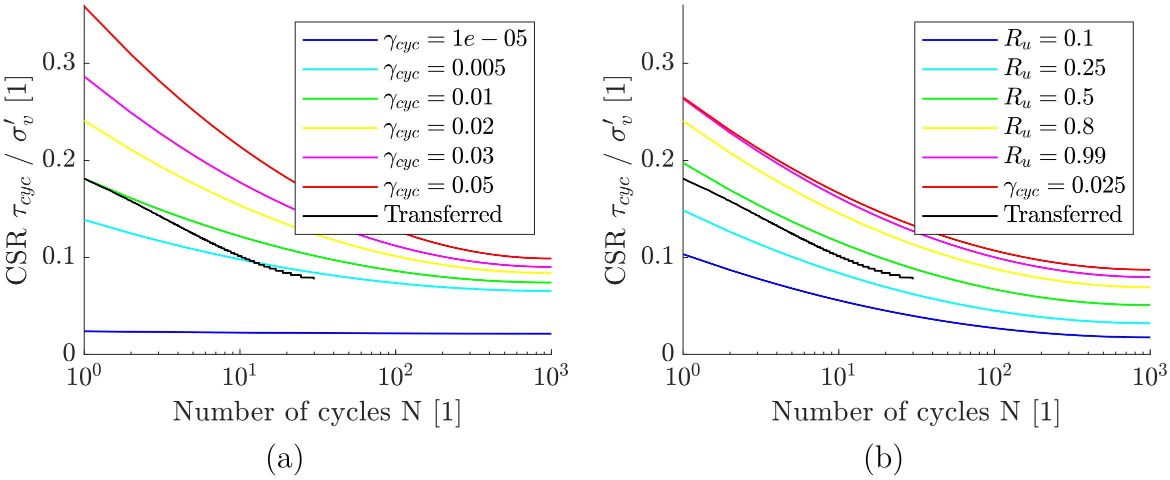

(a) (b)

Figure D.4: Contour plot LTR = 0 with transferred $\gamma_{cyc} = 0.01$ (a) and R_u contour LTR = 0 with position of back-calculation (b).

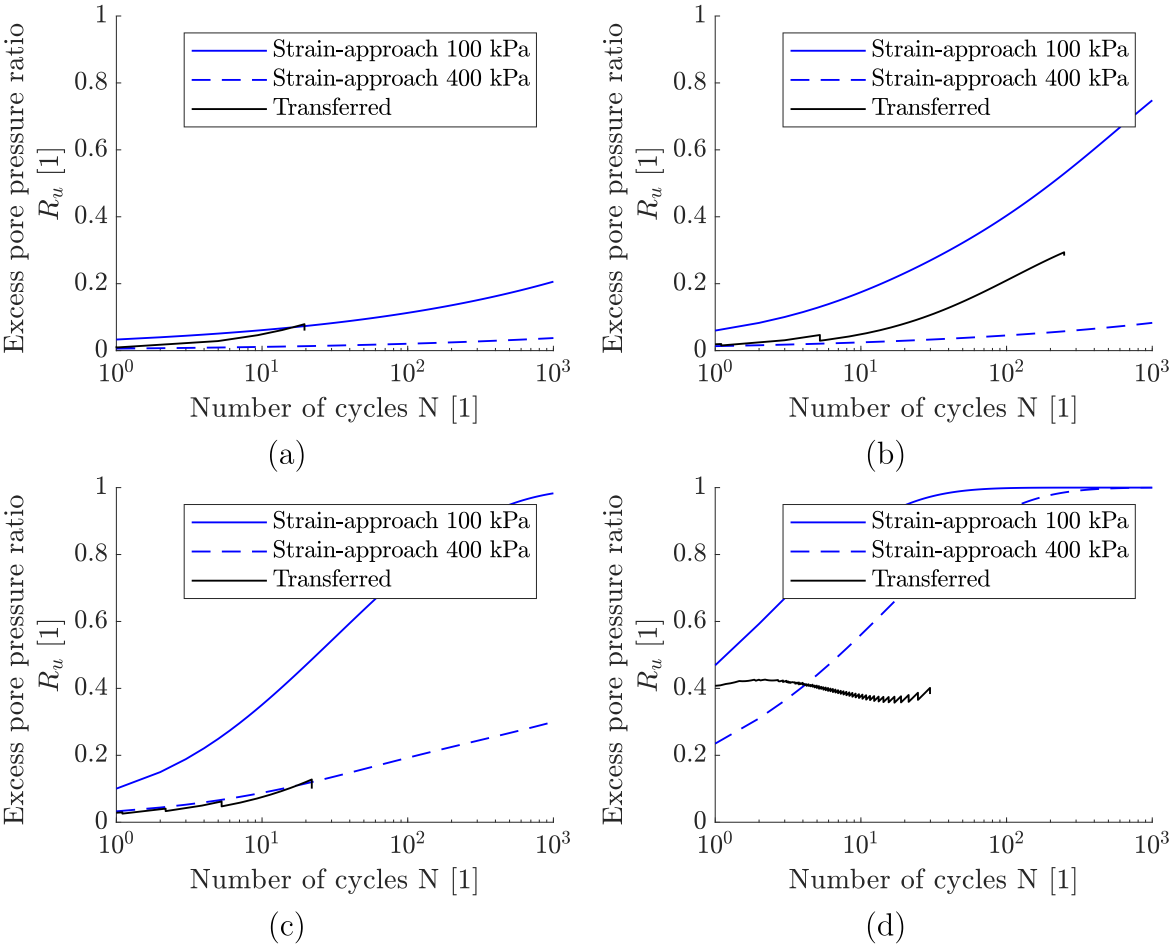

(a) (b) (c) (d)

Figure D.5: Comparison of excess pore pressure ratio over number of cycles for back-calculated displacement-controlled tests with results from directly measured test results for two different vertical stresses for a shear strain amplitude of $\gamma_{cyc} = 1.7 \times 10^{-4}$ (a), $\gamma_{cyc} = 3 \times 10^{-4}$ (b), $\gamma_{cyc} = 5 \times 10^{-4}$ (c) and $\gamma_{cyc} = 0.01$ (d).

E Strain-approach from displacement-controlled cyclic direct simple shear tests

Besides load-controlled tests, also displacement-controlled tests have been performed. The main results have already been presented in Chapter 5. Figure E.1 shows the excess pore pressure generation over the number of cycles and the related cyclic shear strain amplitude. The undrained soil response can very easily be described with displacement-controlled tests and categorized with shear strain threshold values. The following equations were established based on a regression analysis combined with shear strain thresholds.

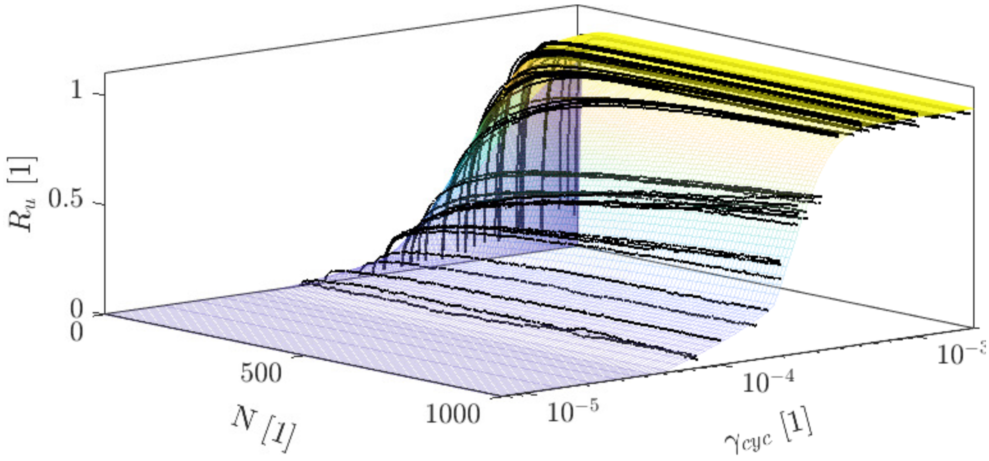

Figure E.1: 3D plot for a vertical stress of 100 kPa and a relative density of $D_r = 0.85$ for reference sand.

E.1 Linear shear strain threshold

The linear threshold can be read from resonant column results at 0.99 G/G_0 (Vucetic, 1994). It represents the region in which very small shear strains occur and the soil responses are quasi-linear elastic. The values from the literature vary between shear strain values of 5×10^{-6} to 6×10^{-5} (Wichtmann et al., 2010; Wichtmann and Triantafyllidis, 2013).

E.2 Volumetric shear strain threshold

The volumetric threshold represents the transition from intermediate-strains to irrecoverable deformation and small changes in the soil skeleton. A shear strain smaller than the volumetric threshold lies in the non-linear elastic region including no sliding of grain-to-grain; for larger shear strains a mainly non-linear-plastic response can be expected (Dobry et al., 1982). At this threshold the excess pore pressure has build up and the shear modulus is degraded for only a limited number of cycles, but the damage within the soil is not gradually increasing up to failure for more cycles. Similar behaviour was reported, for instance, by Lefebvre et al. (1989) and Drnevich and Richart (1970). A small load will only cause elastic, reversible alternation and not lead to an accumulation of degradation. The value of the volumetric shear strain threshold was investigated by many researchers and is assumed to be roughly 5×10^{-5} to 5×10^{-4} often defined as the beginning of settlement (Vucetic, 1994; Silver and Seed, 1971a; Dobry et al., 1985b; Wichtmann et al., 2010; Wichtmann and Triantafyllidis, 2013). Silver and Seed (1971b), Youd (1972) and Pyke (1973) assume it to be roughly $\gamma_{tv} = 1 \times 10^{-4}$ for clean sand. Chen et al. (2019) give an overview of literature data with a bandwidth of the threshold starting from 1×10^{-5} to 9×10^{-4} with most values between 1×10^{-4} to 3×10^{-4}. Furthermore, Drnevich and Richart (1970), Youd (1972) and Pyke (1973) concluded that there is a volumetric threshold at $\gamma_{tv} = 1 \times 10^{-4}$.

E.3 Degradation shear strain threshold

There is no clear definition for the degradation threshold. It is the start of a transition of the general soil behaviour. The degradation threshold is the transition to irreversible changes in the microstructure and unstable behaviour. The material undergoes a stiffening due to the cyclic deformation and also a softening due to reduction of effective stress (Chen et al., 2019; Vucetic and Mortezaie, 2015). This implies that there is a large decrease in the shear modulus resulting in an increase of the deformation behaviour of the soil.

More information can be found in Saathoff and Achmus (2021).

The regression approach bases on the following framework:

$\gamma_{tv} = 5 \times 10^{-5}$

$\gamma_{td} = 0.0001527 \exp(0.001953\, \sigma'_{v,c})$

$$R_{u,\gamma_{td0}} = \tanh(0.03626\, N^{0.267}) \tag{E.1}$$

$$\kappa = \max(18.18\, \sigma'^{-0.6281}_{v,c}, 0.4) \tag{E.2}$$

$$R_{u,\gamma_{td}} = R_{u,\gamma_{td,0}}\, \kappa \tag{E.3}$$

if γ_{cyc} smaller γ_{td}:

$$a_f = 0.2816\, \sigma'^{0.2245}_{v,c} \tag{E.4}$$

$$R_{u,N_{eq}} = R_{u,\gamma_{td}}((\gamma_{cyc} - \gamma_{tv})/((\gamma_{td} - \gamma_{tv})))^{a_f} \tag{E.5}$$

if γ_{cyc} greater γ_{td}:

$$N_{liq} = 0.5447\,\sigma'_{v,c} \, - 21.5424 \tag{E.6}$$

$$R_{\gamma_{max}} = \tanh(2.2263\,(N/N_{liq})^{0.4223}) \tag{E.7}$$

$$t_1 = 0.7414\exp(-0.02231\,\sigma'_{v,c}) \tag{E.8}$$

$$f_{factor} = 473\,N^{(t_1+0.3963\,exp(-0.002342\,\sigma'_{v,c}))} \tag{E.9}$$

$$t_2 = tanh(f_{factor}\,(\gamma_{cyc} - \gamma_{td})) \tag{E.10}$$

$$R_{u,N_{eq}} = (R_{\gamma_{max}} - R_{u,\gamma_{td}})\,t_2 + R_{u,\gamma_{td}} \tag{E.11}$$

if γ_{cyc} smaller γ_{tv}:

$$R_{u,N_{eq}} = 0 \tag{E.12}$$

E.4 Overview strain-based approach

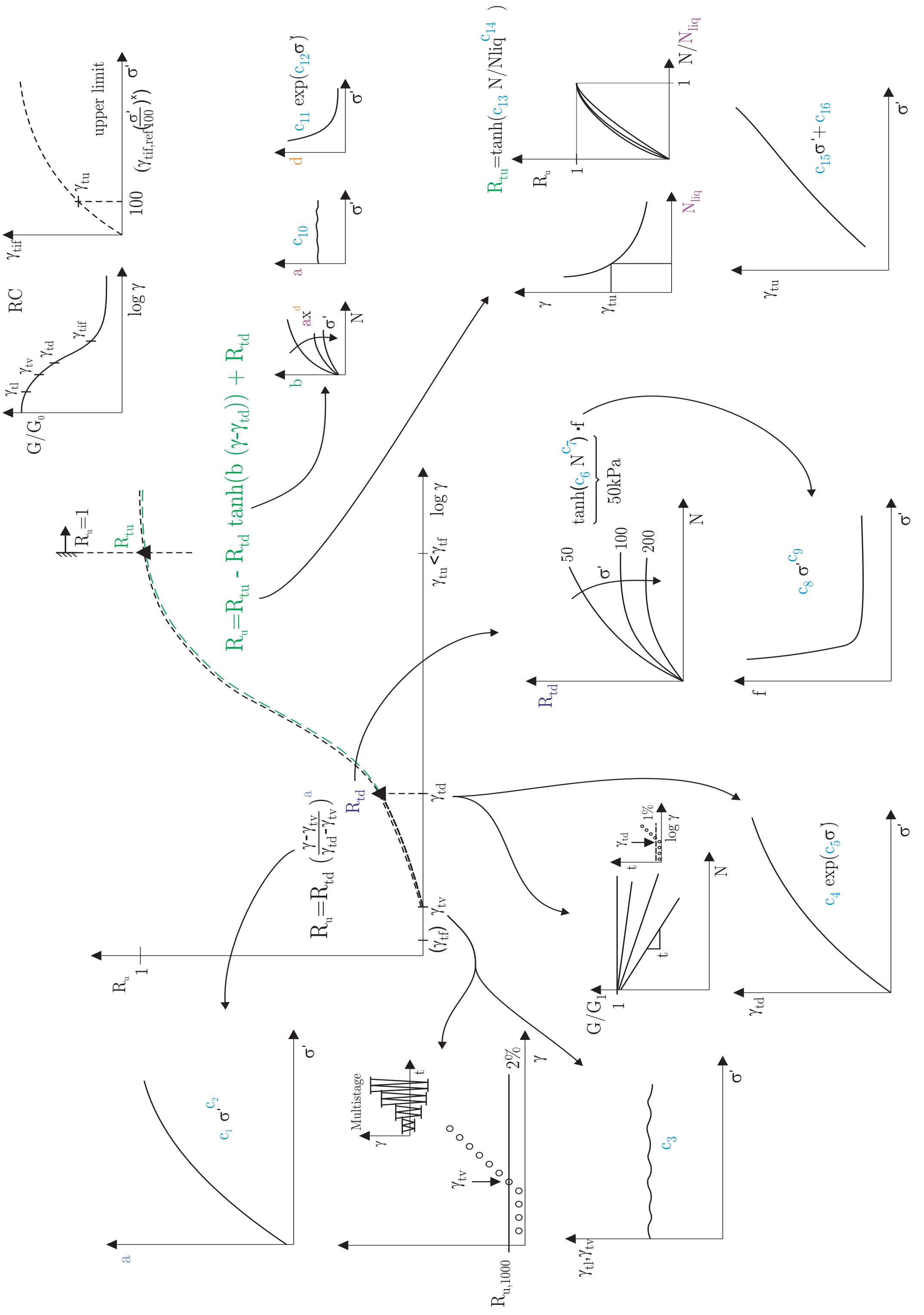

Figure E.2: Schematic overview of regression analysis.

F Simplified flow charts

In the following simplified flow charts are presented.

F.1 EPPE – equation approach

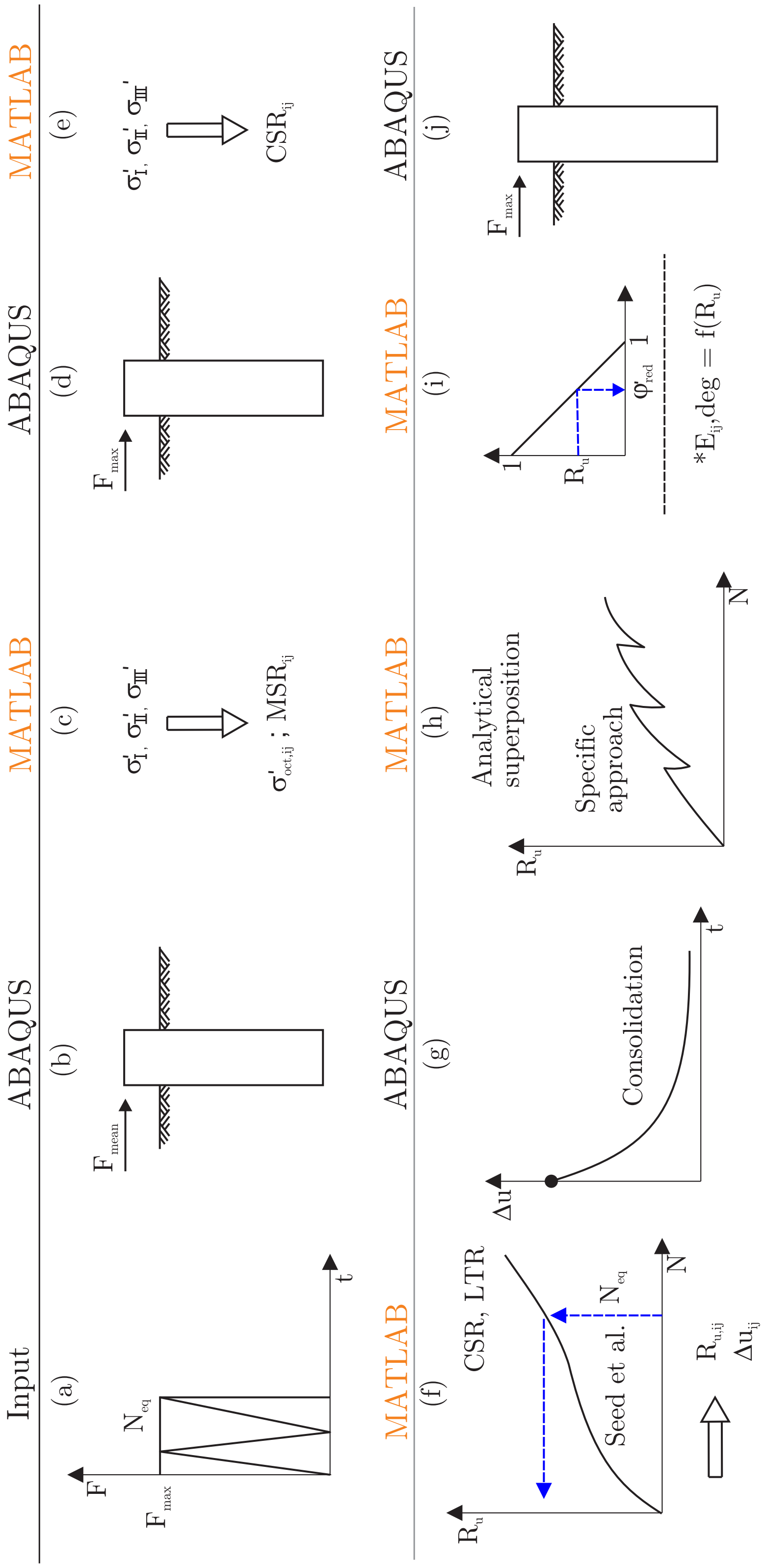

Figure F.1: Flow chart for EPPE - equation approach.

F.2 EPPE – iteration approach

The excess pore pressure, which is predicted based on the monotonic step, results in a changed bedding reaction for the post-cyclic model. This in turn also influences the stresses used for the prediction. Therefore, it is possible to carry out a second iteration with the already reduced soil elements in order to reproduce this effect. This results in an iterative process in which a final state is reached depending on the load variable. Thus, a post-cyclic behaviour is no longer determined with a monotonic model, but an equilibrium of global load, stress distribution and the soil response in the form of the contour plots is determined over several calculations.

The contour approach was first implemented by Jostad et al. (1997) for axisymmetric conditions in a FE environment with a hardening of the friction angle (based on Kavli et al. (1989)). Unlike the other approaches, only one overall run is required here to obtain the post-cyclic foundation response. It is similar to iterating the EPPE approach several times. This approach is based on the so-called UDCAM/PDCAM method of NGI, which is similar to the methods presented (Chapter 4 – more information can be found in Andersen (2015)).

The soil reaction depends on mean and cyclic components. Therefore, both have a certain ratio for a certain number of cycles. To obtain the complete soil response including shear strain and excess pore pressure, an iterative procedure is required. Therefore, the mean shear strain is estimated based on a two-way load under the mean drained load from the contour plots. In the cyclic phase the cyclic shear stress amplitude is applied. The mean shear strain is used as input to the cyclic loading and the derivation of the cyclic shear strain. The resulting CSR (in terms of cyclic shear strain) is used to recalculate the mean model. This condition is no longer a two-way load. A new mean shear strain results from which a new cyclic shear strain amplitude can again be generated.

For this method, two coupled FE models are required, which are organized via a Python script and monitored over the complete calculation process. They are correlated with the mean and cyclic shear strain and not shear stress in order to always have valid stress states within the contour plot (Jostad et al., 2015a).

One model considers the mean part of the global load F_{mean} (output: γ_{mean}) and one the global cyclic amplitude part F_{cyc} (output: γ_{cyc}). Beyond the parameters required for the description of the monotonic (reference) behaviour (ν, E_s, δ), the complete cyclic soil response is incorporated with multidimensional contour plots for each soil layer. The cyclic shear stress, the mean shear stress, the number of cycles as well as the normalized excess pore pressure are considered. No separate regression parameters need to be taken into account. The material is implemented in a user defined material (umat) within ABAQUS. The following steps are performed. A very simplified flow chart is depicted in Figure F.2. The steps are indicated as well.

0. Storm loading

Input: Irregular load **Output:** Load packages with F_{mean}, F_{cyc} N

The irregular storm load is transferred to load parcels with constant amplitude and constant number of cycles (Norén-Cosgriff et al., 2015).

1. Mean model

Input model 1: FE model **Output:** σ'_c

In the numerical model, initial stresses are calculated with k_0-initialization and the foundation is installed in a wished-in-place method. The static dead-weight load is applied under drained conditions. This is done for a contour plot of $N = 1$ (the $\gamma_{cyc} = 0\%$ curve in the contour plot is independent of cycles because it represents static loading). The stresses for all integration points are saved to a database (σ'_c). See Figure F.2 (a).

2. Mean model

Input model 1: F_{mean}, stress paths based on $\gamma_{cyc} = 0$ **Output:** τ_{mean}, γ_{mean}

The stress paths for each integration point are extracted from the type 2 contour plot for an assumed $\gamma_{cyc} = 0$ (monotonic response). The mean load F_{mean} of the first cycle is applied. The stresses for all integration points are saved to a database ($\frac{\tau_{mean}}{\sigma'_c}$). In the contour plot, a load path of the shear stress-strain relation for this specific shear strain γ_{mean} is read for the given N_{eq} and serves as input for the Cyclic model. It should not be confused with the load path in the EPPE contour approach which is derived by the quotient of F_{mean} and F_{cyc} in each element. Here, the path along the shear strain is used. See Figure F.2 (b).

3. Cyclic model

Input model 2: F_{cyc}, stress paths based on γ_{mean} **Output:** τ_{cyc}, γ_{cyc}

In a new model with installed foundation (restart from (2)) with the relation of shear stress to shear strain based on γ_{mean} from (2), the cyclic load F_{cyc} of the first parcel is applied under undrained conditions. This means that within the contour plot for the specific predefined number of cycles a path is read for γ_{mean}. The cyclic shear stress and cyclic shear strain are read at the crossing points with the isocurve of the mean shear strain. This cyclic curve for γ_{mean} is element specific. The normalized shear stress in the finite element model must follow exactly this curve, derived from interpolated laboratory tests. The stresses for all integration points are saved to a database ($\frac{\tau_{cyc}}{\sigma'_c}$). See Figure F.2 (c).

4. Excess pore pressure

Input: $\frac{\tau_{cyc}}{\sigma'_c}$, $\frac{\tau_{mean}}{\sigma'_c}$, N **Output:** Δu

The excess pore pressure is calculated based on the normalized cyclic shear stress and mean shear stress of step (3) and the number of cycles of the first storm parcel. The mean load may be considered as well for the selection of the type 2 contour plot ($\frac{\tau_{mean}}{\sigma'_c}$).

5. Dissipation

Input model 1: F_{mean}, Δu, $\frac{\tau_{mean}}{\sigma'_c}$ **Output:** N_{eq}

The mean load F_{mean} of the first cycle is applied in a restart analysis of the mean model. The calculated excess pore pressure is used to calculate the effective stress in each integration point. Full consolidation is allowed. The dissipation can be done under constant γ_{cyc} or τ_{cyc} resulting in order to estimate a smaller N_{eq}. Herein, a constant CSR is assumed. The excess pore pressure is analytically superposed. The residual dissipated excess pore pressure can be calculated to a new number of cycles for which a new contour plot can be derived. The result of dissipation and change in σ'_{oct} in mean model influences the input for cyclic model (as changes γ_{mean} and stress distribution occur). The principal stresses and strains as well as the equivalent volumetric strains are calculated. See Figure F.2 (d, e). If the load is not incrementally applied also Figure F.2 (f, g, h).

6. Next storm package

Input model 2: F_{cyc}, γ_{mean}, N_{eq} **Output:** γ_{cyc}, τ_{cyc}

The second load parcel is used. The results of the mean model from load parcel 1 are used and the cyclic amplitude of load parcel 2 is added in an undrained manner. The mean shear strain, effective octahedral consolidation stress and the N_{eq} is given from the mean phase. A new shear stress is calculated for load parcel 2.

7. Equivalent number of cycles

Input: τ_{cyc}, N_{eq}, N **Output**: Δu

From the N_{eq} and the number of cycles N of load parcel 2, a new excess pore pressure is calculated with $N_{eq} + N$ and applied to the mean model. Subsequently, the mean load of load parcel 2 is applied in a drained manner.

8. Iteration

Input: - **Output**: -

For larger stress redistributions, an iterative procedure arises before load parcel 3 is applied. After the successful calculation of the same global load increment F_{mean} as in the Mean-model (which can also be 100%), but this time related to the global cyclic load F_{cyc}, a new γ_{cyc} results for all elements, which is now predominantly not equal to zero. This in turn serves as a basis for the first step (Mean-model), so that a new γ_{mean} results as an output from the new input of γ_{cyc} in the Mean-model (the model restarts after the "wished-in-place" installation). The used stress-strain relation, based on the specified shear strain value, moves to larger CSR values for a larger γ_{cyc}. See Figure F.2 (h).

9. Further steps

Input: $\gamma_{mean}, \gamma_{cyc}, \Delta u$, N_{eq} **Output**: -

Due to the fact that an iterative process occurs, several calculation runs are necessary. The final result is a specific stress curve for each element, which can be displayed as a load path in the contour plot for the globally specified N_{eq}. Each integration point has an excess pore pressure, shear strain and number of equivalent cycles which are read from contour plots in order to account for the next load parcels. After an iteration until the convergence criterion is fulfilled, the calculation is finished or the next increment of the global load is added. An incremental load starts from the previous step and not from the initialization step. Convergence is achieved when, in both the Mean model and the Cyclic model, the largest difference in all elements between two consecutive calculation steps is smaller than a limiting criterion.

For a symmetric two-way loading the procedure is drastically simplified since no global mean load is present. A flow chart can be found in the following.

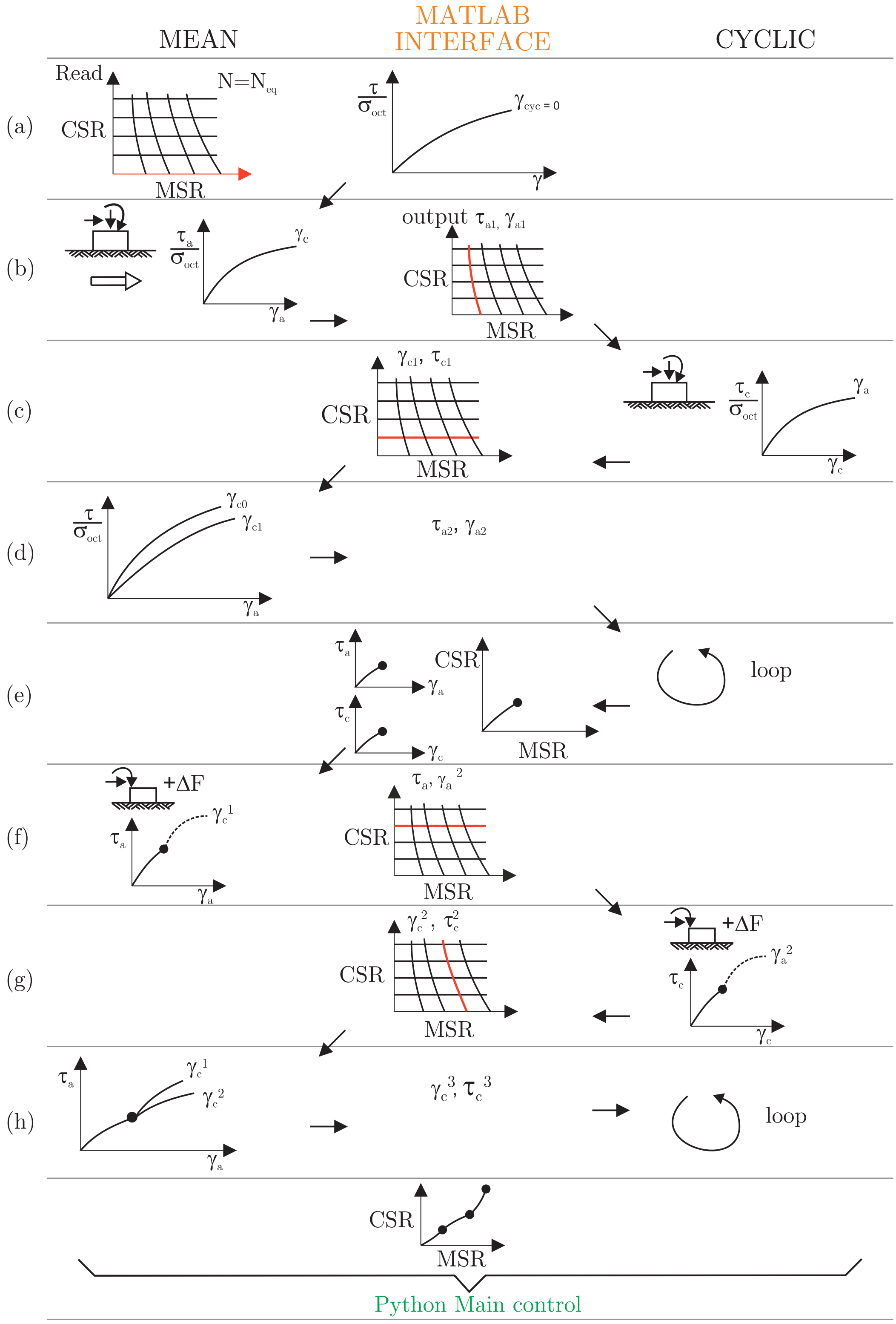

Figure F.2: Flow chart for EPPE - iteration without consideration of dissipation and multiple storm bins.

Curriculum vitae

Personal details

Jann-Eike Sören Saathoff

Born on 22nd August 1991 in Gehrden, Germany

married

Work experience

02/2017 – present	Research Assistant Institute for Geotechnical Engineering, Leibniz University Hannover
2017 – 2022	Occasional Freelancer ACP Geotechnik GmbH Jörss - Blunck - Ordemann GmbH Beratende Ingenieure im Bauwesen

Education

10/2014 – 07/2016	Leibniz University Hannover Master in Water-, Environmental- and Coastalengineering
10/2011 – 07/2014	Leibniz University Hannover Bachelor in Civil- and Environmental Engineering
07/2011	Wittekind-Gymnasium, Lübbecke General higher education entrance qualification (Abitur)

Bisher erschienene Mitteilungshefte des Instituts für Grundbau, Bodenmechanik und Energiewasserbau

Herausgeber: Prof. Dr.-Ing. Dr.-Ing. E.h. Erich Lackner

Heft 1	Rizkallah, V.	Die erdstatische Bemessung von Wänden und Pfählen in Sandböden (1971)
Heft 2 *	Lohmann, H.	Ein Beitrag zur Spannungsberechnung in der elastisch-isotropen Halbebene unter tief angreifenden Lasten und Anwendungsmöglichkeiten auf den Baugrund (1971)
Heft 3 *	Weißenbach, A.	Baugrubensicherung – Berechnung und Konstruktion von Baugrubenumschließungen (1973)
Heft 4 *	Leonhardt, G.	Die Belastung von starren Rohrleitungen unter Dämmen (1973)
Heft 5	Rizkallah, V.	Großbohrpfähle – Beitrag zur Abschätzung der lotrechten Tragfähigkeit und der Wirtschaftlichkeit (1973)
Heft 6	Hahn, F. R.	Ein Beitrag zur Herstellung und Ermittlung der Tragfähigkeit von temporären Erdankern in den Bodenarten der hannoverschen Kreideformation (1974)
Heft 7	Blümel, W.	Ein Beitrag zum eindimensionalen Konsolidierungsverhalten von Klei im Kompressionsversuch (1974)
Heft 8	Grade, H.	Ein Beitrag zur Abschätzung der Tragfähigkeit von Verpreßankern in nicht-injizierbaren, nichtbindigen Böden (1974)
Heft 9	Krämer, U.	Zugwiderstände und Eindringverhalten von Schiffsankern in nichtbindige Böden (1974)
Heft 10	Krämer, U., Rizkallah, V.	Erfahrungen bei der Ermittlung von Scherparametern im Kastenschergerät (1976)
Heft 11 *	Richwien, W.	Zum Einfluß der Konsolidierungsdauer auf die wirksame Spannung und die Scherfestigkeit von aufbereitetem Klei (1976)
Heft 12	Krämer, H.	Abschätzung der Tragfähigkeit von Verpreßankern durch Anwendung der Korrelationstheorie (1977)
Heft 13	Quast, P.	Ein Beitrag zum Kriechverhalten eines norddeutschen Kleis (1977)
Heft 14	Paschen, R.	Konsolidierungs- und Scherverhalten von salzhaltigem Klei (1977)
Heft 15 *	Liedtke, L.	Berechnung der Tragfähigkeit von temporären Erdankern mit der Methode der finiten Elemente (1978)
Heft 16	Blümel, W.	Ein Verfahren zur Verminderung des Porenwasserdrucks bei Baugruben im Ton durch Entspannungsbohrungen (1979)

* vergriffen.

Herausgeber: Prof. Dr.-Ing. Dr.-Ing. E.h. Victor Rizkallah

Heft 17 *	Hellweg, V.	Ein Vorschlag zur Abschätzung des Setzungs- und Sackungsverhaltens nichtbindiger Böden bei Durchnässung (1981)
Heft 18	Richwien, W.	Das Formänderungs- und Festigkeitsverhalten weicher bindiger Böden (1981)
Heft 19 *	Maschwitz, G.	Ein Beitrag zur Abschätzung des Tragverhaltens von unbewehrten pfahlartigen Tragelementen (1983)
Heft 20	Cunze, G.	Ein Beitrag zur Abschätzung des Porenwasserüberdrucks beim Rammen von Verdrängungspfählen in bindige Böden (1985)
Heft 21	Wehner, T.	Seegangserzeugte Spannungsänderungen im Sandkern eines Seedeichs (1987)
Heft 22 *	Rizkallah, V. et al.	Festschrift aus Anlaß des 75. Geburtstages von o. Prof. em. Dr.-Ing. Dr.-Ing. E.h. Erich Lackner (1988)
Heft 23 *	El Sherif, M. M.	Ein Beitrag zur Stabilisierung von bindigen Sedimentböden in Entwicklungsländern (1988)
Heft 24 *	Buchmann, K.-J.	Zum Tragverhalten ausgesteifter Bohrpfahlwände im Hannoverschen Ton (1988)
Heft 25	Harder, H.	Numerische Modellierung des "Cone Penetration Testsïn wassergesättigten bindigen Böden (1989)
Heft 26 *	Rizkallah, V., Hilmer, K.	Bauwerksunterfangung und Baugrundinjektion mit hohen Drücken (Düsenstrahlinjektion) (1989)
Heft 28 *	Rizkallah, V. et al.	Bauschäden im Spezialtiefbau (Baugruben, Rohrvortriebe, unterirdische Bauanlagen) (1990)
Heft 29	Rizkallah, V. et al.	Geböschte Baugruben, Baugruben mit Stahlspundwänden (1991)
Heft 30	Eklu-Natey, D.	Erodierbarkeit zementstabilisierter tropischer Böden im Straßenbau Togos (1992)
Heft 31	Achmus, M., Rizkallah, V.	Vortrieb von Rechteckprofilen (Belastungen-Bemessung-Anwendung) (1992)
Heft 32	Jebe, P., Rizkallah, V. et al.	Untersuchung von Hochbauschäden in den neuen Bundesländern Teil 1: Globale Bestandsaufnahme und systematische Erfassung (1993)
Heft 33	Beilke, O.	Interaktionsverhalten des Bauwerks "Fernwärmeleitung-Bettungsmaterial"(1993)
Heft 34	Jebe, P., Rizkallah, V. et al.	Untersuchung von Hochbauschäden in den neuen Bundesländern Teil 2: Dokumentation des baulichen Zustands historischer Bauwerke (1993)
Heft 35 *	Vogel, J.	Untersuchungen bauschadensrelevanter Faktoren beim Vorpressen begehbarer Rohre (1993)
Heft 36	Vogel, J. et al.	Festschrift aus Anlaß des 60. Geburtstages von Univ.-Prof. Dr.-Ing. V. Rizkallah (1993)
Heft 38	Vogel, J., Rizkallah, V. et al.	Begehbare und nichtbegehbare Rohrvortriebe Verfahren, Bauschadensfälle und Empfehlungen zur Schadensminimierung (1993)

Heft 39	Jebe, P., Rizkallah, V.	Beispiele zur Sanierung alter Bausubstanz (1994)
Heft 41	Achmus, M.	Zur Berechnung der Beanspruchungen und Verschiebungen erdverlegter Fernwärmeleitungen (1995)
Heft 43	von Bloh, G.	Verfahren zur Ermittlung des Scherverhaltens von Bagger- und Klärschlamm mit der Flügelsonde (1995)
Heft 44	Clasmeier, H.-D.	Ein Beitrag zur erdstatischen Berechnung von Kreiszellenfangedämmen (1995)
Heft 45	Hasan, M.	Abschätzung der Eindring- und Reibungswiderstände beim unterirdischen Rohrvortrieb (1996)
Heft 47	Rizkallah, V., Richwien, A.	Beschleunigte Bestimmung des Wasserdurchlässigkeitsbeiwertes bindiger Böden (1998)
Heft 48 *	Bruns, T.	Untersuchung des Tragverhaltens von Ortbetonschraubpfählen (1998)
Heft 49	Döbbelin, J. U., Salveter, G. et al.	Festschrift aus Anlaß des 65. Geburtstages von Univ.-Prof. Dr.-Ing. V. Rizkallah (1998)
Heft 52	Salveter, G.	Validierung numerischer Verfahren zur Berechnung des Interaktionsverhaltens ”Fernwärmeleitung–Baugrund” (2000)
Heft 53	Döbbelin, J. U.	Zur geotechnischen Anwendung wissensbasierter Systeme mit Elementen der Fuzzy-Logik (2000)
Heft 54 *	Baesmann, A., Rizkallah, V.	Berechnung und Bemessung von Pfahl-Plattengründungen (2000)
Heft 55	Kaiser, J.	Zu Schadensursachen und zur Setzungsproblematik bei herkömmlichen Bauwerksunterfangungen (2000)
Heft 58	Döbbelin, J.U., Rizkallah, V.	Empfehlungen zur Vermeidung von Planungs- und Ausschreibungsfehlern bei Ingenieurbauwerken (2001)

* vergriffen.

Herausgeber: Prof. Dr.-Ing. Hanno Müller-Kirchenbauer / Prof. Dr.-Ing. Werner Blümel

Heft 27	Friedrich, W.	Ausbreitung chlorierter Kohlenwasserstoffe bei Einkapselung und Inversionsströmung (1989)
Heft 37	Rogner, J.	Modelle zur Beständigkeitsbewertung von Dichtwandmassen auf der Basis von Lagerungsversuchen (1993)
Heft 40	initiiert von Univ.-Prof. Dr.-Ing. habil. S. Savidis	Festschrift aus Anlaß des 60. Geburtstages von Univ.-Prof. Dr.-Ing. H. Müller–Kirchenbauer
Heft 42	Schlötzer, C.	Filtrationsverhalten von Dichtsuspensionen an flüssigkeitsgestützten Erdwänden (1995)

Heft 46	Brummermann, K.	Schutzschichten für Kunststoffdichtungsbahnen in Deponiebasis-Abdichtungen – Prüfung und Bewertung ihrer Wirksamkeit (1997)
Heft 50	Mbonimpa, M.	Injizierfähigkeit von Feistbindemittelsuspensionen zur Abdichtung von Lockergesteinen (1998)
Heft 51	Düser, O.	Verwertung von aus Bauschutt aufbereitetem Recyclingmaterial in mineralischen Dichtungssystemen (1999)
Heft 56	Stoewahse, C.	Ermittlung des Reibungsverhaltens von Geokunststoffen und Erdstoffen im Rahmenschergerät (2001)
Heft 57	Gawalek, K.	Silikatgele auf Organosilanbasis für Abdichtungsinjektionen im Lockergestein (2001)

Herausgeber: Prof. Dr.-Ing. Martin Achmus / Prof. Dr.-Ing. Werner Blümel

Heft 59	Doll, H.	Dimensionierung von Kunststofflinern – Close-Fit-Verfahren (2001)
Heft 60	Kuk, M.	Untersuchungen zur Beeinflussung der Feistbindemittelausbreitung im Lockergestein durch Filtrationsmechanismen (2004)
Heft 61	Achmus, M., Kaiser, J., tom Wörden, F.	Bauwerkserschütterungen durch Tiefbauarbeiten (2005)
Heft 62	Mansour, B.G.S.	Investigations on Design and Rehabilitation Options for River Barrages with Special Respect to Piping (2005)
Heft 63	Achmus, M.	Bodenmechanik und Grundbau – Grundlagen und Konzepte (2007)
Heft 64	Weidlich, I.	Untersuchung zur Reibung an zyklisch axial verschobenen erdverlegten Rohren (2008)
Heft 65	Kuo, Y.-S.	On the behavior of large-diameter piles under cyclic lateral load (2008)
Heft 66	Maßmann, J.	Modeling of Excavation Induced Coupled Hydraulic-Mechanical Processes in Claystone (2009)
Heft 67	Müller-Kirchenbauer, A.	Funktionsnachweis für geotextile Tondichtungsbahnen in Deponieoberflächenabdichtungen (2009)
Heft 68	tom Wörden, F.	Untersuchungen zum räumlichen aktiven Erddruck auf starre vertikale Bauteile im nichtbindigen Boden (2010)
Heft 69	Quast, A.	Zur Baugrundsteifigkeit bei der gesamtdynamischen Berechnung von Windenergieanlagen (2010)
Heft 70	Bosseler, B.	Prüfung und Bewertung von Produkten und Verfahren zum Bau und zur Instandhaltung unterirdicher Kanälen und Leitungen (2010)

Bisher erschienene Mitteilungshefte des Instituts für Geotechnik

Herausgeber: Prof. Dr.-Ing. Martin Achmus

Heft 71	Peralta, P.	Investigations on the behavior of large diameter piles under long-term lateral cyclic loading in cohesionless soil (2010)
Heft 72	Ahlinhan, M.F.	Untersuchungen zur inneren Erosionsstabilität nichtbindiger Böden (2011)
Heft 73	Linero-Molina, C.	Vulkanische Ascheböden als Straßenbaustoff (2011)
Heft 74	Ghassoun, S.	Numerical Modeling of Spatial Passive Earth Pressure (2012)
Heft 75	Zapf, D	Dimensionierung von Gasspeicherkavernen im Salzstockrandbereich (2014)
Heft 76	Thieken, K.	Geotechnical Design Aspects of Foundations for Offshore Wind Energy Converters (2015)
Heft 77	Albiker, J.	Untersuchungen zum Tragverhalten zyklisch lateral belasteter Pfähle in nichtbindigen Böden (2016)
Heft 78	Heinemann, M.	Experimentelle Ermittlung und Bewertung des Reibungsverhaltens von Geokunststoffen (2016)
Heft 79	Klameth, M.	Praktische Anwendungsmöglichkeiten des MAC-Tests für die Zustandsbewertung von Kanälen (2017)
Heft 80	Schmoor, K.A.	Probabilistische Analyse zum Sicherheitsniveau von Offshore-Gründungspfählen (2017)
Heft 81	Schäfers, A.M.	Berechnung der Oberflächenverformungen über Speicherkavernen im Steinsalz mittels eines erweiterten Einflussfunktionsverfahrens und numerischer Methoden (2018)
Heft 82	Naarmann, M.	Kluftinjektionen mit hohen Dichtheitsanforderungen (2018)
Heft 83	Yildirim, S.	Berücksichtigung des mechanischen Schädigungsverhaltens von Salzgestein bei der Berechnung von Infiltrationsrissen im Randbereich von Gasspeicherkavernen (2019)
Heft 84	Wilmsmeier, D.	Ein Beitrag zur Rohr-Boden-Interaktion von grabenlos verlegten Fernwärmeleitungen (2020)
Heft 85	Gütz, P.	Tensile-Loaded Suction Bucket Foundations for Offshore Structures in Sand (2020)
Heft 86	Wolfrum, D.	Wechselwirkungsverhalten von thermisch beanspruchten Rohren und zeitweise fließfähigen, selbstverdichtenden Verfüllbaustoffen (2021)
Heft 87	Terceros, M.	A new p-y Approach to Pile Foundations with Arbitrary Dimensions under Monotonic Load in Cohesive Soils (2021)
Heft 88	Saathoff, J.-E.	Modelling of Excess Pore Pressure Accumulation in Sand around Cyclically Loaded Foundations (2022)